Aus der Klinik für Strahlentherapie und Radioonkologie
der Medizinischen Fakultät Mannheim
(Direktor: Prof. Dr. med. Frank A. Giordano)

Characterization of the tumor microenvironment after combined radio- and immunotherapy in a murine glioblastoma model

Inauguraldissertation
zur Erlangung des Doctor scientiarum humanarum (Dr. sc. hum.)
der
Medizinischen Fakultät Mannheim
der Ruprecht-Karls-Universität
zu
Heidelberg

vorgelegt von
Barbara Link

aus
Hardheim
2023

Dekan: Prof. Dr. med. Sergij Goerdt
Referent: Prof. Dr. med. Frank A. Giordano

INDEX

LIST OF ABBREVIATIONS

°C	degrees Celsius	GBM	glioblastoma
µL	microliter	GFP	green fluorescent protein
µm	micrometer	GM-CSF	granulocyte macrophage-colony stimulating factor
µM	micromolar		
5-ALA	5-aminolevulinic acid	Gy	Gray, SI-unit of ionizing radiation dose
Ab	antibody		
ACK	ammonium chloride potassium	h	hour
AMP	adenosine monophosphate	HE	hematoxylin and eosin
ANGPT2	angiopoietin 2	HIF-1α	hypoxia-induced factor 1 alpha
APC	antigen-presenting cell	HMGB1	high-motility group protein B1
ARG1	arginase	IARC	International Agency for Research on Cancer
ATP	adenosine-5′-triphosphate		
B7-H1	B7 homolog 1	ICAM 1	intercellular adhesion molecule 1
BAC-1	B cell-attracting chemokine 1	IDH	isocitrate dehydrogenase
BBB	blood-brain barrier	IFN-γ	interferon γ
BSA	bovine serum albumin	IL	interleukin
BW	body weight	IMRT	intensity-modulated radiotherapy
CCLx	CC-chemokine ligand x	incl.	including
CCRx	CC chemokine receptor type x	ip.	intraperitoneal(ly)
CD	cluster of differentiation	IP-10	interferon gamma-induced protein 10
CFA	colony-forming assay		
cm	centimeter	I-TAC	interferon-inducible T cell alpha chemoattractant
CNS	central nervous system		
CO_2	carbon dioxide	KC	keratinocytes-derived chemokine
CT	computed tomography	kDa	kilodalton
CTACK	cutaneous T cell-attracting chemokine	kg	kilogram
		KPS	Karnofsky performance status
CTL	cytotoxic T cell	LINAC	linear accelerator
CXCLx	CXC-motive chemokine ligand x	LQ	linear-quadratic
CXCRx	CXC motif chemokine receptor x	M	molar
D_{50}	dose that reduces survival to 50%	MCP	monocyte chemoattractant protein
DAB	3,3'diaminobenzidine	MCP-1	monocyte chemotactic protein 1
DAMP	damage-associated molecular pattern	MDC	macrophage-derived chemokine
		MDSC	myeloid-derived suppressor cell
DC	dendritic cell	MERT	Macrophage Exclusion after Radiation Therapy
DICOM	Digital Imaging and Communications in Medicine standard		
		MFI	mean fluorescence intensity
DMEM/F-12	Dulbecco's Modified Eagle Medium/Nutrient Mixture F-12	mg	milligram
		MGMT	O^6-methylguanine methyltransferase
DSB	double-strand break	MHC	major histocompatibility complex
EBRT	external-beam radiotherapy	min	minutes
EDTA	ethylenediaminetetraacetic acid	MIP	macrophage inflammatory protein
ENA	epithelial-derived neutrophil-activating protein	mL	milliliter
		mm	millimeter
EOR	extent of resection	M-MDSC	monocytic MDSC
FBS	fetal bovine serum	MMF	Medetomidine-Midazolam-Fentanyl solution
FFF	flattening filter-free		
FGR	fluorescence-guided resection	MOI	multiplicity of infection
FoV	Field of view	mOsm	milliosmole
g	gram	MRI	magnetic resonance imaging
G	gauge	ms	milliseconds
GAM	glioma-associated microglia/macrophage	MST	median survival time

MV	megavolt	sc.	subcutaneous(ly)
NFκB	nuclear factor κB	SCYB16	small inducible cytokine B16
NK	natural killer	SDF-1	stromal cell-derived factor 1
nm	nanometer	SEM	standard error of mean
NO	nitrogen monoxide, nitric oxide	SF	surviving fraction
NOS	nitric oxide synthase	SOC	standard of care
NOS2	nitric oxide synthase 2	STING	stimulator of interferon genes
O^6-MG	O^6-methylguanine	SVZ	subventricular zone
OS	overall survival	TA	time acquisition
PBS	phosphate-buffered saline	TAM	tumor-associated macrophage
PBST	PBS/Triton Solution	TARC	thymus- and activation-regulated chemokine
PD-1	programmed cell death protein 1		
PD-L1	programmed death ligand 1	Tcon	conventional T cells
PE	plating efficiency	TE	echo time
Pen-Strep	penicillin-streptomycin	TGF-β	cytokines transforming growth factor β
PFA	paraformaldehyde		
pH	power of hydrogen	TIL	tumor-infiltrating lymphocyte
PMN-MDSC	polymorphonuclear MDSC	TLR4	toll-like receptor 4
q2d	every other day	TME	tumor microenvironment
QA	quality assurance	TMZ	temozolomide
RBE	relative biological effectiveness	TNF-α	tumor necrosis factor α
ROI	regions of interest	TR	repetition time
ROS	reactive oxygen species	Treg	regulatory T cell
RT	radiotherapy	VCAM-1	vascular cell adhesion molecule 1
s	seconds	VEGF	vascular endothelial growth factor
SA-PE	Streptavidin-PE	VMAT	volumetric-modulated arc therapy

LIST OF TABLES

LIST OF FIGURES

1   INTRODUCTION

1.1   Glioblastoma

Glioblastomas (GBMs) are the most invasive and aggressive tumors of the central nervous system (CNS). The International Agency for Research on Cancer's (IARC) global cancer statistics GLOBOCAN 2020 estimated 18,577 cases of newly diagnosed malignant primary brain tumors in adults for both sexes in Western Europe (10,312 men and 8,265 women). For Germany alone, the statistics determined an incidence number of 7,697 new cases (Sung et al., 2021). Up to 50% of all these malignant tumors are GBMs (Miller et al., 2021; Visser et al., 2015). Consequently, the European incidence rate of GBM is defined as 3.0 cases per 100,000 people per year, making GBM the most commonly diagnosed primary brain tumor in the Western European countries (Crocetti et al., 2012; Rock et al., 2012; Thakkar et al., 2014).

The 2016 WHO Classification of Tumors classified diffuse astrocytic tumors as diffuse astrocytoma, anaplastic astrocytoma, or glioblastoma based on histologic parameters; furthermore, GBMs were further divided into three groups depending on their isocitrate dehydrogenase (IDH) mutations: IDH wild-type, IDH-mutant and not otherwise specified (NOS) (Louis et al., 2016). Approximately 90% of primary GBMs correspond to the IDH wild-type, with only the remaining 10% of cases are IDH mutant and occurring preferentially in younger patients (Tamimi and Juweid, 2017).

The latest edition of the WHO Classification of Tumors of the Central Nervous System (WHO CNS5), published in 2021, adopts three genetic parameters to replace the previous exclusively histological classification. It groups all IDH-mutated diffuse astrocytic tumors as a single type (astrocytoma, IDH-mutated), which can be differentiated into tumor of grades 2, 3 or 4, and characterizes GBM IDH wild-type as grade 4 tumors in all cases, even when histologically presenting as lower grade (Louis et al., 2021).

Primary GBM affects more frequently men than women but can occur at any age. Furthermore, the incidence increases with age, resulting in median age at diagnosis of approximately 64 years with a diagnostic peak between 75 and 84 years (Miller et al., 2021; Tamimi and Juweid, 2017; Thakkar et al., 2014).

The typical symptoms of GBM are not only extremely variable but also appear late in the etiopathology. The symptoms depend on the specific location and geometry of the tumor and are developed due to the mass effect of the tumor or tumor-induced edema on the brain tissue. The increased pressure in the brain leads to rapid and unexpectedly developed common symptoms, present in about 50% of all patients. These include persistent headaches with a nonspecific pain pattern, seizures, dizziness, vomiting, ataxia, half-sided-weakness (hemiparesis), visual field disturbances and recurrent syncope. Because of these unspecific symptoms, GBM is also often misdiagnosed as various infections, immunological disorders or cardiovascular diseases (Urbanska et al., 2014). Other signs of disease are likely mistaken for degenerative brain diseases like progressive changes in mood and personality as well as cognitive dysfunctions such as the loss of memory or speech (Omuro and DeAngelis, 2013).

In order to define specific risk factors for GBM, various environmental factors and genetic markers have been investigated. Only a few environmental risk factors such as therapeutic ionizing radiation during prior radiotherapy (RT) trigger the development of GBMs. No association with diagnostic irradiations, like computed tomography (CT) scanning or dental X-rays, has been confirmed (Johnson et al., 2015). Other risk factors include immune factors and immune genes. Less than 5% of GBMs develop due to genetic predispositions such as various single nucleotide polymorphisms. On the other hand, no substantial evidence of an association between GBM and lifestyle could be detected (Lapointe et al., 2018; Thakkar et al., 2014).

GBMs are routinely classified by histologic features. The tumors are characteristically rapidly growing and highly malignant, accompanied by necrotic areas and abnormal growth of blood vessels around the tumor (Louis et al., 2007). They are typically located supratentorially in the four lobes of the brain with varying frequency: frontal (25%), temporal (20%), parietal (13%) and occipital (3%) (Davis, 2016).

GBMs are highly heterogeneous tumors that typically appear as single, irregular shaped lesions with heterogenic areas exhibiting multifocal hemorrhage, necrosis (approximately 80% of the total tumor mass) and cystic or gelatinous parts in the white matter (Agnihotri et al., 2013; Iacob and Dinca, 2009; Phillips et al., 2006).

Histopathologically, GBMs are pleomorphic tumors characterized by pseudopalisading nuclei, nuclear atypia, cellular and nuclear polymorphism, vascular thrombosis microvascular proliferation, prevalent high mitotic activity and necrosis (Iacob and Dinca, 2009). The tumors consist of cells in different sizes, shapes, differentiation stages as well as molecular and biological characteristics that are decisive for the therapy response or resistance (Bonavia et al., 2011; Hanif et al., 2017). In the core of the tumor, necrotic cells are found primarily (Omuro and DeAngelis, 2013).

GBMs arise from three different cell types with neural stem cell-like properties that form the brain supportive tissue. Neural stem cells, neural stem cell-derived astrocytes and oligodendrocyte precursor cells at various stages of differentiation grow malignantly with molecular alterations in different signaling pathways (Davis, 2016). The cellular origin of the GBM tumors has a significant contribution to tumor development leading to different growing behaviors, treatment resistance and tumor recurrence after resection (Bonavia et al., 2011; Yao et al., 2018).

GBM spread only along with pre-existing brain structures intrafascicular or within and along perivascular spaces resulting in satellite tumors in other brain areas that are difficult to treat. The tumors are able to proliferate rapidly by forming new blood vessels that support their aggressive growth. At the time of diagnosis, the GBM cells are already widely distributed in the surrounding parenchyma (Iacob and Dinca, 2009; Wang and Jiang, 2013).

Untreated GBM is lethal within a median survival time (MST) of three months, under the current standard of care (SOC) the median overall survival (OS) can be only extended to 16-21 months post-diagnosis (Ladomersky et al., 2019). For the first year after diagnosis, this adds up to 35%, with a significant survival advantage for men (Thakkar et al., 2014). Just around 43% of patients survive for 2 years and less than 5% of patients are still alive 5 years following diagnosis (Ladomersky et al.,

2019; Tamimi and Juweid, 2017). The survival rates for GBM patients have not improved notably over the last three decades (Tamimi and Juweid, 2017).

1.1.1   The current standard of treatment

For more than a decade, since 2005, the standard of GBM therapy still follows the so-called 'Stupp protocol' consisting of maximal cytoreductive surgical resection followed by combined external-beam RT (EBRT) and chemotherapy with the alkylating agent temozolomide (TMZ). This therapy concept leads to an increased median OS from 12.1 to 14.6 months compared with that of patients receiving radiation alone (Stupp et al., 2005). Mainly patients with a Karnofsky performance status (KPS) over 60 benefit from this therapy standard. Elderly or frail patients receive short-course RT of 40 Gy in 15 daily fractions with concomitant and adjuvant TMZ. Alternatively, patients with functional impairment, geriatric syndromes and methylated O^6-methylguanine methyltransferase (MGMT) promoter are usually treated with TMZ alone. On the other hand, an unmethylated promoter tumor status leads to a single treatment with hypofractionated RT meaning 25-40 Gy in 5-15 daily fractions (Minniti et al., 2019).

The key factor for prolonged survival of the GBM patients is the maximal safe extent of resection (EOR) of the tumor without compromising neurological function which can be very difficult depending on size, shape, localization and infiltration of the tumors. Reducing the radiation- and chemotherapy-resistant cells in the tumor center of a larger EOR correlates with improved therapeutic efficacy and an increased median survival rate (Lacroix et al., 2001; Stummer et al., 2011). The one-year survival is significantly increased in patients with an EOR greater than 90% compared with a lower EOR (Orringer et al., 2012).

To maximize EOR during surgery, neurosurgeons perform fluorescence-guided resection (FGR) using the fluorescent precursor 5-aminolevulinic acid (5-ALA). 5-ALA specifically labels the tumor tissue and helps to differentiate between normal brain cells and residual tumor cell tissue, in addition to computer-assisted imaging and intraoperative mapping techniques (Leroy et al., 2015). The use of 5-ALA improved the cases of complete resection from 36% using conventional methods to 65% (Stummer et al., 2006).

However, most GBMs are surgically incurable by their diffuse invasiveness, not clearly defined borders and permeation into the healthy surrounding parenchyma (Holland, 2000; Wang and Jiang, 2013).

GBM tumor cells not only infiltrate the surrounding brain tissue but also upregulate DNA repair enzymes and produce their own immunosuppressive cytokines to escape therapeutic interventions (Sousa et al., 2019; Weil et al., 2017; Yamada et al., 1995). Thus, complete resections of GBMs are nearly impossible; a large proportion of the tumor cells remain and invade later healthy brain tissue leading to an 85% local recurrence rate at the site of surgery (Petrecca et al., 2013; Ryken et al., 2008).

After surgery, the elimination of the residual tumor cells that have infiltrated the cavity surrounding normal brain tissue by an additional RT is recommended (Olson et al., 2009). The current SOC for postoperative RT consists of 30 sessions of focal, fractionated EBRT with a treatment dose of 60 Gy delivered in fractions of 2-2.67 Gy

daily to the surgical resection cavity and a 2 cm margin of surrounding brain tissue over 6 weeks. The RT is started after surgical wound healing around four weeks after resection (Batash et al., 2017; Wilson et al., 2014). The usually performed RT uses the three-dimensional conformal beam, intensity-modulated RT (IMRT) or volumetric-modulated arc therapy (VMAT). It delivers a high dose of radiation to the target volume while sparing surrounding critical structures and reducing radiation-related toxicity to normal tissue as well as the planned target volume margin, but requires accurate targeting (Gzell et al., 2017). This adjuvant RT increases the median survival by 3 to 12 months compared with surgery alone (Stupp et al., 2005).

Among other effects, irradiation can induces severe DNA damage to both the malignant cells as well as the healthy antitumor immune cells, during each treatment session, forcing a substantial cells to undergo apoptosis due to double-strand breaks (DSBs) (Baskar et al., 2014). The GBM cells vary in responsiveness to RT. Often, the therapy induces a remission phase of GBM. This response period is typically short and stopped by the recurrence of the tumor within one year after resection (Park et al., 2010).

The chemotherapy agent TMZ induces the formation of methylated DNA bases like O^6-methylguanine (O^6-MG), which interacts with thymine instead of cytosine during DNA replication. During the mismatch repair, the cell initiates apoptosis in response to numerous DSBs caused by the not complementary O^6-MG (Stupp et al., 2001). In this way, the addition of TMZ chemotherapy to the EBRT helps to force more tumor cells into apoptosis, leading to increased median patient survival. Also, the number of long-term survivors increases after RT plus TMZ from 11% to 27% at 2 years and from 2% to 10% at 5 years (Stupp et al., 2009). However, the median progression-free survival time is only 7 months. TMZ is administered in a daily dose of 75 mg per square meter of the body-surface area during RT, followed by a rest period of about one month after completion of RT. After radiation, six cycles of chemotherapy followed. Each cycle lasts 28 days and a daily dose of 150-200 mg per square meter is administered for 5 days in every cycle (Stupp et al., 2005).

The methylation of O^6-MG can be removed by MGMT, whose expression is regulated by the methylation of the promoter regions of the *MGMT* gene. Therefore, the tumor cells from patients with an unmethylated *MGMT* gene are less responsive to TMZ as a chemotherapeutic agent, making the gene methylation a prognostic factor (Blanc et al., 2004; Reifenberger et al., 2012; Weller et al., 2015). Patients with promoter methylation benefit from TMZ chemotherapy in terms of a prolonged median OS of 21.7 months and a two-year survival rate of 46% (Hegi et al., 2005).

GBM treatment is very challenging due to the complexity of the tumors and their microenvironments. The different cell types forming the GBM tumors respond in various ways to certain therapies which lead to tumor recurrence after some time. Still today, no SOC is established for the treatment of recurring GBM leading to a progression-free survival after recurrence of 10 weeks and OS of 30 weeks (Wong et al., 1999). In most, corresponding to 75% of cases, the patients could be not treated with a second surgery (Gallego, 2015). Re-irradiation with a dose of 30-60 Gy is recommended after local relapse, when feasible (KPS > 60, lesion size > 40 mm) (Torok et al., 2011).

However, all standard care modalities have characteristic side effects. The surgical

resection may cause focal neurological deficits. Depending on the tumor location, radiation volume, fraction size as well as total RT dose, the RT can complicate the clinical outcome by causing long-term adverse effects such as sleep disturbances, fatigue, depression, vascular injury, local radionecrosis and neurocognitive impairment. RT can potentiate the neurotoxic effects of TMZ following radiation-induced leakage of the blood-brain barrier (BBB). Other side effects of TMZ include unspecific effects like nausea, vomiting, headache and fatigue, but also anemia, lymphopenia or abnormally low levels of white blood cells (Klein, 2012; Lawrie et al., 2019).

1.1.2 Glioblastoma tumor environment

The GBM mass, in addition to the heterogeneous tumor cells, also consists of an accumulation of various resident and infiltrating host cells, secreted factors, and extracellular matrix, collectively referred to as the tumor microenvironment (TME) (Anderson and Simon, 2020; Laplagne et al., 2019) .

GBMs are poorly immunogenic tumors with few characterized cancer antigens localized in the immunologically distinct CNS (Patel and Pardoll, 2015). The tumors are so-called 'cold' tumors that are marginally interspersed with tumor-infiltrating lymphocytes (TILs) mostly expressing exhaustion makers. The TME in GBM is highly immunosuppressive characterized by cells such as regulatory T cells (Tregs), myeloid-derived suppressor cells (MDSCs) and restrictive cytokines secreted by tumor cells as well as glioma-associated microglia/macrophages (GAMs) (Brown et al., 2018).

The brain was a long time considered as an immune-privileged organ that is protected from immune cell invasion by the BBB. The BBB shows selective permeability that limits the diffusion of circulating antibodies (Abs) from the blood into the brain parenchyma (Wilson et al., 2010). In high-grade GBM, the BBB is perturbed, allowing various immune cells and immune metabolites to enter the brain (Wolburg et al., 2012). Also, the absence of a conventional lymphatic drainage in the brain restricts the trafficking of antigens from the inflammatory focus in the brain to the antigen-presenting cells (APCs) in the lymph nodes. However, antigen-specific primed T cells from cervical lymph nodes could enter the brain via the glial lymphatic system (Louveau et al., 2015). In addition, dendritic cells (DCs) constitute a less-prevalent subgroup of APCs that migrate from the brain to lymph nodes and elicit an antitumor immune response (D'Agostino et al., 2012).

Patrolling activated antigen-specific T cells are found in the brain itself, however, specialized APCs are underrepresented and the antigen presentation is further suppressed by the downregulation of the major histocompatibility complex (MHC) expression in GBM (Hickey et al., 1991; Smolders et al., 2018; Zagzag et al., 2005).

The several kinds of TILs within the CD3$^+$ T cell subset are inferior to the number of tumor-associated macrophages and microglia found in GBM tumors, with mainly CD8$^+$ cytotoxic T cell (CTL), conventional CD4$^+$ T helper cells and Tregs (CD4$^+$CD25$^+$FoxP3$^+$) comprising this tumor-infiltrating cell subset (Mohme and Neidert, 2020).

The amount of GBM-infiltrating CD8$^+$ CTLs, depending on whether detected by flow cytometry or histologically in pathological cross-sections, ranges from 0.002-12% of all cells, and the amount of CD8$^+$ T cells correlated with prolonged patient survival

(Hussain et al., 2006; Orrego et al., 2018). The cells accumulation is associated with increased expression of the chemoattractants CXC-motive chemokine ligand 9 (CXCL9), CXCL10, intercellular adhesion molecule 1 (ICAM 1, the cells themselves produce interferon γ (IFN-γ) in addition to a substantial amount of functionally exhaustion makers like CD39 or programmed cell death protein 1 (PD-1), also called CD279 (Weenink et al., 2019; Woroniecka et al., 2018). The PD-1 on the T cells interacts with programmed death ligand 1 (PD-L1), also known as CD274 or B7 homolog 1 (B7-H1), which is expressed on GBM cells, leading to the inhibition of T cell activation (Butte et al., 2007).

The ratio of Tregs ($CD3^+CD4^+CD25^+FoxP3^+$) in the $CD4^+$ subset in the GBM microenvironment varies widely. The infiltrating amount of immunosuppressive Tregs increases in GBM due to their chemoattraction by CCL22 or CCL2 produced by tumor cells (Chang et al., 2016; Crane et al., 2012; Jordan et al., 2008). This increase of Tregs in the TME could be detected already early in the tumor progression in preclinical GBM models (Kennedy et al., 2009).

The T cell function in the GBM microenvironment is downregulated by the immunosuppressive cytokines transforming growth factor β (TGF-β) and interleukin (IL) 10, which are released by tumor cells and are also characteristic for Tregs (Nduom et al., 2015; Perng and Lim, 2015). The effector T cells in the GBM microenvironment characteristically express checkpoint molecules like PD-1, CTLA-4, TIM-3 and CD39 and are in a state of functional impairment called exhaustion (Woroniecka et al., 2018). The two cytokines TGF-β and IL-10 reduce the production of IL-2 and IFN-γ and the tumor-specific function of $CD8^+$ CTLs (Grabowski et al., 2021).

In GBM, up to approximately 30-40% of the total viable tumor mass is composed of GAMs, a collective of bone marrow-derived tumor-associated macrophages (TAMs) and brain-resident microglia (Badie and Schartner, 2000; Gutmann et al., 2013; Morantz et al., 1979; Simmons et al., 2011). Microglia are the unique CNS resident macrophages that act as the first line of defense in the brain. Residing microglia defined as $CD45^{low}CD11b^+$ function as the predominant APCs in the CNS, but are a small minority of around 15% compared with TAMs in the GBM microenvironment (Chen et al., 2017; De Vleeschouwer and Bergers, 2017; Glass and Synowitz, 2014). TAMs defined as $CD45^{high}CD11b^+$ are with up to 85% of all GAMs the dominant infiltrating immune cells in the GBM microenvironment (Chen et al., 2017). The recruitment of these myeloid-derived macrophages in tumor-bearing brains is controlled by glioblastoma-derived chemoattractants, especially by the stromal cell-derived factor 1 (SDF-1, CXCL12) and the monocyte chemotactic protein 1 (MCP-1, CCL2) (Brown et al., 2018; Domingues et al., 2016; Platten et al., 2003; Wang et al., 2012).

In GL261 xenograft tumors, which are used as the gold standard in experimental GBM research due to their characteristic similarities to human GBM, 16% of all cells are microglia and 6.5% are macrophages/monocytes (Maes and Van Gool, 2011; Oh et al., 2014; Szulzewsky et al., 2015).

GAMs can be found in immune permissive or activated (M1) as well as in cytoprotective or immunosuppressive (M2) phenotypes. The M1 macrophages are induced by granulocyte macrophage-colony stimulating factor (GM-CSF) and produce

pro-inflammatory cytokines like tumor necrosis factor α (TNF-α), IL-1β or IL-6 at a low level. GBM polarizes macrophages into the immunosuppressive M2 phenotype via metabolites. Activated M2 macrophages are characterized by the high-level production of potent inhibitors of macrophage function TGF-β and IL-10 (Gieryng et al., 2017).

GBM-associated macrophages are poor inducers of T cell responses due to their lack of key molecules involved in T cell co-stimulation (CD86, CD80, CD40) (Hussain et al., 2006). GAMs can also shape the CD8$^+$ T cell activity in the GBM microenvironment by their production of arginase and nitric oxide synthase (NOS), which inhibits T cell proliferation (Weenink et al., 2020). GBM cells secret cytokines that promote the upregulation of PD-L1 on GAMs, leading to T cell apoptosis (Won et al., 2019).

MDSCs from an extremely heterogeneous cell population of myeloid cells that fail to differentiate into macrophages, granulocytes or dendritic cells. They play a critical role in the development of the immunosuppressive GBM microenvironment by inhibiting T cell mediated antitumor reactivity through various mechanisms (Bronte et al., 2016; Veglia et al., 2018).

Human MDSCs could be identified and separated into two major subsets based on their phenotypic and morphological features. The polymorphonuclear MDSCs (PMN-MDSCs) are defined as CD11b$^+$CD14$^-$CD15$^+$HLA$^-$DR$^-$ or CD11b$^+$CD14$^-$CD66b$^+$ and the monocytic MDSCs (M-MDSCs) are characterized by CD11b$^+$CD14$^+$CD15$^-$HLA$^-$DR$^{low/-}$ (Gieryng et al., 2017). The density of MDSCs in GBM correlates with disease progression. In GBM, with 82% the majority of MDSCs are PNM-MDSCs and just only 3% of monocytic nature (Raychaudhuri et al., 2015).

In mice, these MDSCs subsets can be separated by their expression of GR1, Ly6G and Ly6C surface molecules: CD11b$^+$Ly6G$^+$Ly6C$^{low/-}$ PMN-MDSCs and CD11b$^+$Ly6G$^-$Ly6C^{hi} M-MDSCs (Bronte et al., 2016).

The murine PMN-MDSCs downregulate the antigen-specific CD8$^+$ T cell activity mainly through the production of reactive oxygen species (ROS). Mouse M-MDSCs express high levels of nitric oxide (NO) and inducible nitric oxide synthase 2 (NOS2) as well as arginase (ARG1) which impair the antitumor response and directly lead to the damage of antitumor effector cells or the nitration of chemokines and T cell receptors (Ohl and Tenbrock, 2018; Youn et al., 2008).

Intra-tumoral MDSCs are able to inhibit the antitumor activity of effector T cells due to their strong expression of PD-L1. The interaction between PD-1 expressed on effector T cells and PD-L1 on the MDSCs surface downregulates the antitumor T cell-mediated reactivity (Ballbach et al., 2017; Lu et al., 2016; Noman et al., 2014).

MDSCs are involved in adenosine-related immune regulation as a consequence of their expression of the two ectoenzymes CD39 and CD73. Adenosine-5′-triphosphate (ATP) is degraded to adenosine monophosphate (AMP) by hydrolysis which is mediated by CD39, the rate-limiting enzyme in the extracellular adenosine production (Zhao et al., 2017). The final hydrolysis step of AMP to immunosuppressive adenosine is catalyzed by CD73 (Li et al., 2017). The generation of other immunosuppressive cells, particularly Tregs, is supported by the secretion of TGF-β by MDSCs (Pan et al., 2010).

MDSCs are recruited from the bone marrow to the tumor site after the secretion of diverse chemokines by malignant cells, especially CCL2 and CCL3. The affinity of CCL2

and the chemokine receptor CCR2 is very high. The blocking of CCR2 significantly reduces the accumulation of MDSCs, especially of M-MDSC, in tumor (Chang et al., 2016; Li et al., 2020). MDSCs are also recruited via the CCR5 receptor and the ligands CCL3, CCL4 and CCL5. In this regard, these CCR5^{+} MDSCs have a stronger immunosuppressive pattern compared with other MDSCs (Blattner et al., 2018).

As preclinical studies pointed out, the depletion of MDSCs in GBM improves the survival of the animals proving that MDSCs have a significant part in the immunosuppression, promotion of tumor progression and recurrence in GBM (Fujita et al., 2011; Raychaudhuri et al., 2015).

1.2   Radiation-induced immune effects

RT plays a crucial role in the standard treatment of GBM, resulting not only in tumoricidal but also in multiple immune-modulatory and micro-environmental changes.

1.2.1   Immune activation by irradiation

High-dose RT (10-25 Gy) can act as an immunologic adjuvant and stimulate the antitumor immune response. Hypofractionated or single-dose RT works effectively via immunogenic cell death (Demaria et al., 2005; Demaria et al., 2016; Lee et al., 2009; Yoshimoto et al., 2014). Preclinical studies have shown that RT may influence the anti-cancer response by enhancing the cross-presentation of tumor antigens and altering the TME in terms of T cell recruitment and activation (Burnette et al., 2011; Gupta et al., 2012; Lee et al., 2009; Lugade et al., 2005). The enhanced immune response is usually provoked as an indirect response to different cellular stress signals by direct irradiation of the tumor (Lugade et al., 2005).

The reaction is initiated by release of damage-associated molecular patterns (DAMPs) such as high-motility group protein B1 (HMGB1) (Rovere-Querini et al., 2004; Scaffidi et al., 2002). HMGB1 as a toll-like receptor 4 (TLR4) agonist activates DCs, promotes their maturation, the release of ATP and, in this way, activates antitumor-specific T cells (Apetoh et al., 2007; Messmer et al., 2004). Activated macrophages and monocytes induced by ionizing radiation secrete a higher amount of HMGB1 into the TME, which activates the nuclear factor κB (NFκB) signaling pathway. NFκB regulates the transcription of various cytokines, including pro-inflammatory cytokines such as IL-1β, IL-6, IL-8 and TNF-α, early after RT (Messmer et al., 2004; Monjazeb et al., 2020). Moreover, the HMGB1 release, the subsequent activation of TLR4 as well as the production of IFNγ in the post-irradiated TME lead to enhanced antigen uptake and T cell-dependent tumor regression through the cross-priming capacity of tumor-infiltrating DCs (Apetoh et al., 2007; Lugade et al., 2008). Cross-priming is the result of a process in which APCs take up, process and present extracellular antigens via MHC class I molecules and stimulate naïve cytotoxic CD8^{+} T cells (Embgenbroich and Burgdorf, 2018; Sanchez-Paulete et al., 2017).

The cross-priming of the DCs is also enhanced via the stimulator of interferon genes (STING) pathway release of type I IFNs. Both attract DCs to the tumor tissue, leading to IL-1β secretion and priming of INFγ-producing CD8^{+} T cells, resulting in the

shrinkage of the tumor volume after RT (Burnette et al., 2011; Deng et al., 2014b; Ghiringhelli et al., 2009; Zanoni et al., 2022).

The enhanced induction of chemokines by the irradiated microenvironment increases immune cell trafficking, resulting in a significant tumor infiltration by activated T cells, which is additionally evoked by the irradiation-induced up-regulation of vascular cell adhesion molecule 1 (VCAM-1) expression on tumor vessels (Lugade et al., 2005). Nevertheless, one of the most essential promoter of antitumor immune response is the increased release of tumor antigens after the radiation-induced tumor cell death. This leads to an enhanced cross-presentation to T cells by APCs, clonal expansion and infiltration of tumor-primed active lymphocytes (Kaur and Asea, 2012).

1.2.2 Immune suppression by irradiation

Neither RT alone nor in combination with chemotherapy is able to prevent recurrence of GBM within the irradiated tumor volume. The survival of GBM-initiating cells in the radiation field, even after high-dose RT, indicates that RT not only has immune-boosting effects but also directly alters the tumor cells and results in a TME immune response that mediates radiation resistance (Seo et al., 2019).

RT could also have immunosuppressive effects. Immune cells are very sensitive to irradiation. Mature natural killer (NK) cells, B and T lymphocytes as well as precursors of monocytes initiate apoptosis already after exposure to radiation of around 2 Gy and are rapidly cleared from the radiation field (Falcke et al., 2018). Therefore, irradiation reduces the tumor antigen-specific T cell populations in the radiation field and induces local immunosuppression.

Irradiation doses of 5-15 Gy result in a significant loss of tumor-supplying blood vessels in the radiation field as a consequence of endothelial cell death. The outcome is a hypoxic TME that leads to advanced apoptosis of tumor cells but also triggers contradictive effects like reduced effector T-cell recruitment (Portella and Scala, 2019).

As a second response to the hypoxic environment, hypoxia-surviving cells start to overexpress the heterodimeric transcription factor *hypoxia-induced factor 1 alpha* (*HIF-1α*). This overexpression of *HIF-1α* activates genes like *vascular endothelial growth factor* (*VEGF*) and *angiopoietin 2* (*ANGPT2*). In the cascade, the activation of these genes leads to an increase in the expression of CXC-motive chemokine ligand 12 (CXCL12), also known as SDF-1, in the radiation field, which in turn promotes angiogenesis (Giordano et al., 2019; Jani et al., 2016).

CXCL12 is the only corresponding ligand for the heptahelical G protein-coupled chemokine receptor CXCR4 (CD184), which is highly expressed on myeloid-derived cells and so essential for their recruitment in the irradiated tumor tissue (Yang et al., 2018). In addition, CXCL12 binds to the chemokine receptor CXCR7, renamed as atypical chemokine receptor 3 (ACKR3), which is expressed on myeloid-derived or endothelial cells (Nagasawa, 2014; Walters et al., 2014). CXCR7 has a high affinity for CXCL12 and is often co-expressed with CXCR4 on the same cells (Wang et al., 2018).

CXCL12 exhibits a high homology level between humans and mice at the genomic and proteomic levels (90%) (Janssens et al., 2018). Preclinical studies have shown that mesenchymal-derived endothelial cells influx into the irradiated tumor tissue due to the

CXCL12-CXCR4 signaling. The accumulation of endothelial cells restores the radiation-induced vascular damage by vasculogenesis (Du et al., 2008; Kioi et al., 2010). In this way, the CXCL12-CXCR4 signaling pathway ensures vascular supply for the surviving tumor cells, allowing them to regrow and support their invasiveness and migration, which results in recurrence of the GBM (Kioi et al., 2010). Moreover, the CXCL12-CXCR4 interaction attracts tumor cells from the tumor point of origin into the subventricular zone (SVZ) which is reported as a radioresistant niche (Goffart et al., 2017).

Monocytes recruited via CXCL12-CXCR4 interaction differentiate into TAMs in the TME, which also promote immune suppression and vascular damage repair (Brown et al., 2017; Wang et al., 2013). Besides, these cells selectively recruit the immune-suppressive Tregs via the release of chemokines like CCL22 (Curiel et al., 2004).

Additionally, different tumor models had shown that the release of CXCL12 in the irradiated tumor bed as a driving molecule leads to the accumulation of $CXCR4^+$ immune-suppressive cells such as Tregs and MDSCs at the tumor site. In this way, the immune-suppressive cell populations in the TME expand and switch back to tumor-supporting status (Eckert et al., 2018; Obermajer et al., 2011).

The immunosuppressive characteristics of MDSCs are further supported by the radiation-induced release of ATP from the tumor cells as well as by the release of immunosuppressive cytokines (TGF-β and IL-10) (Aymeric et al., 2010).

Furthermore, radiation-induced upregulation of the PD-L1 expression on tumor cells and tumor-infiltrating macrophages depending on IFN type I and II secretion has been described (Garcia-Diaz et al., 2017; Sato et al., 2020; Wang et al., 2017). The MDSCs in the irradiated field also characteristically express high levels of PD-L1 after RT. As a result of this up-regulation, TAMs and MDSCs secrete the immunosuppressive cytokines TGF-β and IL-10, which promote the development of Tregs, in addition to their direct cytotoxicity against effector TILs via the interaction of PD-1 and its ligand PD-L1 (Deng et al., 2014a; Vatner and Formenti, 2015).

The PD-L1 molecule binds to its receptor PD-1 on antitumor-activated TILs. Binding activates the inhibitory characteristics of PD-L1 and initiates the T cell apoptosis cascade via IL-10 secretion as well as stimulates Treg proliferation and T cell exhaustion (Dong et al., 2002; Xue et al., 2017). Accordingly, the PD-1/PD-L1 pathway plays a major role in the suppression of tumor-specific T cell activation after RT, making the PD-1 expression of tumor-infiltrating T cells the most important marker of T cell exhaustion (Wherry, 2011).

C-C motif chemokine ligand 2 (CCL2), also called MCP1, and its receptor CCR2 are discussed as another possible recruitment axis leading to an increased influx of myeloid cells into the irradiated tumor bed after RT. After chemotherapy, $CCR2^+$ monocytes were identified as precursors to M2-polarized TAMs (Brown et al., 2020; DeNardo et al., 2011; Nakasone et al., 2012). Before treatment, CCL2 as a proinflammatory chemotactic factor induces Treg migration in GBM *in vitro* and *in vivo* via the CCR4 receptor. In the same tumor model, MDSCs were also recruited to the GBM microenvironment via the CCL2-CCR4/CCR2 axis (Chang et al., 2016). However, whether this recruiting path plays a relevant role after RT remains to be proven.

1.3 Novel treatment strategies for GBM

With the standard therapy of GBM, a median patient survival of only approximately 15 months is achieved, because surviving GBM cells can mediate an immune suppressive and tumor-friendly microenvironment supported by the previous treatment. For this reason, the search for newer therapeutic approaches focuses on the selective extinction of GBM cells using the patient's immune system. Thereby, the combination of local RT and the targeted systemic manipulation of the body's immune system appears to be the most promising therapeutic approach. Various treatment strategies focusing on the combination of vaccines (NCT02649582; NCT03395587; NCT04013672), checkpoint inhibitors (NCT03743662; NCT03961971; NCT04047706; NCT04817254), adoptive therapies (NCT03347097) or cytokine therapy (NCT04573192; NCT05131711) with radiation are currently under active clinical investigation.

Preclinical studies of different tumor models described RT as an enhancer of the antitumor responses combined with an immune checkpoint inhibitor, either a PD-1 or PD-L1 inhibitor (Gong et al., 2018). In GBM, the combination treatment of PD-1 blockade with high dose RT improves the survival of the animals significantly compared with either single treatment, resulting in a doubled median survival and enhanced long-term survival in 15-40% tumor-bearing mice. The amount of tumor-infiltrating cytotoxic T cells was increased in addition to decreased Treg activity (Kim et al., 2017; Zeng et al., 2013). The effect of the combination therapy may be correlated early after RT with the activation of infiltrating cytotoxic CD8$^+$ T cells and later with interactions of TAMs (Stessin et al., 2020).

The immune checkpoint inhibitors targeting PD1 or PD-L1 are tested as single treatments or in combination with other therapies in newly diagnosed or recurrent GBMs in phase II and III trials. However, no trial has demonstrated a meaningful benefit yet (Khasraw et al., 2020).

As a reason for these failures, the complex and multi-factorial systemic and intra-tumoral immunosuppression initiated by the GBM microenvironment or by the standard treatment used is discussed (Medikonda et al., 2020). Hyperfractionated RT reduces the CD4$^+$ T cells and supports in this way the immunosuppression in GBM (Grossman et al., 2011). The standard chemotherapy with TMZ abrogates the effect of anti-PD-1 therapy and represses the function of the effective T cells (Mathios et al., 2016).

As another immune-suppressive component of the post-treated GBM microenvironment, the dependence of the post-irradiation tumor revascularization on the CXCL12/CXCR4-mediated recruitment of myeloid cells like MDSCs is discussed.

To overcome this immune suppression is the key to an effective antitumor immune response in the treatment of GBM. Therefore, the influence of tumor-infiltrating MDSCs and the resulting lack of TILs in the GBM microenvironment became a target of a novel immune-based treatment strategy in GBM, which is termed by Brown et al. (2020) as macrophage exclusion after radiation therapy (MERT) (Brown et al., 2020)(Fig. 1). The main goal of this strategy is to prevent macrophage accumulation in irradiated tissues by disrupting the SDF-1/CXCR4-CXCR7 pathway, thereby improving local control and survival after RT (Thomas et al., 2019).
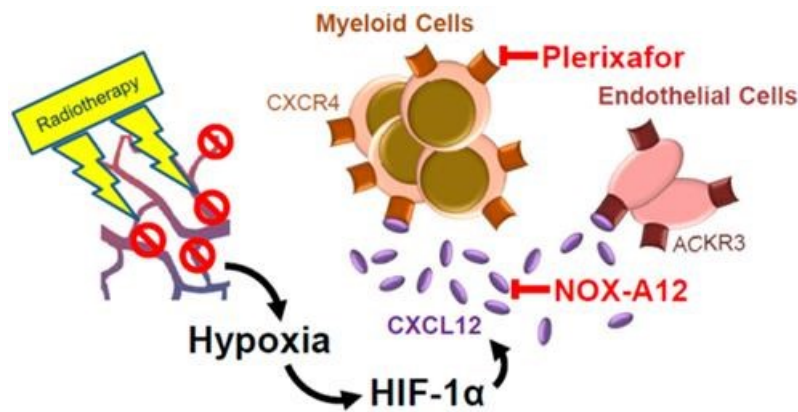
Fig. 1: Representation of the macrophage exclusion after radiation therapy (MERT) strategy. (Giordano et al., 2019)

The radiation-induced killing of endothelial cells of the tumor vasculature resulted in reduced tumor blood flow and increased hypoxia in the GBM microenvironment. As a consequent effect, HIF-1α is released which leads to an upregulation of CXCL12 which attracts CXCR4^{+} myeloid cells. The action of CXCL12 could be specifically inhibited by the Spiegelmer NOX-A12 (TME Pharma). Similarly, Plerixafor (AMD3100) could block the receptor CXCR4 and prevent its accumulation with its ligand. Both inhibition actions enhanced the tumor response to irradiation in previous studies.

Several preclinical studies of agents that block the influx of macrophages into the post-irradiated tumor environment or prevent the polarization of GAMs to the M2 phenotype result in an improved antitumor response after irradiation, regardless of the tumor model (Brown et al., 2020). Therefore, new therapeutic strategies focus on the combination of checkpoint inhibitors with immune modulators targeting the CXCR4/CXCL12 chemokine signaling axis with or without RT to block the influx of MDSCs (Brown et al., 2020; Wu et al., 2019).

Kioi et al. (2010) showed in an intracranial GBM xenograft model using the cell lines U251 and U87 that the irradiation-induced recruitment of MDSCs could be blocked by Plerixafor (AMD3100), a small molecule antagonist of the cell-surface receptor CXCR4, in addition to RT (Kioi et al., 2010). Under physiological conditions, Plerixafor specifically interacts with the carboxylate groups of the CXCR4 receptor, thereby inhibiting the binding of CXCL12 (National Center for Biotechnology Information, 2020). In the model used by Kioi et al. (2010), the inhibition of the CXCR4 function by Plerixafor influenced the tumor progression up to the complete tumor regression and prevented the recurrence of the irradiated tumors after RT (Kioi et al., 2010). A phase I/II study added the CXCR4 antagonist Plerixafor to GBM standard therapy. This inhibition was shown to improve the local control of tumor recurrence and to prolong the median OS to 21.3 months with a progression-free survival of 14.5 months. Magnetic resonance imaging (MRI) and histopathology proved that the inhibition of post-irradiation tumor revascularization was responsible for this (Thomas et al., 2019).

In the orthotropic preclinical GL261-C57BL/6 model, the effects of an anti-CXCR4 Ab in combination with an anti-PD-1 Ab were compared with the effects of the monotherapies alone. The combination therapy significantly reduced the CXCR4^{+} microglia population compared with the controls, and the long-term OS was significantly improved to 60%. Moreover, in the same model, the CD4^{+}/CD8^{+} T cell ratio and the ratio of Tregs to CD8^{+} T cells were significantly decreased as a result of the combination therapy (Wu et al., 2019).

Another treatment approach does not target the CXCR4 receptor, but rather inhibits its ligand CXCL12. This direct neutralization of CXCL12 was first tested in an immune-competent rat model of autochthonous brain tumors by Liu et al. (2014). The whole brain of the animals was irradiated with a single dose of 20 Gy and also treated with the CXCL12-inhibitor NOX-A12 (Olaptesed pegol, TME Pharma, Berlin, Germany). 28 days after treatment start, the tumors treated with RT and NOX-A12 were no longer detectable. The same effect was not observed in animals treated with the control therapies (Liu et al., 2014).

NOX-A12 is a PEGylated mirror-image RNA oligonucleotide binding with a high binding affinity to CXCL12 thereby preventing the binding to its receptor and inhibiting the CXCL12-CXCR4/CXCR7 pathway. The molecule size of the so-called Spiegelmer lies between biological molecules and small chemical molecules allowing to cross the BBB. Spiegelmers belong to the class of aptamers, which are synthesized from natural nucleotide blocks in a D-nucleotide conformation (manufacturer information, TME Pharma, Berlin, Germany). In preclinical studies, the half-life of NOX-A12 was approximately 40 h. It leads to a mobilization of white blood cells, hematopoietic stem cells and progenitor cells into the peripheral blood (Vater et al., 2013).

The recently completed clinical trial of NOX-A12 in advanced microsatellite-stable metastatic colorectal and pancreatic cancer (NCT03168139) demonstrated that the monotherapy with the anti-CXCL12 Spiegelmer NOX-A12 is safe and tolerable for patients. The determined post-treatment CXCL12 levels in blood and tumor tissue increased in correlation with the neutralization of the cytokine, an immunologically hotter tumor and clinical outcome. The T cell activation was also improved by NOX-A12, which was shown by increased levels of IFN-γ, IL-2, IL-16, TNF-β, CXCL9 and/or CXCL10 (Halama et al., 2019).

As another novel therapeutic approach, the neutralization of the main chemoattractant for the macrophages CCL2 could stop the recruitment of immunosuppressive GAMs and tumor angiogenesis.

Another drug candidate from the same company, NOX-E36 (Emapticap pegol, TME Pharma, Berlin, Germany), a 40-nucleotide oligonucleotide aptamer, binds to the CCL2 chemokine, and simultaneously neutralizes the highly related chemokines CCL8, CCL11 and CCL13 (Oberthur et al., 2015). This reduces the potential bypass pathways for the targeted bone marrow monocytes, which are relocated at the tumor after differentiation into pro-tumoral TAMs (manufacturer information, TME Pharma, Berlin, Germany).

Cho et al. (2019) used the rodent-specific Spiegelmer mNOX-E36 in a CCL2-expressing U87 MG rat GBM model in combination with the anti-VEGF Ab bevacizumab. The tumor volume of the treated animals and the CCL2 levels in the tumor tissue were smaller after the administration of mNOX-E36. The group also used the immunogenic glioma mouse model C57BL/6J with GL261 cells to determine the long time effects of the combination therapy with bevacizumab and mNOX-E36. In the model, the expression of CCL2 was significantly decreased in the tumor tissue and the survival extended for some days compared with the control groups (Cho et al., 2019).

1.4   Purpose

The combination of hypofractionated RT, checkpoint inhibitors such as an anti-PD-1 Ab, and/or immune modulators like CXCL12 and CCL2 inhibitors could significantly improve OS in GBM patients. However, clinical application of these new forms of therapy first require a preclinical assessment of the expected effects based on the OS time, tumor growth and the reactions of the tumor-associated immune cells in the tumor and TME. Thus, one goal of our study was to provide the basis for a clinical trial of the most effective combination therapy of immunomodulators and radiation.

The main objective of the study was to investigate the consequences associated with the blockade of the CXCR4-CXCL12 axis within the brain of C57BL/6JRj mice using NOX-A12, focusing on the overall survival of the animals, and to compare these results with the results of other therapeutic approaches. Moreover, an integral aspect of this study was the characterization of the immunological composition of the TME after the concurrent co-administration of RT and anti-CXCL12 therapy.

Therefore, the following aims were pursued:

- development of a suitable study design and establishment of an orthotopic immunocompetent murine glioma model to demonstrate the immune effects of different treatment strategies like RT combined with MERT using a CXCL12 and/or CCL2-inhibitor and RT with checkpoint inhibition involving an anti-PD-1 Ab;
- observation of the OS of different combination therapies in an immunocompetent GL261 murine model over a period of 100 days compared to the respective stand-alone therapies;
- investigation of the effect of the CXCL12-inhibitor NOX-A12 in combination with RT on tumor-infiltrating immune cells like CD4$^+$ or CD8$^+$ T cells, Tregs and MDSCs by analyzing in the tumor tissue, spleen and peripheral blood of tumor-bearing mice 20 days after tumor inoculation using flow cytometry;
- investigation of the expression of activation and suppression markers on the tumor-infiltrating lymphocytes after RT and administration of the immune modulator NOX-A12;
- analysis of the receptor pattern of immune cells, especially CD8$^+$ effector cells, Tregs and MDSCs after RT, measuring the expression of chemokine receptors CCR2, CCR4, CCR5, CXCR2, CXCR4 and CXCR7 on these cells by flow cytometry;
- investigation of the treatment-related changes by RT and/or CXCL12-inhibitor in the production of over 30 chemokines in tumor tissue and plasma of tumor bearing mice using a bead-based multiplex immune assay (Luminex$^®$ xMap technology).

2   MATERIAL

2.1   Animals and cells

reagent/ device	manufacturer	information
C57BL/6JRj mouse, female	Janvier Labs, Saint-Berthevin, France	female, 6-8 week old, weight: approx. 18 g
Mouse cage EUROSTANDARD TYP III	Tecniplast, Hohenpeissen-berg, Germany	820 cm^2 cage
SSNIFF grain-based regular diet	SSNIFF Spezialdiäten, Soest, Germany	suitable for long term experiments, moderate energy density, very low nitrosamine content
Brandt Markenzwieback	Hagen, Germany	additional diet after RT
GL261 cells		gift from AG Platten (UMM/ DKFZ)
Dulbecco's Modified Eagle's Media/Nutrient Mixture F-12 (DMEM/F-12)	Gibco, Life Technologies Europe, Bleiswijk, Netherlands	1:1 mixture of DMEM and Ham's F-12, 7.0-7.4 pH, with high glucose, L-glutamine, phenol red
HyClone™ Research Grade Fetal Bovine Serum (FBS)	GE Healthcare, Freiburg, Germany	low in Abs, high in growth factors, 3x 100 nm filtered, South American origin
Penicillin-streptomycin solution	Sigma-Aldrich Chemie GmbH, Munich, Germany	stabilized, with 10,000 units penicillin and 10 mg streptomycin/ mL, sterile-filtered
Dulbecco's Phosphate Buffer Saline (PBS) no Calcium, no Magnesium	Gibco, Life Technologies, Bleiswijk, Netherlands	osmolality: 270-300 mOsm/kg, formulation: potassium chloride (KCl) 200.0 mg/L, potassium phosphate monobasic (KH_2PO_4) 200.0 mg/L, sodium chloride (NaCl) 8000.0 mg/L, sodium phosphate dibasic (Na_2HPO_4-$7H_2O$) 160.0 mg/L
Polybrene Infection/ Transfection reagent 8 µg/mL	Sigma-Aldrich Chemie GmbH, Munich, Germany	cationic polymer, enhance the efficiency of the retroviral or lentiviral infection 100 to 1,000 fold
Lentiviral vector HR'SIN-cPPT-SEW	provided by Linda Hartmann (UMM, Strahlentherapie),	Date: 05.10.2012, Demaison et al. (2002)
Methanol	Carl Roth, Karlsruhe, Germany	32.04 g/mol
Acetic acid 100%	Carl Roth, Karlsruhe, Germany	60.05 g/mol
Crystal violet solution, 1%, aqueous solution	Sigma-Aldrich Chemie GmbH, Munich, Germany	407.98 g/mol
Centrifuge 5810 R	Eppendorf, Hamburg, Germany	refrigerated, different rotors

2.2   Intracerebral Implantation of GL261-GFP

reagent/ device	manufacturer	information
Small animal isoflurane vaporizer	AbbVie, Wiesbaden, Germany	
Polycarbonate narcosis box with sliding lid	Orthopedics laboratory UMM, Mannheim	

Injekt® Solo single-use syringes 2 ml	B. Braun Melsungen AG, Melsungen, Germany	made of polypropylene, Luer slip
Fentadon 50 µg/mL	Eurovet animal health, Bladel, Netherlands	active ingredient: fentanyl 50 µg (fentanyl citrate 78.5 µg), adjuvants: methyl parahydroxybenzoate (E218) 1.6 mg, propyl parahydroxy-benzoate (E216) 0.2 mg
Midazolam-Ratiopharm® 15 mg/3 mL injection solution	Ratiopharm GmbH, Ulm, Germany	active ingredient: midazolam hydrochloride 16.68 mg (benzo-diazepine), adjuvants: water for injections, sodium chloride, sodium hydroxide, hydrochloric acid for pH adjustment
Cepetor® 1 mg/mL	CP-Pharma Burgdorf, Germany	active ingredient: medetomidine hydrochloride injection, 1 mg/mL (0.85 mg medetomidine),adjuvants: methyl parahydroxy-benzoate (E 218) 1.0 mg, propyl parahydroxy-benzoate (E 216) 0.2 mg
Revertor® 5 mg/mL	CP-Pharma Burgdorf, Germany	active ingredient: atipamezole hydrochloride injection, 5 mg/mL, adjuvant: methyl 4-hydroxy-benzoate (E218) 1 mg
Flumazenil HEXAL® 0.1 mg/mL injection solution	Hexal AG, Holzkirchen, Germany	active ingredient: flumazenil 0.5 mg; adjuvants: sodium edetate, acetic acid 99%, sodium chloride, sodium hydroxide, hydrochloric acid for pH adjustment, water for injections (excipient)
Naloxon-Ratiopharm® 0.4 mg/mL injection solution	Ratiopharm GmbH, Ulm, Germany	active ingredient: naloxone hydrochloride dihydrate 0.44 mg (naloxone hydrochloride 0.4 mg), adjuvants: sodium chloride, hydrochloric acid for pH adjustment, water for injections
Surgical disposable scalpels	B. Braun Melsungen AG, Melsungen, Germany	double precision grinding, stainless steel
Bepanthen® eye and nose ointment	Bayer AG, Leverkusen, Germany	ingredients: rac-(3R)-3-hydroxy-4,4-dimethyloxolan-2-one, wool wax, viscose paraffin, white petroleum jelly, water for injections
Softasept® N skin disinfection	B. Braun Melsungen AG, Melsungen, Germany	alcoholic skin disinfectant, acts against bacteria (incl. MRSA, TbB) and fungi; limited virucidal (incl. HBV, HCV, HIV)
Aesculap Exacta GT416 shearer	Aesculap Suhl GmbH, Suhl, Germany	
Pilca depilatory creme	DMV Diedrichs Marken-vertrieb GmbH & Co. KG, Bad Pyrmont, Germany	maximum contact time: 3 minutes (human skin)
Stereotactic frame	TSE Systems, Bad Homburg, Germany	ensure accurate and reproducible placement of implantation syringe
Marathon Escort 3 drill	Marathon, Saeyang, China	

Rose-head burr	Gebr. Brasseler GmbH & Co. KG, Lemgo, Germany	diameter: 1.6 mm
Stereo microscope	Leica Camera AG, Wetzlar, Germany	
Gastight® Neuros™ syringe model 1702 RN point style 3, volume 25 µL	Hamilton Company, Reno, USA	delivering microvolume of cell solution to exact location, very little to no dead volume
Neuros™ replacement needle	Hamilton Company, Reno, USA	fine needle creates smaller injection sites, 33 gauge, small Hub RN needle, 3.03 in, point style 3 (blunt)
Rimadyl® Carprofen injectable 50 mg/mL	Zoetis, Berlin, Germany	active ingredient: carprofenum 50 mg, adjuvant: benzyl alcohol 10 mg
Bone wax	Ethicon/Johnson & Johnson, Diegem, Belgium	mixture of beeswax, paraffin and isopropyl palmitate, used to control bleeding from bone surfaces, non-absorbable
Vicryl (Polyglactin 910) suture 6-0, 3/8c, P-1 MP, 11 mm 45 cm undyed	Ethicon/Johnson & Johnson, Diegem, Belgium	synthetic, braided, absorbable suture, remaining tensile strength: 50% 21 days, 0% 35 days, absorption time: 56-70 days
Novaminsulfon-Ratiopharm® 500 mg/mL drops	Ratiopharm GmbH, Ulm, Germany	active ingredient: metamizole sodium 1 water 500 mg (metamizole 443.08 mg), adjuvant: cream aroma, purified water, saccharin sodium, sodium cyclamate, citric acid monohydrate, sodium hydroxide

2.3 Magnetic resonance imaging

reagent/ device	manufacturer	information
Isotonic sodiumchlorid-solution 0,9%	DELTAMEDICA GmbH, Reutlingen, Germany	liquid substitution, diluent
Gadovist® 1.0 mmol/mL injection solution	Bayer AG, Leverkusen, Germany	active ingredient: gadobutrol 39.31 g, adjuvants: calcobutrol sodium, trometamol, hydrochloric acid for pH adjustment, water for injections
Forene® 100% (V/V)	Abbvie, Wiesbaden, Germany	active ingredient: isofluran
Icon™ Avance III compact MRI system	Bruker/ Aspect imaging, Ettlingen, Germany	cryogen-free, permanent magnet bench-top MRI system (1 Tesla) for molecular and preclinical MRI (small rodents like rats and mice)

2.4 Treatments

reagent/ device	manufacturer	information
5% glucose solution	DELTAMEDICA GmbH, Reutlingen, Germany	diluent for Spiegelmers

reagent/ device	manufacturer	information
InVivoMAb anti-mouse PD-1 (CD279) Clone: 29F.1A12	BioXCell, Lebanon, USA	reacts with mouse PD-1 (CD279), formulation: PBS, pH 7.0, molecular weight: 150 kDa, application: *in vivo* blocking of PD-1/PD-L1 signaling, isotype: Rat IgG2a, kappa
InVivoMAb rat IgG2a isotype control; anti-trinitrophenol Clone: 2A3	BioXCell, Lebanon, USA	reacts with trinitrophenol, because trinitrophenol is not expressed by mammals this Ab is used as an isotype-matched control for rat IgG2a Abs
NOX-A12 (olaptesed pegol) Batch No: A5381L1-L4M1	TME Pharma, Berlin, Germany	Spiegelmer, targets CXCL12, binds to two key sites in chemokine protein, concentration 2mg/mL
mNOX-E36 (emapticap pegol) Batch-No: A9738L3M1	TME Pharma, Berlin, Germany	Spiegelmer, binds and neutralizes the mouse chemokine CCL2, concentration 2mg/mL
Omnifix®-F Luer Solo	B. Braun Melsungen AG, Melsungen, Germany	3-piece fine dosage syringe, volume: 1 mL
BD Microlance 3 Needles	Becton Dickinson, Eysins, Switzerland	2 different types: • 30G x 1/2", length:13 mm • 27G x 3/4", length: 19 mm
Combination stopper PE closing cones	B. Braun Melsungen AG, Melsungen, Germany	Luer Lock fitting male and female, sterile closing pre-filled syringes
SnuggleSafe® heat pad	Lenric C21 Ltd., Littlehampton, UK	wireless heat pad, up to 10 h warm
SOMATOM Force	Siemens Healthcare Diagnostics, Eschborn	delivering CT images for irradiation planning
LINAC Versa HD™ with an Agility™ 160-leaf multileaf collimator	Elekta AB, Stockholm, Sweden	

2.5   Perfusion

reagent/ device	manufacturer	information
Xylazine 2%	Serumwerk Bernburg, Bernburg, Germany	active ingredient: Xylazine hydrochloride 23.27 mg (20 mg xylazine), adjuvants: methyl 4-hydroxybenzoate 0.7 mg
Domitor 1 mg/mL	Vetoquinol GmbH, Ismaning, Germany	active ingredient: medetomidine hydrochloride 1.0 mg, adjuvants: methyl 4-hydroxybenzoate 1.0 mg, propyl 4-hydroxybenzoate 0.2 mg
Ketamidor 100 mg	WDT, Garbsen, Germany	active ingredient: ketamine 10%, adjuvant: benzethonium chloride
Micro-sample tube K3E potassium - EDTA, 1.3 mL	Sarstedt AG & Co., Nürnbrecht, Germany	
BD Perfusions™ syringe, 50 mL	Becton Dickinson GmbH, Heidelberg, Germany	made of polypropylene
In-Vivo Xtreme®	Bruker, Ettlingen, Germany	preclinical fluorescence and RGB white light imaging

2.6   Flow cytometric analysis

reagent/ device	manufacturer	information
Conjugated Abs listed in Table A-1 and Table A-2	See Table A-1 and Table A-2	
MACS SmartStrainers (100 µm)	Miltenyi Biotec B.V. & Co. KG, Bergisch Gladbach, Germany	cell strainer, mesh size: 100 µm, reservoir volume: 16 mL, generation single-cell suspensions after tissue dissociation, removal of cell aggregates and clumps
ACK (Ammonium-Chloride-Potassium) lysis buffer	Gibco, Life Technologies, Bleiswijk, Netherlands	used for lysis of red blood cells in samples containing white blood cells
Sodium azide (NaN$_3$)	SigSigma-Aldrich Chemie GmbH, Munich, Germany	for FACS buffer (PBS, 2% FBS, 0.05% NaN$_3$)
FcR Blocking Reagent	BD Biosciences, Heidelberg, Germany	used to block unwanted binding of Abs to mouse cells expressing Fc receptors (B cells, monocytes, macrophages)
BD FACS Lyric™	BD Biosciences, Heidelberg, Germany	3 lasers (blue, red, violet), 10 colors

2.7   Immunohistology

reagent/ device	manufacturer	information
Cryostat CM 1900	Leica Biosystems, Nussloch, Germany	
Leica Autostainer XL	Leica Biosystems, Nussloch, Germany	
Paraformaldehyde (PFA)	Alfa Aesar, Kandel, Germany	32% w/v aq. soln., methanol free, ampouled
Ki-67 (D3B5) Rabbit mAb	Cell Signaling Technology, Danvers, USA	1:200 dilution, mouse preferred, IHC formulated
Biotinylated anti-rabbit IgG (H + L)	VECTOR Laboratories INC., Burlingame, USA	1:200 dilution
Triton X-100 detergent	Bio-Rad Laboratories, Feldkirchen, Germany	
VECTASTAIN Elite ABC HRP Kit (peroxidase, standard)	VECTOR Laboratories INC., Burlingame, USA	sensitive avidin/biotin based peroxidase system
DAB Peroxidase (HRP) Substrate Kit (with nickel)	VECTOR Laboratories INC., Burlingame, USA	produces a brown reaction product in the presence of peroxidase (HRP) enzyme
ROTI® Histokitt	Carl Roth, Karlsruhe, Germany	results in permanent specimens, protects against bleaching
Microscope object slides	Fisher Scientific, Schwerte, Germany	76×26×1 mm, Superfrost
Microscope Cover Glasses 15H	Fisher Scientific, Schwerte, Germany	24×50 mm

2.8 Cytokine and Chemokine analysis

reagent/ device	manufacturer	information
Bio-Plex Pro Mouse Chemokine Standards	Bio-Rad Laboratories, Feldkirchen, Germany	mixture of 34 standard analytes for detecting mouse cytokines and chemokines
Bio-Plex Pro Mouse Chemokine 31-plex	Bio-Rad Laboratories, Feldkirchen, Germany	simultaneous analysis of multiple cytokines and chemokines using the Luminex technology in tumor tissue und plasma of the animals analytes: BCA-1/ CXCL13, IL-4, MIP-1α/ CCL3, CTACK/ CCL27, IL-6, MIP-1β/ CCL4, ENA-78/ CXCL5, IL-10, MIP-3α/ CCL20, Eotaxin/ CCL11, IL-16, RANTES/ CCL5, Eotaxin-2/ CCL24, IP-10/ CXCL10, MIP-3β/ CCL19, Fractalkine/ CX3CL1, I-TAC/ CXCL11, SCYB16/ CXCL16, GM-CSF, KC/ CXCL1, SDF-1/CXCL12 , I-309/ CCL1, MCP-1/ CCL2, TARC/ CCL17, IFN-γ, MCP-3/ CCL7, TNF-α, IL-1β, MCP-5/ CCL12, IL-2, MDC/ CCL22
Bio-Plex Pro Reagent Kit 5 Flat Plate	Bio-Rad Laboratories, Feldkirchen, Germany	components: HP detection Ab diluent, standard diluent, sample diluent, assay buffer, wash buffer, streptavidin-PE, flat bottom plate, sealing tape for magnetic separation
ReadyPrep™ Protein Extraction Kit (Total Protein)	Bio-Rad Laboratories, Feldkirchen, Germany	preparation of total cellular protein extracts from a wide variety of biological samples, trongly chaotropic extraction solution containing zwitterionic detergent ASB-14, up to 20 extractions
Pierce™ BCA Protein Assay Kit	Thermo Fisher Scientific, Rockford, USA	detergent-compatible formulation based on bicinchoninic acid (BCA) for the colorimetric detection and quantitation of total protein, required sample volume: 25 µl
Bovine serum albumin (BSA)	Sigma-Aldrich Chemie GmbH, Munich, Germany	~ 66 kDa, solubility: 40 mg/ml (water)
Tecan infinite M200 with Nanoquandt-Plate	Tecan Trading, Männedorf, Switzerland	multimode monochromator instrument with excellent sensitivity, multiplexing capabilities and high format flexibility for absorbance, fluorescence and luminescence measurement
Luminex® 200™ System	Luminex, Austin, USA	system to simultaneously measurement of up to 100 analytes based on flow cytometric principles

2.9   Software

reagent/ device	manufacturer	information
GraphPad Prism 6.0	GraphPad Software, San Diego, USA	statisic and graphic tool for data analysis
RAD-ADAPT	Biomedical Simulations Resource at the University of Southern California, USA	Zhang et al. (2017)
RadiAnt DICOM Viewer	Medixant, Poznan, Poland	viewer for medical images
Microsoft Office®	Microsoft, Redmond, USA	
Horos™ free DICOM Medical Image Viewer	horosproject.org	GNU Lesser General Public License, Version 3.0 (LGPL 3.0), open-source code software (FOSS)
ParaVision 6.0.1	Bruker, Ettlingen, Germany	preclinical MRI acquisition software
Molecular Imaging Software "MI" 7.5 win	Bruker, Ettlingen, Germany	for data acquisition and analysis of preclinical fluorescence and RGB white light imaging
BD FACSuite	BD Biosciences, Heidelberg, Germany	for data acquisition and analysis with the BD FACSLyric™ System
FlowJo™ v10.6	Tree Star, Ashland, USA	platform for single-cell flow cytometry analysis

3   METHODS

3.1   Study design

The preclinical study described in the following was designed to test the effectiveness of new combination therapies of immune therapy and RT. For a detailed overview of the performed study workflow see Fig. 2.
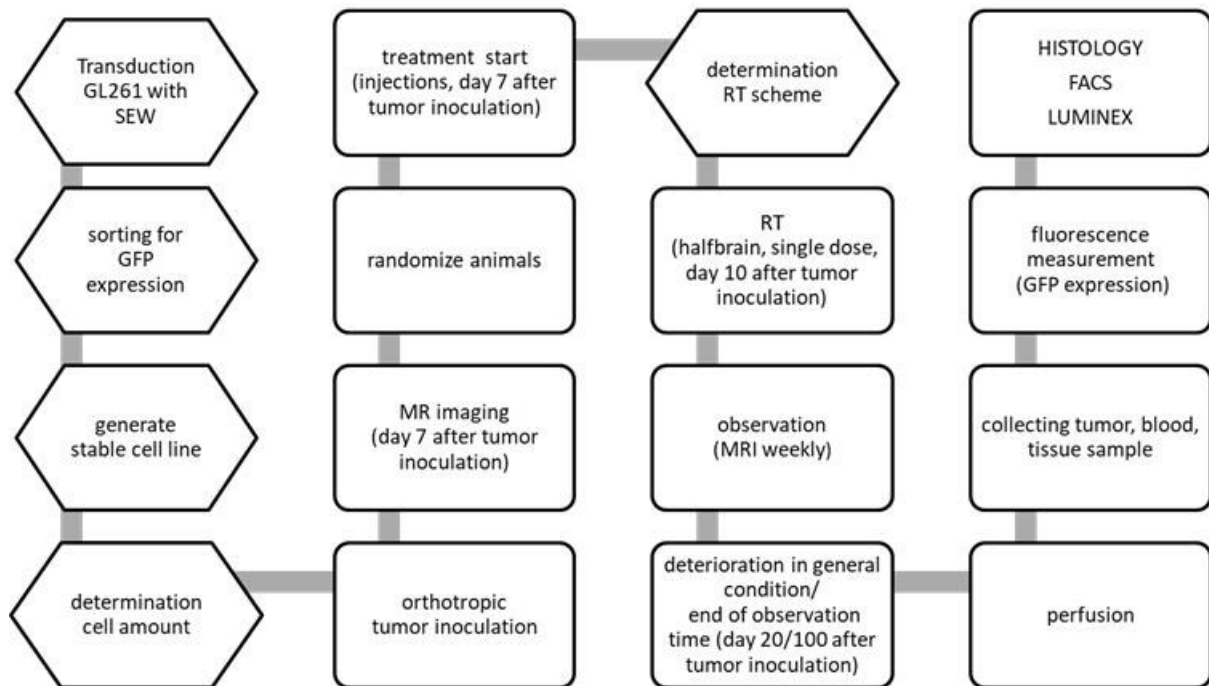
Fig. 2: Systematic overview of the study.
First, the murine glioma cell line used was stably transduced with resulting in expression of the GFP gene. Cell numbers of these GFP⁺ cells that favored a moderate tumor growth were determined. The animals were monitored with MRI after tumor inoculation. After confirmation of tumor growth, mice were randomized into treatment groups and the agents were administrated for the first time on day 7 after tumor inoculation. On day 10, RT was performed. Then, the animals were observed until deterioration of their general condition or ending of the observation period (depending on further analyses day 20 or day 100). After perfusion, the blood, spleen and brain of the mice were collected and the brains were screened for GFP expression before being used in further analyses. Hexagons: preliminary experiments, retangles: regular workflow.

Before starting the comparative tests, tumor cells from a murine glioma cell line were stably transduced with a lentiviral vector to express GFP and sorted for GFP expression. After the determination of the amount of cells, that favors moderate tumor growth, the same cell number was used for tumor inoculation in all subsequent experiments. To monitor tumor growth, the animals were examined weekly by MRI starting on the seventh day after tumor cell implantation. After the first MRI examination, the animals were randomized into different experimental groups and the therapeutic injections were applied for the first time.

In preliminary experiments, the inhibitory effects on the tumor growth after different fractions and doses of RT were examined and tested for their MST and risk of side effects. The results of these preliminary tests led to the RT scheme used in all further experiments on day 10 after tumor inoculation.

Then, in the survival experiments, the animals were observed weekly by MRI until a deterioration of their general condition could be detected or until the end of the

observation period of 100 days after tumor inoculation. For specific analyses, including flow cytometry or cytokine analysis via multiplex immune assay, the animals were observed only for 20 days after tumor inoculation.

The animals were sacrificed per perfusion. The brain was collected, as well as the spleen and blood, to analyze the tumor and systemic response of the treatments. The tumor-bearing brains were screened for GFP expression using fluorescence monitoring and then the tumor samples were isolated from the normal brain tissue for further analysis such as flow cytometry, cytokine analysis or immunohistochemistry.

3.2   Cell line

The preclinical evaluation of the combination therapies is based on a syngeneic mouse model. The immune-competent mouse strain C57BL/6J was implanted intracerebrally with murine glioma cells from the cell line GL261. Thanks to their characteristic similarities to human GBM, the tumors growing from them are considered as the gold standard for experimental GBM research (Maes and Van Gool, 2011; Oh et al., 2014).

In the 1990s, the Glioma 261 (GL261) cell line was established as an *in vitro* growing cell culture from the GL261 tumors. These tumors were induced as early as 1939 by intracranial injection of 3-methylcholanthrene in C57BL/6 mice and then obtained by serial transplantation (Jacobs et al., 2011; Oh et al., 2014; Szatmari et al., 2006).

In vitro, the cells have a population doubling time of 20 h and are rather radiosensitive with a 50% cell mortality after administration of less than 2 Gy. The *in vivo* radiosensitivity, in contrast, does not correlate with this dose. Local tumor irradiation with 4 Gy only slows the tumor progression, even if the treatment was applied very early after tumor inoculation (Szatmari et al., 2006).

The tumors growing from implanted GL261 cells are partially immunogenic because of their high expression levels of MHC class I molecules. Therefore, it is also the most commonly used GBM preclinical test model for new or optimization of older immunotherapies as well as for immunosuppressive effects and mechanisms (Oh et al., 2014; Szatmari et al., 2006). The tumors are invasive because of their typical formation with perivascular organization, proliferation near vasculature, hypoxia through blood vessel degeneration and neovascularization towards necrotic regions, but are not metastatic (Szatmari et al., 2006). However, the tumors do not spontaneously regress as in other murine tumor models (Oh et al., 2014). In previous studies, a 100% mortality rate was observed after implantation of 1×10^5 cells within 25 days (Szatmari et al., 2006).

The murine GL261 glioma cell line used (gift from AG Platten UMM/DKFZ) was first stably transduced with GFP to be able to identify the tumor-bearing tissue for further analyses. The GFP-positive GL261 cells were grown in Dulbecco's Modified Eagle Media/Nutrient Mixture F-12 (DMEM/F-12, Gibco, Bleiswijk, Netherlands) supplemented with 10% fetal bovine serum (FBS, GE Healthcare, Freiburg, Germany), and 1% penicillin-streptomycin (Pen-Strep, Sigma-Aldrich, Munich, Germany) at 37 °C and in an atmosphere of 5% CO_2 (Fig. 12, A).

3.2.1 Transduction with lentiviral vector

GL261 cells were seeded at a density of 8×10^4 cells per well in DMEM/F-12 containing 10% FBS and 1% Pen-Strep in a 24-well plate. After incubation at 37 °C and 5% CO_2 overnight, the medium was removed and polybrene (final concentration 8 µg/mL, Sigma-Aldrich, Munich, Germany) with the lentiviral vector was added. There were three wells used for each lentiviral construct and control. The cells were transduced with a multiplicity of infection (MOI) of 10.

For this propose, a suspension of the lentiviral vector HR'SIN-cPPT-SEW (Demaison et al., 2002) was used, which was prepared by Dr. Linda Hartmann (UMM, Strahlentherapie, Date: 20.12.2013) and contained 2×10^8 virions. For its production, 293T/17 cells (5×10^6) in DMEM/F-12 (Gibco, Bleiswijk, Netherlands) were transfected with the lentiviral plasmid pHR'SIN-cPPT-SEW and two packaging plasmids (pCMVΔR8.91 and pMD.G) using Metafectene (Biontex, Martinsried/Planegg, Germany). 24 h later, the medium was changed to DMEM/F-12 containing 10% FCS and 10 mM sodium-butyrate (Sigma-Aldrich, Munich, Germany). After another 10 h, the medium was replaced by serum-free DMEM/F-12 and cultured overnight. Subsequently, the virus-containing supernatant was purified by filtration through a 0.45 µm pore-size filter (Millipore, Carrigtwohill, Ireland) and concentrated using Vivaspin filter (100.000 MW, Sartorius, Goettingen, Germany) before being stored at -80°C. Viron titer was determined by fluorescence-activated cell sorting analysis for eGFP marker gene expression.

For transduction, 15 µL of the lentiviral suspension was mixed with 30 µL polybrene and 2955 µL medium without FBS. As a negative control, 30 µL polybrene and 2970 µL medium without FBS were mixed.

500 µL of the specific polybrene mixture was added to each well respectively. After gently swirling the plate, the cells were incubated for 4 h at 37 °C in a humidified incubator in an atmosphere of 5% CO_2. After 4 h, the media containing the lentiviral particles were removed from the wells and replaced with 1.5 mL fresh media with FBS. The cells were controlled for GFP expression under a fluorescence microscope on the next day. The cells were removed from the 24-well plate, pooled and seeded in a T75 flask and cultured for three passages.

After that, the cells were counted and sorted based on GFP expression at the Cell Sorting Core Facility of the Medical Faculty Mannheim. The purified cells were then plated in DMEM/F-12 containing 10% FBS and split once they reached confluence. To obtain a cell stock for all further experiments, the cells were cultured for three more passages before starting to implant the cells into animals.

3.2.2 Characterization of the radiation sensitivity of the transduced cell line

The cellular radiation sensitivity of the transduced GL261 cell line was determined by the clonogenic cell survival after irradiation using the colony-forming assay (CFA).

Eight hours before irradiation, GFP-expressing GL261 cells were sequentially diluted to ten times the desired concentration in the flask, meaning if 100 cells were planted per T25 flask, a suspension of 1000 cells/mL was prepared. The cells were seeded in triplicates in T25 flasks at the densities according to Table 1 with 5 mL of fresh culture medium.

After irradiation with different doses using 6 megavolts (MV) X-rays from a clinical linear accelerator (LINAC; Versa HD™, Elekta Instrument, Stockholm, Sweden), the cell solutions were incubated for 11 days at 37 °C in a humidified incubator in an atmosphere of 5% CO_2. Then, the surviving colonies were washed with PBS, fixed with 1:3 methanol/acetic acid solution for 10 min and stained with crystal violet solution (1 g/L) for 10 min. Three independent experiments were performed.

Table 1: Cell numbers seeded for CFA in relation to the irradiation dose

dose (Gy) 6 MV X-rays	cell number
0	100
2	200
4	500
6	2000
8	5000

The colonies with more than 50 cells were counted and the plating efficiency (PE) was calculated. The resulting surviving fractions (SFs) were fitted to the linear-quadratic (LQ) equation $SF(D) = PE \cdot e^{-(\propto D + \beta D^2)}$, with D being the radiation dose and α and β being the cell-specific parameters. αD represents the initial slope of the curve at low doses and βD the curvature of the curve at higher doses. The curve fitting was performed by using RAD-ADAPT software for modeling clonogenic assay data in radiation biology developed by the University of Southern California (Zhang et al., 2017).

3.3   Animals

All animal experiments were performed following all relevant ethical regulations for animal testing and research. In addition, all protocols were approved by the regional animal care committee (Regierungspräsidium Karlsruhe, Germany, approval number: 35-9185.81/G68/17).

In the present study, six- to nine-week-old female C57BL/6J wild-type mice (Janvier Labs, Saint-Berthevin, France) were purchased and used at the age of seven to twelve weeks.

The animals were housed under pathogen-free, controlled conditions (12-hour light/dark cycle, 23 ± 2 °C, 47% ± 5% relative humidity) at the animal facility of the Medical Research Center of the Medical Faculty Mannheim of Heidelberg University and the Bruker Preclinical Imaging Reference Center at the University Medical Centre Mannheim. The mice were kept in groups of a maximum of 8 animals in conventional mouse cages (Tecniplast, Hohenpeissenberg, Germany) and received a grain-based standard diet (SSNIFF Spezialdiäten, Soest, Germany) with water *ad libitum*.

After tumor inoculation, the animals were monitored daily for tumor-related symptoms including weight reduction of over 20%, convulsions, paralysis, stereotypies, apathy and/or pronounced motor disturbances for up to 100 days. The tumor growth was monitored using MRI on a weekly basis.

3.4 Intracerebral implantation of glioma xenografts

To implant the tumor cells, the animals were anesthetized with a subcutaneously (sc.) injected mixture of medetomidine (0.5 g/kg body weight (BW), Cepetor®, CP-Pharma, Burgdorf, Germany), midazolam (5 mg/kg BW, Ratiopharm, Ulm, Germany) and fentanyl (0.05 mg/kg BW, Eurovet animal health, Bladel, Netherlands) (MMF). After reaching the surgical tolerance, the fur on the head of the animals was trimmed with a small animal shearer (Aesculap, Suhl, Germany). Then, depilation cream (DMV Diedrichs Markenvertrieb, Bad Pyrmont, Germany) was applied and incubated for a maximum of 2 min to remove the remaining hair completely from the surgical area.

After disinfection of the scalp (skin disinfection, Braun, Melsungen, Germany) and application of an ophthalmic ointment (Bepanthen®, Bayer, Leverkusen, Germany), the head of the mouse was positioned in a stereotactic frame (TSE Systems, Bad Homburg, Germany) under a surgical stereomicroscope (Leica, Wetzlar, Germany) (Fig. 3, A). A linear skin incision was made starting in the midline between the eyes and ending in the midline shortly behind the bregma. A 0.5 mm trepanation was drilled into the right hemisphere of the skull 2.5 mm to the right lateral to the midline and 0.5 mm anterior to the bregma. Through this burr hole, a 25 µL gastight syringe (Neuros Syringe, Hamilton, Reno, USA) with a 33 G blunt needle was inserted at a depth of 4 mm from the dural surface (Fig. 3, B).

location of cell implantation:
2.5 mm right of midline
0.5 mm anterior to bregma
4.0 mm deep
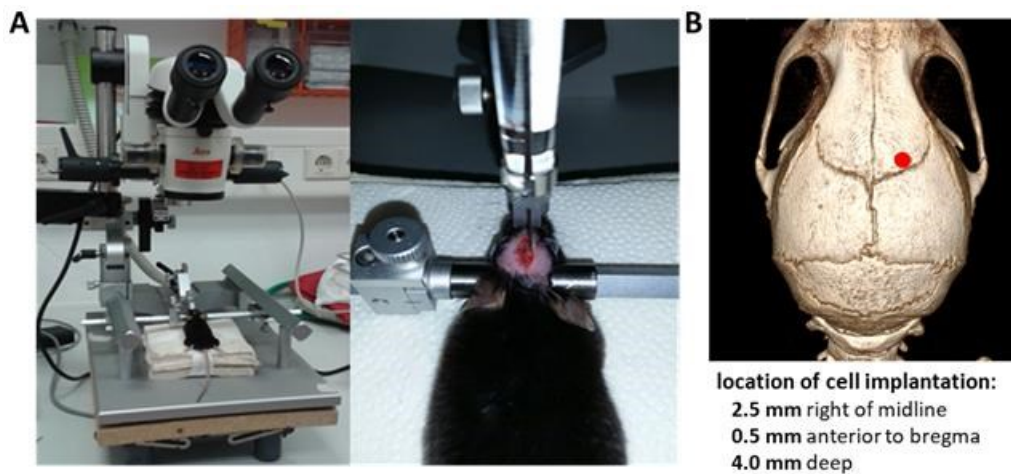
Fig. 3: Stereotactic engraftment of GL261-GFP cells.
(A) The animals anesthetized were fixed in a stereotactic frame under a surgical stereomicroscope to ensure the proper placement of the inoculation needle. (B) The tumor cells were implanted in the basal ganglia 0.5 mm in front of the bregma and 2.5 mm to the side of the midline at a depth of 4.0 mm. Red dot = place of implantation.

1×10^7 tumor cells were cultured to 80% confluence, trypsinized, washed and resuspended in sterile phosphate-buffered saline (PBS, Gibco, Bleiswijk, Netherlands). Then, the cells were diluted in 100 µL sterile PBS and filled into the gastight syringe free of air bubbles.

A maximum of 2 µL of GL261-GFP cell suspension was slowly injected over 10 min. After the inoculation of the cells, the burr hole was sealed with bone wax (Ethicon, Diegem, Belgium) and the margin of the incision was sewn up with simple interrupted stitches using absorbable suture material (Ethicon, Diegem, Belgium). For pain relief, the animals received sc. a non-steroidal anti-inflammatory drug 5 mg/kg BW carprofen

(Rimadyl[®], Zoetis, Berlin, Germany). The anesthesia was antagonized by sc. injection of a mixture of atipamezole (2.5 mg/kg BW, CP-Pharma, Burgdorf, Germany), flumazenil (0.5 mg/kg BW, Roche Pharma, Grenzach-Wyhlen, Germany) and naloxone (1.2 mg/kg BW, Ratiopharm, Ulm, Germany). Hydration was maintained by the sc. administration of 0.9% isotonic sodium chloride solution (DELTAMEDICA, Reutlingen, Germany) up to 1 mL. The mice were monitored on a heated pad until regaining consciousness.

The mice received postoperative pain treatment (novaminsulfon (200 mg/kg), Ratiopharm, Ulm, Germany) administered via drinking water for three days.

Thereafter, the animals were observed every other day up to 100 days post-inoculation.

3.5   Establishment of the animal model

The *in vivo* cell growth of the cell line used may vary significantly compared with to that as described in the literature due to different culture conditions and the effect of the transduced genes. Therefore, preliminary implantation experiments were used to determine the cell implantation quantity of tumor cells that favors moderate tumor growth.

After a maximum of four passages, the tumor cells were implanted at three different cell numbers in the basal ganglia of 10 animals. The tumor growth for the cell quantities 2.5×10^6 cells (n = 3), 1.5×10^6 cells (n = 3) and 1.5×10^5 cells (n = 4) was assessed by MRI after 21 days. This allowed the determination of the cell volume that enables optimal tumor growth for testing after orthotopic cell implantation.

Based on data in the literature, implantation experiments with lower cell counts were avoided (Oh et al., 2014). In addition, higher animal number were not considered for these preliminary experiments in accordance with the reduction principle for animal testing.

3.6   Survival experiments

For survival experiments, 1.5×10^5 GL261-GFP tumor cells were implanted into the right hemisphere of seven to twelve-week-old female C57Bl/6J mice. After confirmed signs of a tumor on day 7 post-inoculation, the animals were treated with different combinations of checkpoint inhibitors and immune modulators with or without RT as described under 3.7. In addition, an untreated control group was observed simultaneously, resulting in 15 animals not receiving any treatment.

The tumor growth was monitored weekly by MRI for up to 100 days after tumor inoculation. Then, the brains were checked for complete tumor regression. Complete tumor regression was defined as no tumor sign detectable by MRI and no positive fluorescence signal measured due to the GFP expression of the tumor cells after 100 days. For further verification, histological sections of the brains were screened for dividing tumor cells after hematoxylin and eosin staining (HE) as well as after Ki-67 staining (Fig. 15, C).

The RT scheme was chosen after exploratory comparison of different applications for their median survival and side effects.

Mice were examined daily for tumor-related symptoms and sacrificed when the tumor volume began to grow exponentially at an unrestrained rate and/or the animals' general condition deteriorated reaching the termination criteria. Survival curves represent the pooled data from two or three independent experiments, each with 3-6 animals.

3.7   Treatment of the animals

The animals were treated with different combination therapies to evaluate the effectiveness of these treatments. One checkpoint inhibitor (anti-PD-1 Ab) and two different immune modulators (NOX-A12, mNOX-E36) were tested for their efficacy as a single treatment (mono), as a combination treatment with each other (duo) and/or with radiotherapy (combination) according to the treatment scheme in Table 2 and Fig. 4.

Table 2: Overview of the treatment groups.

group	treatment				N animals
	RT 1 x 12 Gy	NOX-A12 20 µg/g in 5% glucose every 2 days sc.	mNOX-E36 20 µg/g in 5% glucose every 2 days sc.	Anti-PD-1 Ab 250 µg in PBS 6x every 3 days ip.	
control					15
mono 1	X				8
mono 2		X			9
mono 3			X		9
mono 4				X	9
duo 1		X		X	9
duo 2			X	X	9
combination 1	X			X	12
combination 2	X	X			10
combination 3	X	X		X	12
combination 4	X		X		12
combination 5	X		X	X	12
combination 6	X	X	X	X	9

3.7.1   Immunotherapy

An anti-PD-1 Ab (inVivoMAb anti-mouse PD-1, Clone 29F.1A12, BioXCell, Lebanon, USA) was used to clarify the effect of the immune checkpoint blockade in the model. The applied Ab blocks the PD-1 (CD279) receptor of activated T and B lymphocytes and myeloid cells which prevents the binding of its ligand PD-L1 expressed on the surface of tumor cells. This inhibition of the PD-1 signaling supports antitumor immune activity by preventing the inactivation of the T cells and reducing immunesuppressive cytokine production.

The Ab stock was diluted with PBS to a final concentration of 1.25 µg/µL, then aliquots of 250 µg Ab were prepared and stored at 4 °C until administration to the animals. The Ab was given intraperitoneally (ip.) six times every third day starting on day 7 after tumor inoculation (Fig. 4).
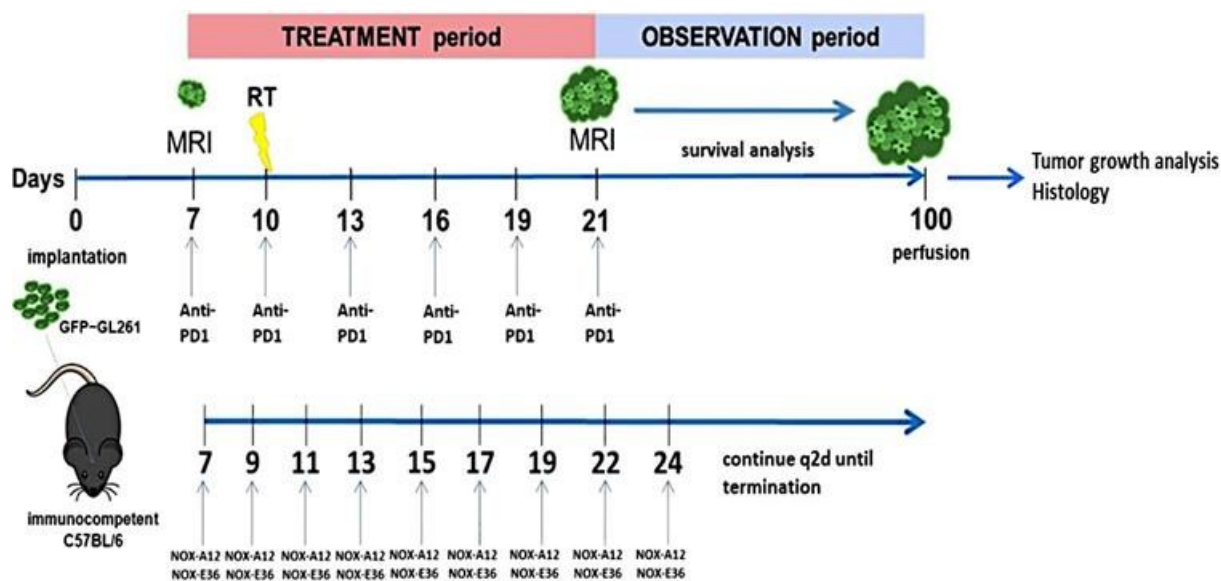
Fig. 4: Timeline illustrating the experimental treatment setup in the study.
Seven days after tumor inoculation, the animals were randomized into the respective treatment groups after MRI examination. Starting on day 7, the anti-PD-1 Ab was administered six times every three days. The CXCL12 antagonist NOX-A12 and the CCL2 antagonist mNOX-E36 were injected sc. every other day (q2d) until the end of the experiment on day 100. On day 10, the tumors were irradiated with 12 Gy.

The CXCL12 antagonist NOX-A12 (TME Pharma, Berlin, Germany) consists of RNA oligonucleotides in a L-configuration, also called Spiegelmers, which bind to CXCL12 like an Ab with high affinity and specificity. Spiegelmers are not vulnerable to degradation by nucleases nor hybridize with native nucleic acids. The molecules are immunologically passive thereby not eliciting an immune reaction.

The test substance, which was formulated as a lyophilisate, was diluted with sterile 5% glucose solution under aseptic conditions according to the manufacturer's handling instructions. To ensure proper dilution of the test substance, the tube containing 100 mg NOX-A12 oligonucleotide base was first filled up with 10 mL of 5% glucose, incubated at room temperature for up to 30 min and shaken occasionally during the incubation period. Then, the container was filled up to 50 mL with 5% glucose to a concentration of 2 µg/µL and aliquoted under aseptic conditions. The prepared injections were tightly sealed and stored protected from light at -20 ± 5 °C until administration to the animals.

The animals were treated with 20 µg/g BW NOX-A12 in 5% glucose solution sc. every other day (q2d) starting on day 7 after tumor cell implantation until the end of the observation period of 100 days. This treatment routine was recommended by the manufacturer after previous studies with the Spiegelmer immune modulator in consideration of its plasma half-life in mice (Boels et al., 2017; Kalnins et al., 2015; Vater et al., 2013) (Fig. 4).

The rodent-specific CCL2 Spiegelmer antagonist mNOX-E36 (TME Pharma, Berlin, Germany) was prepared and applied in the same manner as mentioned for NOX-A12 (Fig. 4).

3.7.2 Radiotherapy

Radiation treatment planning was based on CT scans using a representative body size of 20 g mice. Irradiation was performed with 6 MV flattening filter-free (FFF) X-rays from a clinical LINAC equipped with a multi-leaf collimator with 0.5 cm beam width at the isocenter, resulting in a half brain-irradiation. Removing the flattening filter increases the dose rate by at least a factor of 2. The FFF beams have a sharper penumbra, less head scatter and a lower out-of-target dose than with flattening filter (Cashmore, 2008). Consequently, these settings allow the targeted radiation dose to be delivered with the lowest radiation exposure outside the radiation field and the greatest protection of the healthy brain tissue (Fig. 5, A). The radiation dose was applied from below through the patient table.
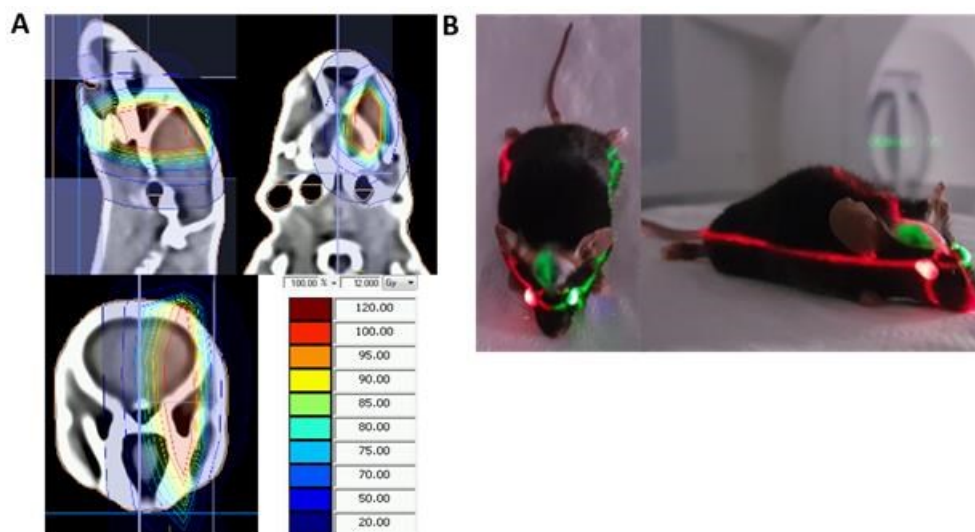
Fig. 5: Irradiation planning and position raster.
(A) Irradiation planning and isodose distribution for irradiation with a LINAC without compensation filter. (B) Laser raster for positioning of the anesthetized animal above the gantry of the clinical linear accelerator.

To mimic the standard clinical fractionation of whole-brain treatment of 10 x 3 Gy (total dose 30 Gy), a similar high-dose irradiation scheme was chosen for the preclinical comparison of the different treatment combinations. Therefore, different fractions and doses used in other preclinical studies were first tested for their MST and risk of metastasis or other side effects when delivered by the clinical linear accelerator. Three different fraction and dose schemes (1 x 2 Gy, 1 x 20 Gy, 2 x 10 Gy) were tested in each of six tumor-bearing animals similar to other preclinical studies on the 10th day after tumor inoculation (Gaber et al., 2003; Halperin et al., 1992; Liu et al., 2014; Zeng et al., 2013; Zhou et al., 2014). It was attempted to achieve a relatively fast response of the irradiated tissue, either tumor or healthy tissue. Since several studies on cellular and molecular responses of irradiated healthy mouse brain tissue have already described that a rapid response can be expected to single-dose irradiation, whereas the response to fractionated irradiation is relatively slow (Yang et al., 2017), a higher fractionated treatment was not considered.

After dose determination (4.2.1), tumor-bearing mice were treated with a single dose of 12 Gy by half brain-irradiation on day 10. For this purpose, the animals were anesthetized with MMF for 45 min. The mice were positioned on the clinical unit with

the help of a laser raster (Fig. 5, B). The irradiation dose was delivered through the patient table in a single beam. Immediately after the treatment, the anesthesia was antagonized by sc. injection of a mixture of atipamezole (2.5 mg/kg), flumazenil (0.5 mg/kg) and naloxone (1.2 mg/kg), and the animals were observed until all were completely awakened. To avoid anorexia as a side effect of the RT, the animals received zwieback (Brandt Markenzwieback, Hagen, Germany) in addition to their normal diet for one week.

3.8   Magnetic Resonance Imaging (MRI)

The animals were examined daily for tumor-related symptoms and the tumor growth was monitored longitudinally using MRI at least once per week, starting on day 7 until day 100 after tumor inoculation. T1-weighted imagines of the brains were generated using a preclinical 1 Tesla MRI system (ICON™ (Avance III MRI) 1 Tesla MRI, Bruker, Ettlingen, Germany) and acquisition software (ParaVision 6, Bruker, Ettlingen, Germany) with the parameters as listed in Table 3.

Table 3: MRI measurement parameter for monitoring of the tumor size.

measurement	T1 RAREnav highres
TE [ms]	21.08
TR [ms]	617.271
Averages	22
Repetition	1
TA [min]	14 m 42 s 696 ms
echo spacing [ms]	21.083
rare factor	2
Slices	10
slice thickness [mm]	0.5
slice gap [mm]	0.25
slice orientation	Axial
read orientation	V-D
FoV [mm]	22.98×23.285
resolution [mm]	0.177×0.179

TR: repetition time. TE: echo time. TA: time acquisition. FoV: field of view.

After the animals were anestesized by inhalation of a 3% isoflurane-oxygen gas mixture (Forene[®], Abbvie, Wiesbaden, Germany), 200 µL of a 200 µM solution of the paramagnetic MRI-contrast agent gadobutrol (Gadovist[®], Bayer, Leverkusen, Germany) were injected ip. Subsequently, the animals were placed on a respiratory sensor in the handling unit of the MRI system in a horizontal, untwisted position. To ensure that the animals remained in this position, the animals' heads were fixed. Before the mouse was placed in the MRI instrument, an ophthalmic ointment (Bepanthen[®], Bayer, Leverkusen, Germany) was applied.
The handling unit was inserted into the whole body coil inside the instrument and the imaging protocol was initiated. During the image acquisition, the animals were under general anesthesia with a maximum of 1% isoflurane-oxygen gas mixture. The deepness of anesthesia was adjusted according to the respiratiory monitoring and the

respiratiory rate was kept stable at approximately 65 breaths per minute. To maintain a stable body temperature of the animals, the build-in heating device of the handling unit was used to generate a temperature of 30 °C inside the MRI coil. The temperature was monitored during the scan by a thermal sensor. After performing the MRI, the mice were removed from the cradle of the handling unit and observed until awakened.

The resulting digital imaging data were transformed into Digital Imaging and Communications in Medicine standard (DICOM). In the following, the images were objectively analyzed by a veterinarian using the Horos™ imaging software (HorosProject.org). The volumetric measurements were performed by contouring contrast-enhancing regions of interest (ROIs) in coronal sections and the application of a wrapping calculation of these regions. The software calculated then the tumor volumes.

If the first MRI on day 7 showed contrast-enhanced regions, but the software could not calculate a tumor volume based on the structure of the implant, the tumor size was undefined. Animals with such a finding were also included in the study.

A maximum tumor size could not be defined, because the location of the tumor in the brain may also affect the general condition. The animals were sacrificed when they showed a high tumor volume and/or the general condition of the animal deteriorated with symptoms such as weight loss of over 20%, unkempt fur, apathy, massive changes in behavior or signs of neurologic deficits.

3.9   Perfusion

The animals were sacrificed by transcardiac perfusion with PBS if the general condition of the animal deteriorated and/or if a high tumor volume was observed by MRI.

The animals were deeply anesthetized via an ip. injected ketamine/xylazine mixture (ketamine 120 mg/kg (WDT, Garbsen, Germany), xylazine 20 mg/kg (Serumwerk Bernburg, Bernburg, Germany), 0.1 mL/ 10 g) to secure a painless death of the animals. A 50 mL syringe with a perfusion needle was filled with PBS without air bubbles. Once the animal reached a surgical plane of anesthesia, blood was drawn by retro-orbital bleeding and collected into tubes coated with 0.5 M ethylenediaminetetraacetic acid (EDTA).

After that, each mouse was secured in the supine position. Then, a midline incision was made using scissors through the integument and abdominal wall just beneath the rib cage to open the abdomen cavity. The xiphoid process, the white tip of the sternum, was grasped and the diaphragm was incised before parallel cuts were made on either side of the ribs to open the thorax and expose the heart. A butterfly needle connected with the perfusion syringe was introduced into the apex of the left ventricle. Immediately after inserting the needle and squeezing the syringe to allow the PBS buffer to enter the circulation, the right atrium was cut open allowing the perfusate to exit from the circulation. The animal was perfused with 10 mL of PBS administered over 10 min (flow rate 1 mL/min).

After perfusion, the head of the animal was removed and the skull was exposed by a midline incision from the neck to the nose. The remaining neck muscle and cervical spine were trimmed off to expose the base of the skull. Then, the skull was opened

by carefully breaking off portions of the skull roof with tweezers, starting from the opened spinal canal. After turning the head, the olfactory bulbs and nervous connections along the ventral surface of the brain were carefully disconnected. The brain could then be carefully shaken out of the opened skull. For all further examinations of the brain, the cerebellum was detached.

The spleen was removed by cutting away the mesentery as well as connective tissue and preserved in PBS for further processing.

3.10 Flow cytometric analysis of the tumor microenvironment

3.10.1 Analysis of the tumor-infiltrating immune cells

To investigate the effects of immune modulators and RT on the tumor-infiltrating immune cells, the animals were implanted with 1.5×10^5 GFP-labeled GL261 tumor cells. On day 7 post-inoculation, the mice were examined for tumor signs by MRI and four animals were randomized into each of four treatment groups (Table 4). Starting from this day, the animals received injections of the CXCL12 antagonist (NOX-A12) q2d and/or partial brain irradiation with a single radiation dose of 12 Gy on day 10 (Table 4).

Table 4: Treatment groups for flow cytometric studies of the tumor environment.

group	treatment	
	RT 1x 12 Gy	**NOX-A12** 20 µg/g in 5% glucose all 2 days sc.
control		
RT	X	
NOX-A12		X
RT + NOX-A12	X	X

After the treatment period, the tumor growth was monitored again by MRI on day 20/21 after tumor cell inoculation, after which the animals were sacrificed. Subsequently, the tumor tissue, spleen and blood from tumor-bearing mice were collected and were analyzed by flow cytometry (Fig. 6, A). The flow cytometric analysis was performed in cooperation with Dr. Christopher Groth from the Umansky Group of the Department of Dermatology, Venereology and Allergology at the University Medical Center Mannheim. The entire experimental setup for the flow cytometric analyses of the tumor environment was repeated in three independent experiments and the obtained data were pooled.

Blood was taken by retro-orbital bleeding and collected in tubes coated with 0.5 M EDTA. Animals were then perfused with PBS (3.7) and the brain and spleen were removed. To isolate the tumor-bearing brain tissue, the two cerebral hemispheres were dissected by a sagittal cut along the midline while the fluorescence of the GFP-labeled tumor cells was monitored with a preclinical optical/X-ray imaging system (In vivo Xtreme, Bruker, Ettlingen, Germany). Two additional sections at the level of the cerebellum and the olfactory bulb were made to separate the tumor implant (Fig. 6, B).
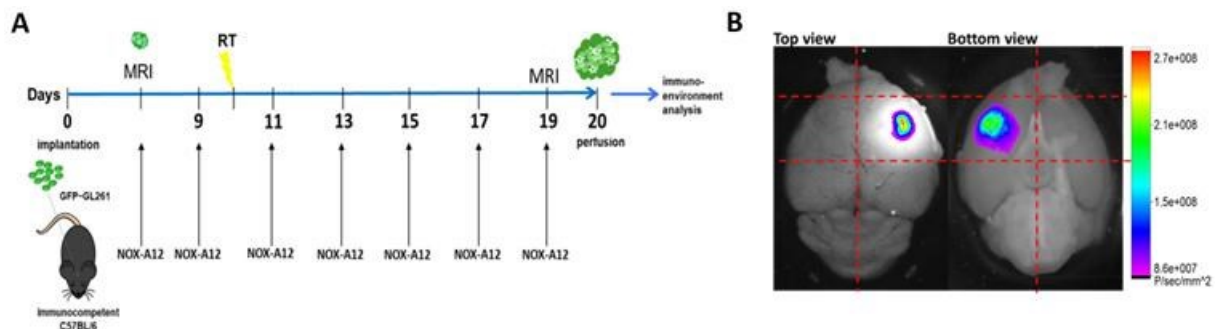
Fig. 6: Generation of tumor samples for flow cytometric studies of the tumor environment.
(A) In accordance with the long-term survival experiments, the animals were examined for the presence of a tumor by MRI on day 7 and randomized into treatment groups. The first dose of the CXCL12 antagonist was administered on day 7 and then q2d until one day before end of the experiment. On day 10 after tumor inoculation, the animals received a radiation dose of 12 Gy. The tumor size at the end of the experiment was determined by MRI on day 19/20. (B) The tumor-bearing tissue was identified and isolated based on the fluorescence signal of the GFP-labeled tumor cells. The red dashed lines show the sections made to isolate the tumor.

Immediately after sample collection, the tumor tissue and spleen were mechanically disrupted by forcing the samples through a cell strainer with a pore size of 100 µm to obtain a single-cell suspension. The cells were centrifuged at 300 g for 7 min at 4 °C and after discarding the supernatant, cell pellets were resuspended in either 1 mL PBS (tumor tissue) or 1 mL ACK lysis buffer (blood, spleen) (Gibco, Bleiswijk, Netherlands). The tumor samples were mashed through a 70 µm cell stainer to singulate the cells further. The blood sample plus ACK buffer was incubated at room temperature for 5 min. The lysis of the erythrocytes was stopped through the addition of 5 mL of PBS before the cells were centrifuged again. The pellets were resuspended in 1 mL of PBS and the cell amount was determined using a Neubauer Chamber.

To avoid nonspecific binding of Abs conjugated with fluorochromes, the single-cell suspensions were treated for 30 min at 4 °C in FACS buffer (PBS supplemented with 2% FBS and 0.05% sodium azide (NaN_3, Sigma-Aldrich, Munich, Germany)) containing FcR Blocking Reagent (BD Biosciences, Heidelberg, Germany). After that, the cell suspensions were stained with fluorescent Abs in accordance with the panels listed in Table A-1 in the appendix. Therefore, the cells were incubated with monoclonal Ab for 30 min at 4 °C. The stainings for quantification of NO and ROS were performed in PBS only.

The data acquisition was performed using a flow cytometer with ten fluorescence channels (BD FACS Lyric™, BD Biosciences, Germany) with the recommended software (BD FACSuite, BD Biosciences, Germany), which includes cytometer setup and tracking system. During the acquisition, the optimal cytometer values were monitored by the software maintaining the standards from experiment to experiment. The internal compensation values of the flow cytometer were used for compensation and duplets were excluded based on the scatter profile.
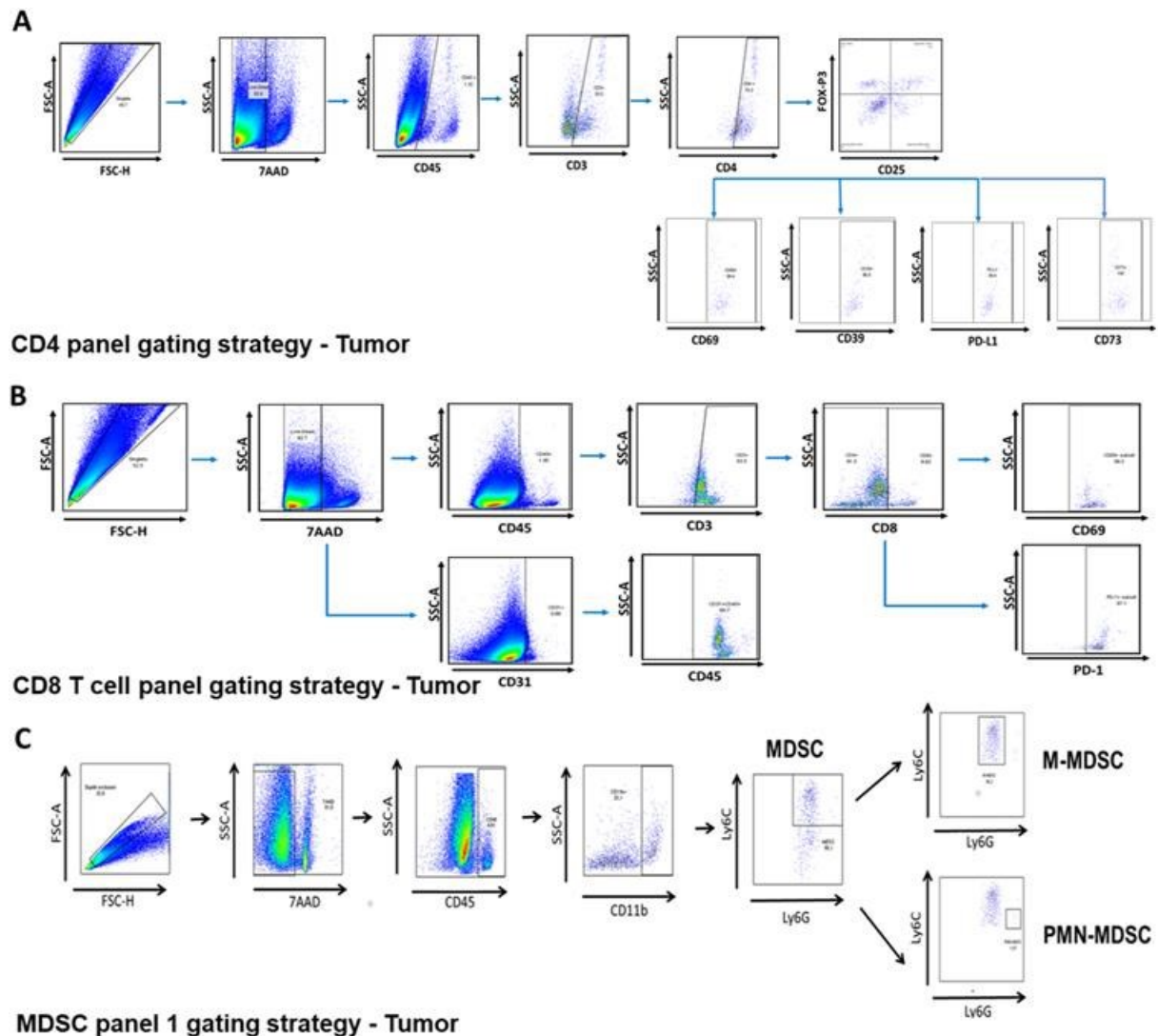
Fig. 7: Gating strategy of flow cytometric analysis of the tumor-infiltrating T cell and MDSC subpopulations.

(A) Gating the CD4^{+} T cell population on a tumor sample. After the CD4^{+} subpopulation of the T cells was identified, they were separated into CD25^{+} and FoxP3^{+} T cells, the surfaces of which were subsequently examined for activity markers. (B) Gating the CD8^{+} T cell population on a tumor sample. In addition to the identification of the CD8^{+} subpopulation of the T cells, the living cells were analyzed for the endothelial cell marker CD31. (C) Gating of the MDSC cell population in a tumor sample. CD11b^{+}Gr1^{+} myeloid-derived suppressor cells (MDSCs) were separated into polymorphonuclear (PMN-MDSC) or monocytic MDSCs (M-MDSC) according to their Ly6G or Ly6C expression and then further examined according to their receptors and activity markers.

Before each experiment, the performance quality of the instrument was measured according to the manufacturer's instruction using beads dyed with fluorochromes which are excitable by the cytometer's lasers (CS&T RUO Beads, BD Biosciences, Germany). To determine the quantities of different T cell and MDSC subpopulations, the recorded data were represented as dot plots and evaluated in accordance with the gating strategies shown in Fig. 7. Stainings that lack the Abs for the molecules of interest were used as gating controls.

Samples containing less than 100,000 measured events were omitted from further analyses, which were performed using FlowJo software (Tree Star, Ashland, USA).

3.10.2 Receptor profiling after radiotherapy

In order to investigate radiation effects on the expression of the receptors CCR2, CCR4, CCR5, CXCR4 and CXCR7 on the surface of CD8$^+$ effector cells, CD4$^+$ FOXP3$^+$ Tregs and CD11b$^+$Gr1$^+$ MDSCs, eight animals were irradiated with a single dose of 12 Gy and another eight animals were observed as untreated controls. After confirmation of the growth of the implanted cells by MRI on the 20th day after tumor inoculation, the tumors were examined for the respective subpopulations in accordance with the panels in Table A-2. The receptor profiling of the CD8$^+$ effector cells, CD4$^+$ FOXP3$^+$ Tregs and CD11b$^+$Gr1$^+$ MDSCs in the tumor environment were repeated in two independent experiments with 8 animals each and the obtained data were pooled.
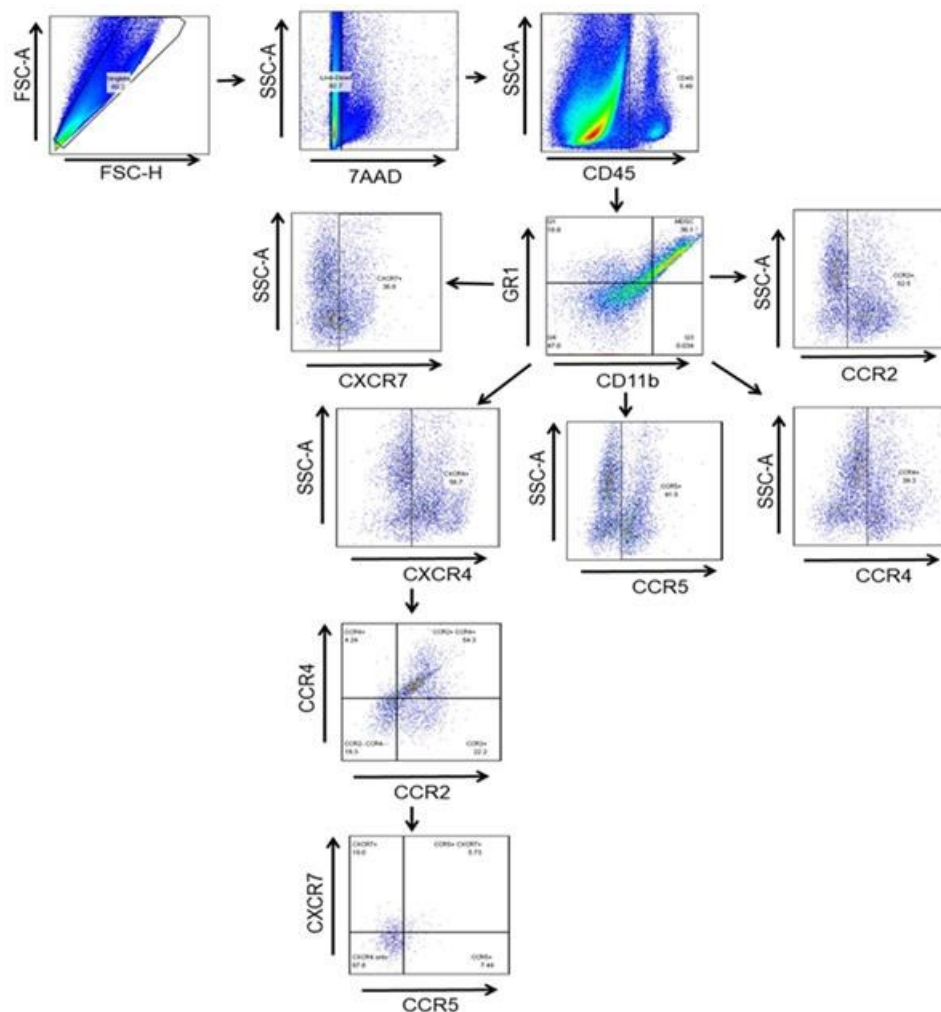
Fig. 8: Exemplary gating strategy of flow cytometric analysis of the chemokine receptors on the tumor-infiltrating MDSCs.
Gating of the MDSC cell population in a tumor sample. CD11b$^+$Gr1$^+$ MDSCs were separated according to their receptor expression and the receptor profile of the MDSCs with individual and co-expression of the receptors was determined.

The sample preparation and data acquisition were performed as described above (3.10.1). The receptor profiles were detected using the gating strategy from the flow cytometric analysis of the chemokine receptors on the tumor-infiltrating MDSCs (Fig. 8).

3.11 Cytokine and chemokine analysis of the tumor microenvironment

Twenty days after tumor inoculation, the concentrations of cytokines and chemokines in the tumor tissue and plasma were measured using a bead-based multiplex immune assay (Luminex® xMap technology). The treatment and sampling were performed as described under 3.10.

The blood drawn was centrifuged at 1,000 g for 15 min at 4 °C immediately after withdrawal. The plasma was transferred to a polypropylene tube and a further centrifugation step at 10,000 g for 10 min at 4 °C was performed to completely remove all platelets and precipitates. The tumor tissue was also isolated as described under 3.10 and immediately frozen in liquid nitrogen. The frozen samples were mechanically disrupted before being treated with lysis solution (Bio-Rad, Munich, Germany) and centrifuged at 4,500 g for 10 min at 4°C. The supernatant was removed and stored at -80 °C until analysis.

This analysis was also performed in cooperation with Dr. Christopher Groth from the Umansky Group of the Department of Dermatology, Venereology and Allergology at the University Medical Center Mannheim.

Total protein concentrations in tumor lysates and plasma were determined from representative samples by BCA assay (Pierce™ BCA Protein Assay Kit, Thermo Fisher Scientific, Rockford, USA). This was done by adding 25 µL of a freshly prepared bovine serum albumin (BSA, Sigma-Aldrich, Munich, Germany) standard dilution series containing from 0.025 mg/mL to about 2 mg/mL protein as doublets into wells of a 96-well plate. 25 µL of all samples were also added in duplicates to the 96-well plate. Then, 200 µL of BCA working reagent, consisting of 50 parts of BCA reagent A mixed with one part BCA reagent B, were carefully intermixed into each well to avoid the formation of air bubbles. After incubation of 30 min at 37 °C, the absorbance was measured at 562 nm on a Tecan infinite M200 microplate reader (Tecan Trading, Männedorf, Switzerland).

The average absorbance of the measured blank standard replicates was subtracted from the average absorbance of all individual standard and unknown sample replicates. With the standard curve plotted from the corrected measurements of the BSA standards used, the protein concentration of each unknown sample was determined.

The Bio-Plex Pro™ Mouse Chemokine Panel Assay (Bio-Rad, Feldkirchen, Germany) was used for immune assay analysis, which was performed according to the manufacturer's instructions.

As a control, a fourfold standard diluent series with seven measurement points was prepared. After adding 250 µL of the assay diluent in the viral kit standard and incubating the dilution on ice for 30 min, 50 µL of this starting solution was transferred into 150 µL of standard diluent and mixed before 50 µL of this first dilution was removed and added to 150 µL of diluent for the next dilution step. The next four dilution steps were prepared similar.

After thawing, the plasma samples were diluted 1:5 with sample diluent and kept on ice. Also, the coupled beads stock was diluted to 1x in assay buffer, vortexed and

protected from light before pipetting 50 µL into each well of the assay plate. Then, the plate was washed twice with 100 µL of wash buffer per well. 50 µL of the standards, samples, blanks and controls were added to each well. The plate was incubated on a shaker at 850 ± 50 rpm at room temperature for 30 min light protected. After dilution of the detection Abs to 1x and washing the plate three times with 100 µL per well, 25 µL detection Ab solution was added to each well and incubated again for 30 min at room temperature and 850 ± 50 rpm on a shaker protected from light. Afterward, 100x Streptavidin-PE (SA-PE) was diluted to 1x and added after three washing steps (100 µL per well). In addition, 50 µL of the SA-PE solution was added to each well of the assay plate, and the sealed plate was incubated for 30 min again. After that, the assay was visually inspected to ensure that all wells were properly filled, the sealing tape was removed and the plate was analyzed in the multiplex analyzing system (Luminex, Austin, USA). After the data acquisition, the measured control values were compared with the observed concentration using the ranges provided in the assay kit. The standard curve determined was used to ascertain the cytokine and chemokines concentration in the measured samples.

A total of 31 cytokine and chemokines were analyzed, including the immune factors TNF-α, GM-CSF, IFN-γ, the interleukins IL-1β, IL-2, IL-4, IL-6, IL-10, IL-16, the CC chemokines CCL1 (I-309), CCL2 (MCP-1), CCL3 (MIP-1α), CCL4 (MIP-1β), CCL5 (RANTES), CCL7 (MCP-3), CCL11 (eotaxin), CCL12 (MCP-5), CCL17 (TARC), CCL19 (MIP-3β), CCL20 (MIP-3α), CCL22 (MDC), CCL24 (Eotaxin-2), CCL27 (CTACK) and the CXC chemokines CXCL1 (KC), CXCL5 (ENA-78), CXCL10 (IP-10), CXCL11 (I-TAC), CXCL12 (SDF-1), CXCL13 (BCA-1), CXCL16 (SCYB16) and the CX3C chemokine CX3CL1 (Fractalkine).

In order to determine the effects of the different treatments on the local and systemic cytokine and chemokine production, the measured levels of the analytes were normalized to the respective total protein amount in the tumor tissue and the plasma, as determined via BCA assay.

3.12 Immunohistochemistry

Frozen brain sections of animals without a positive tumor sign on MRI were screened for tumor cells by Ki-67 and HE staining 100 days after tumor inoculation.

For this purpose, the frozen brains were sliced into 5 µm sections using a cryostat (Leica CM 1900, Leica Biosystems, Nussloch, Germany).

The histopathological staining of the brain section slides with HE was performed using an automatized tissue staining station (Leica Autostainer XL, Leica Biosystems, Nussloch, Germany). For Ki-67 staining, the sections slides (5 µm) were fixed by 3.7% paraformaldehyde (PFA, Alfa Aesar, Kandel, Germany) and blocked with 1% BSA/PBS for 10 min each before they were stained with a primary Ab against Ki67 (1:200, Rabbit, Cell Signaling Technology, Danvers, USA). The primary Ab incubation was performed overnight at 4 °C and the secondary Ab (1:200, biotinylated anti-rabbit IgG (H+L), VECTOR Laboratories INC., Burlingame, USA) was added to the slides after a washing step with a PBS/Triton Solution (PBST;

50 mL PBS/ 150 µL Triton X-100, Bio-Rad Laboratories GmbH, Feldkirchen, Germany). The biotinylated anti-rabbit IgG was incubated at room temperature for 1 h. Then, an avidin-biotin complex (VECTASTAIN Elite ABC Kit, VECTOR Laboratories INC., Burlingame, USA) was added and incubated for 30 min. After this incubation, the staining was visualized with DAB (VECTOR Laboratories INC., Burlingame, USA) for 10 min at room temperature. All slides were counterstained with hematoxylin, dehydrated and permanently mounted with mounting medium (ROTI® Histokitt, Carl Roth, Karlsruhe, Germany).

The stained slides were examined for tumor cells under a microscope.

3.13 Statistics

In all experiments, the statistical analyses were performed using GraphPad PRISM software version 6 (GraphPad Software, Inc., San Diego, USA). The significance limit was set at 5% ($p < 0.05$) for all tests.

The survival experiments were statistically analyzed using the Kaplan-Meier method and compared with the Log-rank (Mantel-Cox) test.

The results of the flow cytometric analysis as well as the cytokine and chemokine analysis were expressed as mean ± standard error of mean (SEM). The means of more than two treatment groups were assessed with a one-way ANOVA/Tukey posthoc multiple comparisons test to analyze for significance among all groups. For the statistical comparison of two treatment groups, an unpaired t-test was used. Outliers were identified using the ROUT method, setting Q at 1% and excluded. Specific cell groups were correlated with the tumor volume and the correlation coefficients r were calculated via Pearson correlation.

4   RESULTS

4.1   Establishment of the GBM mouse model

4.1.1   Generation of a stable cell line

The original murine glioma cell line (GL261) was first transduced with a GFP encoding lentiviral vector (HR'SIN-cPPT-SEW). The expression of the transduced fluorescent reporter molecule was monitored starting immediately after transduction. After three passages, the cells were sorted by their GFP expression to achieve the highest possible purity. Consequently, the cells were sorted twice.

2.1×10^7 GFP-transduced cells were used as starting cell quantity. After the first sort, 11.9% of the cells expressed the gene during sorting. These cells were purified up to 97.6% in the second sorting run, resulting in 6.85×10^5 GL261-GFP cells (Fig. 9, A and B). The cells not expressing GFP at the time of sorting were not cultured further.
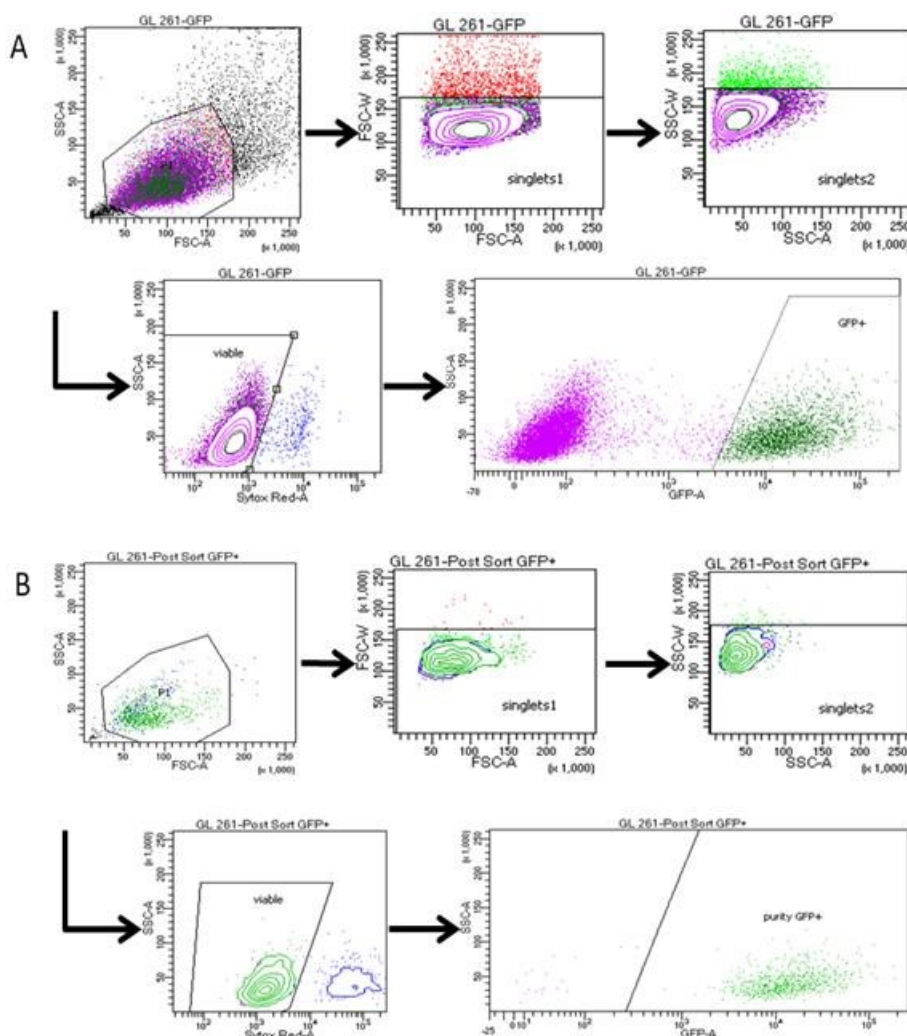
Fig. 9: Results of the sorting process.
(A) 11.9% of the sorted cells were positive for GFP expression. (B) The purity sort cleaned up the previous cell population to a purity of 97.6%.

The purified cells were cultured in DMEM/F-12 containing 10% FCS up to a maximum of 6 passages. During this culture period, the cells grew rapidly without contact inhibition (doubling time of 20 h) while observing their GFP expression under the fluorescence microscope. As a result, the majority of the tumor cells consistently expressed a stable green-fluorescent signal (Fig. 10).
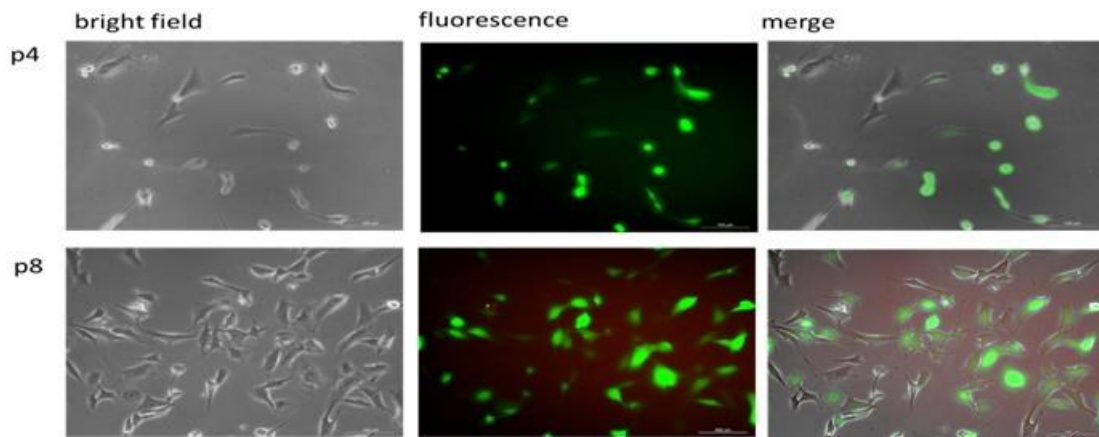
Fig. 10: Stable expression of GFP under fluorescence microscopy after lentiviral infection.
Bright field and fluorescence images of different passages. After lentiviral transduction with the HR'SIN-cPPT-SEW vector and fluorescence sorting, the majority of cells exhibit green fluorescence through GFP expression. The fluorescent signal remains stable in further passages (p4 = passage 4, p8 = passage 8). Scale bar = 100 µm. Bright field, GFP and merged image.

4.1.2   Characterization of the in vitro radiation sensitivity

To characterize the *in vitro* radiosensitivity of the transduced GL261 cell line, three independent colony-forming assay experiments were performed. The resulting survival curve was fitted using the LQ model.

The resulting surviving fractions SF(D) plot showed the mean and standard error of mean of the survival fraction data and model predictions. The PE was calculated as 0.802. A value of $0.053\,\text{Gy}^{-1}$ was estimated for the coefficient α and a value of $0.081\,\text{Gy}^{-2}$ was estimated for β as parameters of the LQ model, resulting in an α/β ratio of 0.63 Gy. The goodness of fit of the fitted surviving fraction plot was determined to be $R^2 = 0.973$ (Fig. 11, A and B).
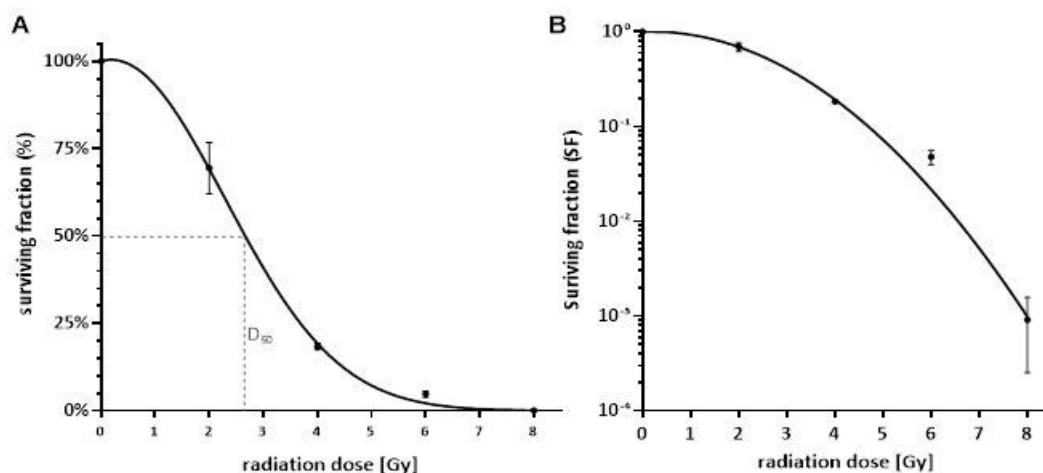
Fig. 11: Clonogenic cell survival curves of GL261-GFP cells.
The surviving fraction of colony-forming GL261-GFP cells versus dose was fitted in three independent experiments by the LQ model. (A) Linear and (B) semi-logarithmic plots of the results, plotted as means ± SEM.

In the literature, the radiosensitivity of the original GL261 cell line is reported with 50% cell survival after administration of less than 2 Gy (Szatmari et al., 2006). Based on the survival curve fitted to the LQ model, the transduced GFP-expressing cell line showed an *in vitro* cell mortality of 65.1% after irradiation with 2 Gy. In contrast, after irradiation with twice the dose (4 Gy), the surviving amount of the GL261-GFP cells

was estimated to be 22.1%. After administration of 6 Gy, only 3.9% of the cells survived and irradiation with 8 Gy killed over 99% of the cells. Within these values, the *in vitro* median radiation dose that reduces survival to 50% (D_{50}) was determined to be 2.62 Gy (Table 5).

Table 5: Surviving fractions obtained from the survival curve fitted to the LQ model.

	dose	surviving fraction
	[Gy]	mean
	2	65.1%
	4	22.1%
	6	3.9%
	8	0.4%
D_{50}	2.62	50%

4.1.3   Characterization of the tumor development

To establish the used model, the stably transduced GL261-GFP cells were used in preliminary implantation experiments to determine the cell number that favors the most moderate tumor growth observed after a definied time period. Therefore, three different cell numbers were implanted into the basal ganglia of at least three animals. The MRI showed noticeable differences between the volumes of tumors grown from the three different implanted cell amounts 21 days after tumor inoculation (Fig. 12, A).
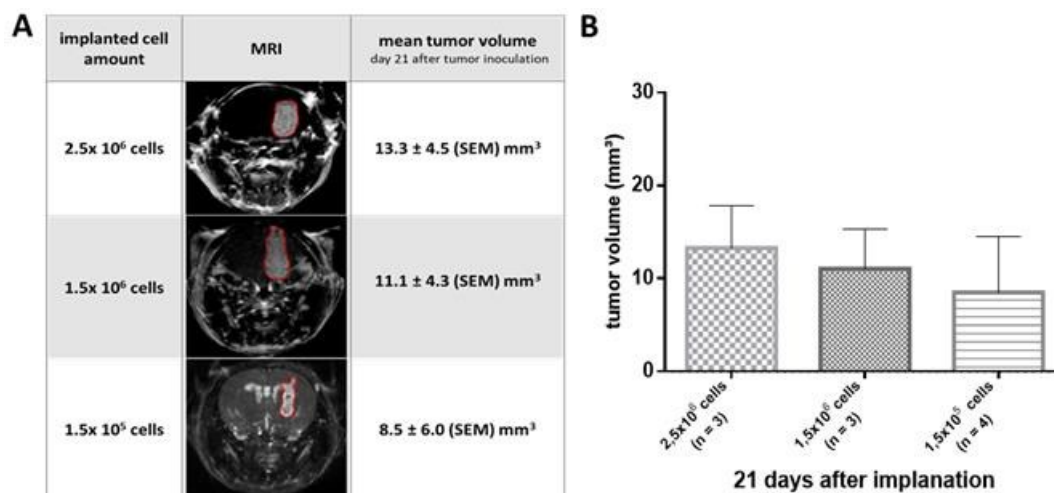
Fig. 12: Establishment of the orthotopic murine GBM model.
(A) Typical tumor growth of different cell amounts recorded by T1-weighted MRI 21 days after tumor inoculation (3D images). The tumor volume was objectively determined from MRI by a veterinarian using the image processing software Horos™. The tumor arising from 1.5×10^5 GL261-GFP cells is shown as a T2-weighted MRI, a T1-weighted image was not available for technical reasons. (B) Tumor volumes at day 21, plotted as means ± SEM. Without treatment, the animals implanted with 1.5×10^5 tumor cells (n = 4) had the lowest average tumor volume of 8.5 ± 6.0 mm³. With 2.5×10^6 cells (n = 3), the tumors reached an average volume of 13.3 ± 4.5 mm³, and with 1.5×10^6 cells (n = 3), the tumors grew to an average of 11.1 ± 4.3 mm³.

The tumor growth assessed by MRI for the cell quantity 2.5×10^6 cells (n = 3) reached between 4.3 mm³ and 18.8 mm³, with an average volume of 13.3 ± 4.5 mm³. For 1.5×10^6 cells (n = 3) the mean volume adds up to 11.1 ± 4.3 mm³ after 21 days. The smallest tumor volume could be measured after implantation of 1.5×10^5 cells (n = 4) with an average of 8.5 ± 6.0 mm³. However, this cell number also showed the most individual outgrowth (Fig. 12, B).
The cell amount of 1.5×10^5 GL261-GFP cells was implanted in the brain of the

animals in all further experiments. Therefore, the tumor progression and the survival were recorded after the inoculation of this cell number in a group of 15 animals as untreated control data. The tumor progression of the untreated control group showed an exponential behavior over the observation period with a doubling time of approximately 6 days. The fitted curve could be described with $y = 1.272 \cdot e^{0.1085x}$ ($R^2 = 0.4764$) (Fig. 13, A). Without treatment, the median survival of animals with initially 1.5×10^5 implanted tumor cells was 26 days. The conditions of the animals became critical at the earliest on the 20th day and the latest on the 34th day after tumor inoculation (Fig. 13, B).
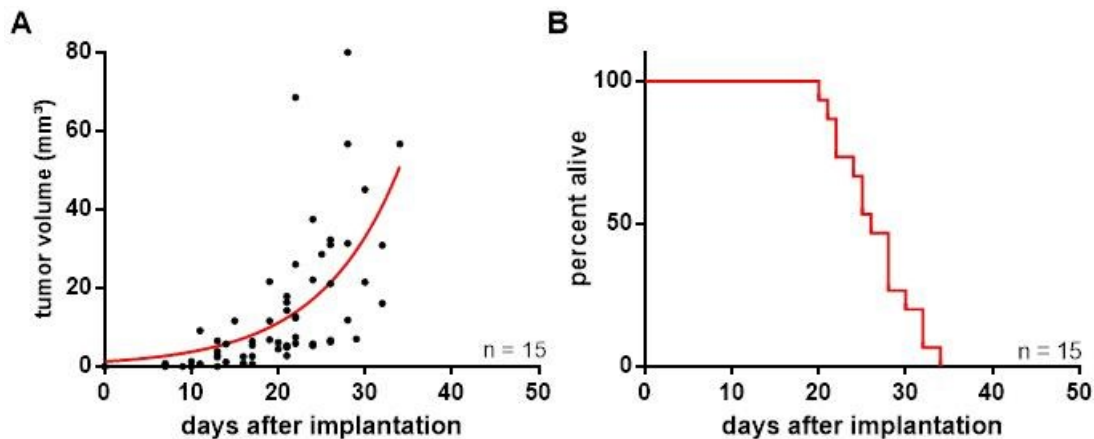
Fig. 13: Tumor progression and survival curve of the untreated control group.
Left untreated, (A) the tumor progression could be fitted to an exponential curve (B) leading to a median survival of 26 days.

4.2   Effect of different treatments on *in vivo* survival

4.2.1   Determination of the radiation dose of stereotactic radiotherapy and its effects

In order to define a suitable irradiation scheme for further comparative experiments, tumor-bearing animals were irradiated with different fractions and doses (1 x 12 Gy (n = 8), 1 x 20 Gy (n = 6), 2 x 10 Gy (n = 6)) according to other preclinical studies on the 10th day after tumor inoculation. Irradiation was performed as half-brain treatment in the area of tumor implant on a linear accelerator without compensation filter according to the radiation plan (Fig. 5).

In all therapy groups, animals lost their hair (alopecia) as a side effect after receiving the treatment. The hair loss was limited to the applied radiation field. The regrown fur changed its color to gray as a result (Fig. 14, A). Furthermore, regardless of the dose received, a remarkable weight loss of about 7% on average due to anorexia was observed within one week after irradiation. However, this could be compensated by adding zwieback to the normal diet (Fig. 14, B).

After irradiation with 1 x 12 Gy, typical tumor development showed a plateau phase between the 10th and 20th day after irradiation before the first tumor grow exponentially without restriction around 40 days after tumor inoculation (Fig. 14, C and D). For animals that responded positively to the same irradiation dose, the curve started to flatten during this time period. Then, the measured tumor volume decreases within the observation period of 100 days until complete tumor regression (Fig. 14, D).

The tumor growth curve of animals treated with 2 x 10 Gy showed an almost identical picture; only the exponential phase of the tumor development was postponed by about a week (Fig. 14, C). After irradiation, transition of tumor cells into the ventricular system of the mouse brain was observed in 16.7% of the animals in this group resulting in detection of tumor tissue in the opposite hemisphere which led to the end of the experiment.
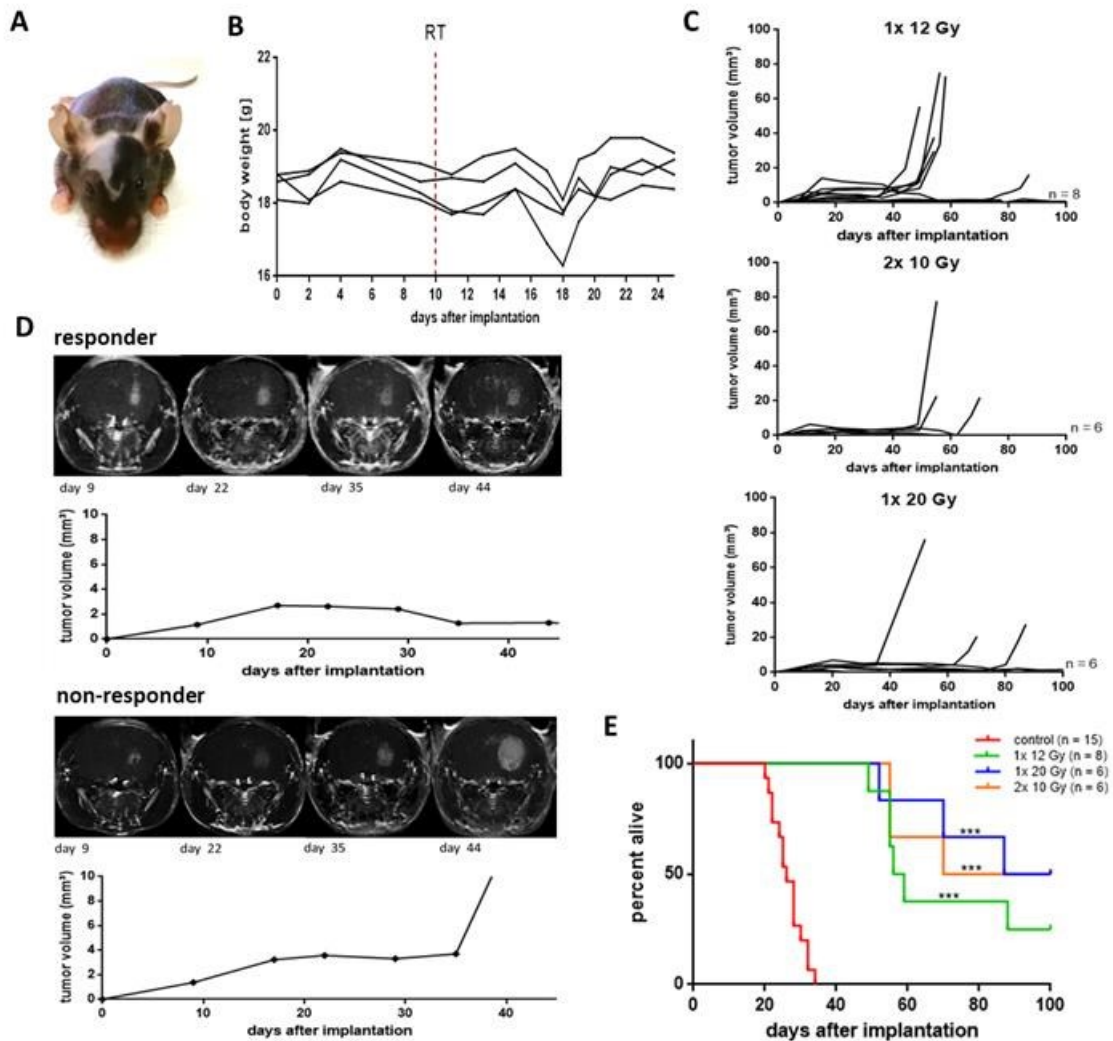
Fig. 14: Effects of different radiation doses of stereotactic radiotherapy.
(A) Mouse irradiated with 1 x 12 Gy, 10 days after irradiation. After RT, the mice lost their hair on the irradiated half of the head and the fur regrew gray. (B) Bodyweight curve of four animals treated with 1 x 12 Gy. One week after receiving RT, the animals stopped eating. This effect could be counteracted by additional feeding of a special diet. (C) Tumor growth profiles of the different RT regimes based on MRI. (D) Representative examples of the tumor development of responders and non-responders under 1 x 12 Gy RT recorded by T1-weighted MRI. (E) Survival curves after RT compared by log-rank Mantel-Cox test. When exposed to radiation, OS increased significantly compared with the untreated control group ($p \leq 0.0001$). The longest median survival can be achieved with radiation of 1 x 20 Gy at 93.5 days. The other two radiation regimes do not differ significantly from this treatment (2 x 10 Gy, 85 days; 1 x 12 Gy, 57.5 days). * $p \leq 0.05$; ** $p \leq 0.01$; *** $p \leq 0.001$

The tumor growth profile of the 1 x 20 Gy treatment regimen showed an inhibited tumor progression in most animals at the beginning of treatment which led to complete tumor regression in 33.3% of the animals. In one mouse, faint tumor signs were still detectable at day 100, while in another, exponential tumor growth began approximately 60 days after tumor inoculation. Two other animals showed a

ventricular collapse after irradiation and tumor cells in the opposite hemisphere which grew exponentially (Fig. 14, C).

The irradiation resulted in a significant positive shift in OS compared with the untreated control group (p ≤ 0.0001, all regimes). While after a single dose of 12 Gy only 25% of the animals survived the observation period of 100 days, the other two irradiation regimes were able to achieve the same in 50% of the animals. The longest median survival was achieved by irradiation with 1 x 20 Gy with 93.5 days (52-87 days). The other two irradiation regimes did not differ significantly from this result with 85 days (2 x 10 Gy, 55-70 days, p = 0.938) and 57.5 days (1 x 12 Gy, 49-88 days, p = 0.316) as median survival (Fig. 14, E).

Because of the typical courses of tumor development under stereotactic irradiation of 1 x 12 Gy, this treatment regimen was used for all further comparative examinations (mono 1).

4.2.2 Survival effects of monotherapies with checkpoint inhibitors and immunomodulators

In order to compare the effectiveness of the examined combination therapies, baseline data on the respective monotherapies were generated first. For this purpose, nine animals were treated six times with an anti-PD-1 Ab (inVivoMAb anti-mouse PD-1, Clone 29F.1A12, BioXCell) after tumor detection. From day 7, nine addditional animals each received a CXCL12 (NOX-A12) or CCL2 antagonist (mNOX-E36) q2d (Table 6).

Table 6: Monotherapies with checkpoint inhibitors and immune modulators.

group	treatment				N animals
	RT 1 x 12 Gy	NOX-A12 20 µg/g in 5% glucose every 2 days sc.	mNOX-E36 20 µg/g in 5% glucose every 2 days sc.	Anti-PD-1 Ab 250 µg in PBS 6x every 3 days ip.	
mono 2		X			9
mono 3			X		9
mono 4				X	9

The tumors of the group treated with CXCL12 antagonist NOX-A12 (mono 2, n = 9) progressed continuously in the observation period without any tumor regression. The group showed no significant shift in median survival (28 days, 23-42 days) compared with the untreated test group (p = 0.649). (Fig. 15, A, B and C1).

Interestingly, the CCL2 antagonist group (mono 3, n = 9) showed an even faster-increasing tumor growth and most animals had to be sacrificed on day 23/24, only one animal survived till day 38. Therefore, the survival curve of this group (23 days, 23-38 days) was not significantly shifted compared with the untreated animals (p = 0.525) (Fig. 15, A and B).

Under anti-PD-1 monotherapy (mono 4, n = 9), complete tumor regression was achieved in 22% of the animals within the observation period and the MST was extended from 26 to 32 days (22-42 days). Consequently, only the anti-PD-1 Ab had a significant positive treatment effect compared with the untreated animal group (p = 0.025) (Fig. 15, A, B and C2).
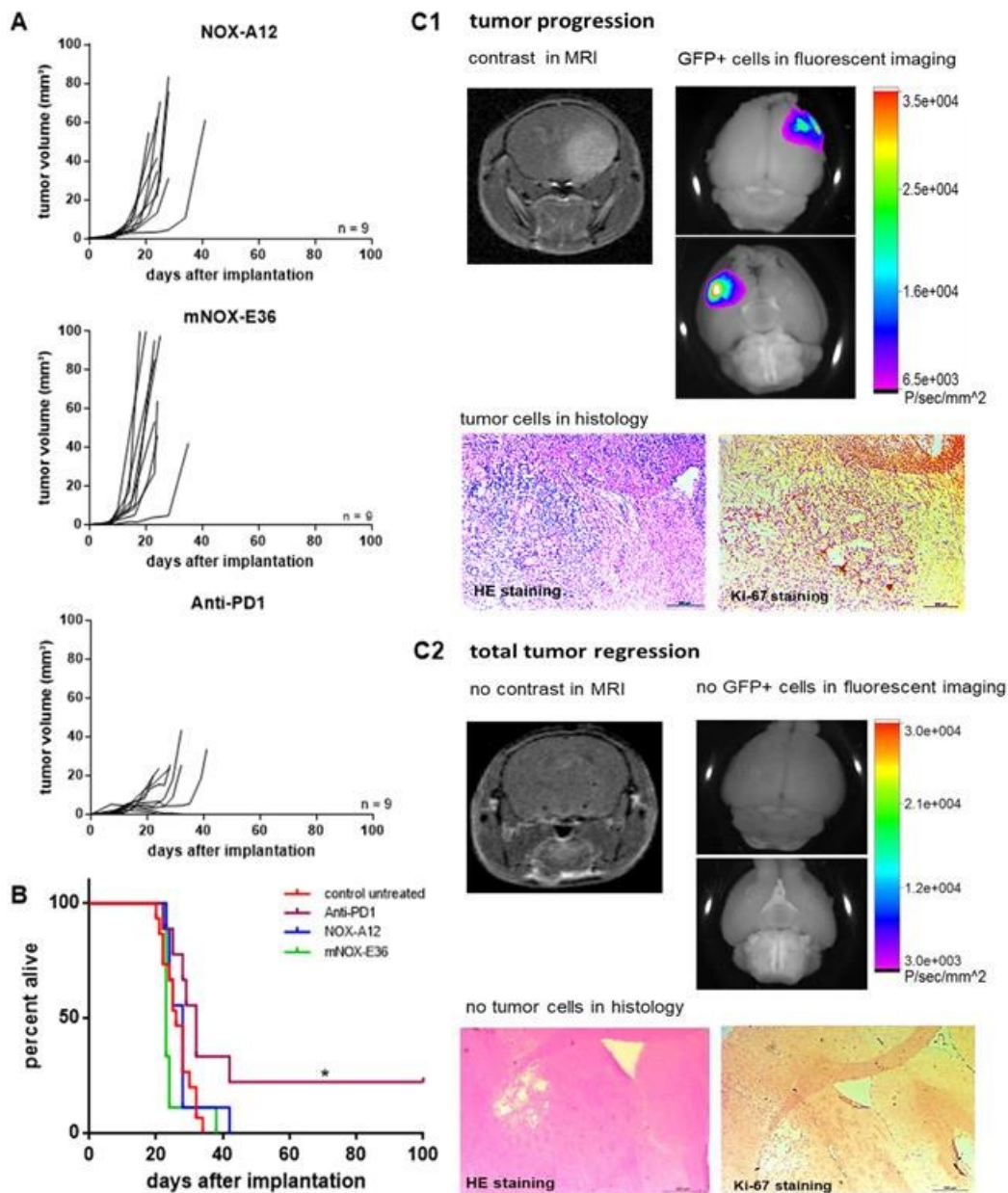
Fig. 15: Effects of monotherapies with checkpoint inhibitors and immune modulators.
(A) Tumor growth profiles of the monotherapies based on MRI. CXCL12 inhibitor NOX-A12 alone failed to suppress tumor growth, administration of CCL2 inhibitor mNOX-E36 alone resulted in an increase in tumor growth very early in the observation period. Administration of anti-PD1 Ab led to complete tumor regression in two animals. (B) Survival curves analyzed by the Kaplan-Meier method and compared by log-rank Mantel-Cox test. Survival analysis of the monotherapies showed no significant change when NOX-A12 was given (28 days), deterioration was observed when mNOX-E36 was administered alone (23 days). When PD-1 was inhibited, median survival was significantly extended to 32 days ($p = 0.025$) and OS was achieved by complete tumor regression in two animals (22%). (C) Typical T1-weighted MRI, fluorescence and histology images showing growing tumors (1) or complete tumor regression (2). * $p \leq 0.05$; ** $p \leq 0.01$; *** $p \leq 0.001$

4.2.3 Survival effects of combined checkpoint inhibitors and immune modulators

To obtain comparative data to assess the efficacy of different combinations of checkpoint inhibitors and immune modulators with additional RT, the survival data of the respective combinations without irradiation were first collected.

For this purpose, nine animals each were treated six times with an anti-PD-1 Ab (clone 29F.1A12, BioXCell) every third day combined with a CXCL12 (NOX-A12) or CCL2 antagonist (mNOX-E36) q2d starting on day 7 (Table 7).

["

p = 0.007), with only one animal showing no tumor signs after 100 days of observation (1/9 of the group examined). Duo 2 also had a significantly prolonged median survival compared with the mNOXE36 monotherapy group (p = 0.001) (Fig. 16, C).

4.2.4 Survival effects of checkpoint inhibitors and immune modulators combined with radiotherapy

The checkpoint inhibitors and immune modulators were also examined as a combination therapy with stereotactic RT (1 x 12 Gy). The respective combinations and their group sizes are listed in Table 8.

Table 8: Combination therapies of checkpoint inhibitors and immune modulators with RT.

group	treatment				N animals
	RT 1 x 12 Gy	**NOX-A12** 20 µg/g in 5% glucose all 2 days sc.	**mNOX-E36** 20 µg/g in 5% glucose all 2 days sc.	**Anti-PD-1 Ab** 250 µg in PBS 6x all 3 days ip.	
combination 1	X			X	12
combination 2	X	X			10
combination 3	X	X		X	12
combination 4	X		X		12
combination 5	X		X	X	12
combination 6	X	X	X	X	9

The combined use of RT and anti-PD-1 therapy (RT + Anti-PD1, n = 12, combination 1) showed synergistic effects superior to those of the single treatments. The treatment resulted in complete tumor regression in 83% of the animals, and only two out of 12 tumors grew exponentially during the observation time. The tumor growing profile showed inhibited growth of tumor cell at the beginning of the treatment, which turned into an exponential tumor progression after about 60 days in only 2 animals (Fig. 17, A). The median survival thus extended from 57.5 days beyond the 100 observation days. Compared with a single RT treatment alone, there was a significant prolongation of median survival (p = 0.004) (Fig. 17, B).

The tumor profile of the combination 2 regimen (RT + NOX-A12, n = 10), contrary to monotherapy with the CXCL12 antagonist, showed complete tumor regression in 5 of 10 animals. Only 2 animals were exposed to an exponential growth phase about 40 days after tumor cell implantation. In all other animals, tumor development shifted to the last half of the observation period (Fig. 17, A). Although NOX-A12 did not affect survival as a single treatment, it increased the OS of the mice when coupled with radiation, resulting in an OS rate of 50%. If animals were treated with a single dose of 12 Gy plus the CXCL12 antagonist (combination 2), the survival of these animals was significantly increased from 26 respectively 28 days to 99 days (55-98 days) after tumor inoculation compared with the untreated group (p < 0.0001) and the monotherapy (mono 2; p < 0.0001). Compared with RT alone, the additional treatment with the CXCL12 antagonist has a benefit of 41.5 days (p = 0.196) (Fig. 17, B).

In addition to the complete tumor regression in seven animals, the tumor growing curves under combination 3 (RT + NOX-A12 + Anti-PD-1, n = 12) showed a similar profile as under combination 2. Herein, a shift of the exponential growth phase into

the second half of the observation period was observed (Fig. 17, A). The addition of anti-PD-1 therapy to RT and CXCL12 inhibition only insignificantly increased the median survival of the tumor-bearing mice compared with the combination of RT and NOX-A12 (combination 2, p = 0.700). The group showed a slight OS effect of 58.3% compared with combination 2. When compared with the combination of the immune modulator and anti-PD-1 Ab (duo 1), the survival benefit of this treatment regimen is based solely on the effect of radiation, which significantly shifted the MST from 42 days to over 100 days (p = 0.013) (Fig. 17, B).
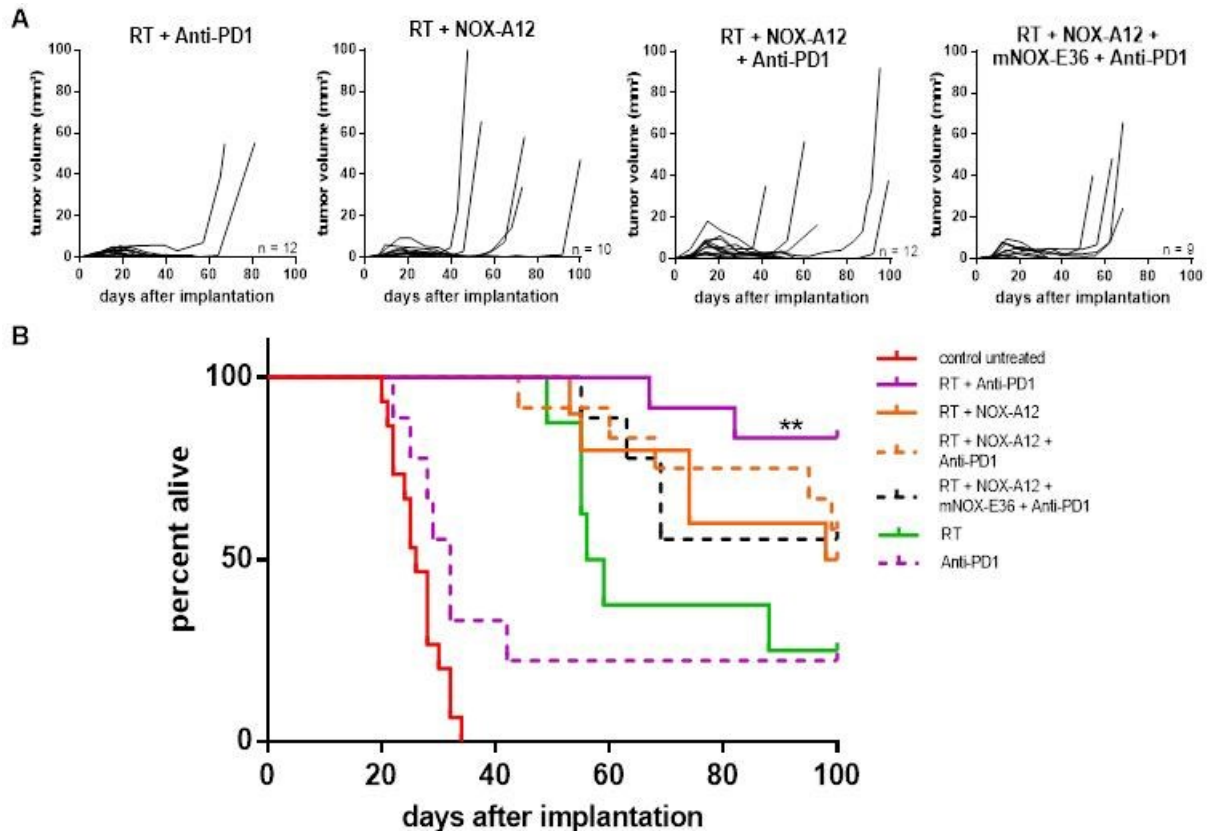
Fig. 17: Tumor growth and survival of tumor-bearing mice under combined therapy with CXCL12 antagonist and radiation therapy.
(A) The typical progression of tumors under different treatment regimens consisting of RT, inhibition of CXCL12 and/or PD-1 as determined by MRI. (B) Survival curves for different combination therapies compared with the untreated control group (n = 15) and RT (n = 8). The treatment combination 1 (RT + Anti-PD-1) significantly prolongs the survival of the animals compared with RT as a single treatment (p = 0.004). The addition of a CXCL12 antagonist or/and CCL2-inhibitor did not significantly increase the survival of the tumor-bearing mice. * p ≤ 0.05; ** p ≤ 0.01; *** p ≤ 0.001

The tumor growth curves of the treatment group RT combined with the CCL2 inhibitor mNOX-E36 (RT + mNOX-E36, n = 12, combination 4) showed a shift of the exponential tumor growing phase into the last third of the observation period in only two animals (Fig. 18, A). In contrast to the CXCL12 inhibitor, this antagonist did not improve the survival of the tumor-bearing mice either as a single treatment nor in combination with RT (RT + mNOX-E36). With a median survival of 64.5 days (46-88 days), there was no significant increase (p = 0.869) compared with RT alone (Fig. 18, B).
However, the typical tumor growth profile changed when an additional PD-1 Ab (RT + mNOX-E36 + Anti-PD1, n = 12, combination 5) was administered. The tumor

size remained relatively constant below 10 mm³ in most animals during the observation period before some began to grow exponentially starting around day 60. This profile is very similar to combination 1. Interestingly, under this treatment regimen, one animal had a stable disease with relatively constant tumor size of around 1.5 mm³ at the end of the observation period, without growing further (Fig. 18, A). The survival curve of this treatment group ran parallel to combination 1 with only slight deviations (p = 0.981), which suggests that the benefit of this treatment can be exclusively attributed to the combination of irradiation and immune checkpoint inhibitor (Fig. 18, B).
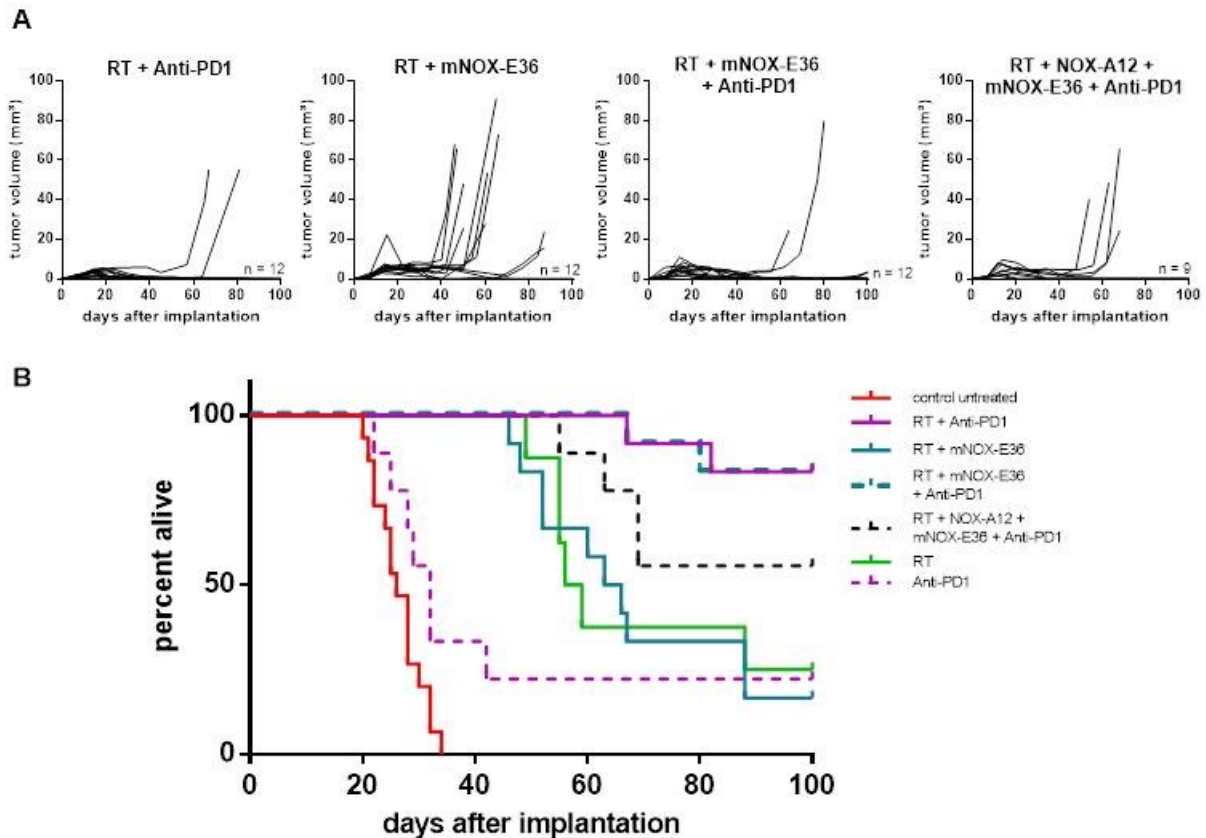
Fig. 18: Tumor growth and survival of tumor-bearing mice under combined therapy with CCL2 antagonist and radiotherapy.
(A) Typical tumor progression under different treatment regimens consisting of RT, inhibition of CCL2 and/or PD-1 as determined by MRI. (B) Survival curves for different combination therapies compared with the untreated control group (n = 15) and RT (n = 8). Treatment combination 1 (RT + Anti-PD-1) shows the same survival profile as combination 5 (RT + mNOX-E36 + Anti-PD-1). There were also hardly any differences in the survival profiles between RT as a single treatment and RT with the adjunctive application of the CCL2 antagonist (RT + mNOX-E36).

When the CCL2 antagonist was added to RT, anti-PD-1 and NOX-A12 treatment (RT + NOX-A12 + mNOX-E36 + Anti-PD1, n = 9, combination 6), the tumors of this treatment group either grew out or the animals showed complete regression of the tumors about 50 days after tumor inoculation (Fig. 17/Fig. 18, A). The survival curves of combination 6 and combination 4 (RT + mNOX-E36) were almost significantly different (p = 0.058). A slightly reduced median survival rate could be observed in the tumor-bearing mice compared with the combination therapies combination 2 (p = 0.938) and combination 3 (p = 0.877). (Fig. 17/Fig. 18, B).

4.3   Flow cytometric studies of the tumor environment

Long-term survival experiments showed an adjuvant effect of CXCL12 inhibition on the applied RT by increasing the OS, represented as tumor-free animals after the observation period (4.2.4). In order to investigate the effects of this combination therapy on immune cells and tumor tissue, spleen and blood of the tumor-bearing mice were analyzed by flow cytometry 20 days after tumor inoculation.

For this purpose, 47 animals were implanted with 1.5×10^5 GFP-labeled GL261 tumor cells, examined for tumor signs by MRI and randomized into four treatment groups on day 7 (Table 9). From day 7, the injections of the CXCL12 antagonist (NOX-A12) were administered q2d and/or a radiation dose of 12 Gy was applied on day 10. The tumor growth was monitored via MRI on day 7 and day 19/20 after tumor cell inoculation. On day 20, blood was retroorbitally collected from the mice, the brain and spleen were removed after perfusion and the tumor tissue was isolated using the fluorescence signal of the GFP-labeled tumor cells (Fig. 6).

Table 9: Treatment groups for flow cytometric studies of the tumor microenvironment.

group	treatment		N animals
	RT 1 x 12 Gy	NOX-A12 20 µg/g in 5% glucose all 2 days sc.	
Control			12
NOX-A12		X	12
RT	X		11
RT + NOX-A12	X	X	12

Single-cell suspensions from blood, tumor and spleen tissues were stained with conjugated Abs from five different panels (Appendix Table A-1). The stained samples were analyzed with a ten-color flow cytometer, using unstained samples as gate controls. The quantities of different cell subpopulations were determined by evaluating recorded dot plots following the gating strategies in Fig. 7.

4.3.1   Tumor volumes and tumor cells

After confirming that the inoculated GL261-GFP cells had grown in the brain on day 7, the progression of the grafts was again monitored by MRI on day 20 after cell inoculation (Fig. 19).

The images showed significant differences between the average tumor growth of the four treatment groups. While the mean tumor volume of the untreated animals did not differ significantly from those of the CXCL12 antagonist group, the mean tumor volume was significantly lower after RT (control vs. RT, $p = 0.027$; NOX-A12 vs. RT, $p = 0.0009$; NOX-A12 vs. RT + NOX-A12, $p = 0.003$). No additional reducing effect of the combination of RT and CXCL12 inhibitor was detected (RT vs. RT + NOX-A12, $p = 0.971$) (Fig. 20, A). However, no significant changes in the analyzed tumor cell numbers among all live cells were detected in the studied samples from different treatment groups (all $p > 0.936$) (Fig. 20, B).
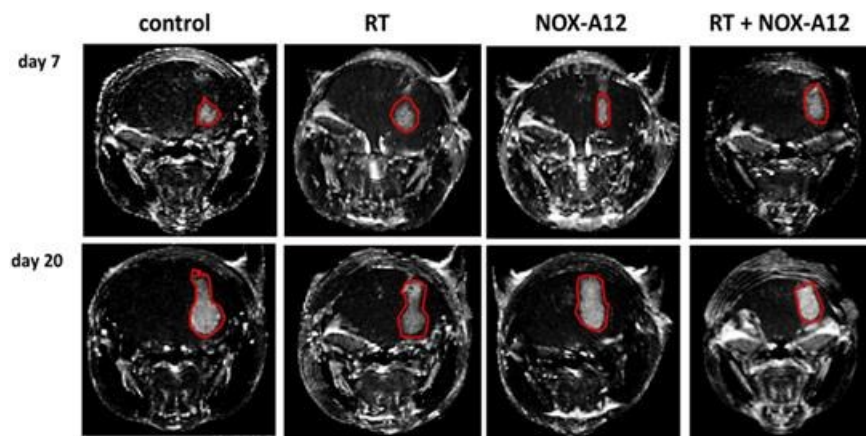
Fig. 19: Representative MRI of the analyzed tumors.
3D images of GL261-GFP murine glioma form observed mice acquired by T1-weighted MRI 7 and 20 days after tumor inoculation.
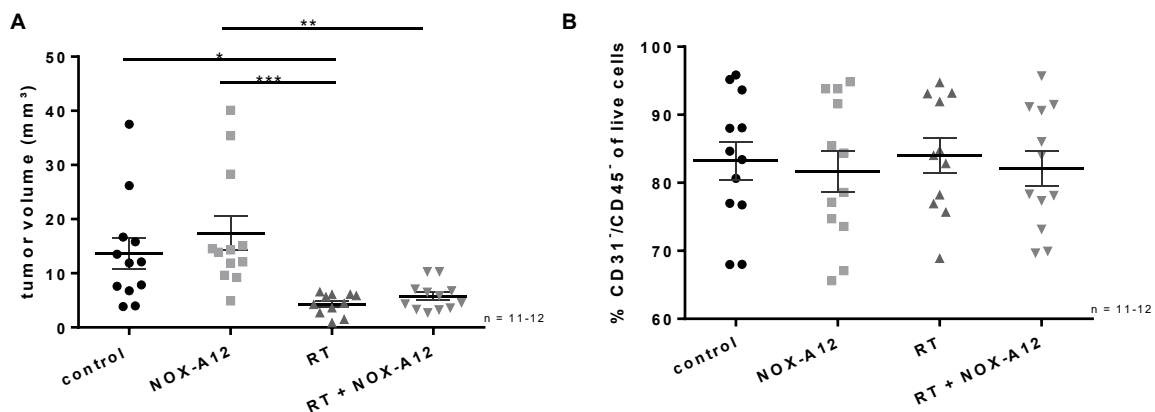
Fig. 20: Tumor volume measured by MRI and frequencies of tumor cells.
(A) The volume of tumor grafts after analyzing the MRIs 20 days after tumor inoculation. Under RT, the tumor-bearing mice showed a significantly lower tumor volume with less individual spread (n = 11-12 animals per group; mean tumor volume ± SEM). (B) The ratio of tumor cells (CD45⁻/CD31⁻) among the living cells examined. Living tumor cells showed no treatment-related significant differences (n = 11-12 animals per group; mean ratio ± SEM). * $p \leq 0.05$; ** $p \leq 0.01$; *** $p \leq 0.001$

4.3.2 Distribution of endothelial cells

Endothelial cells line the walls of all blood vessels and thus provide an indirect information into the nutrient and oxygen supply of a tumor. A determination of the abundance of endothelial cells was made in order to infer the effects of the different treatment regimes on the tumor vasculature.

The frequency of CD31 expressing cells in the blood samples of the untreated control group was determined to be $0.92 \pm 0.4\%$ of all living cells. The treatments reduced the mean value of CD31$^+$ cells to $0.76 \pm 0.3\%$ after administration of the CXCL12 inhibitor (control vs. NOX-A12, $p = 0.992$), increased it to $1.4 \pm 0.5\%$ after RT (control vs. RT, $p = 0.83$) , and to $1.2 \pm 0.3\%$ after RT in combination with NOX-A12 (control vs. RT + NOX-A12, $p = 0.971$) (Fig. 21).

High frequencies of endothelial cells were found in the splenic tissue of the mice. The untreated animals had a frequency of $89.2 \pm 0.5\%$ CD31$^+$ cells. The treatment resulted in a reduction to approximately 87% of all living cells with only a marginal difference between the types of therapy used (0.3-1.3%, all $p > 0.3$) (Fig. 21).

The amount of CD31$^+$ endothelial cells in the tumor tissue was also not significantly altered from $13.7 \pm 2.6\%$ by the treatment. The percentage of CD31$^+$ cells remained at around $15.3 \pm 2.6\%$ of all living cells isolated from the tumor after administration of

the CXCL12 antagonist alone (control vs. NOX-A12, p = 0.963) or in combination with RT (control vs. RT+ NOX-A12, p = 0.968). The RT alone did not change the cell ratio at all (13.7 ± 2.6%, control vs. RT, p > 0.99) (Fig. 21).
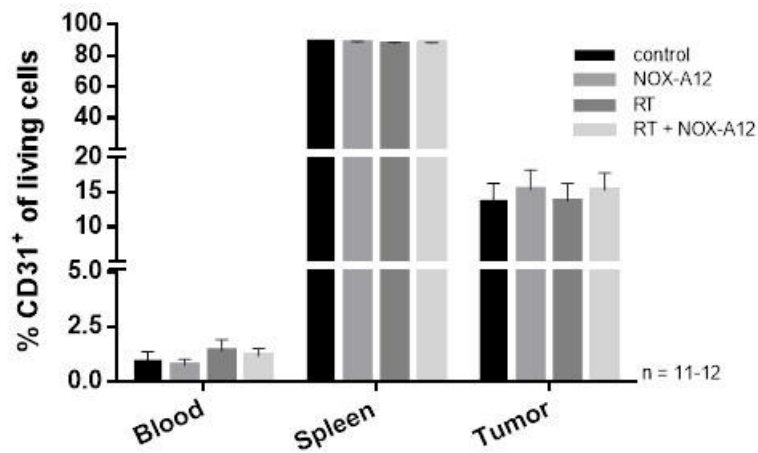
Fig. 21: Frequencies of CD31$^+$ endothelial cells.
Frequencies of CD31 expression among live cells in blood, spleen and tumor tissues of tumor-bearing mice under therapy. The proportion of CD31$^+$ cells among the living cells remains nearly constant in all treated tissues compared with the untreated control (n = 11-12 animals per group; mean living cells ± SEM).

4.3.3 Distribution of tumor-infiltrating leukocytes

The different treatments did not cause a significant change in the number of tumor-infiltrating leukocytes (CD45$^+$) based on all living cells analyzed (all p > 0.2) (Fig. 22, A). The relation between CD45$^+$ cells and the tumor volume was determined by correlation analysis. The correlation coefficient r describes, how the cell amount tends to change with the tumor volume. For the control group, a correlation coefficient r = 0.3042 (p = 0.337) was determined. The blockade of CXCL12 resulted in a higher r-value of 0.5274 (p = 0.078), which was reduced to r = 0.4415 (p = 0.151) by irradiation. The RT group showed a negative correlation between the tumor-infiltrating leukocytes and the measured tumor volume (r = -0.1048, p = 0.759). No relation was significant (Fig. 22, B).
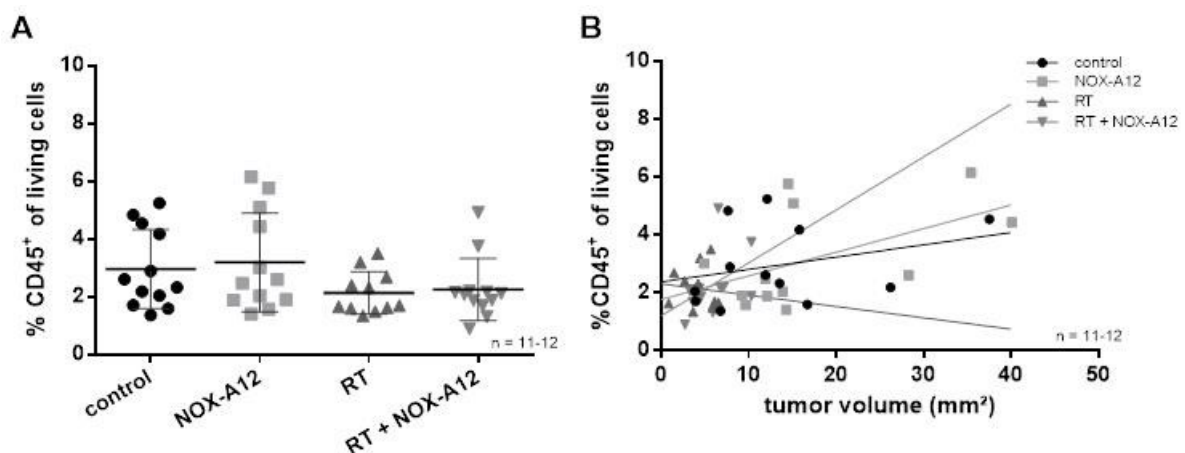
Fig. 22: Frequencies of the tumor-infiltrating leukocytes.
(A) The frequencies of tumor-infiltrating leukocytes (CD45$^+$) among all living cells slightly decreased under RT (n = 11-12 animals per group; mean CD45$^+$ cells ± SEM). (B) Frequencies of CD45$^+$ cells in relation to the determined tumor volume. Relative to the respective tumor volume according to MRI, the RT group showed a trend toward fewer leukocytes with a larger tumor volume (n = 11-12 animals per group).

4.3.4 Distribution of T cell subsets

Neither the CXCL12 antagonist nor RT nor the combination of both affected the frequency of $CD3^+$ cells among the leukocyte population in all organs investigated. However, the administration of NOX-A12 and the irradiation of the tumor had a minor influence on the frequency of the tumor-infiltrating T cells in the tumor tissue analyzed. Under the inhibition of CXCL12, the frequency of T cells was slightly reduced in comparison to the control group (control vs. NOX-A12, p = 0.894). In contrast, after RT, with or without additional immune modulation, the number of tumor-infiltrating T cells was moderately increased (control vs. RT, p = 0.796; control vs. RT+ NOX-A12, p = 0.702; NOX-A12 vs. RT + NOX-A12, p = 0.292) (Fig. 23, A). The frequency of $CD3^+$ cells was correlated with the tumor volume determined via MRI. Thereby, the correlation coefficient of the RT was negative (r = -0.2835, p = 0.398). For the control group, the highest coefficient was determined to be r = 0.5551 (p = 0.061). The administration of the CXCL12 inhibitor led to an r-value of 0.3059 (p = 0.334), which was increased to 0.4019 by adding RT (p = 0.195) (Fig. 23, C).
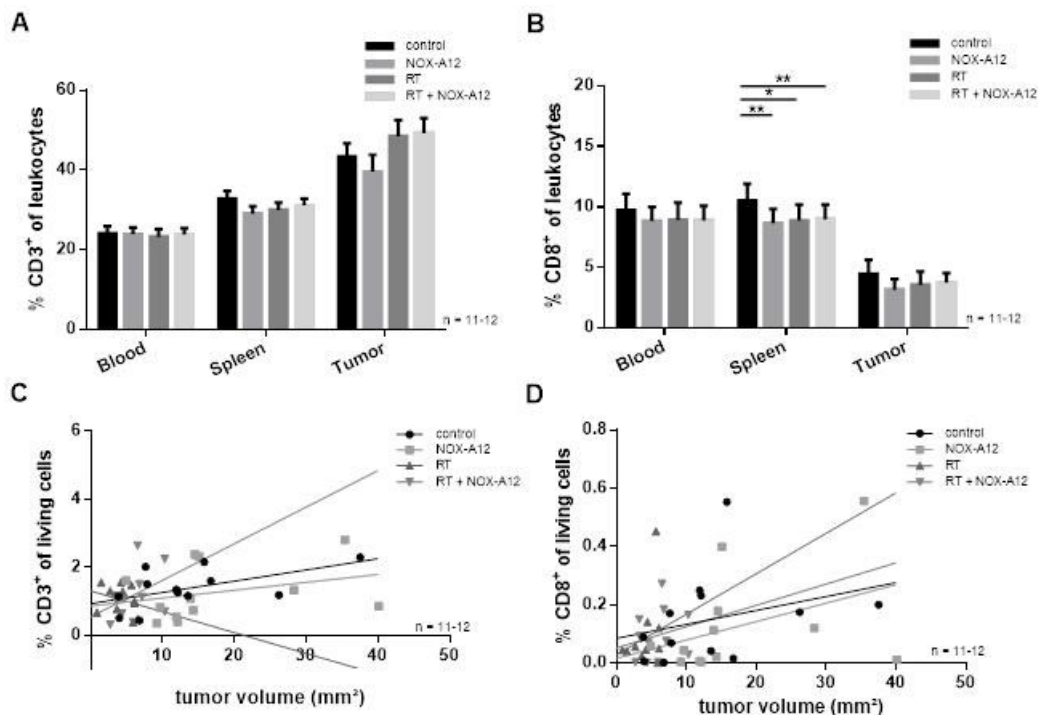
Fig. 23: Frequencies of T cells in different tissues and in relation to tumor volume.
(A) Frequencies of $CD3^+$ cells among all leukocytes ($CD45^+$) in the spleen, blood and tumor tissues of the animals determined by flow cytometry. The amount of T cells in tumor tissue was moderately decreased under CXCL12 inhibition and slightly increased after RT (n = 11-12 animals per group; mean $CD3^+$ ± SEM). (B) Frequencies of $CD8^+$ cells among all leukocytes ($CD45^+$) in the spleen, blood and tumor tissues determined by flow cytometry. In all organs investigated, the percentage distribution of $CD8^+$ T cells among all leukocytes showed only a slight decrease by treatments (n = 11-12 animals per group; mean $CD8^+$ ± SEM). (C) Frequencies of $CD3^+$ cells in relation to the determined tumor volume. The correlation between the $CD3^+$ T cells and the tumor volume is reduced due to the treatments and even negative for the RT group (n = 11-12 animals per group). (D) Frequencies of $CD8^+$ cells in relation to the determined tumor volume. Irradiation of the tumor reduced the correlation between the $CD8^+$ frequency and the tumor volume (n = 11-12 animals per group). * p ≤ 0.05; ** p ≤ 0.01; *** p ≤ 0.001.

The percentage distribution of $CD8^+$ T cells among all leukocytes declined marginally under treatment in all tissue investigated. Only in the spleen, significantly lower ratios of $CD8^+$ T cells were found compared with the untreated animals. Thereby, the

treatment groups with the CXCL12 antagonist showed greater significances compared with the untreated control (control vs. NOX-A12, p = 0.002; control vs. RT, p = 0.015; control vs. RT + NOX-A12, p = 0.009). However, no differences could be defined between the different treatments. The tumor-infiltrating CD8$^+$ effector cells were slightly reduced by the treatment (Fig. 23, B).

The distribution of the CD8$^+$ cells in relation to the tumor volume changed only slightly by the treatments. The application of the CXCL12 antagonist showed the highest correlation coefficient of 0.3953 (p = 0.203). Compared with the r-value of the control group (r = 0.301, p = 0.341), the irradiated tumors showed a reduced but almost equal coefficient value (RT, r = 0.2138, p = 0.528; RT + NOX-A12, r = 0.2239, p = 0.484) (Fig. 23, D).

The subpopulation of CD8$^+$ T cells was investigated for their expression of the regulation and activation markers CD69 and PD-1.

CD69 is an early activation marker that is rapidly expressed on the surface of T lymphocytes after CD3 and/or cytokine activation. However, the expression of the marker on tumor-infiltrating CD8$^+$ T cells is also involved in the exhaustion of the cells themselves. The CD69 expression is responsible for cell retention in the TME and the CD69 expression on T cells is associated with the expression of PD-1 in T cells

The circulating CD8$^+$ T cells expressed the CD69 marker only at very low levels. This marker was even almost absent on circulating CD8$^+$ T cells in the blood (0.07-0.26%). CD69 was found at a higher ratio on systemic CD8$^+$ T cells after administration of CXCL12 inhibitor in combination with RT (0.26 ± 0.14%) than in mice treated with RT (0.07 ± 0.05%) or NOX-A12 (0.22 ± 0.09%) alone. In the spleens, the CD69$^+$ cells corresponded to around 11% of CD8$^+$ T cells without any detectable difference between the treatment groups (all p> 0.95). The tumors showed a frequency of CD69$^+$CD8$^+$ T cells of more than 93%, which is equivalent to level of the PD-1$^+$CD8$^+$ T cells (80-90%) (Fig. 24, A). A closer look at the co-expression of these two markers reveals that 17.9 ± 5.6% of the CD69$^+$CD8$^+$ T cells observed after RT express only the CD69 marker on their surface, whereas in the other treatment groups 12-13 ± 3% of CD8$^+$ expressed this marker alone. In all groups, more than 75.6 ± 6.4% of the CD8$^+$ cells observed in the RT group co-expressed the activation marker CD69 along with the exhaustion marker PD-1 (Fig. 24, C).

The PD-1 inhibitory receptor (CD279) is expressed at the cell surface of activated T cells; it is also known as a negative co-stimulatory receptor which functions as an immune checkpoint. In cancer, PD-1 expression on CD8$^+$ T cells is associated with exhaustion of the effector T cells. On the one hand, the blood circulating CD8$^+$ T cell expressed PD-1 only to a very low extent on their surface (0.18-0.62%), whereas in the spleen the frequency of this cell type was more than sixty times higher (15.1-17.9%). The majority of the tumor-infiltrating CD8$^+$ T cells expressed the marker PD-1 on their surface (82-89.2%). However, no significant differences in the expression of this marker could be detected under therapy (all p > 0.52) (Fig. 24, B). Only the tumor-infiltrating CD8$^+$ cells that express only PD-1 showed a significant difference when the CXCL12 antagonist was administered compared with the control, even when all treatments reduced their amount (control vs. NOX-A12, p = 0.044; control vs. RT + NOX-A12, p = 0.005) (Fig. 24, C).
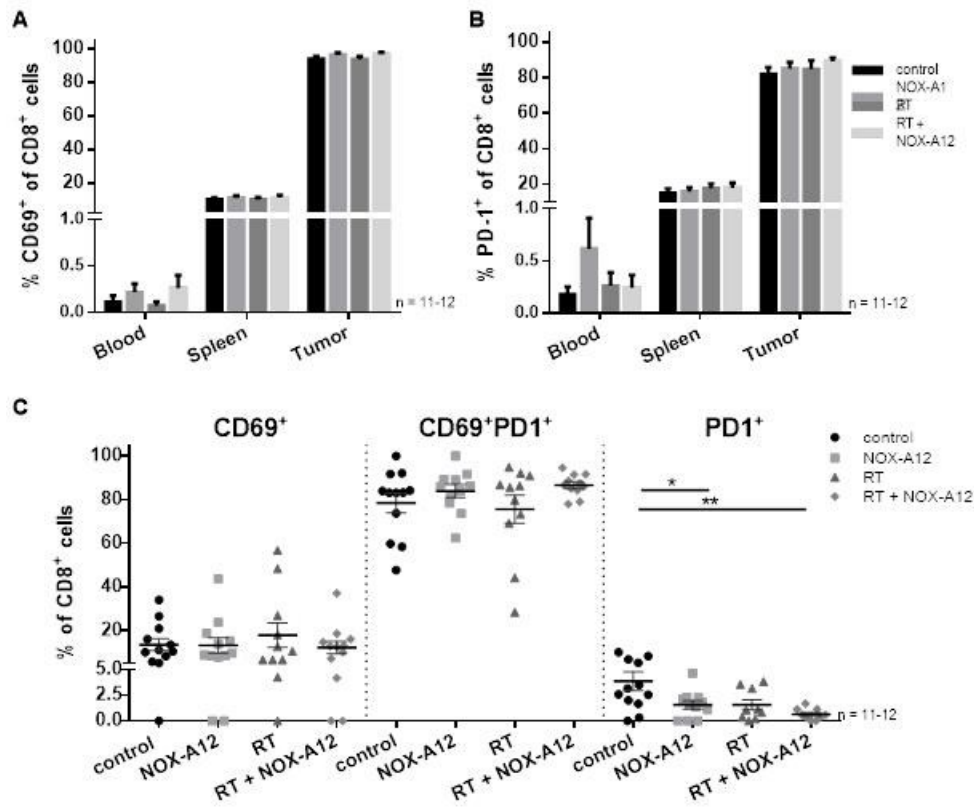
Fig. 24: Expression of the regulation and activation markers on CD8$^+$ T cells in blood, spleen and tumors.

(A) Frequencies of CD69$^+$CD8$^+$ T cells from blood, spleen and tumors under therapy measured by flow cytometry and expressed as a percentage of total CD8$^+$ T cells (n = 11-12 animals per group; mean CD69 ± SEM). (B) Percentage distribution of PD-1$^+$CD8$^+$ T cells measured by flow cytometry in blood, spleen and tumors under therapy and untreated control group (n = 11-12 animals per group; mean PD-1 ± SEM). (C) Expression of CD69 and PD-1 on tumor infiltrating CD8$^+$ cells. The gross of the CD8$^+$ cells co-express CD69 and PD-1 on their surface. Only a portion of 12-18% of the CD8$^+$ cells was positive for CD69 alone, while cells expressing only PD-1 were present at very low levels (0.6-3.9%) (n = 11-12 animals per group; mean marker ± SEM). * p ≤ 0.05; ** p ≤ 0.01; *** p ≤ 0.001.

In blood and spleen, the CD4$^+$ T cell population showed no significant alteration by the different treatments (all p > 0.807). RT only slightly increased the tumor-infiltrating population of this observed cell type (control: 33.6 ± 4.1% vs. RT: 37 ± 5.6%, p = 0.963; NOX-A12: 31.6 ± 4.5% vs. RT + NOX-A12: 36.7 ± 5.2%, p = 0.881) (Fig. 25, A).

According to the correlation analysis, the coefficients for the control group and the combination of RT and the immune modulator were relatively similar (control: r = 0.477, p = 0.117; RT + NOX-A12: r = 0.4585, p = 0.134). A lower coefficient was observed for the animals treated with the CXCL12 antagonist only (r = 0.1604, p = 0.618). The correlation for the CD8$^+$ cells was negative after irradiation (r = -0.2033, p = 0.549) (Fig. 25, C).

Taking a closer look at the CD4$^+$ T cell subpopulations of activated conventional T cells (Tcon) CD4$^+$CD25$^+$FoxP3$^-$, naïve conventional T cells CD4$^+$CD25$^-$FoxP3$^-$ and Tregs CD4$^+$CD25$^+$FoxP3$^+$ in the tumor, there was also no significant change in the percentage distribution of the cells by the different treatments (all p > 0.826) (Table 10). The naïve conventional T cells CD4$^+$CD25$^-$FoxP3$^-$ were reduced by approximately 3.9% by the combination of RT and immune modulator in comparison with the control (p = 0.907) and the other treatment arms (all p > 0.826). The RT was responsible for an insignificant increase in the frequency of Tregs CD4$^+$CD25$^+$FoxP3$^+$ of also around 3.9% relative to all groups (all p > 0.845) (Fig. 25, B).

Table 10: Frequencies of the CD4$^+$ subgroups.

	treatment (mean (± SEM))			
	control	**NOX-A12**	**RT**	**RT + NOX-A12**
active Tcon (CD25$^+$FoxP3$^-$)	12.2% (± 2.4%)	11.3% (± 2.1%)	13.0% (± 2.5%)	13.0% (± 3.4%)
naïve Tcon (CD25$^-$FoxP3$^-$)	34.8% (± 4.4%)	35.8% (± 4.7%)	35.0% (± 4.7%)	31.3% (± 5.2%)
Treg (CD25$^+$FoxP3$^+$)	23.2% (± 1.9%)	23.5% (± 2.4%)	27.6% (± 4.6%)	24% (± 4.1%)

The correlation analysis of the Tregs reveals a coefficient of 0.0989 (p = 0.76) for the control group. Both monotherapies showed a smaller negative r-value (NOX-A12, r = -0.0222, p = 0.945; RT, r = -0.3595, p = 0.278). The highest correlation coefficient was determined for the combination therapy (r = 0.1205, p = 0.709) (Fig. 25, D).
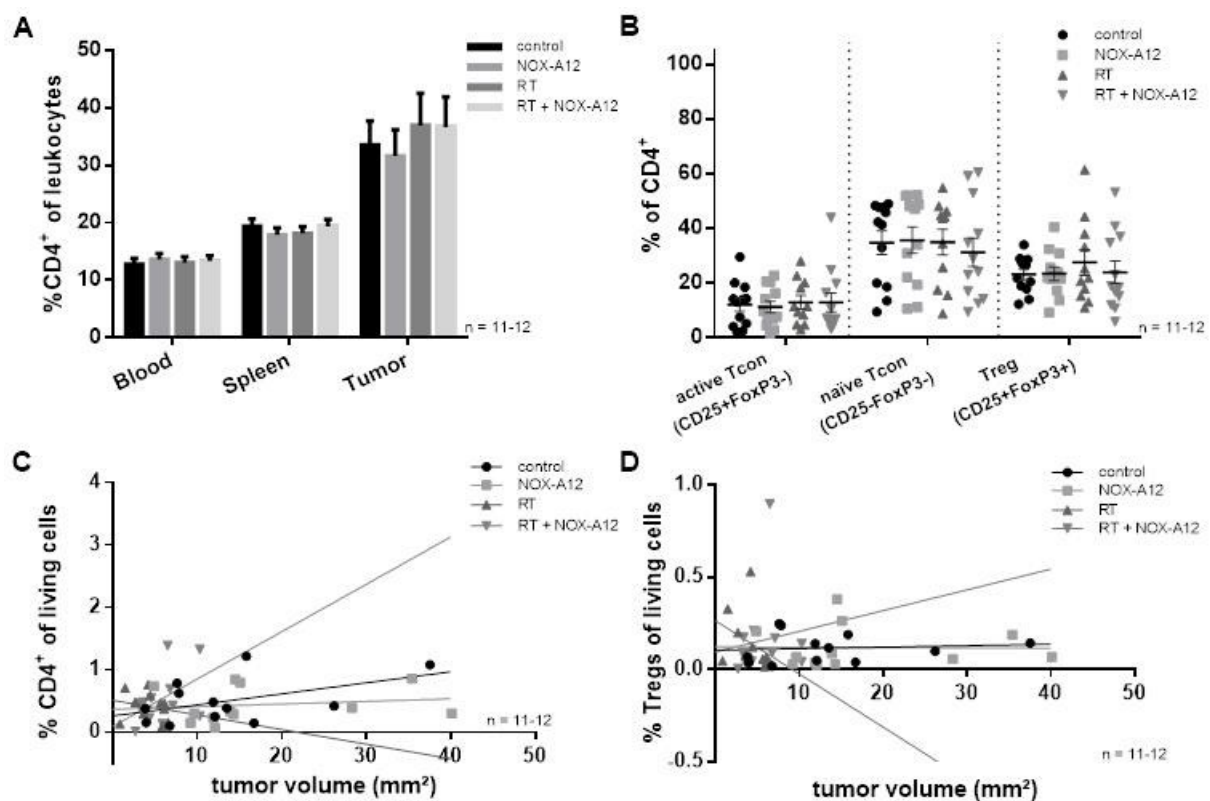
Fig. 25: Frequencies of CD4$^+$ T cells and the amounts of different tumor-infiltrating subpopulations.
(A) Frequencies of total CD4$^+$ T cells among leukocytes in studied organs after therapy detected by flow cytometry (n = 11-12 animals per group; mean CD4 ± SEM). (B) Amount of activated Tcon (CD4$^+$CD25$^+$FoxP3$^-$), naïve Tcon (CD4$^+$CD25$^-$FoxP3$^-$) and regulatory T cells (CD4$^+$CD25$^+$FoxP3$^+$) in the tumor presented as percentage of total CD4$^+$ T cells. The different CD4$^+$ T cell subpopulations showed no changes relative to the untreated control group (n = 11-12 animals per group; mean of specific subpopulation ± SEM). (C) Frequencies of CD4$^+$ cells in relation to the determined tumor volume (n = 11-12 animals per group). (D) Frequencies of Tregs in relation to the determined tumor volume. The correlation analysis revealed that only in the irradiated tumors the number of CD4$^+$ cells decreased with a higher tumor volume, whereas, the Tregs also showed a negative correlation after the administration of NOX-A12 (n = 11-12 animals per group).

The subpopulation of the Tregs detectable in the tumor tissue showed high expression levels of the immune regulatory surface molecules CD39, CD73 and PD-L1 of 82% to

96% in untreated animals. The frequency of these markers for the immunosuppressive activity of Tregs did not change under the influence of the different treatments, indicating that almost all cells co-expressed all three markers. Only in Tregs from samples treated with RT and immune modulator, marker levels decreased slightly but not significant compared with the control group (CD39$^+$, p = 0.834; CD73$^+$, p = 0.838; PD-L1$^+$, p = 0.464) (Fig. 26).
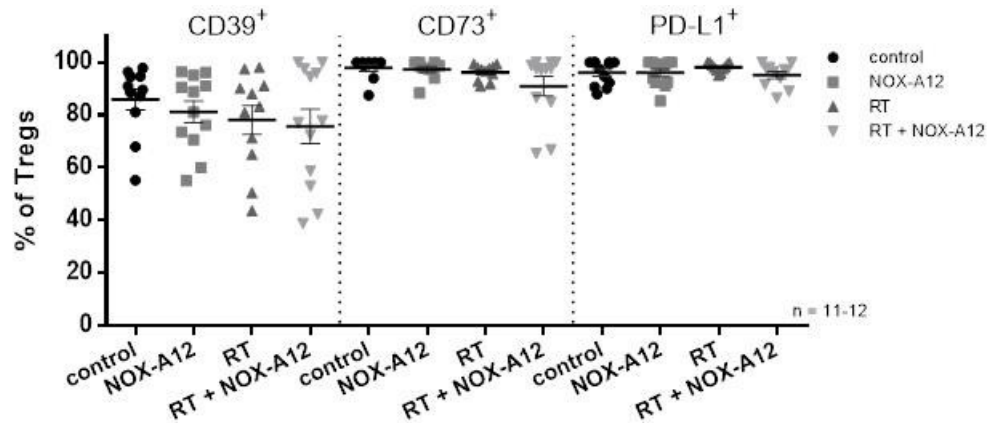
Fig. 26: Frequencies of immunosuppressive markers on tumor-infiltrating Tregs.
Markers CD39, CD73 and PD-L1 on tumor-infiltrating Tregs (CD25$^+$FoxP3$^+$). The markers showed no treatment-related changes post-therapy detected by flow cytometry and expressed as a percentage of total Tregs (n = 11-12 animals per group; mean marker ± SEM).

When compared with the control arm, the single treatments with CXCL12 inhibitor (p = 0.405) or RT (p = 0.392) enhanced the CD4$^+$/CD8$^+$ ratio. The combination therapy resulted in fewer CD4$^+$ T cells per CD8$^+$ effector cell than in the control group (p = 0.999) (Fig. 27, A).

The ratio of Tregs to CD8$^+$ effector cells indicates immune escape in GBM due to the suppressive activity of the Treg. After RT alone, there was the most unfavorable increase in the Treg/CD8$^+$ ratio indicating suppression of the activity of CTLs (control vs. RT, p = 0.181). In contrast, the combination therapy improved the Treg to CD8$^+$ T cell ratio compared with all arms (control vs. RT + NOXA12, p = 0.999; NOXA12 vs. RT + NOXA12, p = 0.942; RT vs. RT + NOXA12, p = 0.147) (Fig. 27, B).
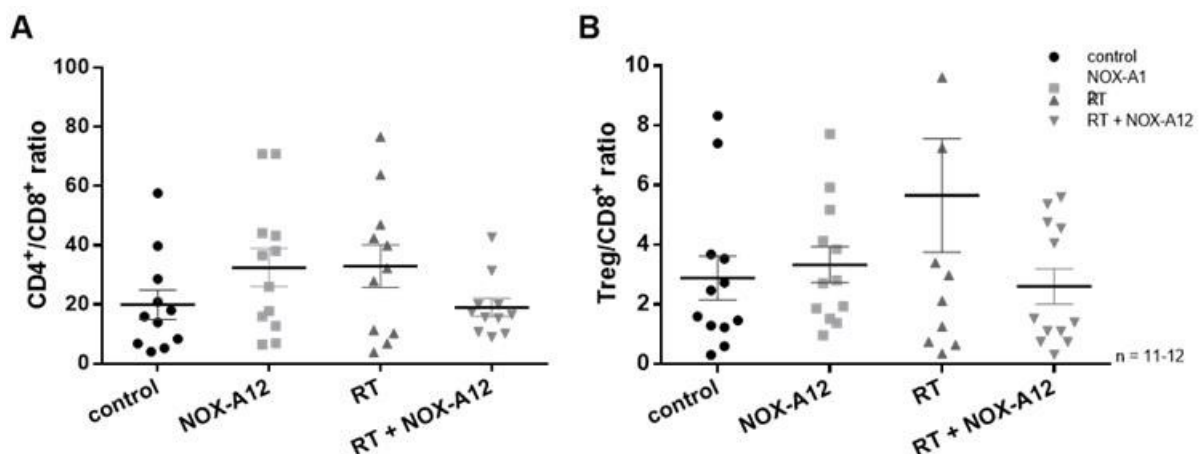
Fig. 27: Ratios of CD4$^+$ and regulatory T cells to CD8$^+$ effector cells.
(A) CD4$^+$/CD8$^+$ ratio in the tumor tissue of all control and treatment arms (n = 11-12 animals per group; mean ratio ± SEM). (B) Regulatory T cell to CD8$^+$ effector cells ratio in tumor tissue (n = 11-12 animals per group; mean ratio ± SEM).

4.3.5 Distribution of Myeloid Derived Suppressor Cells

The measured frequency of CD11b$^+$Gr1$^+$ MDSCs varied from 10.6 ± 1.3% of the total leukocyte population in the blood of untreated tumor-bearing mice to 13.7 ± 2.1% after combination therapy (p = 0.62). In the spleen, the corresponding MDSCs populations accounted for 1.6 ± 0.2% and 2.3 ± 0.5% of all leukocytes, respectively (p = 0.468). The proportion of tumor-infiltrating MDSC population slightly decreased under the influence of RT compared to the control group and amounted to 12.3 ± 2% of all tumor-infiltrating leukocytes (p = 0.906). In contrast, combination therapy increased the proportion to 19.1 ± 2.5% (p = 0.319). When the CXCL12 inhibitor was administered a slight increase in the tumoral MDSC population was detected in comparison to the untreated control group (p = 0.361) and the group of animals that received RT alone (p = 0.116) (Fig. 28, A).

Based on the tumor volume determined by MRI, the correlation analysis for the MDSC subpopulation revealed significant r-values for the control group (r = 0.5832, p = 0.047) and the monotherapy of CXCL12 blockade (r = 0.6957, p = 0.012). The correlation coefficients for the RT treatment groups did not differ markedly (RT, r = 0.3028, p = 0.365; RT + NOX-A12, r = 0.2831, p = 0.373) (Fig. 28, B).
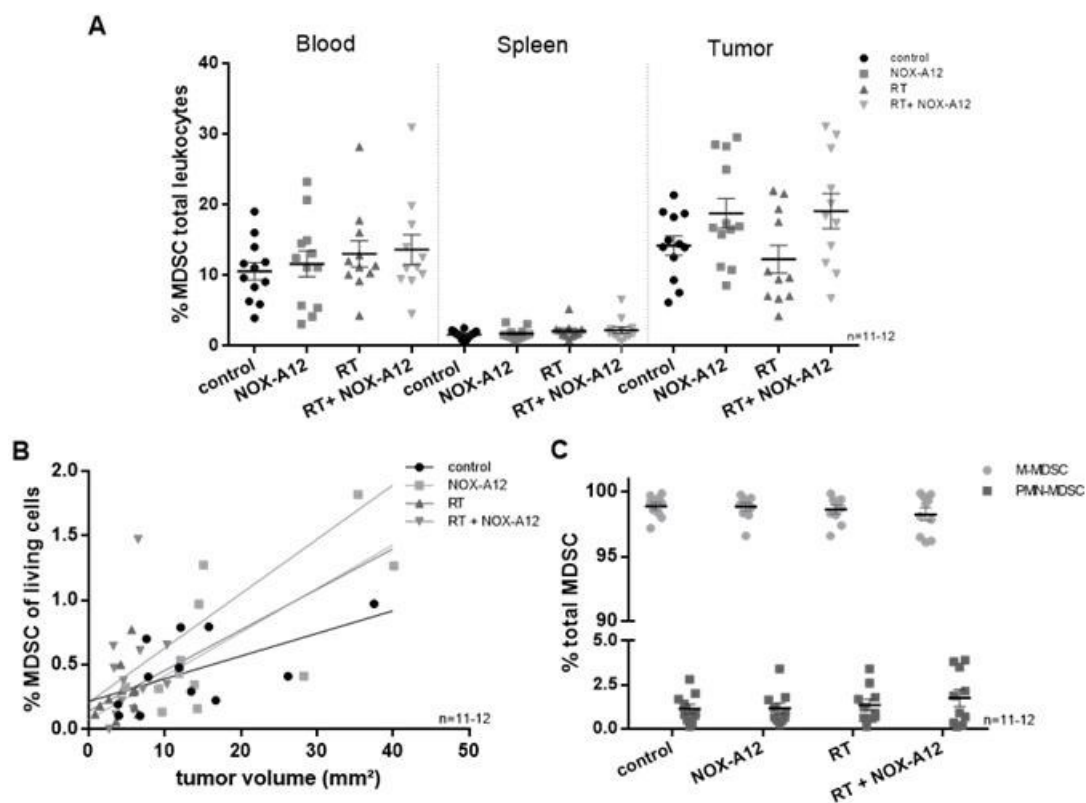
Fig. 28: Frequencies of MDSCs in different tissues and in relation to tumor volume.
(A) Proportion of MDSCs among all leukocytes in blood, spleen and tumor tissue of tumor-bearing mice under different therapies (n = 11-12 animals per group; mean MDSC ± SEM). The relative frequency of MDSCs among leukocytes in tumor tissue showed a slight increase by the administration of a CXCL12 antagonist. (B) Frequencies of MDSCs in relation to the determined tumor volume. Correlated to the determined tumor volume, the MDSC frequency increased in the control group and after the administration of CXCL12 inhibitor. In the irradiated groups, the correlation was reduced and not statistically relevant (n = 11-12 animals per group). (C) Percentage of monocytic MDSCs (M-MDSCs) and polymorphonuclear MDSCs (PMN-MDSCs) in the analyzed MDSC population. The MDSC population consisted mainly of M-MDSCs, PMN-MDSCs being negligible in the model used (n = 11-12 animals per group; mean MDSC ± SEM).

The tumor-infiltrating MDSC populations were composed almost exclusively of monocytic Ly6C$^+$Ly6G$^-$ MDSCs (M-MDSC), whose measured levels ranged from 98.3 ± 0.5% to 98.9 ± 0.3% of all MDSCs determined. However, contamination of this population with Ly6C$^+$ microglia cells could not be excluded. In this animal model, the polymorphonuclear Ly6C$^-$Ly6G$^+$ MDSCs (PMN-MDSC) could only be detected at a negligible percentage in all treatment groups. Accordingly, the PMN-MDSC levels ranged from around 1.1 ± 0.3% to 1.7 ± 0.5% of all MDSCs, showing a slight increase after RT (p = 0.963), although polymorphonuclear cells have been described to infiltrate gliomas (Gielen et al., 2016; Raychaudhuri et al., 2015; Wu et al., 2019) (Fig. 28, C).

The MDSCs from blood, spleen, and tumor tissues were analyzed for their immunosuppressive pattern based on the expression of the activation markers CD39, CD73 and PD-L1. By hydrolyzing ATP to AMP, CD39 contributes as a rate-limited enzyme to the extracellular adenosine production and thus to immune regulation, whereas the final hydrolysis step of AMP to immunosuppressive adenosin in this production cascade is catalyzed by the enzyme CD73 (Antonioli et al., 2013). Moreover, PD-L1 interacts with PD-1 expressed on T cells and leads to their exhaustion, suggesting that the expression of PD-L1 is an indicator of the immunosuppressive activity of MDSCs (Dieterich et al., 2017; Lu et al., 2016; Noman et al., 2014; Ostrand-Rosenberg et al., 2014).

In blood, the lowest expression levels of the marker CD39 was detected at 70.8 ± 6.5% on the MDSCs of mice treated with the combination of RT and immune modulator (control vs. RT + NOX-A12, p = 0.447), whereas the highest expression was observed after treatment with RT alone (85.1 ± 1.2%, RT vs. RT + NOX-A12, p = 0.154). However, the differences relative to any other treatment groups were not significant (all p > 0.89). For the marker CD73, a significant increase from 3.6 ± 1.1% (control) to 8.5 ± 1.5% of all CD73$^+$ MDSCs was observed after administration of the CXCL12 antagonist alone (control vs. NOX-A12, p = 0.0006; RT vs. NOX-A12, p = 0.002). The expression of PD-L1 on the MDSCs isolated from blood increased slightly under the influence of the CXCL12 inhibitor (control: 50.8 ± 6.3% vs. NOX-A12: 55.8 ± 7.4%, p = 0.956). The treatment with NOX-A12 alone led to a rise of PD-L1$^+$ MDSCs by 4.9 ± 9.9% (p = 0.956), and the combination of RT and NOX-A12 even caused a 6.1 ± 9.9% higher PD-L1 expression (p = 0.925) compared with the untreated control group (50.8 ± 6.3%). Regarding RT as single therapy, the combination showed 8.6 ± 10.1% more PD-L1$^+$ MDSCs in blood (p = 0.994) (Fig. 29, A).

The MDSCs isolated from the spleens showed no change in the expression of immunosuppressive molecule CD39 by therapy (all p > 0.548). The determined frequency of CD39$^+$ MDSCs ranged from 85.2 ± 0.8% and 87.3 ± 1.3% in all treatment groups. No treatment-related difference was detected in the amount of PD-L1$^+$ MDSCs either (all p > 0.889). The measured frequency of this subpopulation varied from 31.9 ± 2.2% to 35.3 ± 5.3%. Only the immune-suppressive marker CD73 was not significantly increased after administration of NOX-A12 alone (21.1 ± 3.3%) and in combination with RT (23.7 ± 2.8%) compared with the control group (16.3 ± 2.4%; control vs. NOX-A12, p = 0.641; control vs. RT + NOX-A12, p = 0.266) or RT alone (16.2 ± 2.8%; RT vs. RT + NOX-A12, p = 0.272) (Fig. 29, B).

A **Blood**

CD39⁺   CD73⁺   PD-L1⁺

- control
- NOX-A12
- RT
- RT+ NOX-A12

n=11-12

B **Spleen**

CD39⁺   CD73⁺   PD-L1⁺

- control
- NOX-A12
- RT
- RT+ NOX-A12

n=11-12

C **Tumor**

CD39⁺   CD73⁺   PD-L1⁺

- control
- NOX-A12
- RT
- RT+ NOX-A12

n=11-12
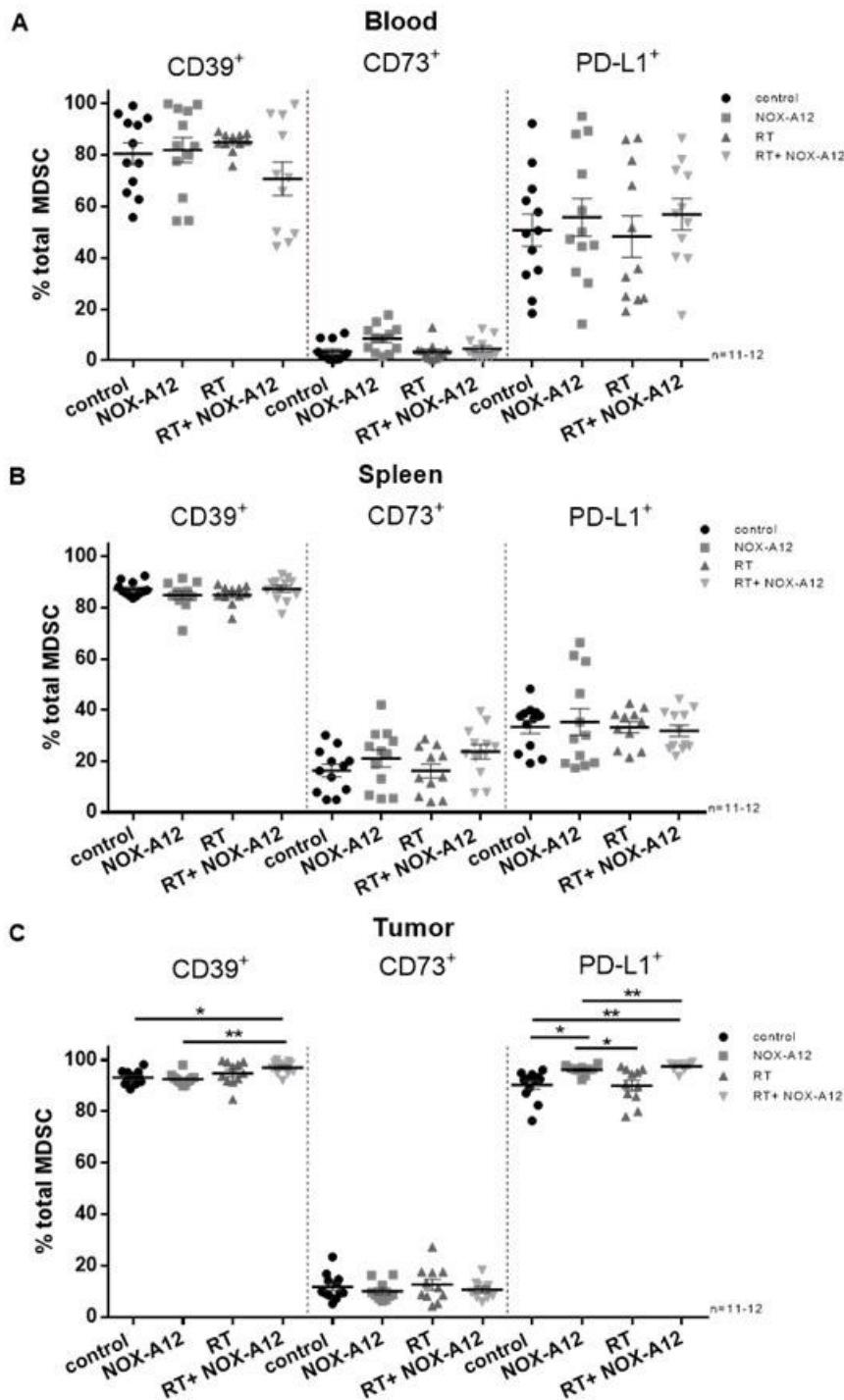
Fig. 29: Frequencies of immune-suppressive markers on MDSCs in blood, spleen and tumor. (A) Frequencies of MDSCs expressing immune-suppressive markers in blood after therapy, measured by flow cytometry and expressed as the percentage of total MDSCs. The MDSCs with CD39 on the surface represented the largest proportion of the circulating MDSCs. The CD73$^+$ expression was significantly influenced by the administration of the CXCL12 antagonist alone (n = 11-12 animals per group; mean MDSC ± SEM). (B) Frequencies of MDSCs expressing immune-suppressive markers in the spleens after therapy as measured by flow cytometry and expressed as the percentage of total MDSCs. The frequencies of CD39$^+$ and PD-L1$^+$ MDSCs isolated from the spleens of tumor-bearing mice did not change in their expression by therapy. The immune-suppressive marker CD73 was not significantly increased after the administration of NOX-A12 alone and in combination with RT (n = 11-12 animals per group; mean MDSC ± SEM). (C) Frequencies of MDSCs expressing immune-suppressive markers in the tumors after therapy, measured by flow cytometry and expressed as the percentage of total MDSCs. Like in the blood or spleen, MDSCs expressing CD39 and PD-L1 were also highly expressed in the tumor samples. The CD73$^+$ MDSCs accounted for only about 15% of the MDSCs found in the tumor tissues (n = 11-12 animals per group; mean MDSC ± SEM). * $p \leq 0.05$; ** $p \leq 0.01$; *** $p \leq 0.001$.

Almost all intratumoral MDSCs expressed the two immunosuppressive markers CD39 and PD-L1 on their surface. The proportion of CD39 expressing tumor-infiltrating MDSC was comparable to the frequency of circulating or splenic MDSCs. Maximum expression levels of this immune-suppressive marker were found in the

tumor samples, varying from 92.6 ± 0.6% to 97 ± 0.7%. In this regard, the untreated animals (93.2 ± 0.8%) and mice treated with the CXCL12 antagonist alone (92.6 ± 0.6%) expressed significantly less CD39 on the surface of intra-tumoral MDSCs than the animals treated with RT and antagonist (97 ± 0.7%) (control vs. RT + NOX-A12, p = 0.028; NOX-A12 vs. RT + NOX-A12, p = 0.007). With over 90% of all MDSCs, the frequency of MDSCs expressing PD-L1 was increased in the tumor compared with the amount found in blood (around 50%) or spleen (around 35%). The levels of PD-L1$^+$ MDSCs in the tumor differed significantly by the administration of the CXCL12 inhibitor. The treatment groups NOX-A12 alone (96.1 ± 0.6%) and RT + NOX-A12 (97.5 ± 0.6%) showed significantly increased PD-L1 expression compared to the untreated control (control vs. NOX-A12, p = 0.033; control vs. RT + NOX-A12, p = 0.008). The expression in these groups was also significantly increased compared with the RT alone (RT vs. NOX-A12, p = 0.029; RT vs. RT + NOX-A12, p = 0.007). In contrast, CD73 was found to a lower extent on the MDSCs in the tumor tissue, ranging from 10.0 ± 1.2% (NOX-A12) to 12.6 ± 2.1% (RT), with no evidence of a treatment effect (all p > 0.633) (Fig. 29, C).

MDSCs produce as immunsuppressive species nitrogen monoxide (NO) and ROS which suppress T cells by inhibiting their proliferation and inducing apoptosis (Kusmartsev et al., 2004; Markowitz et al., 2017; Raber et al., 2014; Wang et al., 2010). Therefore, the production of NO and ROS by MDSCs from peripheral blood, spleen and tumors was analyzed for the dependence on the forms of therapy used.

The production of NO by the MDSCs from blood and spleen was almost equal as measured by the mean fluorescence intensity (MFI) of the MDSCs. In contrast, the tumor-infiltrating MDSCs produced NO at a considerably higher level. The combination of RT and the immune modulator NOX-A12 did not leed to a measurable increase of NO in the tumor compared with the control group (control vs. RT + NOX-A12, p = 0.991). Compared with the RT alone, the combination of RT and NOX-A12 showed an increase (RT vs. RT + NOX-A12, p = 0.173) (Fig. 30, A).
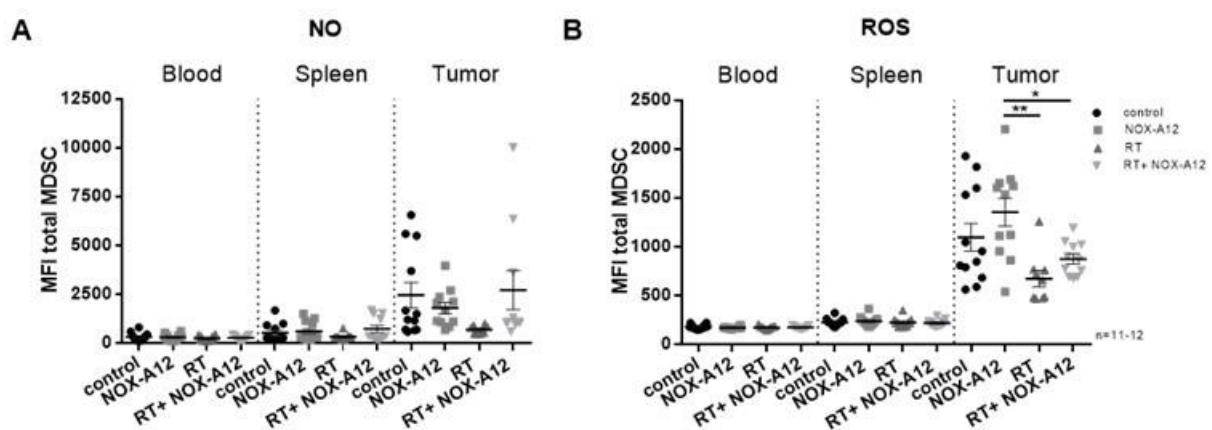
Fig. 30: Production of reactive nitric oxide (NO) and oxygen species (ROS).
(A) Production of NO by MDSCs in blood, spleen and tumor under the therapy measured by flow cytometry and presented as mean fluorescence intensity (MFI). The production in the tumor tissue was slightly affected by each therapy, the lowest production was determined after RT alone (n = 11-12 animals per group; MFI ± SEM). (B) Production of ROS by MDSCs in blood, spleen and tumor under the therapy measured by flow cytometry and presented as MFI. The MFI for ROS showed a significant decrease in production after irradiation of the brain tissue (n = 11-12 animals per group; MFI ± SEM). * p ≤ 0.05; ** p ≤ 0.01; *** p ≤ 0.001.

A similar behavior was observed for the production of ROS by MDSCs, which in this model is mainly dependent on the irradiation of the tumor tissue. The MFI of this staining displayed a lower level for the analyzed circulating and splenic MDSCs than for their intra-tumoral counterparts. After irradiation of the tumor-bearing hemisphere, ROS production in the tumor tissue was slightly decreased (control vs. RT, p = 0.074), resulting in a significant difference between the RT and immune modulator-treated group (RT vs. NOX-A12, p = 0.002). The combination of RT and immune modulator also showed a significantly lower ROS production compared to the NOX-A12 group alone (NOX-A12 vs. RT + NOX-A12, p = 0.028) (Fig. 30, B).

4.3.6 Chemokine receptor expression of MDSCs

In order to investigate the expression of chemokine receptors involved in MDSC migration, the expression of receptors CCR2, CCR4, CCR5, CXCR2, CXCR4 and CXCR7 on the MDSCs isolated from blood, spleen and tumor tissue analyzed in more detail.

After treatment, the frequency of MDSCs in the blood expressing these specific receptors was not significantly altered in the animals observed. The frequency of peripheral MDSCs that expressed CCR2 ranged from 12.5 ± 1.7% to 17.2 ± 3.3% of all MDSCs circulating in the blood (all p > 0.461). CCR4 was reduced expressed by 9.6 ± 2.8% of all blood-circulating MDSCs after treatment with CXCL12 antagonist compared to the control group (15.2 ± 3.6%; control vs. NOX-A12, p = 0.215). The lowest expression levels were measured for CCR5$^+$ (0.5-2.5%) and CXCR7$^+$ MDSCs (1.7–5.6%). In this context, the average value of CCR5$^+$ MDSCs did not change appreciably as a consequence of any treatment variant (all p > 0.554), however, CXCR7$^+$ MDSCs showed a lower mean value after each treatment (all p > 0.41). The frequency of circulating CXCR7$^+$ MDSCs showed a tendency to decrease after the treatment with the CXCL12 inhibitor (control vs. NOX-A12, p = 0.519), RT (control vs. RT, p = 0.846) and the combination of both (control vs. RT + NOX-A12, p = 0.41) compared with the non-treated control group. By contrast, the highest expression levels were measured for CXCR2 with 78.3 ± 2.8% to 85.5 ± 1.8% (all p > 0.19), followed by CXCR4 with 25.9 ± 5.3% to 33.8 ± 4.6% of all circulating MDSCs (all p > 0.665). The values for the CXCR4$^+$ cells showed a minor dependence on RT. However, because of the individual distribution of the receptor-positive MDSCs, the influence of treatment could not be verified for the blood samples (control vs. RT, p = 0.93) (Fig. 31, A).

The only significant change in the expression of the recruiting chemokine receptors on splenic MDSCs was observed for the CCR2 receptor. Here, the treatment with CXCL12 antagonist led to a significantly higher expression on the MDSCs isolated from the spleen (31.3 ± 2.1%) compared to the control group (18.5 ± 3.2%) (control vs. NOX-A12, p = 0.003), but the addition of RT significantly reduced this enhancement again (21.5 ± 1.5%, NOX-A12 vs. RT + NOX-A12, p = 0.025). The expression levels of CCR4 (8.1-10.0%), CCR5 (1.2-1.7%) and CXCR7 (1.4-1.5%) showed no change after treatment (all p > 0.23). The frequency of CXCR2 on the splenic MDSCs increased in response to RT from 55.3 ± 6.5% in the untreated control

group to 62.1 ± 3.4% after RT alone (p = 0.747) and 64.6 ± 5.9% after RT with NOX-A12 (p = 0.957), respectively. Compared with the determined levels of circulating CXCR2$^+$ MDSCs, the level of splenic MDSCs was correspondingly lower. The combination of RT and immune modulator resulted in a non-significant decrease in CXCR4$^+$ MDSCs in the spleen (29.6 ± 7.2%) compared with all other treatments (NOX-A12: 37.4 ± 7.9%, p = 0.917; RT: 41.0 ± 8.3%, p = 0.952) as well as the untreated control (35.2 ± 8%, p = 0.665) (Fig. 31, B).
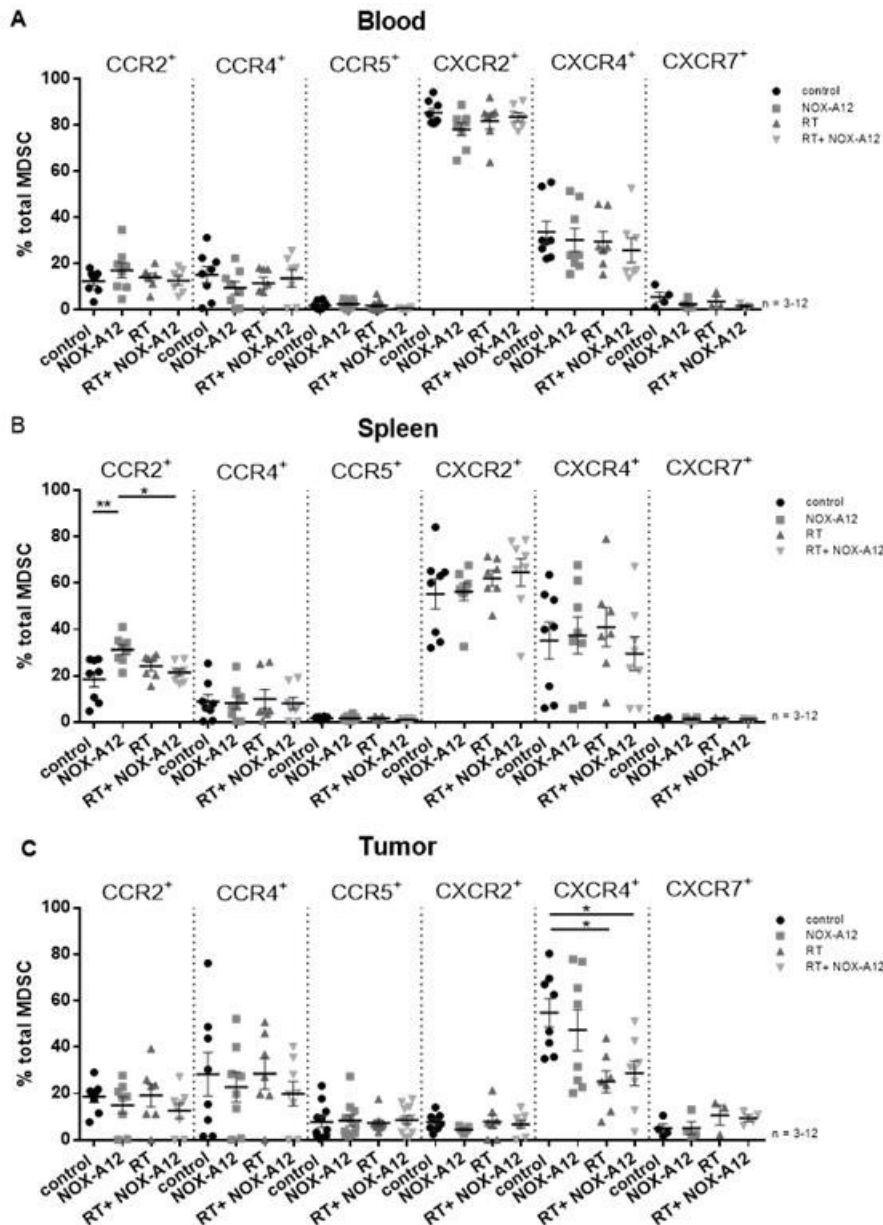
Fig. 31: Frequencies of chemokine receptors involved in MDSC migration. Frequencies of chemokine receptors CCR2, CCR4, CCR5, CXCR2, CXCR4 and CXCR7 involved in MDSC migration expressed on MDSCs from blood measured by flow cytometry. The frequencies of MDSCs in the blood expressing these specific receptors was not significantly altered in the observed animals by the treatments the animals received (n = 3-12 animals per group; mean MDSC ± SEM). (B) Frequencies of chemokine receptors CCR2, CCR4, CCR5, CXCR2, CXCR4 and CXCR7 involved in MDSC migration on splenic-derived MDSCs measured by flow cytometry. The treatment with CXCL12 antagonists led to a significantly higher expression of CCR2 on the MDSCs isolated from the spleens (n = 3-12 animals per group; mean MDSC ± SEM). (C) Frequencies of chemokine receptors CCR2, CCR4, CCR5, CXCR2, CXCR4 and CXCR7 involved in MDSC migration on MDSCs from the tumor as measured by flow cytometry. The frequencies of CCR2, CCR4, CCR5, CXCR2, CXCR4 and CXCR7 expression on the MDSCs in the tumor tissue were only slightly affected by each type of therapy. Only the expression of the CXCR4 receptor was significantly altered by RT (n = 3-12 animals per group; mean MDSC ± SEM). * p ≤ 0.05; ** p ≤ 0.01; *** p ≤ 0.001.

About 16% of all MDSCs in the tumor tissue expressed CCR2, about 25% CCR4 and less than 10% each CCR5, CXCR2 or CXCR7. Thus, the determined mean values of the frequencies of these receptors on the surface of the MDSCs located in the tumor

tissue showed only a minor influence of the applied therapies. The expression level of the CCR2 receptor decreased non-significantly by about 5% under RT and immunotherapy (12.5 ± 3.3%) compared with other forms of therapy (NOX-A12: 14.98 ± 3.6%; p = 0.958; RT: 19.2 ± 4.8%, p = 0.564). Compared with the untreated control group (28.3 ± 9.3%), the mean expression of CCR4 on the tumoral MDSCs decreased with treatment, and this decrease was mainly promoted by the administration of NOX-A12 (NOX-A12: 22.8 ± 6.4%, p = 0.944; RT + NOX-A12: 19.96 ± 5.2%, p = 0.835). In contrast, the levels of the CCR5 receptor showed no changes by applied therapy (all p > 0.978). After cerebral irradiation, a slight increase in CXCR2 (7.9 ± 2.8 %) and CXCR7 (10.6 ± 4.3%) expression was found on MDSCs compared with the untreated control (CXCR2: 7.8 ± 1.3%, p > 0.99; CXCR7: 5.0 ± 1.9%, p = 0.463) in the tumor tissue (Fig. 31, C).

The CXCR4 receptor was detected on 25.1 ± 4.7% to 54.9 ± 6.1% of all MDSCs found in the tumor tissue. These expression frequencies were the only ones that were significantly differentially regulated by therapy. The administration of a CXCL12 antagonist alone caused only a slight downregulation of the CXCR4 receptor on the tumor-infiltrating MDSCs (control: 54.9 ± 6.1% vs. NOX-A12: 47.4 ± 8.8%, p = 0.841). However, the amount of CXCR4$^+$ MDSCs is significantly reduced by the irradiation of the tumor tissue (control vs. RT: 25.1 ± 4.7%, p = 0.019). The additional administration of NOX-A12 showed no further reduction of the receptor on the MDSCs (control vs. RT + NOX-A12: 28.8 ± 5.4%, p = 0.037) (Fig. 31, C).

4.4   Receptor profiling after radiotherapy

In the previously described flow cytometric studies of the TME, it was found that only the subpopulation of tumor-infiltrating MDSCs expressing the CXCR4 receptor was significantly reduced after irradiation. In order to investigate this radiation effect in more detail, eight animals of this experimental model were irradiated with 12 Gy on the 10th day after tumor inoculation. After another 10 days of observation, leukocytes in blood and tumors were analyzed by flow cytometry for their expression of the surface receptors CCR2, CCR4, CCR5, CXCR4 and CXCR7 compared with untreated animals. In particular, the receptor profiles of the subpopulations of the CD8$^+$ effector cells, CD4$^+$FOXP3$^+$ Tregs and the CD11b$^+$Gr1$^+$ MDSCs were detected according to the panels in Table A-2.

The MRI showed significant differences between the mean tumor growth of the two treatment groups (Fig. 32, A). The mean tumor volume determined by MRI was significantly reduced to 3.3 ± 0.4 mm³ in the RT group compared with 8.9 ± 1.9 mm³ in the control group (control vs. RT, p = 0.011) (Fig. 32, B).

Based on the frequency of the CD45$^-$ cells in the tumor mass, the leukocytes to tumor cell ratio among the living cells was determined. The mean ratio of tumor cells (95.4 ± 1.4%) among all living cells in the irradiated tumor, did not significantly differ from that of the control group (96.2 ± 0.6%, p = 0.615) (Fig. 32, C). The ratio of leukocytes to tumor cells was slightly increased by the irradiation compared with the control group (p = 0.184) (Fig. 32, D). This corresponded with previous results (4.2.4).
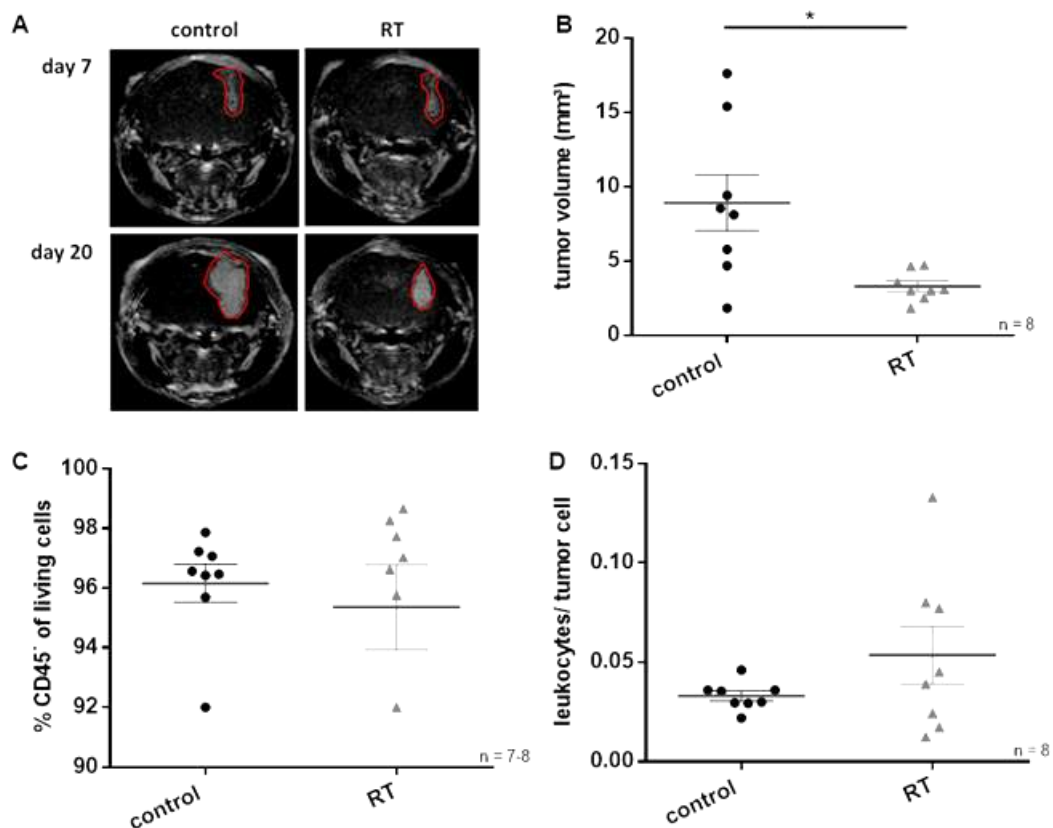
Fig. 32: Tumor volume determined by MRI and frequency of tumor cells.
(A) Representative T1-weighted MRI of the two treatment groups acquired 7 and 20 days after tumor inoculation. (B) The volume of the tumor grafts according to MRI analysis 20 days after tumor inoculation. Under RT, the tumor-bearing mice showed a significantly lower tumor volume with less individual spread (n = 8 animals per group; mean tumor volume ± SEM). (C) Frequencies of tumor cells (CD45⁻) among the living cells. The frequencies showed no treatment-related significant differences (n = 8 animals per group; mean ratio ± SEM). (D) Leukocytes to tumor cell ratio among the living cells examined. The mean ratios showed only a slight influence of RT (n = 8 animals per group, mean ratio ± SEM). * $p \leq 0.05$; ** $p \leq 0.01$; *** $p \leq 0.001$

As in the previously examined samples (4.2.4), the frequency of leukocytes among living cells in tumors after RT did not differ as much as in the blood of the untreated control (p = 0.713). Similarly, no significant change was observed in the number of tumor-infiltrating leukocytes between the animals under RT (3.4 ± 0.8%) and the untreated control group (3.7 ± 0.6%) (p = 0.747) (Fig. 33, A).

The mean frequency of $CD3^+$ T cells among the tumor-infiltrating leukocytes was slightly increased after RT (57.1 ± 3.4%) compared with the untreated control (47.2 ± 4.4%) (p = 0.095), but no difference could be detected systemically (p = 0.329) (Fig. 33, B).

A closer look at the T cell subpopulations $CD4^+$ and $CD8^+$ revealed no significant change in the distribution of the cells related to the treatment. In the blood samples, the mean values for the $CD4^+$ and $CD8^+$ cells were almost the same with or without RT ($CD4^+$, p = 0.988; $CD8^+$, p = 0.599). The mean value of the tumor-infiltrating $CD4^+$ cells also showed only a negative difference of 3.8% after RT (47.9 ± 3.57%) compared with the untreated control group (51.7 ± 4.8%) (p = 0.54). The frequency of the $CD8^+$ cells in the irradiated tumor tissue (24.4 ± 4.7%) was 8.2% higher than in the untreated tissue (16.2 ± 2.2%) (p = 0.137) (Fig. 33, C). Thus, for every $CD8^+$ cell in the untreated TME, there are 3.2 $CD4^+$ cells and after irradiation there are 1.9 $CD4^+$ cells.
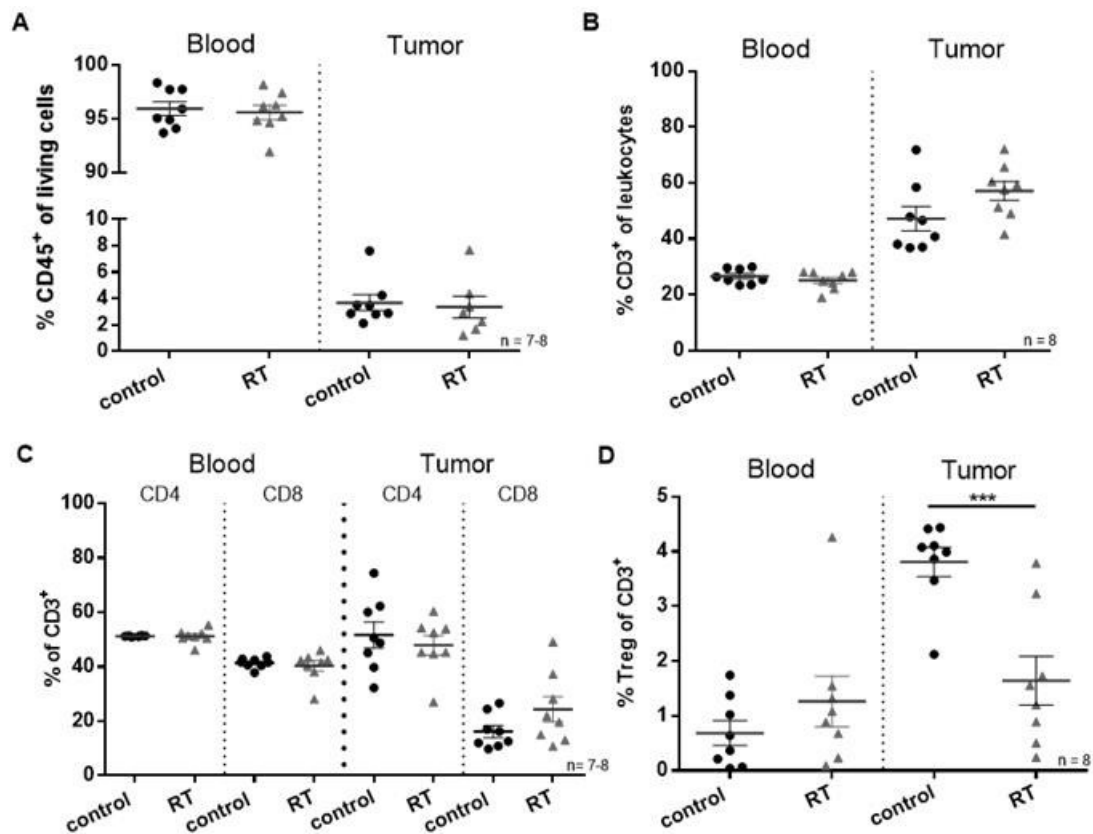
Fig. 33: Frequencies of systemic and tumor-infiltrating T cells.
(A) Frequencies of leukocytes (CD45$^+$) in blood and tumor tissue. After RT, no change was determined (n = 8 animals per group; mean ratio ± SEM). (B) Frequencies of CD3$^+$ T cells in the blood and the tumor tissue. After radiation, slightly more T cells were found in the tumor tissue (n = 8 animals per group; mean ratio ± SEM). (C) Frequencies of CD4$^+$ and CD8$^+$ T cells in blood and tumor tissue. The two subpopulations do not differ according to the treatment (n = 8 animals per group; mean ratio ± SEM). (D) Frequencies of Tregs in blood and tumor tissue. The tumor-infiltrating Tregs are significantly reduced by irradiation (n = 8 animals per group; mean ratio ± SEM). * p ≤ 0.05; ** p ≤ 0.01; *** p ≤ 0.001

In the blood, a doubling of the frequency of the subpopulation of Tregs was found after RT (control: 0.7% ± 0.2% vs. RT: 1.3 ± 0.5%, p = 0.281). However, the frequency of the tumor-infiltrating immunosuppressive Tregs was significantly reduced by the radiation (1.6 ± 0.4%) compared with the untreated samples (3.8 ± 0.3%) (p = 0.0009) (Fig. 33, D). As a result, the Treg to CD8$^+$ ratio was also significantly reduced by irradiation from 0.4 to 0.2 Tregs per CD8$^+$ cell (p = 0.038).

The CD11b$^+$ leukocytes were divided in CD11b$^+$Gr-1$^+$ MDSCs and CD11b$^+$Gr-1$^-$ macrophages or monocytes. The systemic number of macrophages was slightly increased by 0.2% as a result of the applied irradiation (1.4 ± 0.2%) compared with the untreated control (1.2 ± 0.03%) (p = 0.46). In the tumor tissue, less than 0.5% of all leukocytes were identified as CD11b$^+$Gr-1$^-$ monocytes/macrophages, whereas the irradiation decreased the frequency from 0.4 ± 0.2% to 0.3 ± 0.1% (p = 0.55)(Fig. 34, A). However, the mean value of CD11b$^+$Gr-1$^+$ MDSCs in the blood was not affected by the irradiation of the tumor. In the blood of untreated animals, 7.4 ± 0.5% of all leukocytes were MDSCs, after RT the frequency was not significantly changed (7.5 ± 0.7%) (p = 0.873). In the tumor tissue, 42.8 ± 3.9% of all leukocytes were positive for CD11b and Gr-1. This value was reduced by 5.8% to 37 ± 2.9% after irradiation of the malignancy (p = 0.255) (Fig. 34, B).
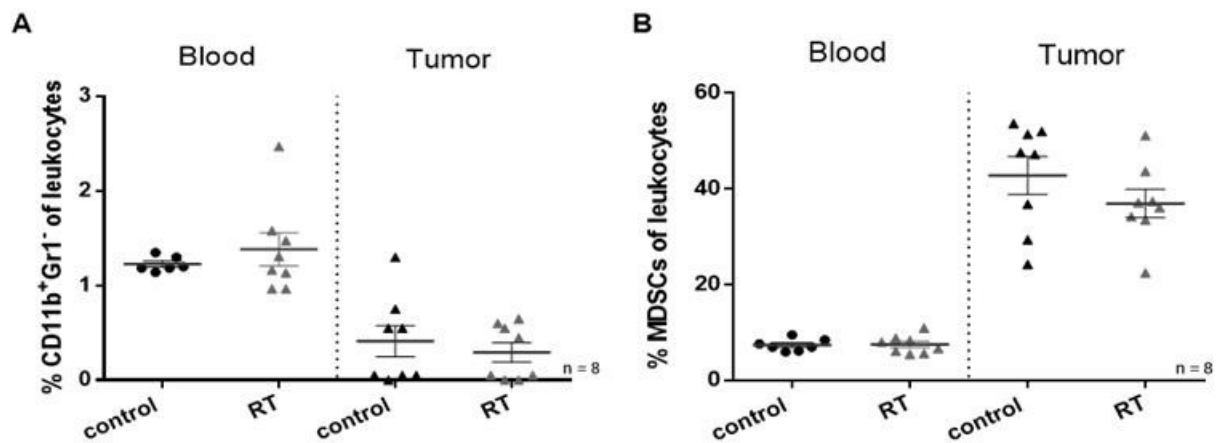
Fig. 34: Frequencies of systemic and tumor-infiltrating CD11b$^+$ cells.
(A) The frequencies of systemic and tumor-infiltrating macrophages and monocytes. The frequencies were only moderately affected by the RT (n = 8 animals per group; mean CD11b$^+$Gr-1$^-$ ± SEM). (B) MDSC frequencies in blood and tumor tissue. The MDSC population in the blood was not affected by the irradiation. The tumor-infiltrating MDSCs were reduced by almost 6% as a result of RT (n = 8 animals per group; mean MDSC (CD11b$^+$Gr-1$^+$) ± SEM).

Profiles of the chemokine receptor distribution focusing on the migration receptors CCR2, CCR4, CCR5, CXCR4 and CXCR7 were obtained from the subpopulations of the tumor-infiltrating CD8$^+$ effector T cells, the immunosuppressive Tregs and MDSCs. Thereby, the cells that express only one of the five receptors examined on their surface (single expression) were distinguished from those that co-express different receptors (multiple co-expression).

4.4.1 Receptor profiling of CD8+ effector cells

Taking a closer look at the CD8$^+$ effector cells in the tumor tissue, which express only one of the five examined receptors on their surfaces, four receptors showed a decrease in the single expression on tumor-infiltrating CD8$^+$ T cells after irradiation (CCR2, CCR4, CCR5 and CXCR4). Among them, the smallest alteration (-0.2% of CD8$^+$) was observed for the receptor CCR5 (0.8 ± 0.3%) after RT compared with the control group (0.9 ± 0.1%) (p = 0.639). The CCR2 (0.8 ± 0.1%, p = 0.167) and the CXCR4 receptor (8.3 ± 1.2%, p = 0.711) were also less expressed after RT. The decrease in CCR4$^+$CD8$^+$ T cells from 4.2 ± 0.7% to 2.8 ± 0.6% was the largest difference detected (p = 0.152). The single expression of CXCR7 was slightly increased after RT from 0.25 ± 0.07% to 0.33 ± 0.1% (p = 0.61) (Fig. 35, A).
The CD8$^+$ T cells, that co-express different receptors on the cell surface, showed increased expression for all five receptors investigated on the surface of the effector cells of animals under RT compared with the untreated control group. After RT, the mean values of the co-expressed receptors differed from 6.5% up to 17% from the untreated group (Fig. 35, B). In the control group, 34.4 ± 4.5% of the CD8$^+$ T cells co-expressed CCR2 along with other receptors investigated, whereas 48.5 ± 5.6% of the CD8$^+$ T cells co-expressed the receptor after RT (p = 0.071). The ratio of CD8$^+$ T cells co-expressing the CCR4 receptor was 38.6 ± 4.4%. After RT, 52.2 ± 5.6% of CD8$^+$ T cells showed the receptor CCR4 on their surface along with other receptors analyzed (p = 0.079). The smallest difference was determined for the CCR5 multi-expressing CD8$^+$ T cells (control: 29.8 ± 4.1% vs. RT: 36.3 ± 4.2%, p = 0.28). For the receptor

CXCR4, a multiple co-expressing ratio of $35.3 \pm 4.6\%$ in untreated animals was compared with $50.1 \pm 5.7\%$ after RT (p = 0.063). Without treatment, the receptor CXCR7 was found on $31.9 \pm 4.8\%$ of CD8$^+$ T cells in the TME, in contrast to $48.9 \pm 5.8\%$ of the same cell type, which was significantly increased in the irradiated tumor tissue (p = 0.04) (Fig. 35, B).

Fig. 35. Receptor profile of the CD8$^+$ T cells in the tumor tissue.
(A) Frequencies of tumor-infiltrating CD8$^+$ T cells expressing only one chemokine receptor. No significant reduction was observed by the irradiation (n = 8 animals per group; mean ratio ± SEM). (B) Distribution of the chemokine receptors on CD8$^+$ T cells considering the co-expression of the receptors. Irradiation causes an significant increase in the expression of the CXCR7 receptor after irradiation (n = 8 animals per group; mean ratio ± SEM). * p ≤ 0.05; ** p ≤ 0.01; *** p ≤ 0.001

A closer look at the co-expression profile of all receptors on the surface of the CD8$^+$ effector cells allows the identification of the most expressed combinations of the five analyzed receptors. Considering all found expression patterns with frequencies above 0.1%, the combination of all receptors analyzed (CCR2$^+$CCR4$^+$CCR5$^+$CXCR4$^+$ CXCR7$^+$) was found expressed on the surface of the most analyzed CD8$^+$ cells. After RT, this subgroup was increased by 4.1% (control: $13.6 \pm 2.8\%$ vs. RT: $17.7 \pm 2.6\%$, p = 0.305). Also, the combinations CCR4$^+$CXCR4$^+$CXCR7$^+$ (control: $3.7 \pm 1.1\%$ vs. RT: $10.7 \pm 2.1\%$, p = 0.012) and CCR2$^+$CCR4$^+$CXCR4$^+$CXCR7$^+$ (control: $3.7 \pm 1.4\%$ vs. RT: $9.9 \pm 2.3\%$, p = 0.035) were determined to be significantly increased by the treatment and listed as second and third most common co-expression configurations after RT. The expression of CCR4$^+$CCR5$^+$CXCR4$^+$CXCR7$^+$ was elevated by 3.1% on the CD8$^+$ cells following irradiation (control: $6.0 \pm 1.4\%$ vs. RT: $9.1 \pm 1.8\%$, p = 0.192). Other significantly increased expressed combinations after RT were CCR5$^+$CXCR4$^+$CXCR7$^+$ (p = 0.049) and CXCR4$^+$CXCR7$^+$ (p = 0.008) (Fig. 36).
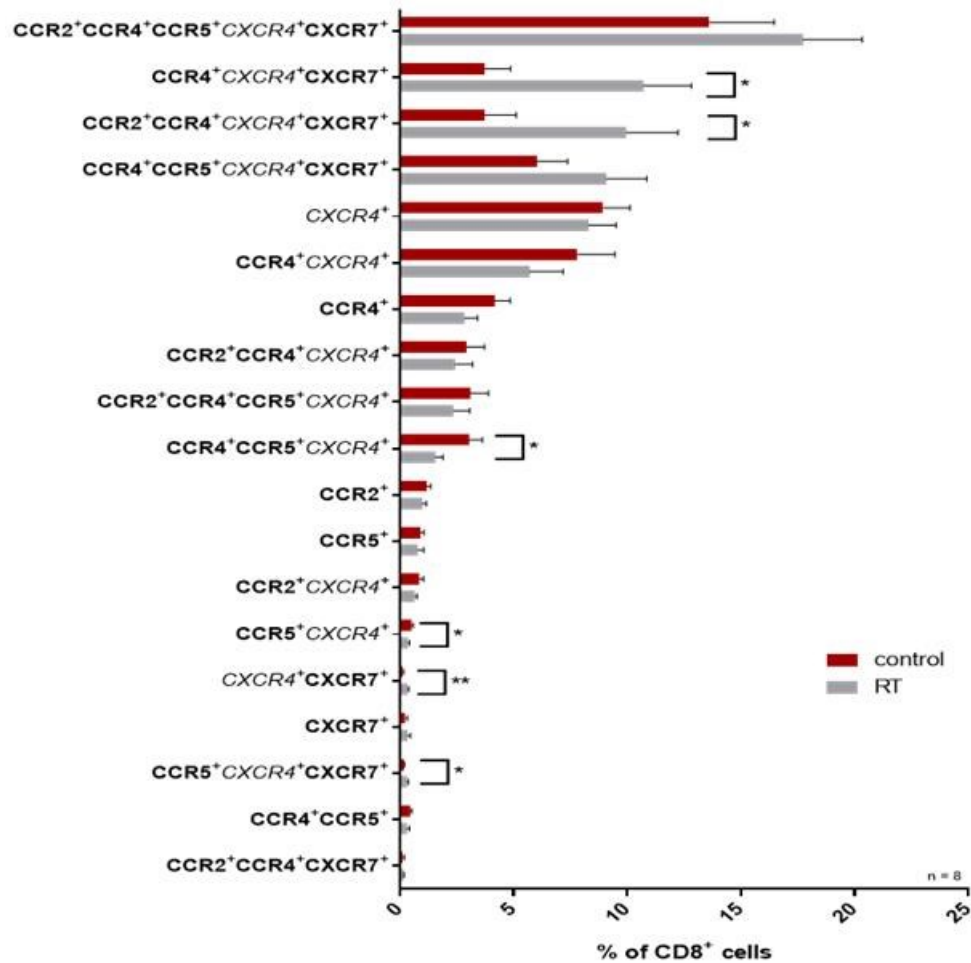
Fig. 36: Overview of the chemokine receptors co-expression pattern on CD8$^+$ cells.
Frequencies of the detected receptor co-expression patterns of CD8$^+$ T cells with a frequency higher than 0.1%, sorted after RT. After irradiation, most of the CD8$^+$ T cells co-expressed all receptors on their surface. The largest increase of expression was detected for the combinations CCR4$^+$CXCR4$^+$CXCR7$^+$ and CCR2$^+$CCR4$^+$CXCR4$^+$CXCR7$^+$ with more than 6%. Outside of the top five of the post-treatment expression patterns, the receptor co-expression was mostly decreased by the treatment (n = 8 animals per group; mean ratio ± SEM). * p ≤ 0.05; ** p ≤ 0.01; *** p ≤ 0.001

Contrastingly, the combinations outside the top five are usually expressed in a reduced manner after RT compared to the control, starting with the co-expression of CCR4 and CXCR4, which was reduced by 2.1% by irradiation. Furthermore, the combinations CCR4$^+$CCR5$^+$CXCR4$^+$ (p = 0.043) and CCR5$^+$CXCR4$^+$ (p = 0.012) were significantly increased expressed on the surface of the irradiated CD8$^+$ cells (Fig. 36).

4.4.2   Receptor profiling of Tregs

The Tregs found in tumor tissue expressed most of the chemokine receptors along with others on their surface. On tumor-infiltrating Tregs, a single expression was detected at a very low level only for the receptor CXCR4. This decreased from 1.6 ± 0.5% to 1.2 ± 0.5% after irradiation (p = 0.642) (Fig. 37, A). Most Tregs - over 97.5% of all Tregs - expressed the receptors CCR4 and CXCR4 simultaneously on their surface unaffected by the treatment (all p > 0.248). The other three receptors were co-expressed in a radiation-induced increased manner (all p > 0.26). The co-expressing ratio of the CXCR7 receptor differed by 10% between the control group (23.4 ± 7.4%) and the RT group (33.4 ± 4.3%) (p = 0.26) (Fig. 37, B).
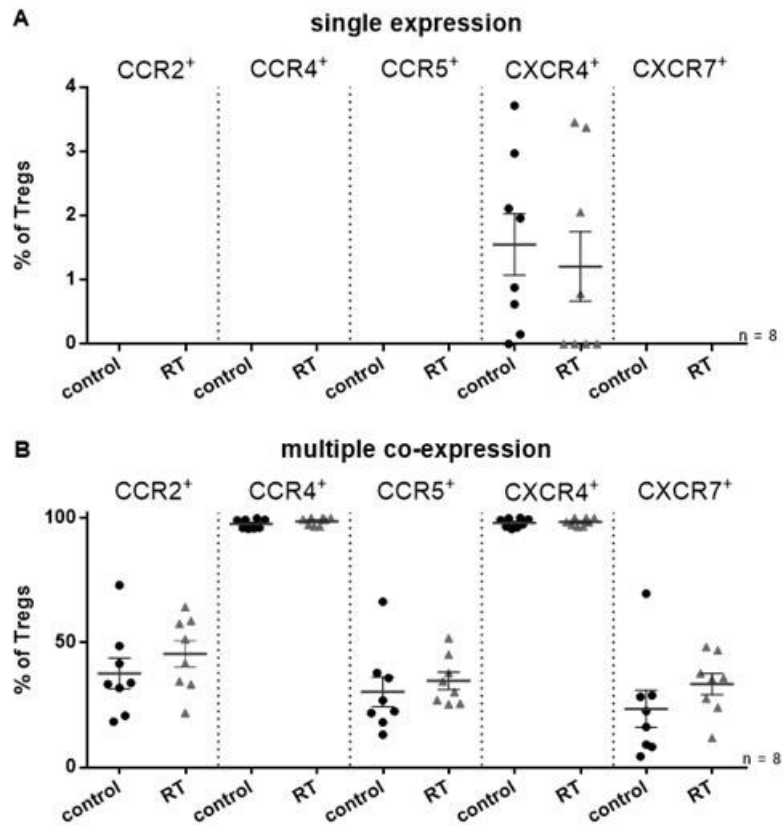
Fig. 37: Receptor profile of the Tregs in the tumor tissue.
(A) Frequencies of Tregs expressing only one chemokine receptor. Only the CXCR4 receptor was expressed individually. After irradiation, the proportion of these cells decreased almost significantly (n = 8 animals per group; mean ratio ± SEM). (B) Distribution of chemokine receptors on Tregs considering the co-expression of the receptors. All Tregs that expressed more than one receptor also showed the receptors CCR4 and CXCR4 on their surface (n = 8 animals per group; mean ratio ± SEM).
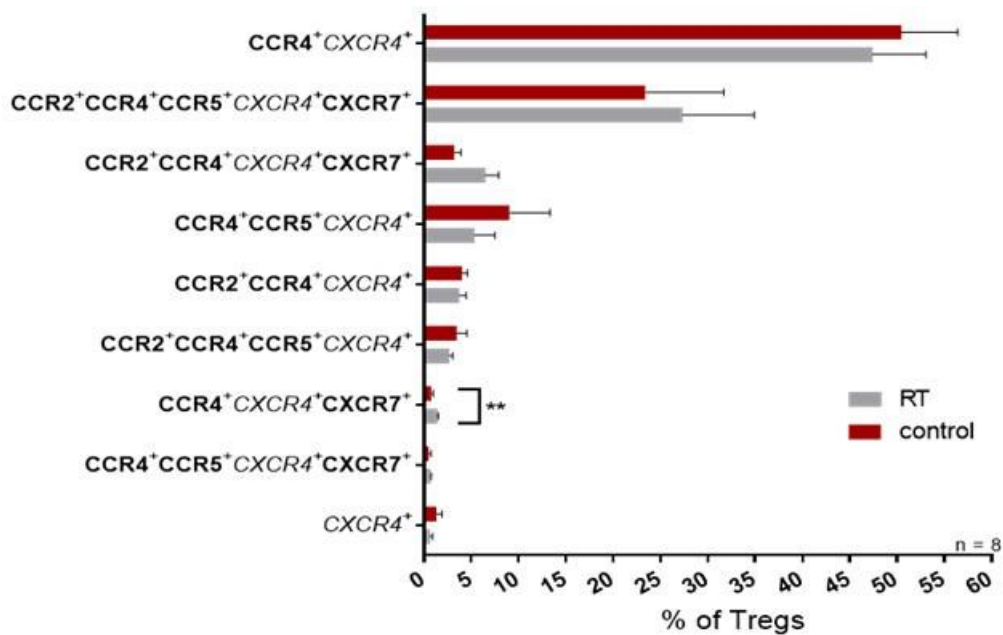
Fig. 38: Overview of the chemokine receptors co-expression pattern on Tregs cells.
Frequencies of the detected receptor co-expression patterns on Tregs sorted after RT. After irradiation, most Tregs co-expressed the receptors CCR4 and CXCR4 on their surface followed by co-expression of all receptors. Only the pattern CCR4$^+$CXCR4$^+$CXCR7$^+$ was significantly increased after the treatment (n = 8 animals per group; mean ratio ± SEM). * p ≤ 0.05; ** p ≤ 0.01; *** p ≤ 0.001

After RT, most of the Tregs found were positive for both CCR4 as well as CXCR4. The frequency of this co-expression pattern was reduced by 3% (control: 50.5 ± 5.9% vs. RT: 47.4 ± 5.6%, p = 0.719) as a result of the irradiation. Over 27.3 ± 7.6% of all post-irradiation Tregs showed all receptors co-expressed on their surface, representing an increase of 3.8% compared with the untreated group (23.5 ± 8.3%; p = 0.735). The co-expression of CCR2, CCR4, CXCR4 and CXCR7 was borderline insignificantly increased by the treatment (control: 3.3 ± 0.7% vs. RT: 6.5 ± 1.4%, p = 0.056). In contrast, the difference of the $CCR4^+CXCR4^+CXCR7^+$ Tregs was significantly enhanced with (1.4 ± 0.1%) and without (0.8 ± 0.2%) treatment (p = 0.009). The Tregs expressing the patterns $CCR4^+CCR5^+CXCR4^+$ (control: 9.1 ± 4.2% vs. RT: 5.3 ± 2.2%, p = 0.442), $CCR2^+CCR4^+CXCR4^+$ (control: 4.0 ± 0.6% vs. RT: 3.7 ± 0.7%, p = 0.778) and $CCR2^+CCR4^+CCR5^+CXCR4^+$ (control: 3.4 ± 1.1% vs. RT: 2.7 ± 0.4%, p = 0.524) were reduced after RT (Fig. 38).

4.4.3 Receptor profiling of MDSCs

On the MDSCs in the tumor tissue, all receptors investigated were individually expressed at a very low extent. The three receptors CCR2, CCR4 and CCR5 showed almost no expression changes after treatment. The proportion of MDSCs expressing the receptor CXCR7 alone increased almost significantly (p = 0.055). However, the CXCR4 receptor was significantly less individually expressed on the intratumoral MDSCs after irradiation (control: 9.6 ± 0.7% vs. RT: 5.7 ± 0.9%, p = 0.004) (Fig. 39, A). The co-expressions of the receptors CCR2 and CCR5 did not change as a result of the irradiation, but the number of CCR4 (p = 0.535) and CXCR7 (p = 0.286) co-expressing MDSCs increased slightly. Like the single-expressing MDSCs, the MDSCs co-expressing CXCR4 along with other receptors were significantly reduced by RT (control: 53.9 ± 3.9% vs. RT: 41.1 ± 3.8%) in the tumor tissue (p = 0.034) (Fig. 39, B).

A closer look at the receptors co-expression patterns on the surface of MDSCs showed that most of the chemokine receptor combinations found were reduced by radiation. In addition to the significant reduction of the CXCR4 single-expression (p = 0.004), the top 70% of all detected receptor co-expression patterns showed nine other combinations significantly reduced by radiation (Fig. 40).

After RT, the combinations $CCR2^+CCR4^+CCR5^+CXCR4^+$ (control: 9.0 ± 0.8% vs. RT: 6.0 ± 0.5%, p = 0.009) and $CCR2^+CXCR4^+$ (control: 6.4 ± 0.6% vs. RT: 3.3 ± 0.5%, p = 0.0009) were reduced by around 3% on the surface of the tumor-infiltrating MDSCs. The ratio of the receptor combination $CCR2^+CCR5^+CXCR4^+$ in the irradiated tissue differed by 1.5% from the control group (control: 3.8 ± 0.4% vs. RT: 2.3 ± 0.3%, p = 0.015). After treatment, approximately 2% less MDSCs in the RT group carried the receptor combination $CCR5^+CXCR4^+$ (control: 3.2 ± 0.5% vs. RT: 1.2 ± 0.3%, p = 0.003) on their surface compared with the untreated control group. The $CCR4^+CCR5^+CXCR4^+$MDSCs were significantly decreased by 1.3% (control: 1.9 ± 0.2% vs. RT: 0.6 ± 0.1%, p = 0.0001). The combinations $CXCR4^+CXCR7^+$ (control: 2.2 ± 0.2% vs. RT: 1.6 ± 0.2%, p = 0.037), $CCR5^+CXCR4^+CXCR7^+$ (control: 1.5 ± 0.1% vs. RT: 0.7 ± 0.2%, p = 0.002), $CCR4^+CCR5^+CXCR4^+$CXCR7+ (control: 0.97 ± 0.05% vs. RT: 0.7 ± 0.1%, p = 0.015) and $CCR2^+CCR4^+CXCR4^+$ (control: 0.8 ± 0.05% vs. RT: 0.5 ± 0.05%, p = 0.002) were found to be reduced between 0.3% and 0.8% in the post-irradiated tumor tissue (Fig. 40).
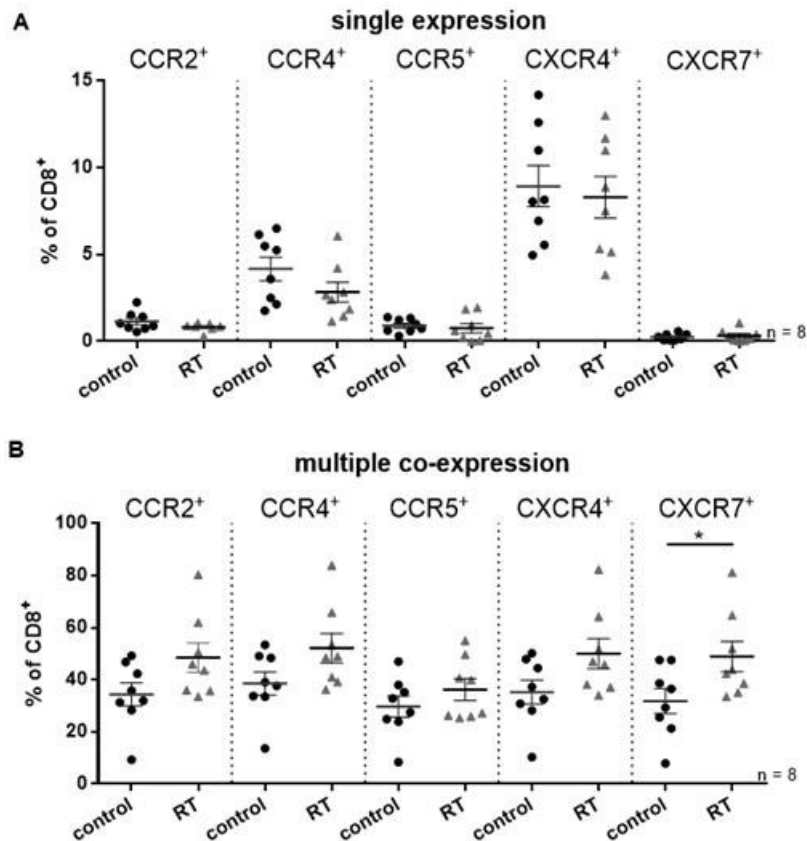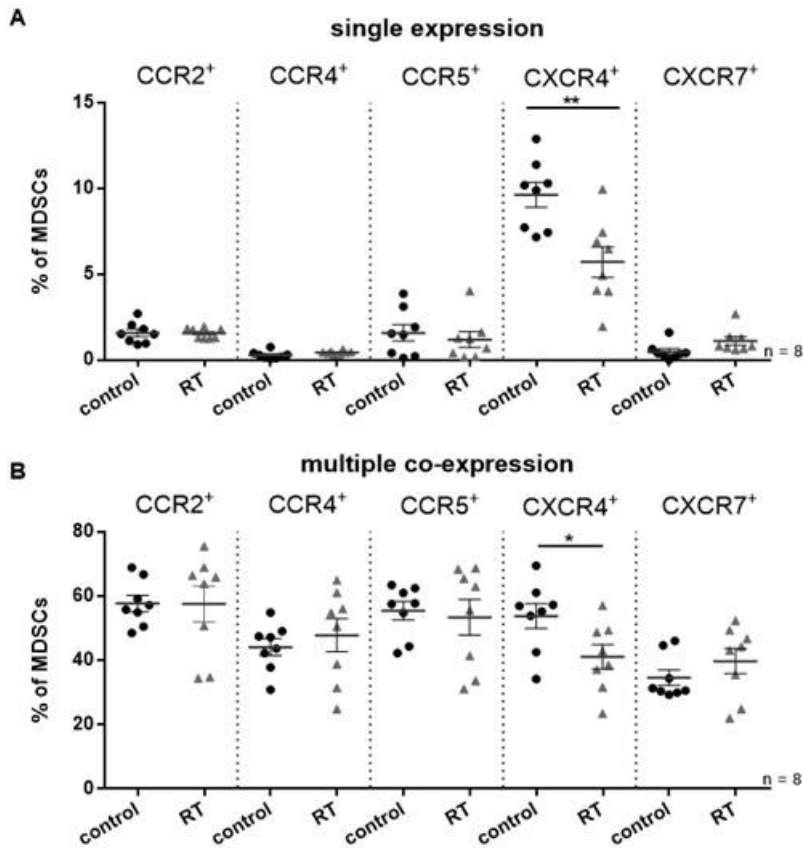
Fig. 39: Receptor profile of the MDSCs in the tumor tissue.
(A) Frequencies of tumor-infiltrating MDSCs expressing one chemokine receptor. The single expressed receptor CXCR4 was significantly reduced on MDSC after irradiation (n = 8 animals per group; mean ratio ± SEM). (B) Distribution of the chemokine receptors on MDSCs considering the co-expression of the receptors. Here, the cells, that co-express the CXCR4 receptor among others, were significantly reduced (n = 8 animals per group; mean ratio ± SEM). * p ≤ 0.05; ** p ≤ 0.01; *** p ≤ 0.001
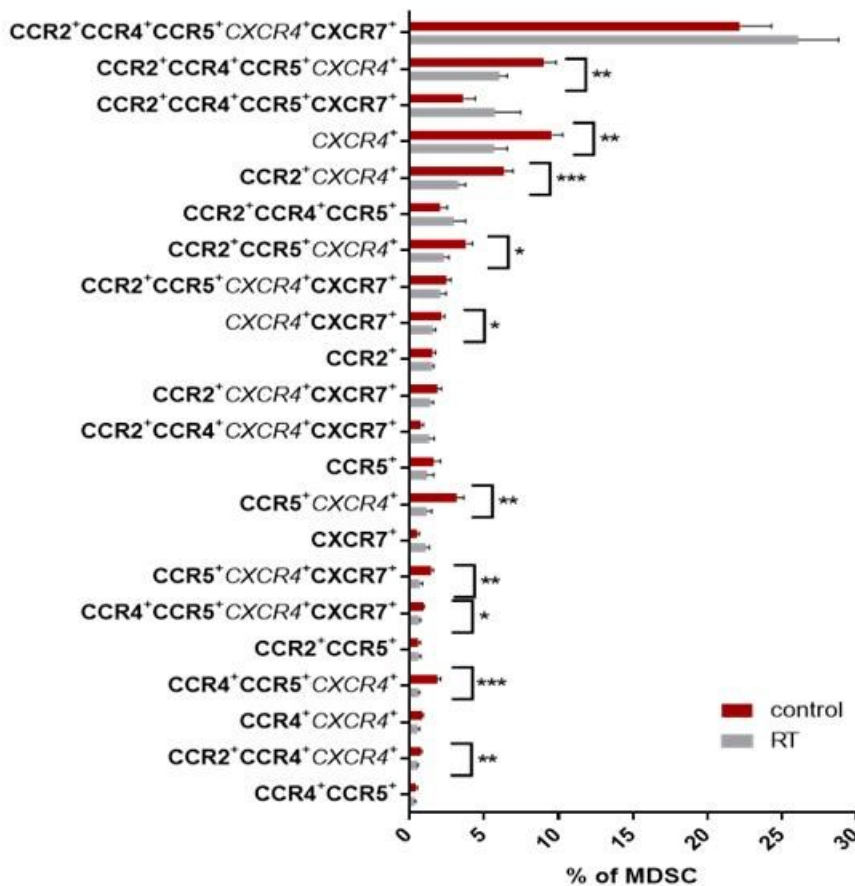
Fig. 40: Overview of the chemokine receptors co-expressed on MDSCs.
The combinations of chemokine receptors co-expressed on the surface of theintra-tumoral MDSCs with a frequency higher than 0.4%. As a result of irradiation, most of the combinations were reduced. In addition to the single expression of the receptor CXCR4, nine other combinations were significantly downregulated (n = 8 animals per group; mean ratio ± SEM). * p ≤ 0.05; ** p ≤ 0.01; *** p ≤ 0.001

On the other hand, the frequencies of co-expressions of the receptors CCR4 and CXCR7 with others were enhanced as a result of irradiation. For example, the combination CCR2⁺CCR4⁺CCR5⁺CXCR7⁺ was increased by 2.1% (control:

3.7 ± 0.7% vs. RT: 5.8 ± 1.7%, p = 0.275). As another example, an additional 0.9% of irradiated MDSCs expressed the receptors CCR2, CCR4 and CCR5 simultaneously after RT (2.9 ± 0.8%, p = 0.333) (Fig. 40).

The combination of all receptors (CCR2$^+$CCR4$^+$CCR5$^+$CXCR4$^+$CXCR7$^+$) proved to be the most frequent co-expression pattern on the analyzed tumor-infiltrating MDSCs. The measured frequency was 3.9% elevated when the tumor tissue was irradiated (26.1 ± 2.7%) compared to the untreated TME (22.2 ± 2.1%) (p = 0.275) (Fig. 40).

4.5   Cytokine and chemokine analysis of the tumor microenvironment

In response to various treatments, cytokines and chemokines are released in the TME. These regulate the coordinated migration and cellular interactions of immune cells in the tumor environment. To evaluate these changes, concentrations of cytokines and chemokines in tumor tissue and plasma were measured in eight animals each 20 days after tumor inoculation using a bead-based multiplex immunoassay. The treatment and sampling for this investigation were performed as described under 3.11. A total of 31 cytokines and chemokines were analyzed. The absolute measured concentrations of the investigated factors in the TME and the plasma were normalized to the respective total protein levels.

After treatment, most analytes showed a high gradient between the cytokine and chemokine concentrations in the TME compared with those in the plasma. Most of the concentrations found showed a dependence on the administration of the immune modulator NOX-A12 in the plasma.

The interleukins IL-2, IL-4 and IL-6 could only be determined in low concentrations in both plasma (max. 1.5 pg/mg protein) and tumor tissue (max. 15 pg/mg protein). In contrast, the interleukins IL-1β, IL-10 and IL-16 were detected in significantly higher amounts in both samples (max. 200 pg/mg protein) (Fig. 41).

The concentration of IL-1β in the plasma increased significantly by the treatment with the CXCL12 antagonist (control vs. NOX-A12 and control vs. RT + NOX-A12, p < 0.0001). Compared with the RT group, the IL-1β secretion into the blood increased significantly with the administration of the CXCL12 inhibitor (RT vs. RT + NOX-A12, p < 0.0001). Irradiation of the tumor demonstrated a significantly lower interleukin production in the TME (control vs. RT, p = 0.0005; control vs. RT + NOX-A12, p = 0.002) (Fig. 41, A).

In contrast, plasma IL-2 levels did not change significantly after therapy (all p > 0.121). Likewise, only slightly increased values could be detected for the treatment groups with NOX-A12 compared to those of the untreated animals (control vs. NOX-A12, p = 0.675; control vs. RT + NOX-A12, p = 0.841). The increases can be neglected due to the generally low level of this interleukin in the tumor tissue (Fig. 41, B).

The concentrations of IL-4 measured in the tumor tissue after the different therapies did not differ from the levels measured in the untreated TME (p > 0.665). However, a significant increase of IL-4 was measured in the plasma following the administration of NOX-A12 (control vs. NOX-A12, p = 0.0009). Additional irradiation significantly increased the secretion of IL-4 (NOX-A12 vs. RT + NOX-A12, p = 0.043) (Fig. 41, C).

In the plasma, treatment with the CXCL12 antagonist led to a significant increase in the secretion of IL-6 (control vs. NOX-A12, p = 0.021). This was even more pronounced after additional irradiation (control vs. RT + NOX-A12, p = 0.0001). In contrast, no dependency of the concentration of IL-6 on the therapies used was observed in the plasma samples (p = 0.649). The administration of the CXCL12 antagonist significantly reduced the IL-6 in the tumor tissue (p = 0.004), but the reduction triggered by RT was even stronger and was not further enhanced by the application of the immune modulator (p < 0.0001) (Fig. 41, D).

As with IL-4, the level of intertumoral IL-10 was not altered by the treatment (all p > 0.134). In contrast, an increase in the plasma level was also observed for this analyte after administration of NOX-A12, but it became significant only with additional radiation compared with the interleukin level of untreated animals (control vs. RT + NOX-A12, p = 0.0005) (Fig. 41, E).

While the concentration of IL-16 did not change in the tumor environment (all p > 0.36) , the plasma showed a higher level of this interleukin in response to the treatment with the CXCL12 antagonist (control vs. NOX-A12, p = 0.003; control vs. RT + NOX-A12, p = 0.001) (Fig. 41, F).

The cytokines GM-CSF, IFN-γ and TNF-α were found at relatively low levels in the tumor tissue and blood (max. 20 pg/mg protein and max. 3 pg/mg protein) (Fig. 41, Fig. 42).

In the tumor, the quantity of granulocyte-monocyte colony-stimulating factor (GM-CSF) was not significantly affected by any treatment compared with the untreated tumor tissue (all p > 0.111). In contrast, the systematic concentration of this cytokine increased due to the CXCL12 antagonist (control vs. NOX-A12, p = 0.0002; control vs. RT + NOX-A12, p < 0.0001) (Fig. 41, G).

For IFN-γ, there was no significant change in the cytokine levels in either the plasma nor tumor (all p > 0.239) (Fig. 41, H).

In the tumor tissue, the decrease of the TNF-α level was dependent on the irradiation dose administered to the animals, with a significant decrease of the cytokine in about 34% by RT alone (control vs. RT, p = 0.003) and 30% in combination with the immune modulator (control vs. RT + NOX-A12, p = 0.012). In plasma, TNF-α was significantly dependent on the therapy with NOX-A12 (control vs. NOX-A12, p = 0.001) and reached the highest measured value after RT with immunotherapy (2.85 ± 0.3 pg/mg protein, p < 0.0001) (Fig. 42, I).

Only the concentration of CCL1 (I-309) in the plasma of the animals treated with RT and immune modulator was significantly increased compared with the control group (control vs. RT + NOX-A12, p = 0.005). No change was found between the levels of this CC chemokine in the TME (all p < 0.739) (Fig. 42, J).

In contrast, the CC chemokine CCL2 (MCP-1) was only found significantly increased in the plasma of animals from the NOX-A12 treatment group (control vs. NOX-A12, p = 0.046). In the tumor tissue, the chemokine was shown to be dependent on irradiation with 12 Gy, which led to a significant reduction in the production of CCL2 (control vs. RT, p = 0.022). The addition of an immune modulator had no further effect (control vs. RT + NOX-A12, p = 0.022) (Fig. 42, K).
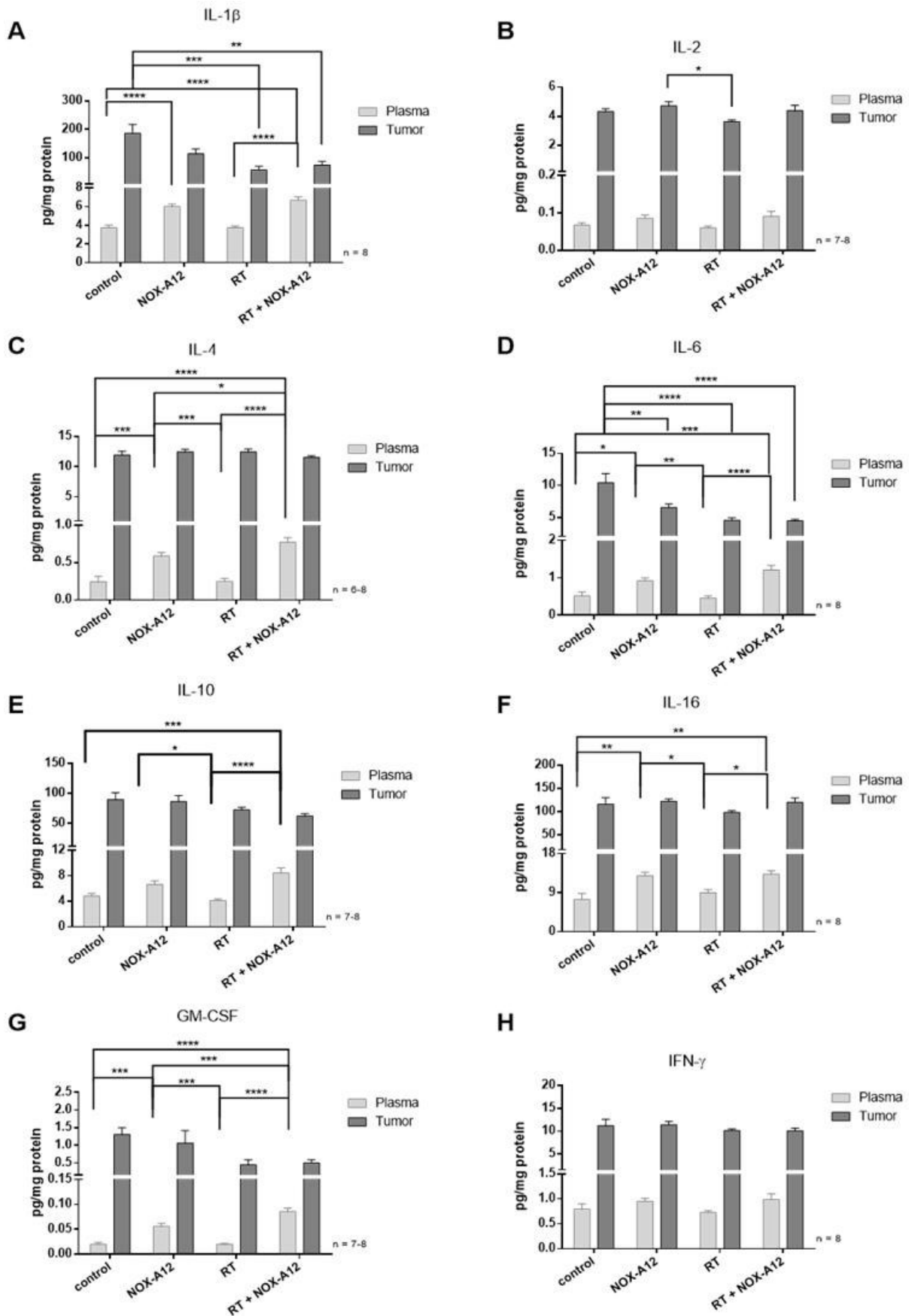
Fig. 41: Protein quantities of the analytes measured in the TME and plasma (1).
Normalized protein concentrations of (A) IL-1β, (B) IL-2, (C) IL-4, (D) IL-6, (E) IL-10, (F) IL-16, (G) GM- CSF and (H) IFN-γ in tumor tissue and plasma as determined by multiplex immune assay (n ≤ 8 animals per group; mean pg/mg total protein (tumor tissue or plasma) ± SEM). * p ≤ 0.05; ** p ≤ 0.01; *** p ≤ 0.001, **** p ≤ 0.0001
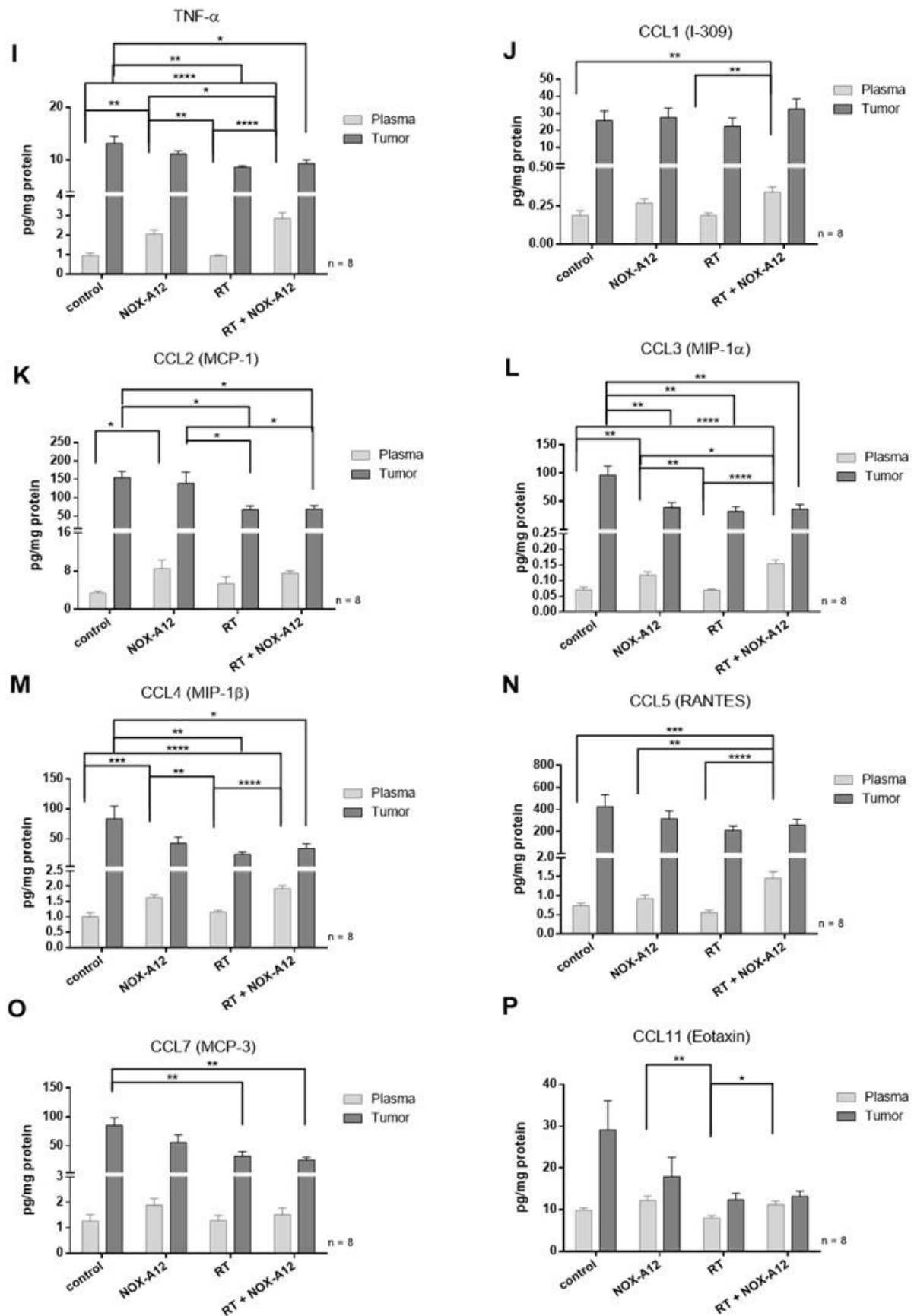
Fig. 42: Protein quantities of the analytes measured in the TME and plasma (2).
Normalized protein concentrations of (I) TNF-α and the CC chemokines (J) CCL1, (K) CCL2, (L) CCL3, (M) CCL4, (N) CCL5, (O) CCL7 and (P) CCL7 in the tumor tissue and plasma as determined by multiplex immune assay (n ≤ 8 animals per group; in pg/mg total protein (tumor tissue or plasma) ± SEM). * $p \leq 0.05$; ** $p \leq 0.01$; *** $p \leq 0.001$, **** $p \leq 0.0001$

As with other cytokines, the chemokine CCL3 (MIP-1α) showed a dependence of the plasma concentration on the treatment with the immune modulator. The amount of CCL3 in the blood significantly increased with NOX-A12 (control vs. NOX-A12, $p = 0.004$). In contrast, its concentration in the tumor tissue decreased significantly with each treatment (control vs. NOX-A12, $p = 0.005$; control vs. RT, $p = 0.001$; control vs. RT + NOX-A12, $p = 0.003$) (Fig. 42, L).

The CCL4 (MIP-1β) concentration in the plasma was also subject to the application of the immune modulator (control vs. NOX-A12, $p = 0.0007$). CCL4 produced by the tumor environment decreased significantly as a result of the irradiation (control vs. RT, $p = 0.009$) (Fig. 42, M).

The plasma concentration of CCL5 (RANTES) after combined radio- and immunotherapy was significantly reduced compared with the other treatments used (control vs. RT + NOX-A12, $p = 0.0003$; NOX-A12 vs. RT + NOX-A12, $p = 0.006$; RT vs. RT + NOX-A12, $p < 0.0001$). The amount of this chemokine in the tumor tissue was not significantly altered, but slightly reduced by the radiation (control vs. RT, $p = 0.243$) (Fig. 42, N).

Similarly, a significant decrease in the measured concentration of CCL7 (MCP-3) was detected only due to the radiation dose in the TME (control vs. RT, $p = 0.008$). The systemic concentrations of this cytokine were not influenced by the treatments (all $p > 0.419$) (Fig. 42, O)

The measured concentrations of CCL11 (Eotaxin) in the tumor samples of untreated animals were highly increased and scattered compared with the RT groups (control vs. RT, $p = 0.061$, control vs. RT + NOX-A12, $p = 0.07$) (Fig. 42, P).

While the secretion of CCL12 (MCP-5) into the plasma was significantly increased by the application of the immune modulator (control vs. NOX-A12, $p = 0.025$), the amount of this chemokine in the tumor tissue was significantly reduced after irradiation (control vs. RT, $p = 0.0008$) (Fig. 43, Q).

As a result of the treatment, no significant changes could be found in the plasma or tumor tissue for the chemokines CCL17 (TARC) and CCL19 (MIP-3β) (all $p > 0.117$) (Fig. 43, R and S).

The CXCL12 antagonist significantly changed the systemic concentrations of CCL20 (MIP-3α, control vs. NOX-A12, $p < 0.0001$) and, with RT, also CCL22 (MDC, control vs. RT + NOX-A12, $p = 0.0003$), but in the tumors, the concentrations of the chemokines showed no significant alterations. CCL20 remained relatively constant in the samples from treated animals compared with the untreated control group (all $p > 0.431$) and the readings of CCL22 showed large individual scatter (all $p > 0.487$) (Fig. 43, T and U).

As with other CC chemokines earlier, no significant changes in the concentrations of CCL24 (Eotaxin-2) in the samples could be measured as a result of the treatments applied (all $p > 0.464$) (Fig. 43, V).

The increased concentration of CCL27 (CTACK) in the blood was based on the application of the immune modulator (control vs. NOX-A12, $p = 0.027$), while the concentration found in the TME remained constant (all $p > 0.783$) (Fig. 43, W).

In plasma samples, only inhibition of CXCL12 showed weak evidence of an effect on the production of CXCL1 (KC) (control vs. NOX-A12, $p = 0.052$). However, significant

reductions in this CXC chemokine were found in the tumor tissue of animals from the three treatment groups, with irradiation having the greatest effect (control vs. NOX-A12, p = 0.01; control vs. RT and control vs. RT + NOX-A12, p < 0.0001) (Fig. 43, X).

Like the concentrations of CCL11 measured in the tumor samples of the untreated animals, the values determined for the chemokine CXCL5 (ENA-78) were also sufficiently scattered that no significant changes were detected in the other groups (all p > 0.117). A similar picture was also seen systemically (all p > 0.194) (Fig. 44, Y).

CXCL10 (IP-10) was detected at very high levels, especially in the tumor samples of the untreated animals. These were dependent on the type of therapy administered, with a strong influence of RT that was not further increased by additional administration of the immune modulator (control vs. RT, p < 0.0001). Immunotherapy showed a higher effect systemically (control vs. NOX-A12, p = 0.027) (Fig. 44, Z).

While the concentration of CXCL11 (I-TAC) in plasma increased significantly upon the application of the CXCL12 antagonist (control vs. NOX-A12, p = 0.002) and was even further increased by irradiation (control vs. RT + NOX-A12, p < 0.0001), the concentration of this chemokine in the tumor was only significantly reduced by RT (control vs. RT, p = 0.021) (Fig. 44, AA).

The ligand of the immune modulator NOX-A12, the chemokine CXCL12, could be measured in very high amounts in the plasma after administration of the antagonist. The concentration in blood increased tenfold due to the binding of the CXCL12 inhibitor and the formation of the difficult-to-metabolize ligand-inhibitor complex (control vs. NOX-A12, p < 0.0001; control vs. RT + NOX-A12, p = 0.0008). This reversed the gradient between the tumor and blood but did not reach the same level as before, since CXCL12 also increased significantly in the TME (control vs. NOX-A12, p = 0.013). The combination of RT and CXCL12 blocking also increased the concentration of the chemokine in the TME (control vs. RT + NOX-A12, p = 0.283), but not significantly compared to RT alone (RT vs. RT + NOX-A12, p = 0.283) (Fig. 44, AB).

After radiation, a significantly lower amount of CXCL13 (BAC-1) was secreted in the tumor environment (control vs. NOX-A12, p = 0.0007) (Fig. 44, AC).

In contrast, a significantly higher concentration of CXCL16 (SCYB16) was measured in the plasma after application of the CXCL12 antagonist (control vs. NOX-A12, p = 0.007) (Fig. 44, AD).

The concentrations of CX3CL1 (Fractalkine) were not significantly altered in neither the plasma nor the tumor tissue (all p > 0.14) (Fig. 44, AE).
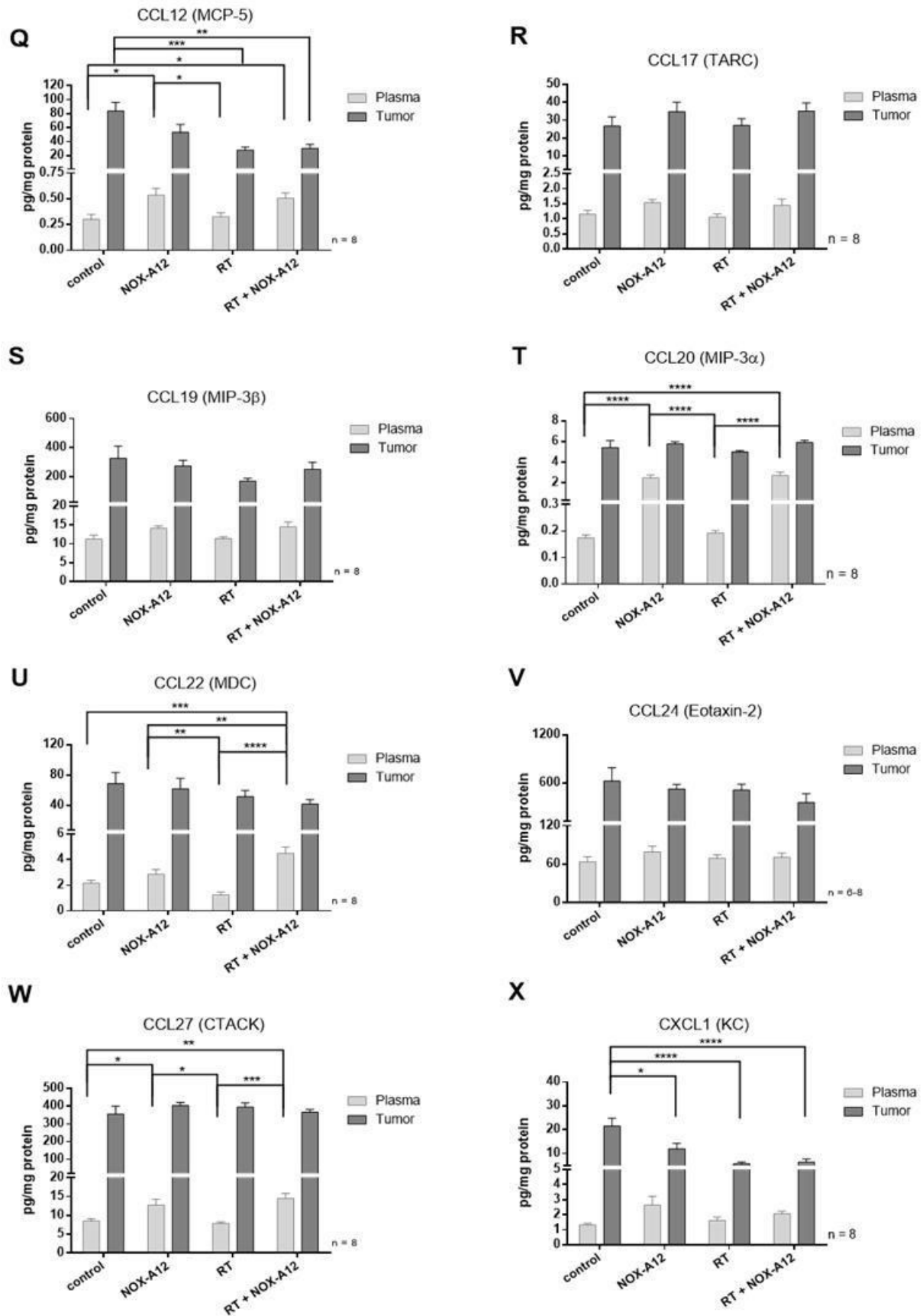
Fig. 43: Protein quantities of the analytes measured in the TME and plasma (3).
Normalized protein concentrations from the CC chemokines (Q) CCL12, (R) CCL17, (S) CCL19, (T) CCL20, (U) CCL22, (V) CCL24, (W) CCL27 and the CXC chemokine (X) CXCL1 in tumor tissue and plasma as determined by multiplex immune assay (n ≤ 8 animals per group; in pg/mg total protein (tumor tissue or plasma) ± SEM). * $p ≤ 0.05$; ** $p ≤ 0.01$; *** $p ≤ 0.001$, **** $p ≤ 0.0001$
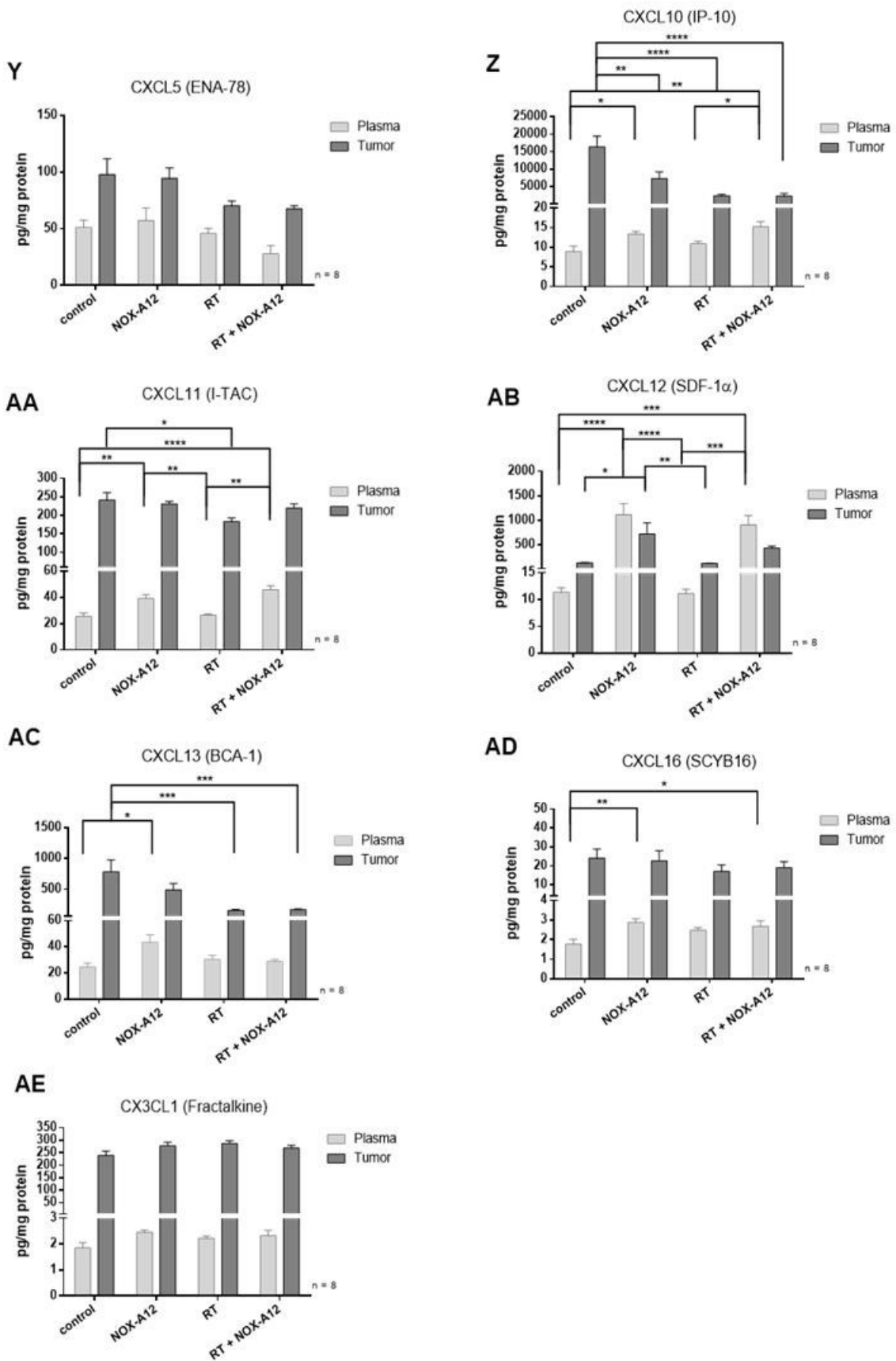
Fig. 44: Protein quantities of the analytes measured in the TME and plasma (4).
Normalized protein concentrations of the CXC chemokines (Y) CXCL5, (Z) CXCL10, (AA) CXCL11, (AB) CXCL12, (AC) CXCL13, (AD) CXCL16 and the CX3C chemokine (AE) CX3CL1 in tumor tissue and plasma as determined by multiplex immune assay (n ≤ 8 animals per group; in pg/mg total protein (tumor tissue or plasma) ± SEM). * $p \leq 0.05$; ** $p \leq 0.01$; *** $p \leq 0.001$, **** $p \leq 0.0001$

5   DISCUSSION

An essential objective of the present study was to establish an orthotopic immunocompetent murine glioma model in order to assess valuable insights into the immunologic effects of various treatment strategies like RT combined with MERT using a CXCL12 and/or CCL2-inhibitor and RT with checkpoint inhibition involving an anti-PD-1 Ab. In this study, the preclinical evaluation of the overall survival of mice treated with combination therapies versus stand-alone therapies was based on a syngeneic mouse model. Specifically, this study examined the impact of the different treatments on immune mechanisms involved in the glioma treatments tested, such as tumor-infiltrating immune cells, their activation and suppression markers as well as their chemokine receptor patterns. In addition, the production of more than 30 chemokines in the TME was compared to their concentration in the plasma.

5.1   Evaluation of the used syngeneic murine GBM model

Syngeneic mouse models of GBM are indispensable tools for analyzing the GBM microenvironment and testing immunotherapeutic compounds. For this purpose, an immune-competent murine model system that accurately mimics several features of GBM, including immune suppression, is needed. The glioma cell line GL261 is frequently used in the GBM research and presents one of the best characterized syngeneic, immune-competent models (Maes and Van Gool, 2011).

For better identification of the tumor cells in the brain tissue, the used cell line GL261 was transduced with GFP. GFP expression-dependent sorting and culturing ensures the stable expression of the gene by the used cells throughout the experimental period, as demonstrated by fluorescence microscopy of different culture passages.

The use of luciferase-producing cells was not considered because GFP-expressing GL261 cells represent a more immunosuppressive and thus a more accurate glioma model. Recently, Sanchez et al. (2020) discussed the immunostimulatory effect of luciferase-expressing GL261 cell lines (GL261 Red-FLuc, GL261-Luc2), which have been frequently used in several translational assessments of immunotherapy (Kim et al., 2017; Wu et al., 2019; Zeng et al., 2013). These cell lines were found to support an immunogenic proinflammatory tumor environment that enhances the immune response, leads to spontaneous regression and thus to longer survival compared with the original GL261 cell line. Luciferase-producing cell lines create an unrepresentative microenvironment and are considered to be insufficient to cause uniform mortality in mice (Sanchez et al., 2020). In contrast, a further cell line comparison detected only minimal immunological differences triggered by added expression of GFP to the original GL261 cell linie. These differences were associated with altered growth kinetics *in vivo* and *in vitro* of GL261-GFP compared to GL261 (Noffsinger et al., 2021). The application of the GL261-GFP model used is limited by the need for MRI for tumor monitoring. The lack of luciferase expression does not allow monitoring of the tumor growth via *in vivo* bioluminescence imaging. On the other hand, the MRI enables the tumor volume to be determined more precisely.

As a consequence of the different culture conditions and the transduced genes, the *in vitro* and *in vivo* cell growth of the GL261-GFP cells could significantly vary from

the original cell line mentioned in the literature. The original GL261 cell line grows rapidly without contact inhibition under *in vitro* conditions (doubling time of 20 h) (Szatmari et al., 2006), the same was observed for the transduced GL261-GFP cells. In order to verify the *in vivo* growth, different numbers of cells were used for tumor grafting in the first tumor inoculation test. This test showed clear volume differences between the tumors grown from the three different implanted cell sets. Moderate tumor growth was required for further experiments, since too rapid growth leads to therapy failure, whereas a too slow growth blurs the contrast between different therapies. Because the other quantities of implanted cells showed potentially critical tumor volume after only 21 days, the smallest cell amount was chosen for all further experiments, although it showed the highest variation between the observed tumor volumes.

The resulting tumors exhibited the typical GL261 invasive growing characteristics, resulting in a median survival of 26 days. The volumes of the untreated tumors could be fitted exponentially, describing an *in vivo* growing curve for the cells used with a doubling time of 6 days. This growing behavior was in accordance with values from the literature, with a small difference of a 100% mortality rate within 35 days instead of 25 days, which is explainable by the slightly different number of implanted initial cells (Szatmari et al., 2006).

In the literature, the *ex vivo* radiosensitivity of the original GL261 cell line has been reported with 50% cell survival after administration of less than 2 Gy (Szatmari et al., 2006). In response to the transduced GFP genes, the used cell line showed a higher radioresistance with a D_{50} at 2.62 Gy. Although the *in vivo* radiosensitivity does not usually correlate with that *in vitro* dose, the data suggest that treating the transduced cell line with a slightly higher RT dose produces the same effect as with the original cell line.

The used GFP-expressing GL261 mouse model showed some differences in its radiosensitivity but not in the tumor development compared with the most extensively used model for preclinical testing of immunotherapeutic approaches for GBM. A more detailed characterization of the transduced cell line was dispensed for serious similarities compared with the original cell line.

Like the original cell line, the used model is limited in its ability to mimic the human microenvironment completely. By their nature, murine GBM models fail to reflect human GBM, especially in immunological aspects (Haddad et al., 2021; Mestas and Hughes, 2004). Szatmari et al. (2006) describe the genetic drift of GL261 away from authentic GBM-like tumors. Moreover, in GL261 tumor-bearing mice, fewer APCs and more T cells were determined than usually seen in GBM patients (Khalsa et al., 2020). On the other hand, a humanized GBM mouse model is not yet available and the use of patient-derived cells requires immune-compromised mice not allowing to investigate antitumor immune responses. Therefore, the limitations of the model must be included in the evaluation as an inevitable evil.

5.1.1 Evaluation of the applied radiotherapy for the mouse model

In the present study, the murine glioma model is used to model and assess potential novel treatment combinations of RT and immune modulators against GBM. For translation purposes, the treatment was kept as close as possible to human

conditions. In contrast to clinical systems, which typically use photon energy between 6 and 15 MV, the available small animal irradiation platforms work with radiation sources with lower energy (range of ~225 kV) or cesium-137 (662 keV). The lower photon energy forces the use of different irradiation beams from different directions to achieve a homogenous dose distribution in the target, which leads to time-consuming irradiation sessions for each animal (> 30min). For this reason, the standard 6 MV clinical LINAC was used for irradiation in a similar fashion to human treatment.

Only a few other groups have used clinical RT devices for mouse brain irradiation because the target accuracy is the limiting factor for the usability of clinical RT devices (Kim et al., 2014; Perez-Torres et al., 2014). Consequently, most comparable irradiation experiments to date have been performed in rats.

In the present study, the smallest possible rectangular irradiation field was used, leading to half-brain irradiation, simultaneously representing the greatest limitation of this method. The irradiation dose was delivered without a compensation filter that enables the delivery of significantly higher dose rates with less scattered radiation. Although the treatment planning was performed only for an exemplary animal, no special positioning system was required during the treatment. Room lasers, light field support and the stereotaxic inoculation of the tumor cells ensured the precise delivery of the irradiation dose to the tumor. The animals were under deep anesthesia making the provision of inhalation gas obsolete and promoting the precise delivery of the radiation beam. In addition, the use of a tissue-equivalent bolus to overcome the build-up effect and provide tumor irradiation at maximum radiation dose could be dispensed as the radiation beam was emitted through the patient table. The delivered dose was applied in a single FFF beam and a dose rate of 4 Gy per minute. In this manner, an irradiation session, including positioning, consumed a maximum of 5 minutes for each animal.

The chosen radiation setup has its limitations in the individualization of the treatment and the size of the irradiation field, but allows a high animal throughput with relatively good delivery accuracy. Also, by using the clinical linear accelerator, each treatment was performed within an accuracy for the radiation field of 1% ensured by the mandatory quality assurance (QA) of the device. FFF beams increase the relative biological effectiveness (RBE) without clinically relevant differences in either tumor control or radiation side effects (Steenken et al., 2015). Laurent et al. (2020) demonstrated that the FFF technique does not have an influence on the antitumor immune response, so this RT technique could be used to test the effects of irradiation combined with immunotherapies. The radiation setup applied can thus be used to mimic the clinical conditions as closely as possible.

Even if the chosen radiation setup extended the survival rate of the tumor-bearing mice, two major side effects were observed that were also described in the literature before (Rancilio et al., 2017). The most serious of these two effects was observed to be an acute weight loss, which peaked around day 8 post-irradiation (Fig. 14, B). This weight loss almost reached the 20% dropout limit in some animals, so countermeasures had to be taken in this case. The animals regained their weight within a few days by being fed zwieback in addition to their normal diet making this

weight loss temporary. Therefore, all irradiated animals were additionally fed with zwieback for a week directly after dose administration. In contrast to the reported cases, the animals that could choose between softened standard diet, glucose syrup and zwieback prefer the latter over all other options (Rancilio et al., 2017).

As the second observed extracranial effect, the radiation-induced alopecia was observed after the administration of at least 10 Gy (Fig. 14, A). The extent of the hair loss correlated with the radiation field and was not accompanied by a problematic condition such as the development of cataracts seen in similar RT applications (Rancilio et al., 2017).

Consequently, the chosen radiation setup allows targeted irradiation of the cerebral hemisphere with the model tumors without inducing any severe side effects.

The irradiation treatment significantly prolonged the survival time of the tumor-bearing animals. In all three examined radiation regimens, the first animals had to be euthanized around day 40 after irradiation due of the tumor growth (Fig. 14, E). The regimes which delivered a total dose of 20 Gy (1 x 20 Gy, 2 x 10 Gy) to the cerebral hemispheres of the animals did not differ in their effect on the survival of the treated animals, resulting in almost equal OS performance. These groups showed ventricle collapses and growing tumor cells in the non-treated hemisphere starting 10 days after irradiation. Because a metastatic behavior is not typical for the tumor model used, it is also possible that the tumor cell migration was a result of a radiation independent lesion of the ventricle system (Szatmari et al., 2006). The MRI observation of the affected animals could not clarify this question, but no similar tumor growth was observed throughout the whole study using a lower treatment dose. Therefore, in the tumor model described, these dose regimens harbor an increased risk of possible radiation-induced ventricular lesions, similar to reported observations after unilateral brain irradiation of 20 Gy (Ansari et al., 2007; Wilson et al., 2009).

As a consequence, the RT regime of 1x12 Gy was chosen as the standard irradiation treatment. It also allows to detect a significant difference between the RT combinations during the observation period by showing a more moderate effect on the MST. Only one-fourth of the animals responded to the RT with complete tumor regression during the observation period, allowing to detect a clear difference in the tumor growth of responder and non-responder (Fig. 14, D).

Responder animals showed no differences in body weight, posture nor gross neurologic deficits in movement or feeding compared with naïve mice of similar age. In all responder animals, no tumor signs could be found in histological brain sections at the end of the experimental period.

5.2   The survival effects of the examined treatments

5.2.1 Survival effect of combined immune checkpoint and chemokine inhibitors was related to anti-PD-1 treatment

First, the effectiveness of the new Spiegelmer immune modulators as a single treatment and in combination with an anti-PD-1 Ab was determined as basic data for assessing the effectiveness of various combinations of the chemokine inhibitors with additional RT.

As the mode of action of the Spiegelmer NOX-A12, it is assumed that it binds free CXCL12 in plasma and thus inhibits the interaction with its receptor CXCR4. This inhibition disrupts the communication bridge between the tumor cells and other cells in their environment which would promote tumor proliferation and new blood vessels formation (Guo et al., 2016). Under this kind of CXCL12 inhibition, the tumors showed a similar growing behavior as the untreated group (Fig. 13,Fig. 15). The data and images of tumor growth did not allow any conclusions regarding a positive inhibition of the cell migration of endothelial cells by reducing the cytokine signal.

The simultaneous treatment with this novel immune modulator and the already clinically used anti-PD-1 Ab leads to complete tumor regression in several animals, resulting in an OS rate of 22% (Fig. 16). Compared with the survival effect of the checkpoint inhibitor alone, this improvement seems to be caused by the anti-PD-1 Ab only.

These results showed some similarities but also differences from the reported outcomes of a similar mouse model after blocking CXCR4, the receptor of CXCL12, alone. Wu et al. (2019) reported a median survival of 25 days for this treatment, which did not differ from the untreated control group. The same was observed in the model described here with a delay of 2-3 days. The survival curves for the anti-PD-1 treated animals were also nearly identical in both studies, with only a small difference between the median survival and the OS rate (30% vs. 22%).

In contrast, Wu et al. (2019) observed also a prolonged OS rate of 11.1% by blocking the CXCR4 receptor with an Ab alone. When the two Abs (CXCR4 and PD-1) were combined, the OS rate reached 60% with an undefined median survival. No similar difference could be detected in the model used in the present study. These results may suggest that blocking the CXCR4 receptor may be more effective than inhibiting the ligand and that the function of CXCL12 may not be entirely inhibited by the Spiegelmer. The second immune modulator mNOX-E36 was tested the first time in a murine glioblastoma model. It showed no positive treatment effect when given as a single treatment starting at day 7 after tumor inoculation. Under the inhibition of CCL2 (MCP-1) in the TME, the tumors developed earlier and grew faster (Fig. 15). These observations suggests that blocking this chemokine in the plasma leads to negative effects on the natural antitumor immune response in the early stage of tumor progression.

CCL2 not only recruits CCR4-expressing Tregs and CCR2-expressing Ly-6C$^+$ monocytic MDSCs (Chang et al., 2016). It also plays a central role in immune surveillance and in reducing primary tumor growth by attracting immune-supportive macrophages and T cells. During the inflammatory response shortly after tumor inoculation, M1 macrophages are among the first cells to enter the implantation side. There, they initiate the secretion of inflammatory mediators such as TNF-α, IL-1β, and NO, which activate defense mechanisms that fight against the implanted tumor cells. As the tumor progress, these initially beneficial cells transform into poor antigen-presenting M2 macrophages which secret growth factors and cytokines promoting an immunosuppressive TME and the tumor development (van der Bij et al., 2005).

In the used model, the CCL2 blocking was initiated shortly after the animals recovered from the implantation surgery. The subsequently faster tumor development indicates that at this stage, blocking of CCL2 primarily excludes antitumor M1

macrophages, leaving tumor growth unregulated. This negative survival effect of mNOX-E36 could not be neutralized by adding a checkpoint inhibitor. Consequently, the OS effect of the anti-PD-1 treatment is reduced when combined with the CCL2 antagonist (Fig. 15).

The Spiegelmer can also neutralizes other members of the monocyte chemoattractant protein family that share a 60% amino acid identity (CCL8, CCL11) (Zlotnik and Yoshie, 2012). Therefore, the inhibition of CCL11 (Eotaxins) may also be relevant for the observed tumor growth. CCL11 suppresses the eosinophil migration to the tumor side and so does the tumor growth control function of the eosinophils. Eosinophils promote the reduction of tumor growth with the help of other leukocytes like CD8$^+$ T cells (Varricchi et al., 2018). Losing this control function could further promote the proliferation of the tumor cells.

5.2.2 Combined radiotherapy with the CXCL12 inhibitor NOX-A12 promotes overall survival

The effectiveness of the immune modulators NOX-A12 and NOX-E36 were evaluated in various combinations with additional stereotactic RT (1x 12 Gy) as well as an anti-PD-1 Ab.

The survival and tumor growth data suggest that the CXCL12 inhibitor enhanced the antitumor response after RT (Fig. 17). The MST after combined RT and immune modulator was increased by 41.5 days to 99 days compared with the RT monotherapy, yet this effect was not significant (p = 0.196). This is equivalent to a 25% prolongation in the OS. This survival benefit correlated with the loss of contrast in the MRI shortly after RT. This reduced accumulation of the contrast agent could be related to the loss of tumor vascularization. Potentionally, the total tumor regression after after RT in positive responders can also be attributed to the additional suppression of vasculogenesis as well as reduction of regrowth of destroyed tumor blood vessels and inhibition of migration of immune-suppressive MDSCs by the CXCL12 inhibitor NOX-A12. All groups additionally treated with NOX-A12 showed total tumor regression in more than 50% of the observed animals. The additional treatment with anti-PD-1 Ab increased the OS rate to approximately 60%, while the addition of a CCL2 inhibitor did not further affect this rate (Fig. 17).

These treatment effects, however, were exceeded by the combination of RT with the anti-PD-1 Ab. This is consistent with the results of Zeng et al. (2013), who examined the survival of an orthotropic GL261-Luciferase tumor model treated with RT and anti-PD-1 Ab. However, in comparison with Zeng et al. (2013), the MST and the OS rate of the RT plus anti-PD-1 therapy arm were more than twice as high when irradiation was delivered to the tumor-bearing hemisphere. Thus, the prolonged survival of the model resulted primarily from RT.

The reaction of T cells to irradiation varies among subsets, non-proliferative and activated cells are more radioresistant (McBride et al., 2004; Qu et al., 2010) . Thus, half-brain irradiation leads to an imbalance in the antitumor response, which is restored over time by infiltrating cytotoxic T cells and Tregs (Schaue and McBride, 2012). The immune checkpoint PD-1 inhibits the activity of the infiltrating antitumor T cells after RT. The additional treatment with an anti-PD-1 Ab may help to limit the

re-infiltration of the tumor immune-suppressive Tregs which express PD-1 on the surface and lead indirectly to a higher unsuppressed CD8$^+$ cell fraction in the tumor (Yoshida et al., 2020).

This may explain the slight survival benefit of the triple combination treatment of RT, CXCL12 inhibitor and anti-PD-1 Ab compared with the RT and CXCL12 inhibitor combination (Fig. 17). In other tumor models, a complementary effect of NOX-A12 and PD-1 checkpoint inhibition has been described previously, but without involvement of RT (Zboralski et al., 2017). The combination of these three treatments, though, had no survival benefit over the combination of RT and the checkpoint inhibitor (Fig. 17). Under the triple combination treatment, the reinfiltration of CXCR4$^+$CD8$^+$ cells after RT might have been reduced by CXCL12/CXCR4 blockade, leading to a reduced antitumor response. However, the flow cytometric data showed no differences in these cells under the combination of RT and NOX-A12 versus RT alone (Fig. 23, Fig. 24), presumably because the most appropriate observation time point was not chosen. Although, NOX-A12 might also promote resistance to PD-1/PD-L1 blockade in a different manner in the present model, which should be investigated in further studies.

Even in combination with RT, the CCL2 inhibitor mNOX-E36 had no effect on the survival of the tumor-bearing animals (Fig. 18). Interestingly, no negative effect similar to that seen after monotherapy was observed. The treatment arm of radiation plus anti-PD-1 Ab best demonstrated that the inhibition of CCL2 did not influence the survival at all in this tumor model. The OS rate of RT with or without the CCL2 inhibitor showed minimal differences in favor of the RT alone. These data suggest that this macrophage migration inhibitor is not an adequate adjunct to the treatment of GBM, since this inhibitor likely already reduces the primary antitumor response in the present model. Consequently, this treatment option was not investigated further. Based on the involvement of CCL2 in the initial antitumor response, it is possible that the administration of the CCL2 inhibitor could be more effective when applied to a developed tumor with an established immunosuppressive TME. In the model used, however, this turns out to be almost impracticable due to the aggressive tumor progression.

5.3   The characterization of the tumor microenvironment

The data of the long-term survival experiments suggest an adjuvant effect of the immune modulator NOX-A12 on the applied RT. Therefore, the effect of this immune modulator and RT was further investigated at the cellular level by analyzing tumor tissue, spleen and blood of the tumor-bearing mice by flow cytometry.

Based on survival and tumor growth data, the 20th day after inoculation was selected as the examination day because of the resemblance of the tumor size and health status of the animals in each treatment arm. Shortly after this time point, animals in the control arm begin to show significant signs of deterioration of their health status. An earlier time point was not considered to give the animals the opportunity to recover from the observed radiation-induced anorexia and to ensure the animals received multiple doses of the immune modulator. Additionally, the timing was

chosen long enough after RT so that the resulting cellular and immunologic changes have already occurred, but also brief enough that they have not yet returned to baseline levels and thus are overlooked. The chosen time point also corresponds with those in comparable studies (Wu et al., 2019; Zeng et al., 2013).

At the observation time point, the tumor sizes in the NOX-A12 arm were not controlled by the treatment and showed the same wide variance as the control group (Fig. 20, A). In the RT treatment arms, the tumor sizes were regulated by the irradiation-induced blood vessel destructions and the resulting oxygen deficiency and malnutrition. Although the amount of living CD31$^+$ endothelial cells in the tumor tissue 10 days post RT did not differ from the control group, it is reasonable to assume that the reduced perfusion of the tumors with the MRI contrast agent observed in the survival experiments was due to the reduction in blood vessels (Fig. 21). According to the literature, the radiation dose of 12 Gy used should have resulted in significant vascular damage (Park et al., 2012).

The influence of the RT was not evident in the indirect measurement of the frequency of all alive tumor cells. Despite the different volumes, alive tumor cell ratios were almost the same in all treatment arms (Fig. 20, B). This similarity can be explained by the higher number of undersupplied cells in the bigger tumors of the unirradiated control arms. Consequently, the frequency of tumor-infiltrating leukocytes behaved accordingly (Fig. 22, A).

Since the frequency of tumor cells could only be determined indirectly due to the limited measurement possibilities, the cells were correlated with the tumor volume. No significant correlation between the tumor volume and leukocytes was detected for any of the treatment groups, only after irradiation were leukocytes reduced with increasing tumor size (Fig. 22, B).

Moreover, it was hypothesized that the irradiated tissue is still in immunological imbalance 10 days after RT, allowing a clear difference to be measured between the treatment arms. RT induced the cell death of tumor cells as well as the more radiosensitive lymphocytes. After RT, surviving tumor cells start to regrow and the cytokine release related to immunogenic cell death leads to temporarily varying re-infiltration of the tumor by different subsets of lymphocytes.

5.3.1 Effect of the therapies on tumor-infiltrating leukocytes in the TME

A closer look at the total amount of T cells in the tumor showed a reducing effect of NOX-A12 alone compared with the RT treatments and the control group (Fig. 23, A), even though CD3$^+$ T cells are considered relatively sensitive to irradiation. The frequency of CD8$^+$ effector cells (Fig. 23, B), as well as the CD4$^+$ T helper cells (Fig. 27), was lower in the tumor tissues of animals with CXCL12 blocked than in the control group. Even though the differences between the treatment arms were not significant, these data suggest that the inhibitor blocked the infiltration of CD3$^+$ cells. This inhibition was not observed in the combination therapy arm which showed the same level of cells as RT monotherapy. This indicates that the RT effect is more dominant here compared with the influence of the inhibitor.

CD69 is rapidly expressed on T cells when they have been activated via CD3 and/or cytokine interaction. In the TME, the T cells were exposed to continuous antigen

stimulation, which drives the differentiation of the cells towards exhaustion. The state of exhaustion is characterized by the upregulation of PD-1 together with the reduction of effector activity. Consequently, the early exhausted CD8^{+} cells co-expressed CD69 along with PD-1, with CD69 regulating the exhaustion of tumor-infiltrating T cells (Mita et al., 2018; Petrelli et al., 2018; Speiser et al., 2014). Accordingly, most of the tumor-infiltrating CD8^{+} cells showed an exhausted marker profile in the form of co-expressing of CD69 and PD-1 (Fig. 24, C). Only around 20% of the CD8^{+} cells were activated, most of them after RT. This difference could be explained by the required re-infiltration of the irradiated tumor with T cells.

However, the amount of CD4^{+} T cells was also affected by the applied RT (Fig. 25, A). The RT enhanced the numbers of Tregs slightly, while the quantities of active and naïve conventional CD4^{+} T helper cells were not affected (Fig. 25, B). These results can be explained by the lower radiosensitivity of Tregs compared with other CD4^{+} subpopulations in mice. Since Tregs are known as the most radiation-resistant subset of T cells and thus have a survival advantage over conventional T cells (Balogh et al., 2013; Heylmann et al., 2014; Kachikwu et al., 2011; Kajioka et al., 2000; Qu et al., 2010), a higher amount of Tregs in the irradiated animals was therefore expected.

The additional administration of the CXCL12 antagonist NOX-A12 slightly reduces this enhancement of the immunosuppressive T cells present in the TME back to the control level. These Tregs were examined for their activation phase. The cells showed high expression levels of the molecules CD39, CD73 and PD-L1 in all treatment arms (Fig. 26). Only the combination therapy lowered these levels noticeably, but not significantly.

In immunocompetent mice, Tregs expressing PD-L1 are associated with immunosuppressive functions such as inhibitory effects on immune-active cells such as DCs and cytotoxic T cells via the PD-1 receptor (Amarnath et al., 2010). The production of adenosine is another immunosuppressive mechanism of Tregs, and the catalytic capacity of CD39 and CD73 is synchronized with the activation of Tregs (Churov and Zhulai, 2021). Highly suppressive Tregs are characterized by the expression of CD39 in concert with CD73 (Zhao et al., 2017). These Tregs reduce the extracellular concentration of the pro-inflammatory factor ATP, which acts as DAMP on purinergic receptors, especially after RT, triggering a signaling cascade to initiate an inflammatory response (Jacob et al., 2013). CD39 thereby regulates the balance of the immune response by phosphohydrolyzing ATP or ADP to AMP (Borsellino et al., 2007). Following the cascade, CD73 hydrolyze AMP to adenosine, which is a potent immune-suppressor (Deaglio et al., 2007). In the ATP-CD39-CD73 cascade, CD39 is the rate-limiting enzyme. This makes CD39 a more consistent and reliable marker for Tregs than CD25 (Timperi and Barnaba, 2021; Zhao et al., 2017). Consequently, the high expression level of the observed Treg population corresponds with the highly active suppressive character of the Tregs in the monitored tumor tissues. The reduction in CD39^{+} Tregs indicates reduced immunosuppression in the TME by RT and immunomodulatory effect. However, the differences detected only allow to suspect a trend under combination therapy.

The relation between T cell subsets and CD8^{+} effector cells might be decisive for the

treatment outcome. In human GBM, the ratio of CD4$^+$/CD8$^+$ is correlated with the prognosis of the malignancy, as the majority of CD4$^+$ TILs in GMB have an immunosuppressive nature. The fewer CD4$^+$ T cells per CD8$^+$ T cell, the more likely an antitumor immune response will occur, in particular, the number of CD4$^+$FoxP3$^+$ Tregs per CD8$^+$ cells is critical (Han et al., 2014). The present model showed particularly high ratios between CD4$^+$ and CD8$^+$ effector cells (Fig. 27). Without differentiation of the CD4$^+$ T cells, these ratios were nearly equal in the NOX-A12 and RT treatment arms and increased nonsignificantly compared to the control group (Fig. 27, A). However, the combination therapy reduced the ratio to the baseline level of the reference group. A careful analysis of the ratio between Treg and CD8$^+$ effector cells reveals the immune suppressive microenvironment after RT with enhanced number of Tregs compared with CD8$^+$ cells (Fig. 27, B). The decrease in the Treg$^+$/CD8$^+$ ratio in the combination therapy group indicates that the inhibition of CXCL12 also impedes the migration of Tregs into the tumor tissue after RT.

Although lymphocytes are known to be highly radiosensitive and T cells die within hours after irradiation (Heylmann et al., 2014), no significant changes in the frequencies of different lymphocytes were detected in the three treatment arms 10 days after irradiation in the model used. In a similar model, Stessin et al. (2020) observed a delayed increase in CD8$^+$ cells caused by an influx of the cells, whereby the differences were rebalanced 5 days after tumor irradiation. This suggests that in the model used, the re-infiltration by lymphocytes after RT may already have been completed at the time of observation and the balance of the lymphoid cells may thus have been restored. This is also supported by the fact, that the measured frequencies of CD31$^+$ cells were only slightly affected by RT.

This raises the question of whether there was a more appropriate time point to observe the radiation-induced changes. Despite the complications from RT, it would probably be useful to include at least one more earlier time point in the study to examine the immunologic effects. This is also associated with the difficulty of ensuring that the TME has not already re-equilibrated after RT and that, in parallel, sufficient time remains for the immune modulator to reach a therapeutic concentration. Retrospectively, to avoid missing immunologic events, additional observations at multiple time points between days 10 and 25 after tumor inoculation would have been reasonable.

5.3.2   Effect of the therapies on MDSCs in the TME

Similar to the other tumor-infiltrating leukocyte populations, the proportion of MDSCs showed no significant differences between treatment arms (Fig. 28, A). The MDSCs in tumors treated with the CXCL12 agonist were increased compared with the control group. Contrary to expectations, the MDSC population was reduced by the RT alone. This MDSC population was mainly composed of highly immunosuppressive monocytic MDSCs (M-MDSCs, Ly6C$^+$Ly6G$^-$) (Fig. 28, C). Patient studies have revealed that the main intratumoral MDSC subpopulation involved in local immunosuppression is composed of polymorphonuclear MDSCs (PMN-MDSCs) (Gielen et al., 2016; Raychaudhuri et al., 2015). Contrary to these results, the PMN-MDSCs do not play a decisive role in the present model, the cell levels found in the tumor were too low.

Tumor-infiltrating MDSCs have been characterized in several other tumor models by

the upregulation of the immune-suppressive markers CD39 and CD79 as well as the immune-suppressive activity of their product exacerbate immunesuppressive adenosine (Chouaib et al., 2018; Morello et al., 2016). A closer look at the expression of the immune-suppressive marker CD39 and CD73 on the MDSCs revealed a low level of CD73$^+$ cells in the model used, but a significantly higher expression of CD39 in the tumors of the combination treatment arm (Fig. 29, C). Even though all treatment arms had very high expression levels, this suggests a higher suppressive TME after RT and CXCL12 antagonist application.

With more than 90% of all MDSCs, the highest expression levels of PD-L1 were found on the tumor-infiltrating MDSCs (Fig. 29), as described in other mouse tumor models. Second lymphoid organs such as the spleen also contained almost the same amount of PD-L1$^+$ MDSC. However, the expression levels of MDSCs in the blood were much higher than in a colon carcinoma model (Lu et al., 2016).

The expression levels of PD-L1 found in the TME allow the conclusion that the MDSC population found has potent suppressive activity against T cell activation and function, regardless of the treatment arms. Interestingly, the application of the CXCL12-inhibitor leads to a significant increase in this expression. Because the expression of PD-L1 on MDSCs in tumor-bearing mice is typically linked to hypoxia and HIF-1α, the results suggest that tumors experience a higher hypoxia effect under the CXCL12 inhibition than under RT alone (Corzo et al., 2010; Noman et al., 2014). The upregulation of PD-L1 on MDSCs under the influence of NOX-A12 also indicates an intensified immune-suppressive environment.

The intratumoral production levels of NO and ROS correspond to the typical expression of the predominant monocytic subset of MDSCs there Fig. 30). MDSCs produce reactive nitrogen species, predominantly NO, that induces and regulates the activity of HIF-1α (Mijatovic et al., 2020). In the model used, no significant difference in the NO production was observed, although the mean production was noticeably decreased after RT. This decreased production was adjusted to the level of the untreated group by the combination of RT and the CXCL12 inhibitor.

MDSCs release ROS as the major mechanism to suppress T cell responses. The measured production of ROS by MDSCs in the tumor tissue showed the highest level under CXCL12 inhibition, followed by a significant reduction when RT was involved. Reduced production of ROS was shown to undermine the repressive immune function. The ROS secreted by MDSCs increases the HIF-1α level in the TME and creates a toxic milieu for infiltrating lymphocytes (Groth et al., 2019; Ohl and Tenbrock, 2018).

These determined data could be interpreted as evidence that applied RT results in a less immunosuppressive TME. Unfortunately, this irradiation-induced effect seems not to be supported by the added CXCL12 inhibitor, as ultimately an insignificant overall survival benefit (p = 0.19) was achieved by the combination therapy.

5.3.3   Radiation-induced receptor profile of leukocytes in the TME

The initial chemokine receptor analysis of the MDSC population revealed a significant alteration of the CXCL12-related receptor CXCR4 expression in the tumor by RT. It was considered that the irradiated-induced reduction of the CXCR4 receptor was counterbalanced by the upregulation of other MDSC attracting receptors or the

secondary CXCL12 receptor CXCR7 because the cellular analysis revealed no significant differences between the observed subpopulations in the TME. This up- or downregulation of specific cytokine receptors could also be responsible for the equalized levels of other immune-relevant cells. Therefore, the receptor expressions on $CD8^+$ effector cells, $CD4^+FOXP3^+$ Tregs and the $CD11b^+Gr1^+$ MDSCs were subsequently examined in more detail by a closer analysis after RT alone.

As in the previous analysis, the tumor volume was found to be significantly reduced after RT alone, while no differences in the amount of tumor cells or leukocytes were detected (Fig. 32, Fig. 33, A). This results in a higher leukocyte to tumor cell ratio. No significant differences were observed in $CD8^+$ and $CD4^+$ cells after RT alone (Fig. 33, C). However, the subpopulation of tumor-infiltrating Tregs was significantly reduced by RT, wheras the MDSC population was not (Fig. 33, D; Fig. 34, B).

The receptor profiles of the subpopulation of the $CD8^+$ effector cells reveal a decrease in the cells single expressing the receptors CCR2, CCR4, CCR5 and CXCR4 due to RT, with the highest reduction only in $CCR4^+CD8^+$ T cells (Fig. 35). Therefore, the co-expression of all analyzed receptors increases on the effector cells, which is also reflected in the enhancement of the combinations $CCR4^+CXCR4^+CXCR7^+$, $CCR2^+CCR4^+CXCR4^+CXCR7^+$ and $CCR4^+CCR5^+CXCR4^+CXCR7^+$ (Fig. 36). In summary, both receptors, CXCR4 (p = 0.063) and CXCR7 (p = 0.04), were found to be increased in expression along with other receptors after RT. Also, the combinations $CCR4^+CCR5^+CXCR4^+$ and $CCR5^+CXCR4^+$ were found significantly increased. The increase of these receptor combinations after RT underscores that the observed $CD8^+$ cells are mostly newly infiltrated. CXCR4 is expressed in both naïve and activated T cells. Naïve $CD8^+$ T cells predominantly express CXCR4 which regulates T cell migration along the CXCL12 gradients on their surface. They lose the CXCR4 receptor during their differentiation into memory or effector $CD8^+$ T cells because the receptor negatively affects the function of cytotoxic $CD8^+$ T cells (Kobayashi et al., 2004). The increase of the CXCL12 receptors after RT indicates that more naïve T cells had infiltrated and differentiated in the irradiated tumor tissue, highlighting the co-expression of the other receptors.

The increased expression of CCR4-containing combinations indicates a lower antitumor activity of the detected $CD8^+$ cells, as $CCR4^+CD8^+$ T cells are predominantly identified as immature effector memory cells (Kondo and Takiguchi, 2009), which are known for limited population expansion and tend to exhaust rapidly and subsequently die (Ando et al., 2020). Activated $CD8^+$ T cells have been found to constitutively express CCR2 and CCR5, whereas CCR5 is higher expressed on memory $CD8^+$ T cells (Fukada et al., 2002; Nansen et al., 2000; Tomiyama et al., 2002). Combinations with these receptors indicate the differenzierung of the found $CD8^+$ cells. The simultaneous expression of CCR5 and CXCR4 is required for chemokine-induced co-stimulation during T cell activation by APCs (Contento et al., 2008).

Based on the detected frequency of exhaustion markers on the $CD8^+$ cells and the receptor profiles found, it can be assumed that the tumor-infiltrating $CD8^+$ cells rapidly converted from naïve to memory effector cells with a reduced antitumor response.

The receptor profiling of $CD4^+FOXP3^+$ Tregs was less variant than the other cell

subpopulations. Almost all analyzed Tregs simultaneously expressed at least the two receptors CCR4 and CXCR4 on their surface, only the receptor CXCR4 was single expressed at a very low level in the Treg receptor profile (Fig. 37).

CCR4 has been described as specific for Tregs and is responsible for their migration into the TME via tumor-expressed chemokines CCL2, CCL22 and CCL17. In data from GBM patients, significantly higher expression levels of CCR4 were detected on circulating Tregs (Jordan et al., 2008). After RT, CXCR4 expression on Tregs is induced under hypoxic stress and recruits the cells into the irradiated tissue (Ondondo et al., 2013).

The ascertained receptor profile supports the hypoxia-driven recruitment of Tregs via CXCL12/CXCR4 signaling. In contrast to other expression patterns found, the tumors showed a reduced influx of $CCR4^+CXCR4^+$ Tregs after RT (Fig. 38). Therefore, the $CCR4^+CXCR4^+CXCR7^+$ Tregs and the co-expression of all five observed chemokine receptors were intensified to overcome the reduction of this receptor combination.

The analyzed Tregs also expressed other migration receptors such as CCR2 and CCR5 for higher migration rates. The Tregs require these two receptors to migrate into inflamed tissues and draining lymph nodes. CCR2 and CCR5 signaling also increase the fitness of the Tregs and enhanced their regulatory function against naïve T cells (Ward et al., 2015; Zhan et al., 2020).

On the $CD11b^+Gr1^+$ MDSCs, the single expression of the five observed receptors was low compared with the receptor combinations found (Fig. 39). Interestingly, MDSCs, expressing only the CXCR4 receptor on their surface, were found significantly less frequently, whereas CXCR7 single expression increased after RT. When focusing on the co-expression of these receptors, the same difference was found. The co-expression of the receptor CCR4 with other receptors was also higher after RT.

As a result of irradiation, most receptor variants were reduced, only the co-expression of all observed chemokine receptors as well as the combinations $CCR2^+CCR4^+CCR5^+CXCR7^+$ and $CCR2^+CCR4^+CCR5^+$ were detected increased on MDSCs (Fig. 40).

The CCR2 receptor is a high affinitive receptor for CCL2 on circulating monocytic progenitors and MDSCs, required for the accumulation of monocytic MDSCs in glioma (Chang et al., 2016). In this model, the major MDSC subset in the tumor tissue was identified as M-MDSCs, being slightly reduced after RT. Therefore, it is no surprise that CCR2 is involved in eight of the 10 most frequently found receptor combinations.

CCR2 and CCR5 share up to 75% homology and share the ligands CCL2, CCL7, CCL8 and CCL16 (Fantuzzi et al., 2019). CCR5 is a key driver of the accumulation of MDSCs at the tumor site and mainly expressed on PMN-MDSCs in the tumor environment (Hawila et al., 2017). In the model used, this MDSC subset was found only marginally (1.1-1.7% of all MDSCs). Even after the reduction of CXCR4, neither a significant increase in $CCR5^+$ MDSCs nor a remarkable development of the PMN-MDSCs was observed. $CCR5^+$ MDSCs are indicators of a stronger immunosuppressive environment that directly correlates with the enhancement of CCR5 ligands like CCL3, CCL4 and CCL5 (Blattner et al., 2018). In the model used, these ligands were reduced in response to RT at the observed time point. This

contrasts with the observed expression of CC chemokine receptors on MDSCs, which seems to indicate that the cytokine production by these cells is less immunosuppressive than that of the total TME after RT.

In contrast to other preclinical studies, that demonstrated a remarkable irradiation-induced accumulation of MDSCs via CXCL12 receptor CXCR4, in the model used, the only significantly reduced cell subset was the CXCR4$^+$ MDSCs subset (Kioi et al., 2010; Liu et al., 2014; Walters et al., 2014). Because the receptor was previously reported to be upregulated after RT, the determined receptor profile of the MDSCs indicates that other pathways instead promote the MDSC re-infiltration in the present setting. The CCL2-CCR2 recruitment pathways seems to be mainly responsible for the re-infiltration and equalization of the TME by MDSCs. The cytokine analysis revealed that the CCL2 production was reduced on the irradiated tumor side and so was the amount of myeloid cells. Whereas, the increased number of CXCR7$^+$ MDSCs in irradiated tumor tissue can be related to the unchanged expression of CXCL12 by irradiation and the higher binding affinity of the receptor with the chemokine. Although this receptor has not been reported to directly mediate chemotaxis of MDSCs, it is involved in chemotactic events through the uptake and degradation of chemokines and thus may also be engaged in the re-infiltration of MDSCs after irradiation (Burns et al., 2006; Quinn et al., 2018; Sanchez-Martin et al., 2013).

5.3.4 Chemokines and cytokines in the TME

To determine the current status of the immune response due to the different treatments (RT, NOX-A12, RT + NOX-A12), 31 different cytokines and chemokines were analyzed in the blood and TME of animals treated. Normalized to the respective total protein levels, most analytes revealed a high gradient between the intratumoral and respective plasma concentrations, which differ mainly depending on the inhibition of CXCL12 promoting the migration of immune cells into the TME.

The interleukins IL-2, IL-4 and IL-6 could only be determined in low concentrations, whereas the interleukins IL-1β, IL-10 and IL-16 were detected in significantly higher amounts in both plasma and tumor samples. The cytokines GM-CSF, IFN-γ and TNF-α were also found in relatively low levels (3 to 20 pg/mg protein) (Fig. 41, A, E-H; Fig. 42, I).

In this model, the concentrations of the proinflammatory cytokines IL-1β, IL-6 and TNF-α were significantly reduced after RT in the TME (Fig. 41, A, D; Fig. 42, I). The IL-6 was also significantly decreased by the CXCL12 antagonist NOX-A12 (Fig. 41, D). Other studies had shown that the expression of the cytokines IL-1, IL-6 and TNF-α was increased by irradiation (Albulescu et al., 2013; Zhou et al., 2015b). A similar marked decrease in the release of IL-1β and TNF-α has previously been observed only after exposure to low-dose X-ray irradiation (Frischholz et al., 2013).

The concentration of IL-1β in the plasma increased significantly under treatment with the CXCL12 antagonist (Fig. 41, A). In the TME, the interleukin was significantly lowered by irradiation. IL-1β is commonly present in GBM and is mainly produced by tumor cells but also by tumor-associated macrophages. As a pro-inflammatory cytokine IL-1β modulates the GBM progression and cell invasion by stimulating the production of the tumor-promoting interleukins IL-6 and IL-8 (Tanabe et al., 2011; Yeung et al., 2012). This effect is dependent on the degree of hypoxia, thus IL-1β

acts as a tumor suppressor under high hypoxia (Sun et al., 2014). After RT, the TME is no longer adequately oxygenated at the tissue level and may be tumor-suppressive even at reduced levels. Therefore, the levels of IL-1β found in the TME were expected. The reduction of IL-1β under RT might be related to reduced GBM cells, rather than to changes in macrophages in the TME. The enhanced stimulation of IL-6 production was not detected, but the measured levels of IL-1β and IL-6 corresponded in each group.

IL-2 was not significantly altered by the therapies in the plasma or TME (Fig. 41, B). This interleukin is produced by activated antigen-specific $CD4^+$ and $CD8^+$ T cells but is mainly consumed by $CD25^+$ Tregs. The strength of the IL-2 secretion modulates the antigen-specific $CD8^+$ T cell population as well as the proliferation of GBM cells (Boyman and Sprent, 2012; Capelli et al., 1999). The $CD4^+$ and $CD8^+$ T cells were also not significantly changed or depleted by the therapies. These findings correlate with the lack of alteration in the interleukin expression, but do not allow to predict a possible outcome.

In the TME, IL-4, a potent regulator of the antitumor activity, did not differ as a result of the therapies (Fig. 41, C). IL-4 is secreted by mast cells, T helper cells, eosinophils and basophils and it regulates tumor growth by blocking angiogenesis or recruiting eosinophils (Gadani et al., 2012). The expected increased blockade of angiogenesis after administration of NOX-A12 was not reflected in the determined levels of this interleukin in the TME, so that the antitumor effect of the treatments, as evidenced by the prolonged survival, could not be attributed to this interleukin.

IL-6 regulates the immune response by decreasing the release of both pro-inflammatory and anti-inflammatory cytokines (Scheller et al., 2011). IL-6 and TNF-α influence each other's expression (West et al., 2018; Zhou et al., 2015b). This was also evident in the levels measured in this GBM model, the concentrations of both cytokines in the TME were nearly equal (Fig. 41, D). IL-6 supports the progression of the tumor as a growth factor, also deregulates the tumor process and acts as a promoter of vascular endothelial cell migration during tumor angiogenesis. It is often predominately expressed by infiltrating macrophages as a reaction to tissue damage or stress due to irradiation of the tumor and other pro-inflammatory cytokines (West et al., 2018; Zhou et al., 2015b). Therefore, the reduction in IL-6 after RT was surprising but corresponds to a lower number of tumor-infiltrating macrophages after RT. The interleukin was also significantly reduced by the inhibition of CXCL12, which suggests inhibition of endothelial cell migration and, in cascade, tumor angiogenesis.

In this model, IL-10 was highly expressed in the GBM tumors but not altered by the treatment (Fig. 41, E). A high concentration of the interleukin was expected because IL-10 is overexpressed in human GBM and acts as an anti-inflammatory cytokine promoting tumor cell proliferation as well as GBM motility (Huettner et al., 1997). It is produced by numerous cell types like Tregs, macrophages and DCs and is involved in the suppression of immune responses by impairing the proliferation, cytokine production and migration of $CD8^+$ effector cells (Dennis et al., 2013; Moore et al., 2001). The amount of the interleukin corresponds with the constant frequency of Tregs found.

IL-16 was significantly increased by the CXCL12 antagonist in the plasma, but in the

TME its high values remained almost unchanged (Fig. 41, F). IL-16 is a chemoattractant for CD4$^+$ cells, a modulator of T cell activation and induces the cytokine release from monocytes and macrophages (Mathy et al., 2000). The high amount of the interleukin at the tumor site creates a gradient that attracts more CD4$^+$ cells to the TME, which is reduced by the CXCL12 inhibition. Therefore, fewer CD4$^+$ cells were found in the TME under CXCL12 blockade but not after RT, which unfortunately was not sufficient for a significant difference.

Intratumoral GM-CSF was also not significantly changed in reaction to irradiation, but the factor was systematically increased by NOX-A12 (Fig. 41, G). In GBM, the colony-stimulating factor is produced by the tumor cells and in response to any damage to the brain tissue from a growing tumor by normal, unstimulated brain neurons. It acts as an immunosuppressive cytokine and is involved in glioma carcinogenesis and progression (Kast et al., 2017). Although the factor is produced as a response to each damage caused by tumor or irradiation, only a small amount was found in the TME, which was even reduced after RT. This indicates that at the observation time point, the irradiation-induced release of the growth factor had already slowed down and the tumor growth had stopped accordingly.

The production of IFN-γ was also not modified in plasma or TME as a result of therapy (Fig. 41, H). IFN-γ is a pro-inflammatory cytokine that enhances the number and activity of various cells involved in the antitumor immune responses. Especially brain DCs are stimulated by IFN-γ in their antigen-presenting function (Zhou et al., 2015b). IFN-γ is involved in the inhibition of cell proliferation and angiogenesis in the TME, particularly in irradiated tumors (Lugade et al., 2008). The absence of an increased expression of this cytokine suggests that no acute immune response was ongoing during the observation time point.

TNF-α was significantly reduced in the irradiated TME and the factor was increased by the CXCL12 inhibition in the plasma (Fig. 42, I). It acts as an important activator of the neuroimmune system and is secreted mainly by GBM infiltrating CD4$^+$ lymphocytes, activated macrophages and NK cells. It provokes the expression of vascular endothelial growth factor (VEGF) in GBM and promotes the tumor angiogenesis (Zhou et al., 2015b). A reduction of this factor indicates a delay in its production due to the infiltration of CD4$^+$ lymphocytes after RT so that suppressed angiogenesis of the irradiated tumor can also be assumed.

CCL1 (I-309) was significantly increased only in the plasma of animals treated with RT and immune modulators (Fig. 42, J). In the TME, the cytokine was found at an intermediate level, and no change in the expression of CCL1 was detected. CCL1, as an inflammatory mediator, stimulates monocyte migration, induced tumor regression and resistance (Liang et al., 2020). Furthermore, CCL1 expression can increase Treg accumulation in cancer (Kuehnemuth et al., 2018). The gradient found supports both the MDSC as well as Treg migration in the TME. However, the absent change through the treatment indicates that the TME was already in a steady-state during the observation time point.

In the tumor tissue, CCL2 (MCP-1) was found at high levels, which were significantly reduced by RT (Fig. 42, K). In the plasma samples, its amount was increased as a

result of the CXCL12 inhibition. This chemokine is mainly produced by tumor-associated macrophages, monocytic MDSCs and microglia. It is crucial for the clinical outcome, as demonstrated in this tumor model treated with the CCL2 inhibitor mNOX-E36. In the early phases of tumor progression, the cytokine promotes a beneficial TME for an antitumor immune response. In established tumors, this cytokine supports an immunosuppressive microenvironment, while acting as an influential recruiting factor for Tregs and MDSCs in GBM (Chang et al., 2016). Based on its functions, the high expression levels correspond to the levels of MDSCs and Tregs found in the TME.

In the plasma, both proinflammatory chemokines, CCL3 (MIP-1α) and CCL4 (MIP-1β) increased significantly due to NOX-A12 (Fig. 42, L, M). Moreover, both chemokines were significantly decreased as a result of irradiation of the TME at almost the same level. They are important chemokines that interact with each other in the initiation of an immune response and induce the recruitment of DCs, neutrophils, monocytes, macrophages and T cells. CCL3 affects the function of CD8^{+} T cells, whereas CCL4 acts on CD4^{+} T cells. But TAMs and MDSCs also produce these chemokines for tumor-promoting effects and the recruitment of MDSCs via CCR5 (Korbecki et al., 2020). Both chemokines were increased in the plasma when CXCL12 was inhibited, indicating an alternative recruitment reaction for MDSCs via the CCR5 receptor, even if the receptor profile of the MDSCs does not clearly support this (Hawila et al., 2017). On the other hand, the reduced concentration of these cytokines in the irradiated TME is associated with the recruitment of MDSCs, but also with the blocked migration of effector T cells, which indicates a chronic inflammation site in the TME with a tumor-promoting effect. The higher expression of CCL3 in the untreated TME suppresses the effect of GM-CSF and more importantly IL-4 there (Herrlinger et al., 2004). In the TME, the production of IL-4 was not altered by treatment, but based on the reduced concentrations of CCL3 after RT, a higher effect of IL-4 can be assumed in the treated animals.

The concentration of CCL5 (RANTES) in the tumor tissue was very high but was not significantly changed by any treatment (Fig. 42, N). Its plasma levels were significantly reduced after RT and immunotherapy. As a pro-inflammatory cytokine, it is responsible for the accumulation of various anti-cancer immune cells to the tumor site. The expression of CCL5 is increased in GBM-associated cells, MDSCs, GAMs and TILs, but also Tregs. It also increases the proliferation of cancer cells and participates in angiogenesis (Korbecki et al., 2020). The consistently high concentration of this chemokine in the TME indicates its importance in the recruitment of TILs, GAMs as well as MDSCs. The reduced gradient after RT and NOX-A12 administration indicates a soft inhibition of this migration in the model used. Because of the stronger immunosuppressive character of the MDSCs recruited via CCL5-CCR5 interaction, the TME appears to be slightly more pro-inflammatory after the administration of the combination therapy compared with the other treatment arms (Blattner et al., 2018).

The CCL7 (MCP-3) in the tumor tissue was determined to be dependent on irradiation (Fig. 42, O). CCL7 acts as a chemotactic attractant for monocytes, DCs, tumor-associated macrophages and activated T lymphocytes. It can also promote

tumorigenesis and progression (Liu et al., 2018). After RT, the reduced expression of this chemokine is indicative for the reduced migration of active T cells into the TME, which also suggests that after RT, the re-infiltration of the TME had already been completed at the observation time point, which can happen within five days as reported by other studies (Stessin et al., 2020).

No significant change in the expression of the important chemoattractant for eosinophils and basophils, CCL11 (Eotaxins) (Fig. 42, P), which causes and inhibits tumor angiogenesis, was detected in the TME (Korbecki et al., 2020). The gradient between the TME and the plasma levels of this chemokine was neutralized as a reaction to treatment. This suggests, that it did not have a role in the recruitment of eosinophils and basophils in the TME of treated animals neither in the tumor angiogenesis in the model used.

The amount of CCL12 (MCP-5) in the tumor tissue was significantly reduced by the radiation, while it increased in plasma due to the CXCL12 blockade (Fig. 43, Q). Murine CCL12 is closely related to human CCL2 and is a major cytokine produced by macrophages that recruits eosinophils, monocytes and lymphocytes (Jia et al., 1996). The dependence of CCL12 expression on macrophages explains the lower gradient in the treatment groups with CXCL12 inhibition, which is supported by the effect of RT. The lower gradient results in a lower migratory pressure for monocytes and lymphocytes, which may lead to a survival advantage over a longer time span.

For the chemokines CCL17 (TARC) and CCL19 (MIP-3), no significant changes were determined by the treatment (Fig. 43, R, S). CCL17 is produced by myeloid DCs and endothelial cells. It enhances antitumor immunity by inducing the chemotaxis of T cells and activating CD8$^+$ T cells through APCs (Henry et al., 2008; Kumai et al., 2015). CCL19 is responsible for the homing of T cells to lymph nodes. In the tumor, the chemokine induces an anti-cancer activity via cytotoxic TILs and inhibition of angiogenesis (Korbecki et al., 2020). The constant ranges indicated that all these functions are not relevant to the diverse behaviors of the different treatment groups in our model.

Significant changes in the plasma concentrations were determined for the chemokines CCL20 (MIP-3α) and CCL22 (MDC) after administration of NOX-A12 (Fig. 43, T, U). As a pro-inflammatory chemokine, CCL20 is essential for the functions of DCs, T cells and B cells. In tumors, its main function is the recruitment of Tregs, TAMs or DCs. It increases the anticancer response, but also promotes tumor immune evasion to a greater extent. It also causes angiogenesis and increases cancer cell proliferation (Korbecki et al., 2020). The low concentration of this chemokine in both, plasma and TME, demonstrates that it does not affect the migration of Tregs, TAMs and DCs here. In GBM, reduced plasma levels of CCL22, a chemoattractant for DCs, CD4$^+$ and CD8$^+$ T cells, can be associated with low CD4$^+$ T cell counts and shorter survival times (Mantovani et al., 2000; Zhou et al., 2015a). These lower plasma levels were observed after RT, but not when the CXCL12 inhibitor was added. The larger gradient in the RT group also has a greater recruiting effect for T cells, which compensates for the lack of lymphocytes in the irradiated TME. Consequently, the CCL22 expression could be an indicator of a survival benefit of the combination therapy of RT with NOX-A12.

The treatments did not alter the concentrations of CCL24 (Eotaxin-2) in plasma or tumors (Fig. 43, V). CCL24 induces the chemotaxis in eosinophils, resting T cells and neutrophils in the TME, but this function is not decisive for the tumor growth under the different treatments in this GBM model (Korbecki et al., 2020).

The CXCL12 inhibition modified the blood concentration of CCL27 (CTACK) but did not affect the high concentrations in the tumor (Fig. 43, W). CCL27 is responsible for the $CD3^+$ and $CD4^+$ lymphocyte migration and is thus involved in the anticancer response of the immune system. However, it is also involved in tumor development, especially in the hypoxic tumor regions (Korbecki et al., 2020). Because the gradient remains stable under the treatment in all groups, a chronic inflammatory state has to be considered.

Contrastingly, no significant changes in the blood concentration of CXCL1 (KC) were detected, but the in-tumor concentration was changed by irradiation (Fig. 43, X). CXCL1 has been reported to be enriched in GBM and related to the radioresistance of GBM cells (Alafate et al., 2020). However, the low levels in all treatment groups were not a sign of a relationship between the chemokine and the radioresistance of the tumor cells.

For CXCL5 (ENA-78), no significant changes were detected between the treatment groups, either in the plasma nor in the TME (Fig. 44, Y). CXCL5 has been reported to be upregulated in GBM and involved in tumorigenesis as well as cancer progression (Dai et al., 2016). The gradients found do not promote any differences between the treatment regimes.

CXCL10 (IP-10) was found at very high concentrations in the untreated tumor samples and was strongly influenced by RT (Fig. 44, Z). After RT, the concentration of this chemokine was drastically reduced, so that the gradients were almost neutralized. CXCL10 is highly secreted by leukocytes, activated neutrophils, eosinophils, monocytes and endothelial cells in pro-inflammatory environments during cancer. It attracts activated T helper cells and monocytes, T cells and NK cells. In CNS, microglia, astrocytes and neurons express CXCL10, which in turn attracts microglia cells. In the murine model, CXCL10 mediates the immune stimulation and has been described as responsible for the therapeutic effect (Liu et al., 2011). On the one hand, the reduction by RT is caused by the loss of endothelial cells, but the flow cytometric analysis of these cells revealed no significant differences. On the other hand, and this seems to be the more important point, the leukocytes, monocytes and microglia in the TME are slightly lower in number as well as mainly exhausted, consequently, they secrete less CXCL10. The expression of the chemokine is also reduced in animals under CXCL12 inhibition, but the effect occurs to a lower extent and does not add up with irradiation.

NOX-A12 significantly increased the concentration of CXCL11 (I-TAC) in plasma but not in the TME (Fig. 44, AA). There, the chemokine was significantly reduced by RT. CXCL11 mediates the recruitment of T cells, NK cells, monocytes and macrophages. It is involved in the maturation of T cells and vasculogenesis. It also acts as an antagonist for CCR5 as well as a negative modulator in leukocyte migration and activation (Petkovic et al., 2004). The determined concentrations of this chemokine in the TME indicate that these functions are suppressed only after irradiation.

After RT, CXCL13 (BAC-1) was significantly reduced in the TME. CXCL13 is mainly

responsible for the B-cell tumor response (Fig. 44, Ac). It promotes B cell chemotaxis and proliferation in tumors in a CXCR5 expression-dependent manner (Kazanietz et al., 2019). Locally reduced amounts of tumor-associated B cells are correlated with a positive outcome (Lee-Chang et al., 2019). This suggests not only a reduced B cell activation on the irradiated side but also a survival benefit for the irradiated animals.

The concentrations of CXCL16 (SCYB16) were affected by NOX-A12 in the plasma (Fig. 44, AD). CXCL16 is overexpressed in GBM and released by tumor cells promoting GAMs (Lepore et al., 2018). In mice, it is produced by DC in lymphoid organs and attracts T and NK cells (Tabata et al., 2005). The secreted levels of this chemokine do not indicate a relevant function for the outcome of the different treatments in this model.

In the CNS, CX3CL1 (Fractalkine), which regulates tumor growth, is expressed by neurons and astrocytes. It is mainly involved in the cross-talk between neurons and microglia. CX3CL1 is a transmembrane protein acting as a chemoattractant for monocytes, DCs and lymphocytes when cleaved by specific proteases (Erreni et al., 2010; Sciume et al., 2010). Therefore, higher quantities of this chemokine were expected in the TME. However, the concentrations were not changed in either the plasma or the tumor tissue by the different treatments (Fig. 44, AE). As Liu et al. (2008) had previously shown, CX3CL1 has no effect on the tumor growth nor migration of microglia or lymphocytes in this GBM model.

The ligand of the immune modulator NOX-A12, CXCL12, was found in high concentrations in the plasma after administration of its Spiegelmer antagonist (Fig. 44, AB). It is the only chemokine for which a switch of the gradient between plasma and TME has been detected. This increase of the chemokine in blood can be explained by the increased formation of the inactive ligand-inhibitor complex of NOX-A12 and CXCL12, which is degraded more slowly than free CXCL12 (Hoellenriegel et al., 2014; Suarez-Carmona et al., 2021). Its formation confirms the successful inhibitory effect of the Spiegelmer tested and the accumulation of the cytokine in the plasma inhibits its messenger function. However, the chemokine also increased significantly in the TME proving that the inhibitor overcame the BBB and successfully blocked this chemokine there as well. In contrast to other studies, RT monotherapy showed no difference in the concentration of CXCL12 in plasma or TME compared with the untreated control (Kioi et al., 2010). Under the combination of RT and NOX-A12, the ligand-inhibitor complex is also formed but to a lower extent than under CXCL12 inhibition alone. This allows to conclude that a weaker inhibition of CXCL12 is established in the TME under this treatment. The similar survival curves of both RT treatment groups showed a slight benefit in the OS by this enhanced blockage compared with RT alone, which manifested itself in the last third of the observation period. This modest advantage was also favored by the suppressed infiltration of CXCR4^{+} MDSCs after RT. The applied RT altered the receptor pattern of the immunosuppressive MDSCs, resulting in significantly reduced recruitment and influx of this specific subgroup of MDSCs over a treatment time of 100 days. The additionally sustained blockade of this recruitment axis results in a moderately less interspersed with MDSCs and therefore less immunosuppressive TME.

5.3.5   Conclusion of the TME analysis

Ten days after irradiation and 20 days after tumor inoculation, respectively, only minor, mostly insignificant differences could be detected for the different cell populations between the treatment arms. Overall, the determined characterization of the TME showed only the actual state at the observation time point. On the one hand, these data lead to the conclusion that the irradiated TME has already recovered from the performed RT and is again in a more or less stable state at the observation time point. On the other hand, the fact that the only significant change was measured in CXCR4$^+$ MDSCs as a result of irradiation, in addition to the late onset of the survival benefit of the combination therapy, suggests that NOX-A12 more significantly affects the irradiated cellular TME at a later time point.

The detected change in the MDSCs receptor profile after irradiation provides a first indication of why some animals responded to irradiation and combination therapy with complete tumor regression. Unfortunately, a correlation between the individual profiles and the outcome could not be obtained in this experimental design.

These findings best describe the limitations of the flow cytometric analysis of the immune response performed and demonstrate that not only a snapshot, but a longitudinal analysis is required to obtain representative data regarding the time point at which the therapies show their full effect and thus provide comprehensive information about the response of the TME to the applied treatments. Especially, since the cytokine and chemokine concentrations can change occasionally within an hour.

The data obtained are associated with further limitations complicating translation into clinical practice in human GBM. For example, it must be considered that a particular response in mice may not occur exactly as in humans. Therefore, the minor changes in survival behavior and the differences at the cellular level or in the cytokine profile might be more pronounced in humans, or the opposite.

5.4   Conclusion

This study describes the first preclinical study combining RT and Spiegelmer immune modulators inhibiting the chemokines CCL2 and CXCL12. The model used was designed to be as similar as possible to the real clinical conditions. Therefore, a clinical irradiation system with a photon energy between 6 and 15 MV was used to apply the irradiation dose, as has been performed by only a few groups in similar preclinical studies before.

The Spiegelmer NOX-E36 was tested for the first time in a preclinical GBM model. The survival studies showed that the administration of the Spiegelmer had no additional positive effect on the survival of the animals in any combination. The plasma inhibition of the cytokine CCL2 leads to increased tumor development. This can be explained by the exclusion of antitumor M1 macrophages at an earlier stage of the tumor progression, as this allows the tumor to grow without resistance. Therefore, the immune modulator is not recommended as a treatment option in the early stage of the disease. However, based on the study design, it cannot be completely ruled out that this treatment could be advantageous in established, radioresistant tumors. Blocking the recruitment of macrophages in already severely immune-suppressive TMEs may

be an additional approach for NOX-E36. Nevertheless, this hypothesis needs to be evaluated in a different experimental setting. For this reason, NOX-E36 is not yet recommended as an adjuvant in GBM therapy.

The CXCL12-inhibitor NOX-A12 has been previously tested in other cancer models, but here for the first time in an immune competent murine GBM model as an adjuvant to RT and checkpoint inhibitors. Several clinically promising combinations have been evaluated for their ability to suppress tumor growth. The data obtained showed a slight improvement in OS with the combination of irradiation of the tumor-bearing tissue and the immune modulator NOX-A12 compared with irradiation of the tissue alone.

Analysis of the cytokine and chemokine levels in the blood and tumor tissue of the mice showed the increased formation of an inactive ligand-inibitor complex of NOX-A12 and CXCL12 in plasma and tumor. This demonstrated that the CXCR4 receptor-ligand CXCL12 was blocked by the NOX-A12 immunotherapy. The accumulation of the chemokine in plasma inhibits the migration gradient between plasma and tumor tissue. Additionally, the intra-tumoral CXCL12 level was increased by the administration of the Spiegelmer, indicating the formation of a CXCL12-NOX-A12 complex and inactivation of CXCL12 in the TME, which impedes the migration of MDSCs into the tumor tissues. However, the flow cytometric analyses data of the tumor environment showed no relevant effect of this blockade on the amount of suppressor or effector cells in the tumor tissue in the used experimental setting, only the subpopulation of MDSCs expressing the CXCR4 receptor was significantly reduced by irradiation in the tumor tissue. In particular, MDSCs individually expressing the CXCR4 receptor were able to infiltrate tumor tissue only in a suppressed manner after irradiation. MDSCs with other co-expressed chemokine receptors were also prevented from infiltrating the microenvironment to a smaller extent. Therefore, the re-infiltrated cells in the irradiated TME exhibited a greater diversity of receptor expression. This may be evidence that in this model, migration of suppressor or effector cells in the tumor after RT is largely mediated by migration processes other than the CXCR4-CXCL12 signaling pathway. Follow-up studies that explore these migratory movements in more detail are recommended to clarify this question.

Adjuvant administration of a CXCL12 antagonist, which impedes CXCR4 ligand function in the blood, may help to maintain the migration blockade of CXCR4-positive immunosuppressive cells after irradiation. The CXCL12 antagonist was able to increase the plasma level of circulating CXCL12, reversing its concentration gradient between plasma and tumor tissue. Furthermore, the observed survival benefit may be a direct effect of the CXCL12 inhibition on the CXCR4-expressing tumor cells. The immune modulator also affects the migration ability, invasiveness or proliferation of the tumor cells. This explains the slight survival benefit of the combination of the immune modulator and irradiation compared with the RT alone. To better reflect this effect, a reduction of the irradiation dose would potentially be beneficial, as it was already shown to be very effective alone in the present model.

Considering that GBMs are particularly malignant tumor entities, any treatment option that improves the quality of life or the survival of the patients affected by this highly malignant disease should be considered highly valuable to them. For this reason, the

modest improvement in survival observed in this study with the combination of RT and NOX-A12 is sufficient to recommend further preclinical studies on the suitability of the CXCL12 antagonist as an adjuvant therapy to radiotherapy.

Thus, the factors that differentiate the animals into positive responders and non-responders to the combination therapy could not be clearly defined within the scope of this project and requires further research.

Prior to clinical application, this study should be complemented by further preclinical experiments aimed at evaluating the potential synergistic effect of chemokine inhibition in glioblastoma therapy compared to blocking the CXCR4 receptor. For this purpose, it would be beneficial to compare the effects of CXCR4 receptor inhibition by plerixafor (AMD3100) and/or a CXCR4-specific antibody in the model used with the previously obtained findings. In this context, it is imperative to perform histological and flow cytometric analyses to achieve a comprehensive understanding of the structural and cellular changes induced by the treatments.

Another aspect that should be investigated is the impact of the administered treatments on tumor angiogenesis/vasculogenesis. To assess the effects of the treatments on the vasculature of the tumor and to make a comprehensive assessment of the architecture and organization of the blood vessels in the tumor, a 3D analysis of the vessels in the tumor could be performed.

6 SUMMARY

Recent therapeutic approaches for glioblastoma (GBM) focus on GBM cells eradication by local radiotherapy (RT) and targeting the tumor microenvironment (TME), e.g. by excluding myeloid-derived suppressor cells (MDSCs) by blocking the CXCR4/CXCL12-signal axis. The effect of RT combined with antagonization of CXCL12 (SDF-1) by a novel Spiegelmer immune modulator on survival, cellular TME and cytokine production was investigated here the first time in an immune-competent murine model as the main objective of the study. Further, the survival effects of a second immune modulator neutralizing CCL2 were evaluated.

Immune-competent 7-12 week-old female wild-type C57BL/6J mice were intracerebrally implanted with 1.5×10^5 murine GFP-expressing glioma cells (GL261) and survival was monitored up to 100 days. Three different immune modulators (anti-PD-1 antibody (6x 250 µg ip.), CXCL12 and CCL2 antagonists (both 20 µg/g body weight s.c. every 2nd day)) were tested in various combinations (13 groups) with or without half-brain irradiation (1 x 12 Gy). To monitor tumor growth, animals (n = 8-15) were observed weekly via MRI (1 Tesla, T1-weighted) and after a maximum of 100 days, brains were examined for complete tumor regression (MRI, fluorescence signal, immunohistochemistry). To investigate the effects of the combination of CXCL12 antagonist and RT on the immune response, tumor tissue, spleen and blood from animals randomized into four groups (untreated control, NOX-A12, RT, RT with NOX-A12) were analyzed by flow cytometry 20 days after tumor inoculation. Besides, the concentrations of 31 cytokines and chemokines in tumor and plasma were measured by bead-based multiplex immune assay and receptor profiles after RT were determined for the $CD8^+$ effector cells, $CD4^+FOXP3^+$ Tregs and $CD11b^+Gr1^+$ MDSCs. Survival data were statistically analyzed by the Kaplan-Meier method, other data using a one-way ANOVA test or an unpaired t-test with a significance limit of 5% (p < 0.05).

As monotherapy, both Spiegelmers had no positive effect on mouse survival, contrary to the anti-PD-1 antibody (32 days median survival (MS), p = 0.025). Only the CXCXL12 antagonist combined with anti-PD-1 treatment had an improved survival effect over the control group (42 days MS, p = 0.003). RT resulted in a MS of 57.5 days with an overall survival (OS) rate of 25%. Addition of CXCL12 antagonist to RT improved MS to 99 days and overall survival to 50% (p = 0.19). CCL2 antagonization combined with other treatments did not result in any survival benefit. Flow cytometry analysis revealed only minor differences in tumor-infiltrating leukocytes and endothelial cells. $CD8^+$ T cells carried exhaustion markers, while a quarter of the $CD4^+$ T cells were regulatory T cells (Tregs). Intratumoral MDSCs ($CD11b^+Gr1^+$) expressing CXCR4 were significantly reduced after RT. Receptor profiling of irradiated MDSCs showed a loss of CXCR4 as single expression or in combination with other receptors. Irradiation leads to a significant increase in receptor combinations $CCR4^+CXCR4^+CXCR7^+$ (p = 0.01) and $CCR2^+CCR4^+CXCR4^+CXCR7^+$ (p = 0.04) on $CD8^+$ effector cells and a slight reduction in $CCR4^+CXCR4^+$ Tregs. Only for CXCL12, an inversion of the gradient between plasma and TME concentration was observed under the influence of the tested immune modulator.

Considering that GBMs are particularly malignant tumor entities, the heterogeneous results under CXCL12 antagonist NOX-A12 as adjuvant to RT warrant further preclinical studies to identify potential impact indicators yet unknown with regard to the suitability of the inhibitor for clinical use.

7   REFERENCES

Agnihotri, S., Burrell, K.E., Wolf, A., Jalali, S., Hawkins, C., Rutka, J.T., and Zadeh, G. (2013). Glioblastoma, a brief review of history, molecular genetics, animal models and novel therapeutic strategies. Arch Immunol Ther Exp (Warsz) *61*, 25-41. 10.1007/s00005-012-0203-0

Alafate, W., Li, X., Zuo, J., Zhang, H., Xiang, J., Wu, W., Xie, W., Bai, X., Wang, M., and Wang, J. (2020). Elevation of CXCL1 indicates poor prognosis and radioresistance by inducing mesenchymal transition in glioblastoma. CNS Neurosci Ther *26*, 475-485. 10.1111/cns.13297

Albulescu, R., Codrici, E., Popescu, I.D., Mihai, S., Necula, L.G., Petrescu, D., Teodoru, M., and Tanase, C.P. (2013). Cytokine patterns in brain tumour progression. Mediators Inflamm *2013*, 979748. 10.1155/2013/979748

Amarnath, S., Costanzo, C.M., Mariotti, J., Ullman, J.L., Telford, W.G., Kapoor, V., Riley, J.L., Levine, B.L., June, C.H., Fong, T.*, et al.* (2010). Regulatory T cells and human myeloid dendritic cells promote tolerance via programmed death ligand-1. PLoS Biol *8*, e1000302. 10.1371/journal.pbio.1000302

Anderson, N.M., and Simon, M.C. (2020). The tumor microenvironment. Curr Biol *30*, R921-R925. 10.1016/j.cub.2020.06.081

Ando, M., Ito, M., Srirat, T., Kondo, T., and Yoshimura, A. (2020). Memory T cell, exhaustion, and tumor immunity. Immunol Med *43*, 1-9. 10.1080/25785826.2019.1698261

Ansari, R., Gaber, M.W., Wang, B., Pattillo, C.B., Miyamoto, C., and Kiani, M.F. (2007). Anti-TNFA (TNF-alpha) treatment abrogates radiation-induced changes in vacular density and tissue oxygenation. Radiat Res *167*, 80-86. 10.1667/rr0616.1

Antonioli, L., Pacher, P., Vizi, E.S., and Hasko, G. (2013). CD39 and CD73 in immunity and inflammation. Trends Mol Med *19*, 355-367. 10.1016/j.molmed.2013.03.005

Apetoh, L., Ghiringhelli, F., Tesniere, A., Obeid, M., Ortiz, C., Criollo, A., Mignot, G., Maiuri, M.C., Ullrich, E., Saulnier, P.*, et al.* (2007). Toll-like receptor 4-dependent contribution of the immune system to anticancer chemotherapy and radiotherapy. Nat Med *13*, 1050-1059. 10.1038/nm1622

Aymeric, L., Apetoh, L., Ghiringhelli, F., Tesniere, A., Martins, I., Kroemer, G., Smyth, M.J., and Zitvogel, L. (2010). Tumor cell death and ATP release prime dendritic cells and efficient anticancer immunity. Cancer Res *70*, 855-858. 10.1158/0008-5472.CAN-09-3566

Badie, B., and Schartner, J.M. (2000). Flow cytometric characterization of tumor-associated macrophages in experimental gliomas. Neurosurgery *46*, 957-961; discussion 961-952. 10.1097/00006123-200004000-00035

Ballbach, M., Dannert, A., Singh, A., Siegmund, D.M., Handgretinger, R., Piali, L., Rieber, N., and Hartl, D. (2017). Expression of checkpoint molecules on myeloid-derived suppressor cells. Immunol Lett *192*, 1-6. 10.1016/j.imlet.2017.10.001

Balogh, A., Persa, E., Bogdandi, E.N., Benedek, A., Hegyesi, H., Safrany, G., and Lumniczky, K. (2013). The effect of ionizing radiation on the homeostasis and functional integrity of murine splenic regulatory T cells. Inflamm Res *62*, 201-212. 10.1007/s00011-012-0567-y

Baskar, R., Dai, J., Wenlong, N., Yeo, R., and Yeoh, K.W. (2014). Biological response of cancer cells to radiation treatment. Front Mol Biosci *1*, 24. 10.3389/fmolb.2014.00024

Batash, R., Asna, N., Schaffer, P., Francis, N., and Schaffer, M. (2017). Glioblastoma Multiforme, Diagnosis and Treatment; Recent Literature Review. Curr Med Chem *24*, 3002-3009. 10.2174/0929867324666170516123206

Blanc, J.L., Wager, M., Guilhot, J., Kusy, S., Bataille, B., Chantereau, T., Lapierre, F., Larsen, C.J., and Karayan-Tapon, L. (2004). Correlation of clinical features and methylation status of MGMT gene promoter in glioblastomas. J Neurooncol *68*, 275-283. 10.1023/b:neon.0000033385.37098.85

Blattner, C., Fleming, V., Weber, R., Himmelhan, B., Altevogt, P., Gebhardt, C., Schulze, T.J., Razon, H., Hawila, E., Wildbaum, G.*, et al.* (2018). CCR5(+) Myeloid-Derived Suppressor Cells Are Enriched and Activated in Melanoma Lesions. Cancer Res *78*, 157-167. 10.1158/0008-5472.CAN-17-0348

Boels, M.G.S., Koudijs, A., Avramut, M.C., Sol, W., Wang, G., van Oeveren-Rietdijk, A.M., van Zonneveld, A.J., de Boer, H.C., van der Vlag, J., van Kooten, C.*, et al.* (2017). Systemic Monocyte Chemotactic Protein-1 Inhibition Modifies Renal Macrophages and Restores Glomerular Endothelial Glycocalyx and Barrier Function in Diabetic Nephropathy. Am J Pathol *187*, 2430-2440. 10.1016/j.ajpath.2017.07.020

Bonavia, R., Inda, M.M., Cavenee, W.K., and Furnari, F.B. (2011). Heterogeneity maintenance in glioblastoma: a social network. Cancer Res *71*, 4055-4060. 10.1158/0008-5472.CAN-11-0153

Borsellino, G., Kleinewietfeld, M., Di Mitri, D., Sternjak, A., Diamantini, A., Giometto, R., Hopner, S., Centonze, D., Bernardi, G., Dell'Acqua, M.L.*, et al.* (2007). Expression of ectonucleotidase CD39 by Foxp3+ Treg cells: hydrolysis of extracellular ATP and immune suppression. Blood *110*, 1225-1232. 10.1182/blood-2006-12-064527

Boyman, O., and Sprent, J. (2012). The role of interleukin-2 during homeostasis and activation of the immune system. Nat Rev Immunol *12*, 180-190. 10.1038/nri3156

Bronte, V., Brandau, S., Chen, S.H., Colombo, M.P., Frey, A.B., Greten, T.F., Mandruzzato, S., Murray, P.J., Ochoa, A., Ostrand-Rosenberg, S.*, et al.* (2016). Recommendations for myeloid-derived suppressor cell nomenclature and characterization standards. Nat Commun *7*, 12150. 10.1038/ncomms12150

Brown, J.M., Recht, L., and Strober, S. (2017). The Promise of Targeting Macrophages in Cancer Therapy. Clin Cancer Res *23*, 3241-3250. 10.1158/1078-0432.CCR-16-3122

Brown, J.M., Thomas, R., Nagpal, S., and Recht, L. (2020). Macrophage exclusion after radiation therapy (MERT): A new and effective way to increase the therapeutic ratio of radiotherapy. Radiother Oncol *144*, 159-164. 10.1016/j.radonc.2019.11.020

Brown, N.F., Carter, T.J., Ottaviani, D., and Mulholland, P. (2018). Harnessing the immune system in glioblastoma. Br J Cancer *119*, 1171-1181. 10.1038/s41416-018-0258-8

Burnette, B.C., Liang, H., Lee, Y., Chlewicki, L., Khodarev, N.N., Weichselbaum, R.R., Fu, Y.X., and Auh, S.L. (2011). The efficacy of radiotherapy relies upon induction of type i interferon-dependent innate and adaptive immunity. Cancer Res *71*, 2488-2496. 10.1158/0008-5472.CAN-10-2820

Burns, J.M., Summers, B.C., Wang, Y., Melikian, A., Berahovich, R., Miao, Z., Penfold, M.E., Sunshine, M.J., Littman, D.R., Kuo, C.J., *et al.* (2006). A novel chemokine receptor for SDF-1 and I-TAC involved in cell survival, cell adhesion, and tumor development. J Exp Med *203*, 2201-2213. 10.1084/jem.20052144

Butte, M.J., Keir, M.E., Phamduy, T.B., Sharpe, A.H., and Freeman, G.J. (2007). Programmed death-1 ligand 1 interacts specifically with the B7-1 costimulatory molecule to inhibit T cell responses. Immunity *27*, 111-122. 10.1016/j.immuni.2007.05.016

Capelli, E., Civallero, M., Barni, S., Ceroni, M., and Nano, R. (1999). Interleukin-2 induces the growth of human glioblastoma cells in culture. Anticancer Res *19*, 3147-3151.

Cashmore, J. (2008). The characterization of unflattened photon beams from a 6 MV linear accelerator. Phys Med Biol *53*, 1933-1946. 10.1088/0031-9155/53/7/009

Chang, A.L., Miska, J., Wainwright, D.A., Dey, M., Rivetta, C.V., Yu, D., Kanojia, D., Pituch, K.C., Qiao, J., Pytel, P., *et al.* (2016). CCL2 Produced by the Glioma Microenvironment Is Essential for the Recruitment of Regulatory T Cells and Myeloid-Derived Suppressor Cells. Cancer Res *76*, 5671-5682. 10.1158/0008-5472.CAN-16-0144

Chen, Z., Feng, X., Herting, C.J., Garcia, V.A., Nie, K., Pong, W.W., Rasmussen, R., Dwivedi, B., Seby, S., Wolf, S.A., *et al.* (2017). Cellular and Molecular Identity of Tumor-Associated Macrophages in Glioblastoma. Cancer Res *77*, 2266-2278. 10.1158/0008-5472.CAN-16-2310

Cho, H.R., Kumari, N., Thi Vu, H., Kim, H., Park, C.K., and Choi, S.H. (2019). Increased Antiangiogenic Effect by Blocking CCL2-dependent Macrophages in a Rodent Glioblastoma Model: Correlation Study with Dynamic Susceptibility Contrast Perfusion MRI. Sci Rep *9*, 11085. 10.1038/s41598-019-47438-4

Chouaib, S., Umansky, V., and Kieda, C. (2018). The role of hypoxia in shaping the recruitment of proangiogenic and immunosuppressive cells in the tumor microenvironment. Contemp Oncol (Pozn) *22*, 7-13. 10.5114/wo.2018.73874

Churov, A., and Zhulai, G. (2021). Targeting adenosine and regulatory T cells in cancer immunotherapy. Hum Immunol *82*, 270-278. 10.1016/j.humimm.2020.12.005

Contento, R.L., Molon, B., Boularan, C., Pozzan, T., Manes, S., Marullo, S., and Viola, A. (2008). CXCR4-CCR5: a couple modulating T cell functions. Proc Natl Acad Sci U S A *105*, 10101-10106. 10.1073/pnas.0804286105

Corzo, C.A., Condamine, T., Lu, L., Cotter, M.J., Youn, J.I., Cheng, P., Cho, H.I., Celis, E., Quiceno, D.G., Padhya, T., *et al.* (2010). HIF-1alpha regulates function and differentiation of myeloid-derived suppressor cells in the tumor microenvironment. J Exp Med *207*, 2439-2453. 10.1084/jem.20100587

Crane, C.A., Ahn, B.J., Han, S.J., and Parsa, A.T. (2012). Soluble factors secreted by glioblastoma cell lines facilitate recruitment, survival, and expansion of regulatory T cells: implications for immunotherapy. Neuro Oncol *14*, 584-595. 10.1093/neuonc/nos014

Crocetti, E., Trama, A., Stiller, C., Caldarella, A., Soffietti, R., Jaal, J., Weber, D.C., Ricardi, U., Slowinski, J., Brandes, A., *et al.* (2012). Epidemiology of glial and non-glial brain tumours in Europe. Eur J Cancer *48*, 1532-1542. 10.1016/j.ejca.2011.12.013

Curiel, T.J., Coukos, G., Zou, L., Alvarez, X., Cheng, P., Mottram, P., Evdemon-Hogan, M., Conejo-Garcia, J.R., Zhang, L., Burow, M., *et al.* (2004). Specific recruitment of regulatory T cells in ovarian carcinoma fosters immune privilege and predicts reduced survival. Nat Med *10*, 942-949. 10.1038/nm1093

D'Agostino, P.M., Gottfried-Blackmore, A., Anandasabapathy, N., and Bulloch, K. (2012). Brain dendritic cells: biology and pathology. Acta Neuropathol *124*, 599-614. 10.1007/s00401-012-1018-0

Dai, Z., Wu, J., Chen, F., Cheng, Q., Zhang, M., Wang, Y., Guo, Y., and Song, T. (2016). CXCL5 promotes the proliferation and migration of glioma cells in autocrine- and paracrine-dependent manners. Oncol Rep *36*, 3303-3310. 10.3892/or.2016.5155

Davis, M.E. (2016). Glioblastoma: Overview of Disease and Treatment. Clin J Oncol Nurs *20*, S2-8. 10.1188/16.CJON.S1.2-8

De Vleeschouwer, S., and Bergers, G. (2017). Glioblastoma: To Target the Tumor Cell or the Microenvironment? In Glioblastoma, S. De Vleeschouwer, ed. (Brisbane (AU)).

Deaglio, S., Dwyer, K.M., Gao, W., Friedman, D., Usheva, A., Erat, A., Chen, J.F., Enjyoji, K., Linden, J., Oukka, M., *et al.* (2007). Adenosine generation catalyzed by CD39 and CD73 expressed on regulatory T cells mediates immune suppression. J Exp Med *204*, 1257-1265. 10.1084/jem.20062512

Demaison, C., Parsley, K., Brouns, G., Scherr, M., Battmer, K., Kinnon, C., Grez, M., and Thrasher, A.J. (2002). High-level transduction and gene expression in hematopoietic repopulating cells using a human immunodeficiency [correction of imunodeficiency] virus type 1-based lentiviral vector containing an internal spleen focus forming virus promoter. Hum Gene Ther *13*, 803-813. 10.1089/10430340252898984

Demaria, S., Bhardwaj, N., McBride, W.H., and Formenti, S.C. (2005). Combining radiotherapy and immunotherapy: a revived partnership. Int J Radiat Oncol Biol Phys *63*, 655-666. 10.1016/j.ijrobp.2005.06.032

Demaria, S., Coleman, C.N., and Formenti, S.C. (2016). Radiotherapy: Changing the Game in Immunotherapy. Trends Cancer *2*, 286-294. 10.1016/j.trecan.2016.05.002

DeNardo, D.G., Brennan, D.J., Rexhepaj, E., Ruffell, B., Shiao, S.L., Madden, S.F., Gallagher, W.M., Wadhwani, N., Keil, S.D., Junaid, S.A., *et al.* (2011). Leukocyte complexity predicts breast cancer survival and functionally regulates response to chemotherapy. Cancer Discov *1*, 54-67. 10.1158/2159-8274.CD-10-0028

Deng, L., Liang, H., Burnette, B., Beckett, M., Darga, T., Weichselbaum, R.R., and Fu, Y.X. (2014a). Irradiation

and anti-PD-L1 treatment synergistically promote antitumor immunity in mice. J Clin Invest *124*, 687-695. 10.1172/JCI67313

Deng, L., Liang, H., Xu, M., Yang, X., Burnette, B., Arina, A., Li, X.D., Mauceri, H., Beckett, M., Darga, T.*, et al.* (2014b). STING-Dependent Cytosolic DNA Sensing Promotes Radiation-Induced Type I Interferon-Dependent Antitumor Immunity in Immunogenic Tumors. Immunity *41*, 843-852. 10.1016/j.immuni.2014.10.019

Dennis, K.L., Blatner, N.R., Gounari, F., and Khazaie, K. (2013). Current status of interleukin-10 and regulatory T-cells in cancer. Curr Opin Oncol *25*, 637-645. 10.1097/CCO.0000000000000006

Dieterich, L.C., Ikenberg, K., Cetintas, T., Kapaklikaya, K., Hutmacher, C., and Detmar, M. (2017). Tumor-Associated Lymphatic Vessels Upregulate PDL1 to Inhibit T-Cell Activation. Front Immunol *8*, 66. 10.3389/fimmu.2017.00066

Domingues, P., Gonzalez-Tablas, M., Otero, A., Pascual, D., Miranda, D., Ruiz, L., Sousa, P., Ciudad, J., Goncalves, J.M., Lopes, M.C.*, et al.* (2016). Tumor infiltrating immune cells in gliomas and meningiomas. Brain Behav Immun *53*, 1-15. 10.1016/j.bbi.2015.07.019

Dong, H., Strome, S.E., Salomao, D.R., Tamura, H., Hirano, F., Flies, D.B., Roche, P.C., Lu, J., Zhu, G., Tamada, K.*, et al.* (2002). Tumor-associated B7-H1 promotes T-cell apoptosis: a potential mechanism of immune evasion. Nat Med *8*, 793-800. 10.1038/nm730

Du, R., Lu, K.V., Petritsch, C., Liu, P., Ganss, R., Passegue, E., Song, H., Vandenberg, S., Johnson, R.S., Werb, Z.*, et al.* (2008). HIF1alpha induces the recruitment of bone marrow-derived vascular modulatory cells to regulate tumor angiogenesis and invasion. Cancer Cell *13*, 206-220. 10.1016/j.ccr.2008.01.034

Eckert, F., Schilbach, K., Klumpp, L., Bardoscia, L., Sezgin, E.C., Schwab, M., Zips, D., and Huber, S.M. (2018). Potential Role of CXCR4 Targeting in the Context of Radiotherapy and Immunotherapy of Cancer. Front Immunol *9*, 3018. 10.3389/fimmu.2018.03018

Embgenbroich, M., and Burgdorf, S. (2018). Current Concepts of Antigen Cross-Presentation. Front Immunol *9*, 1643. 10.3389/fimmu.2018.01643

Erreni, M., Solinas, G., Brescia, P., Osti, D., Zunino, F., Colombo, P., Destro, A., Roncalli, M., Mantovani, A., Draghi, R.*, et al.* (2010). Human glioblastoma tumours and neural cancer stem cells express the chemokine CX3CL1 and its receptor CX3CR1. Eur J Cancer *46*, 3383-3392. 10.1016/j.ejca.2010.07.022

Falcke, S.E., Ruhle, P.F., Deloch, L., Fietkau, R., Frey, B., and Gaipl, U.S. (2018). Clinically Relevant Radiation Exposure Differentially Impacts Forms of Cell Death in Human Cells of the Innate and Adaptive Immune System. Int J Mol Sci *19*. 10.3390/ijms19113574

Fantuzzi, L., Tagliamonte, M., Gauzzi, M.C., and Lopalco, L. (2019). Dual CCR5/CCR2 targeting: opportunities for the cure of complex disorders. Cell Mol Life Sci *76*, 4869-4886. 10.1007/s00018-019-03255-6

Frischholz, B., Wunderlich, R., Ruhle, P.F., Schorn, C., Rodel, F., Keilholz, L., Fietkau, R., Gaipl, U.S., and Frey, B. (2013). Reduced secretion of the inflammatory cytokine IL-1beta by stimulated peritoneal macrophages of radiosensitive Balb/c mice after exposure to 0.5 or 0.7 Gy of ionizing radiation. Autoimmunity *46*, 323-328. 10.3109/08916934.2012.747522

Fujita, M., Kohanbash, G., Fellows-Mayle, W., Hamilton, R.L., Komohara, Y., Decker, S.A., Ohlfest, J.R., and Okada, H. (2011). COX-2 blockade suppresses gliomagenesis by inhibiting myeloid-derived suppressor cells. Cancer Res *71*, 2664-2674. 10.1158/0008-5472.CAN-10-3055

Fukada, K., Sobao, Y., Tomiyama, H., Oka, S., and Takiguchi, M. (2002). Functional expression of the chemokine receptor CCR5 on virus epitope-specific memory and effector CD8+ T cells. J Immunol *168*, 2225-2232. 10.4049/jimmunol.168.5.2225

Gaber, M.W., Sabek, O.M., Fukatsu, K., Wilcox, H.G., Kiani, M.F., and Merchant, T.E. (2003). Differences in ICAM-1 and TNF-alpha expression between large single fraction and fractionated irradiation in mouse brain. Int J Radiat Biol *79*, 359-366. 10.1080/0955300031000114738

Gadani, S.P., Cronk, J.C., Norris, G.T., and Kipnis, J. (2012). IL-4 in the brain: a cytokine to remember. J Immunol *189*, 4213-4219. 10.4049/jimmunol.1202246

Gallego, O. (2015). Nonsurgical treatment of recurrent glioblastoma. Curr Oncol *22*, e273-281. 10.3747/co.22.2436

Garcia-Diaz, A., Shin, D.S., Moreno, B.H., Saco, J., Escuin-Ordinas, H., Rodriguez, G.A., Zaretsky, J.M., Sun, L., Hugo, W., Wang, X.*, et al.* (2017). Interferon Receptor Signaling Pathways Regulating PD-L1 and PD-L2 Expression. Cell Rep *19*, 1189-1201. 10.1016/j.celrep.2017.04.031

Ghiringhelli, F., Apetoh, L., Tesniere, A., Aymeric, L., Ma, Y., Ortiz, C., Vermaelen, K., Panaretakis, T., Mignot, G., Ullrich, E.*, et al.* (2009). Activation of the NLRP3 inflammasome in dendritic cells induces IL-1beta-dependent adaptive immunity against tumors. Nat Med *15*, 1170-1178. 10.1038/nm.2028

Gielen, P.R., Schulte, B.M., Kers-Rebel, E.D., Verrijp, K., Bossman, S.A., Ter Laan, M., Wesseling, P., and Adema, G.J. (2016). Elevated levels of polymorphonuclear myeloid-derived suppressor cells in patients with glioblastoma highly express S100A8/9 and arginase and suppress T cell function. Neuro Oncol *18*, 1253-1264. 10.1093/neuonc/now034

Gieryng, A., Pszczolkowska, D., Walentynowicz, K.A., Rajan, W.D., and Kaminska, B. (2017). Immune microenvironment of gliomas. Lab Invest *97*, 498-518. 10.1038/labinvest.2017.19

Giordano, F.A., Link, B., Glas, M., Herrlinger, U., Wenz, F., Umansky, V., Brown, J.M., and Herskind, C. (2019). Targeting the Post-Irradiation Tumor Microenvironment in Glioblastoma via Inhibition of CXCL12. Cancers (Basel) *11*. 10.3390/cancers11030272

Glass, R., and Synowitz, M. (2014). CNS macrophages and peripheral myeloid cells in brain tumours. Acta Neuropathol *128*, 347-362. 10.1007/s00401-014-1274-2

Goffart, N., Lombard, A., Lallemand, F., Kroonen, J., Nassen, J., Di Valentin, E., Berendsen, S., Dedobbeleer, M., Willems, E., Robe, P.*, et al.* (2017). CXCL12 mediates glioblastoma resistance to radiotherapy in the subventricular zone. Neuro Oncol *19*, 66-77. 10.1093/neuonc/now136

Gong, J., Le, T.Q., Massarelli, E., Hendifar, A.E., and Tuli, R. (2018). Radiation therapy and PD-1/PD-L1 blockade: the clinical development of an evolving anticancer combination. J Immunother Cancer *6*, 46. 10.1186/s40425-018-0361-7

Grabowski, M.M., Sankey, E.W., Ryan, K.J., Chongsathidkiet, P., Lorrey, S.J., Wilkinson, D.S., and Fecci, P.E. (2021). Immune suppression in gliomas. J Neurooncol *151*, 3-12. 10.1007/s11060-020-03483-y

Grossman, S.A., Ye, X., Lesser, G., Sloan, A., Carraway, H., Desideri, S., Piantadosi, S., and Consortium, N.C. (2011). Immunosuppression in patients with high-grade gliomas treated with radiation and temozolomide. Clin Cancer Res *17*, 5473-5480. 10.1158/1078-0432.CCR-11-0774

Groth, C., Hu, X., Weber, R., Fleming, V., Altevogt, P., Utikal, J., and Umansky, V. (2019). Immunosuppression mediated by myeloid-derived suppressor cells (MDSCs) during tumour progression. Br J Cancer *120*, 16-25. 10.1038/s41416-018-0333-1

Guo, F., Wang, Y., Liu, J., Mok, S.C., Xue, F., and Zhang, W. (2016). CXCL12/CXCR4: a symbiotic bridge linking cancer cells and their stromal neighbors in oncogenic communication networks. Oncogene *35*, 816-826. 10.1038/onc.2015.139

Gupta, A., Probst, H.C., Vuong, V., Landshammer, A., Muth, S., Yagita, H., Schwendener, R., Pruschy, M., Knuth, A., and van den Broek, M. (2012). Radiotherapy promotes tumor-specific effector CD8+ T cells via dendritic cell activation. J Immunol *189*, 558-566. 10.4049/jimmunol.1200563

Gutmann, D.H., McLellan, M.D., Hussain, I., Wallis, J.W., Fulton, L.L., Fulton, R.S., Magrini, V., Demeter, R., Wylie, T., Kandoth, C.*, et al.* (2013). Somatic neurofibromatosis type 1 (NF1) inactivation characterizes NF1-associated pilocytic astrocytoma. Genome Res *23*, 431-439. 10.1101/gr.142604.112

Gzell, C., Back, M., Wheeler, H., Bailey, D., and Foote, M. (2017). Radiotherapy in Glioblastoma: the Past, the Present and the Future. Clin Oncol (R Coll Radiol) *29*, 15-25. 10.1016/j.clon.2016.09.015

Haddad, A.F., Young, J.S., Amara, D., Berger, M.S., Raleigh, D.R., Aghi, M.K., and Butowski, N.A. (2021). Mouse models of glioblastoma for the evaluation of novel therapeutic strategies. Neurooncol Adv *3*, vdab100. 10.1093/noajnl/vdab100

Halama, N., Prüfer, U., Frömming, A., Beyer, D., Eulberg, D., Jungnelius, J.U., and Mangasarian, A. (2019). Clinical outcome and safety in patients with microsatellite-stable, metastatic colorectal or pancreatic cancer treated with the CXCL12 inhibitor NOX-A12 in combination with PD-1 checkpoint inhibitor pembrolizumab. In ACR Annual Meeting (Atlanta, GA).

Halperin, E.C., Brizel, D.M., Honore, G., Sontag, M.R., Griffith, O.W., Bigner, D.D., and Friedman, H.S. (1992). The radiation dose-response relationship in a human glioma xenograft and an evaluation of the influence of glutathione depletion by buthionine sulfoximine. Int J Radiat Oncol Biol Phys *24*, 103-109. 10.1016/0360-3016(92)91028-l

Han, S., Zhang, C., Li, Q., Dong, J., Liu, Y., Huang, Y., Jiang, T., and Wu, A. (2014). Tumour-infiltrating CD4(+) and CD8(+) lymphocytes as predictors of clinical outcome in glioma. Br J Cancer *110*, 2560-2568. 10.1038/bjc.2014.162

Hanif, F., Muzaffar, K., Perveen, K., Malhi, S.M., and Simjee Sh, U. (2017). Glioblastoma Multiforme: A Review of its Epidemiology and Pathogenesis through Clinical Presentation and Treatment. Asian Pac J Cancer Prev *18*, 3-9. 10.22034/APJCP.2017.18.1.3

Hawila, E., Razon, H., Wildbaum, G., Blattner, C., Sapir, Y., Shaked, Y., Umansky, V., and Karin, N. (2017). CCR5 Directs the Mobilization of CD11b(+)Gr1(+)Ly6C(low) Polymorphonuclear Myeloid Cells from the Bone Marrow to the Blood to Support Tumor Development. Cell Rep *21*, 2212-2222. 10.1016/j.celrep.2017.10.104

Hegi, M.E., Diserens, A.C., Gorlia, T., Hamou, M.F., de Tribolet, N., Weller, M., Kros, J.M., Hainfellner, J.A., Mason, W., Mariani, L.*, et al.* (2005). MGMT gene silencing and benefit from temozolomide in glioblastoma. N Engl J Med *352*, 997-1003. 10.1056/NEJMoa043331

Henry, C.J., Ornelles, D.A., Mitchell, L.M., Brzoza-Lewis, K.L., and Hiltbold, E.M. (2008). IL-12 produced by dendritic cells augments CD8+ T cell activation through the production of the chemokines CCL1 and CCL17. J Immunol *181*, 8576-8584. 10.4049/jimmunol.181.12.8576

Herrlinger, U., Aulwurm, S., Strik, H., Weit, S., Naumann, U., and Weller, M. (2004). MIP-1alpha antagonizes the effect of a GM-CSF-enhanced subcutaneous vaccine in a mouse glioma model. J Neurooncol *66*, 147-154. 10.1023/b:neon.0000013497.04322.fc

Heylmann, D., Rodel, F., Kindler, T., and Kaina, B. (2014). Radiation sensitivity of human and murine peripheral blood lymphocytes, stem and progenitor cells. Biochim Biophys Acta *1846*, 121-129. 10.1016/j.bbcan.2014.04.009

Hickey, W.F., Hsu, B.L., and Kimura, H. (1991). T-lymphocyte entry into the central nervous system. J Neurosci Res *28*, 254-260. 10.1002/jnr.490280213

Hoellenriegel, J., Zboralski, D., Maasch, C., Rosin, N.Y., Wierda, W.G., Keating, M.J., Kruschinski, A., and Burger, J.A. (2014). The Spiegelmer NOX-A12, a novel CXCL12 inhibitor, interferes with chronic lymphocytic leukemia cell motility and causes chemosensitization. Blood *123*, 1032-1039. 10.1182/blood-2013-03-493924

Holland, E.C. (2000). Glioblastoma multiforme: the terminator. Proc Natl Acad Sci U S A *97*, 6242-6244. 10.1073/pnas.97.12.6242

Huettner, C., Czub, S., Kerkau, S., Roggendorf, W., and Tonn, J.C. (1997). Interleukin 10 is expressed in human gliomas in vivo and increases glioma cell proliferation and motility in vitro. Anticancer Res *17*, 3217-3224.

Hussain, S.F., Yang, D., Suki, D., Aldape, K., Grimm, E., and Heimberger, A.B. (2006). The role of human glioma-infiltrating microglia/macrophages in mediating antitumor immune responses. Neuro Oncol *8*, 261-279. 10.1215/15228517-2006-008

Iacob, G., and Dinca, E.B. (2009). Current data and strategy in glioblastoma multiforme. J Med Life *2*, 386-393.

Jacob, F., Perez Novo, C., Bachert, C., and Van Crombruggen, K. (2013). Purinergic signaling in inflammatory cells: P2 receptor expression, functional effects, and modulation of inflammatory responses. Purinergic Signal

9, 285-306. 10.1007/s11302-013-9357-4

Jacobs, V.L., Valdes, P.A., Hickey, W.F., and De Leo, J.A. (2011). Current review of in vivo GBM rodent models: emphasis on the CNS-1 tumour model. ASN Neuro *3*, e00063. 10.1042/AN20110014

Jani, A., Shaikh, F., Barton, S., Willis, C., Banerjee, D., Mitchell, J., Hernandez, S.L., Hei, T., Kadenhe-Chiweshe, A., Yamashiro, D.J.*, et al.* (2016). High-Dose, Single-Fraction Irradiation Rapidly Reduces Tumor Vasculature and Perfusion in a Xenograft Model of Neuroblastoma. Int J Radiat Oncol Biol Phys *94*, 1173-1180. 10.1016/j.ijrobp.2015.12.367

Janssens, R., Struyf, S., and Proost, P. (2018). The unique structural and functional features of CXCL12. Cell Mol Immunol *15*, 299-311. 10.1038/cmi.2017.107

Jia, G.Q., Gonzalo, J.A., Lloyd, C., Kremer, L., Lu, L., Martinez, A.C., Wershil, B.K., and Gutierrez-Ramos, J.C. (1996). Distinct expression and function of the novel mouse chemokine monocyte chemotactic protein-5 in lung allergic inflammation. J Exp Med *184*, 1939-1951. 10.1084/jem.184.5.1939

Johnson, D.R., Fogh, S.E., Giannini, C., Kaufmann, T.J., Raghunathan, A., Theodosopoulos, P.V., and Clarke, J.L. (2015). Case-Based Review: newly diagnosed glioblastoma. Neurooncol Pract *2*, 106-121. 10.1093/nop/npv020

Jordan, J.T., Sun, W., Hussain, S.F., DeAngulo, G., Prabhu, S.S., and Heimberger, A.B. (2008). Preferential migration of regulatory T cells mediated by glioma-secreted chemokines can be blocked with chemotherapy. Cancer Immunol Immunother *57*, 123-131. 10.1007/s00262-007-0336-x

Kachikwu, E.L., Iwamoto, K.S., Liao, Y.P., DeMarco, J.J., Agazaryan, N., Economou, J.S., McBride, W.H., and Schaue, D. (2011). Radiation enhances regulatory T cell representation. Int J Radiat Oncol Biol Phys *81*, 1128-1135. 10.1016/j.ijrobp.2010.09.034

Kajioka, E.H., Andres, M.L., Li, J., Mao, X.W., Moyers, M.F., Nelson, G.A., Slater, J.M., and Gridley, D.S. (2000). Acute effects of whole-body proton irradiation on the immune system of the mouse. Radiat Res *153*, 587-594. 10.1667/0033-7587(2000)153[0587:aeowbp]2.0.co;2

Kalnins, A., Thomas, M.N., Andrassy, M., Muller, S., Wagner, A., Pratschke, S., Rentsch, M., Klussmann, S., Kauke, T., Angele, M.K.*, et al.* (2015). Spiegelmer Inhibition of MCP-1/CCR2--Potential as an Adjunct Immunosuppressive Therapy in Transplantation. Scand J Immunol *82*, 102-109. 10.1111/sji.12310

Kast, R.E., Hill, Q.A., Wion, D., Mellstedt, H., Focosi, D., Karpel-Massler, G., Heiland, T., and Halatsch, M.E. (2017). Glioblastoma-synthesized G-CSF and GM-CSF contribute to growth and immunosuppression: Potential therapeutic benefit from dapsone, fenofibrate, and ribavirin. Tumour Biol *39*, 1010428317699797. 10.1177/1010428317699797

Kaur, P., and Asea, A. (2012). Radiation-induced effects and the immune system in cancer. Front Oncol *2*, 191. 10.3389/fonc.2012.00191

Kazanietz, M.G., Durando, M., and Cooke, M. (2019). CXCL13 and Its Receptor CXCR5 in Cancer: Inflammation, Immune Response, and Beyond. Front Endocrinol (Lausanne) *10*, 471. 10.3389/fendo.2019.00471

Kennedy, B.C., Maier, L.M., D'Amico, R., Mandigo, C.E., Fontana, E.J., Waziri, A., Assanah, M.C., Canoll, P., Anderson, R.C., Anderson, D.E.*, et al.* (2009). Dynamics of central and peripheral immunomodulation in a murine glioma model. BMC Immunol *10*, 11. 10.1186/1471-2172-10-11

Khalsa, J.K., Cheng, N., Keegan, J., Chaudry, A., Driver, J., Bi, W.L., Lederer, J., and Shah, K. (2020). Immune phenotyping of diverse syngeneic murine brain tumors identifies immunologically distinct types. Nat Commun *11*, 3912. 10.1038/s41467-020-17704-5

Khasraw, M., Reardon, D.A., Weller, M., and Sampson, J.H. (2020). PD-1 inhibitors: Do they have a future in the treatment of glioblastoma? Clin Cancer Res. 10.1158/1078-0432.CCR-20-1135

Kim, H., Fabien, J., Zheng, Y., Yuan, J., Brindle, J., Sloan, A., Yao, M., Lo, S., Wessels, B., Machtay, M.*, et al.* (2014). Establishing a process of irradiating small animal brain using a CyberKnife and a microCT scanner. Med Phys *41*, 021715. 10.1118/1.4861713

Kim, J.E., Patel, M.A., Mangraviti, A., Kim, E.S., Theodros, D., Velarde, E., Liu, A., Sankey, E.W., Tam, A., Xu, H.*, et al.* (2017). Combination Therapy with Anti-PD-1, Anti-TIM-3, and Focal Radiation Results in Regression of Murine Gliomas. Clin Cancer Res *23*, 124-136. 10.1158/1078-0432.CCR-15-1535

Kioi, M., Vogel, H., Schultz, G., Hoffman, R.M., Harsh, G.R., and Brown, J.M. (2010). Inhibition of vasculogenesis, but not angiogenesis, prevents the recurrence of glioblastoma after irradiation in mice. J Clin Invest *120*, 694-705. 10.1172/JCI40283

Klein, M. (2012). Neurocognitive functioning in adult WHO grade II gliomas: impact of old and new treatment modalities. Neuro Oncol *14 Suppl 4*, iv17-24. 10.1093/neuonc/nos161

Kobayashi, N., Takata, H., Yokota, S., and Takiguchi, M. (2004). Down-regulation of CXCR4 expression on human CD8+ T cells during peripheral differentiation. Eur J Immunol *34*, 3370-3378. 10.1002/eji.200425587

Kondo, T., and Takiguchi, M. (2009). Human memory CCR4+CD8+ T cell subset has the ability to produce multiple cytokines. Int Immunol *21*, 523-532. 10.1093/intimm/dxp019

Korbecki, J., Grochans, S., Gutowska, I., Barczak, K., and Baranowska-Bosiacka, I. (2020). CC Chemokines in a Tumor: A Review of Pro-Cancer and Anti-Cancer Properties of Receptors CCR5, CCR6, CCR7, CCR8, CCR9, and CCR10 Ligands. Int J Mol Sci *21*. 10.3390/ijms21207619

Kuehnemuth, B., Piseddu, I., Wiedemann, G.M., Lauseker, M., Kuhn, C., Hofmann, S., Schmoeckel, E., Endres, S., Mayr, D., Jeschke, U.*, et al.* (2018). CCL1 is a major regulatory T cell attracting factor in human breast cancer. BMC Cancer *18*, 1278. 10.1186/s12885-018-5117-8

Kumai, T., Nagato, T., Kobayashi, H., Komabayashi, Y., Ueda, S., Kishibe, K., Ohkuri, T., Takahara, M., Celis, E., and Harabuchi, Y. (2015). CCL17 and CCL22/CCR4 signaling is a strong candidate for novel targeted therapy against nasal natural killer/T-cell lymphoma. Cancer Immunol Immunother *64*, 697-705. 10.1007/s00262-015-1675-7

Kusmartsev, S., Nefedova, Y., Yoder, D., and Gabrilovich, D.I. (2004). Antigen-specific inhibition of CD8+ T cell

response by immature myeloid cells in cancer is mediated by reactive oxygen species. J Immunol *172*, 989-999. 10.4049/jimmunol.172.2.989

Lacroix, M., Abi-Said, D., Fourney, D.R., Gokaslan, Z.L., Shi, W., DeMonte, F., Lang, F.F., McCutcheon, I.E., Hassenbusch, S.J., Holland, E*., et al.* (2001). A multivariate analysis of 416 patients with glioblastoma multiforme: prognosis, extent of resection, and survival. J Neurosurg *95*, 190-198. 10.3171/jns.2001.95.2.0190

Ladomersky, E., Scholtens, D.M., Kocherginsky, M., Hibler, E.A., Bartom, E.T., Otto-Meyer, S., Zhai, L., Lauing, K.L., Choi, J., Sosman, J.A*., et al.* (2019). The Coincidence Between Increasing Age, Immunosuppression, and the Incidence of Patients With Glioblastoma. Front Pharmacol *10*, 200. 10.3389/fphar.2019.00200

Laplagne, C., Domagala, M., Le Naour, A., Quemerais, C., Hamel, D., Fournie, J.J., Couderc, B., Bousquet, C., Ferrand, A., and Poupot, M. (2019). Latest Advances in Targeting the Tumor Microenvironment for Tumor Suppression. Int J Mol Sci *20*. 10.3390/ijms20194719

Lapointe, S., Perry, A., and Butowski, N.A. (2018). Primary brain tumours in adults. Lancet *392*, 432-446. 10.1016/S0140-6736(18)30990-5

Laurent, P.A., Kownacka, A., Boidot, R., Richard, C., Limagne, E., Morgand, V., Froidurot, L., Bonin, C., Aubignac, L., Ghiringhelli, F*., et al.* (2020). In-vivo and in-vitro impact of high-dose rate radiotherapy using flattening-filter-free beams on the anti-tumor immune response. Clinical and Translational Radiation Oncology *24*, 116-122. 10.1016/j.ctro.2020.07.004

Lawrie, T.A., Gillespie, D., Dowswell, T., Evans, J., Erridge, S., Vale, L., Kernohan, A., and Grant, R. (2019). Long-term neurocognitive and other side effects of radiotherapy, with or without chemotherapy, for glioma. Cochrane Database Syst Rev *8*, CD013047. 10.1002/14651858.CD013047.pub2

Lee-Chang, C., Rashidi, A., Miska, J., Zhang, P., Pituch, K.C., Hou, D., Xiao, T., Fischietti, M., Kang, S.J., Appin, C.L*., et al.* (2019). Myeloid-Derived Suppressive Cells Promote B cell-Mediated Immunosuppression via Transfer of PD-L1 in Glioblastoma. Cancer Immunol Res *7*, 1928-1943. 10.1158/2326-6066.CIR-19-0240

Lee, Y., Auh, S.L., Wang, Y., Burnette, B., Wang, Y., Meng, Y., Beckett, M., Sharma, R., Chin, R., Tu, T*., et al.* (2009). Therapeutic effects of ablative radiation on local tumor require CD8+ T cells: changing strategies for cancer treatment. Blood *114*, 589-595. 10.1182/blood-2009-02-206870

Lepore, F., D'Alessandro, G., Antonangeli, F., Santoro, A., Esposito, V., Limatola, C., and Trettel, F. (2018). CXCL16/CXCR6 Axis Drives Microglia/Macrophages Phenotype in Physiological Conditions and Plays a Crucial Role in Glioma. Front Immunol *9*, 2750. 10.3389/fimmu.2018.02750

Leroy, H.A., Vermandel, M., Lejeune, J.P., Mordon, S., and Reyns, N. (2015). Fluorescence guided resection and glioblastoma in 2015: A review. Lasers Surg Med *47*, 441-451. 10.1002/lsm.22359

Li, B.H., Garstka, M.A., and Li, Z.F. (2020). Chemokines and their receptors promoting the recruitment of myeloid-derived suppressor cells into the tumor. Mol Immunol *117*, 201-215. 10.1016/j.molimm.2019.11.014

Li, J., Wang, L., Chen, X., Li, L., Li, Y., Ping, Y., Huang, L., Yue, D., Zhang, Z., Wang, F*., et al.* (2017). CD39/CD73 upregulation on myeloid-derived suppressor cells via TGF-beta-mTOR-HIF-1 signaling in patients with non-small cell lung cancer. Oncoimmunology *6*, e1320011. 10.1080/2162402X.2017.1320011

Liang, P., Chai, Y., Zhao, H., and Wang, G. (2020). Predictive Analyses of Prognostic-Related Immune Genes and Immune Infiltrates for Glioblastoma. Diagnostics (Basel) *10*. 10.3390/diagnostics10030177

Liu, C., Luo, D., Streit, W.J., and Harrison, J.K. (2008). CX3CL1 and CX3CR1 in the GL261 murine model of glioma: CX3CR1 deficiency does not impact tumor growth or infiltration of microglia and lymphocytes. J Neuroimmunol *198*, 98-105. 10.1016/j.jneuroim.2008.04.016

Liu, M., Guo, S., and Stiles, J.K. (2011). The emerging role of CXCL10 in cancer (Review). Oncol Lett *2*, 583-589. 10.3892/ol.2011.300

Liu, S.C., Alomran, R., Chernikova, S.B., Lartey, F., Stafford, J., Jang, T., Merchant, M., Zboralski, D., Zollner, S., Kruschinski, A*., et al.* (2014). Blockade of SDF-1 after irradiation inhibits tumor recurrences of autochthonous brain tumors in rats. Neuro Oncol *16*, 21-28. 10.1093/neuonc/not149

Liu, Y., Cai, Y., Liu, L., Wu, Y., and Xiong, X. (2018). Crucial biological functions of CCL7 in cancer. PeerJ *6*, e4928. 10.7717/peerj.4928

Louis, D.N., Ohgaki, H., Wiestler, O.D., Cavenee, W.K., Burger, P.C., Jouvet, A., Scheithauer, B.W., and Kleihues, P. (2007). The 2007 WHO classification of tumours of the central nervous system. Acta Neuropathol *114*, 97-109. 10.1007/s00401-007-0243-4

Louis, D.N., Perry, A., Reifenberger, G., von Deimling, A., Figarella-Branger, D., Cavenee, W.K., Ohgaki, H., Wiestler, O.D., Kleihues, P., and Ellison, D.W. (2016). The 2016 World Health Organization Classification of Tumors of the Central Nervous System: a summary. Acta Neuropathol *131*, 803-820. 10.1007/s00401-016-1545-1

Louis, D.N., Perry, A., Wesseling, P., Brat, D.J., Cree, I.A., Figarella-Branger, D., Hawkins, C., Ng, H.K., Pfister, S.M., Reifenberger, G*., et al.* (2021). The 2021 WHO Classification of Tumors of the Central Nervous System: a summary. Neuro Oncol *23*, 1231-1251. 10.1093/neuonc/noab106

Louveau, A., Smirnov, I., Keyes, T.J., Eccles, J.D., Rouhani, S.J., Peske, J.D., Derecki, N.C., Castle, D., Mandell, J.W., Lee, K.S*., et al.* (2015). Structural and functional features of central nervous system lymphatic vessels. Nature *523*, 337-341. 10.1038/nature14432

Lu, C., Redd, P.S., Lee, J.R., Savage, N., and Liu, K. (2016). The expression profiles and regulation of PD-L1 in tumor-induced myeloid-derived suppressor cells. Oncoimmunology *5*, e1247135. 10.1080/2162402X.2016.1247135

Lugade, A.A., Moran, J.P., Gerber, S.A., Rose, R.C., Frelinger, J.G., and Lord, E.M. (2005). Local radiation therapy of B16 melanoma tumors increases the generation of tumor antigen-specific effector cells that traffic to the tumor. J Immunol *174*, 7516-7523. 10.4049/jimmunol.174.12.7516

Lugade, A.A., Sorensen, E.W., Gerber, S.A., Moran, J.P., Frelinger, J.G., and Lord, E.M. (2008). Radiation-

induced IFN-gamma production within the tumor microenvironment influences antitumor immunity. J Immunol *180*, 3132-3139. 10.4049/jimmunol.180.5.3132

Maes, W., and Van Gool, S.W. (2011). Experimental immunotherapy for malignant glioma: lessons from two decades of research in the GL261 model. Cancer Immunol Immunother *60*, 153-160. 10.1007/s00262-010-0946-6

Mantovani, A., Gray, P.A., Van Damme, J., and Sozzani, S. (2000). Macrophage-derived chemokine (MDC). J Leukoc Biol *68*, 400-404.

Markowitz, J., Wang, J., Vangundy, Z., You, J., Yildiz, V., Yu, L., Foote, I.P., Branson, O.E., Stiff, A.R., Brooks, T.R*., et al.* (2017). Nitric oxide mediated inhibition of antigen presentation from DCs to CD4(+) T cells in cancer and measurement of STAT1 nitration. Sci Rep *7*, 15424. 10.1038/s41598-017-14970-0

Mathios, D., Kim, J.E., Mangraviti, A., Phallen, J., Park, C.K., Jackson, C.M., Garzon-Muvdi, T., Kim, E., Theodros, D., Polanczyk, M*., et al.* (2016). Anti-PD-1 antitumor immunity is enhanced by local and abrogated by systemic chemotherapy in GBM. Sci Transl Med *8*, 370ra180. 10.1126/scitranslmed.aag2942

Mathy, N.L., Scheuer, W., Lanzendorfer, M., Honold, K., Ambrosius, D., Norley, S., and Kurth, R. (2000). Interleukin-16 stimulates the expression and production of pro-inflammatory cytokines by human monocytes. Immunology *100*, 63-69. 10.1046/j.1365-2567.2000.00997.x

McBride, W.H., Chiang, C.S., Olson, J.L., Wang, C.C., Hong, J.H., Pajonk, F., Dougherty, G.J., Iwamoto, K.S., Pervan, M., and Liao, Y.P. (2004). A sense of danger from radiation. Radiat Res *162*, 1-19. 10.1667/rr3196

Medikonda, R., Dunn, G., Rahman, M., Fecci, P., and Lim, M. (2020). A review of glioblastoma immunotherapy. J Neurooncol. 10.1007/s11060-020-03448-1

Messmer, D., Yang, H., Telusma, G., Knoll, F., Li, J., Messmer, B., Tracey, K.J., and Chiorazzi, N. (2004). High mobility group box protein 1: an endogenous signal for dendritic cell maturation and Th1 polarization. J Immunol *173*, 307-313. 10.4049/jimmunol.173.1.307

Mestas, J., and Hughes, C.C. (2004). Of mice and not men: differences between mouse and human immunology. J Immunol *172*, 2731-2738. 10.4049/jimmunol.172.5.2731

Mijatovic, S., Savic-Radojevic, A., Pljesa-Ercegovac, M., Simic, T., Nicoletti, F., and Maksimovic-Ivanic, D. (2020). The Double-Faced Role of Nitric Oxide and Reactive Oxygen Species in Solid Tumors. Antioxidants (Basel) *9*. 10.3390/antiox9050374

Miller, K.D., Ostrom, Q.T., Kruchko, C., Patil, N., Tihan, T., Cioffi, G., Fuchs, H.E., Waite, K.A., Jemal, A., Siegel, R.L*., et al.* (2021). Brain and other central nervous system tumor statistics, 2021. CA Cancer J Clin *71*, 381-406. 10.3322/caac.21693

Minniti, G., Lombardi, G., and Paolini, S. (2019). Glioblastoma in Elderly Patients: Current Management and Future Perspectives. Cancers (Basel) *11*. 10.3390/cancers11030336

Mita, Y., Kimura, M.Y., Hayashizaki, K., Koyama-Nasu, R., Ito, T., Motohashi, S., Okamoto, Y., and Nakayama, T. (2018). Crucial role of CD69 in anti-tumor immunity through regulating the exhaustion of tumor-infiltrating T cells. Int Immunol *30*, 559-567. 10.1093/intimm/dxy050

Mohme, M., and Neidert, M.C. (2020). Tumor-Specific T Cell Activation in Malignant Brain Tumors. Front Immunol *11*, 205. 10.3389/fimmu.2020.00205

Monjazeb, A.M., Schalper, K.A., Villarroel-Espindola, F., Nguyen, A., Shiao, S.L., and Young, K. (2020). Effects of Radiation on the Tumor Microenvironment. Semin Radiat Oncol *30*, 145-157. 10.1016/j.semradonc.2019.12.004

Moore, K.W., de Waal Malefyt, R., Coffman, R.L., and O'Garra, A. (2001). Interleukin-10 and the interleukin-10 receptor. Annu Rev Immunol *19*, 683-765. 10.1146/annurev.immunol.19.1.683

Morantz, R.A., Wood, G.W., Foster, M., Clark, M., and Gollahon, K. (1979). Macrophages in experimental and human brain tumors. Part 2: studies of the macrophage content of human brain tumors. J Neurosurg *50*, 305-311. 10.3171/jns.1979.50.3.0305

Morello, S., Pinto, A., Blandizzi, C., and Antonioli, L. (2016). Myeloid cells in the tumor microenvironment: Role of adenosine. Oncoimmunology *5*, e1108515. 10.1080/2162402X.2015.1108515

Nagasawa, T. (2014). CXC chemokine ligand 12 (CXCL12) and its receptor CXCR4. J Mol Med (Berl) *92*, 433-439. 10.1007/s00109-014-1123-8

Nakasone, E.S., Askautrud, H.A., Kees, T., Park, J.H., Plaks, V., Ewald, A.J., Fein, M., Rasch, M.G., Tan, Y.X., Qiu, J*., et al.* (2012). Imaging tumor-stroma interactions during chemotherapy reveals contributions of the microenvironment to resistance. Cancer Cell *21*, 488-503. 10.1016/j.ccr.2012.02.017

Nansen, A., Marker, O., Bartholdy, C., and Thomsen, A.R. (2000). CCR2+ and CCR5+ CD8+ T cells increase during viral infection and migrate to sites of infection. Eur J Immunol *30*, 1797-1806. 10.1002/1521-4141(200007)30:7<1797::AID-IMMU1797>3.0.CO;2-B

National Center for Biotechnology Information (2020). PubChem Database. Plerixafor, CID=65015.

NCT02649582. Adjuvant Dendritic Cell-immunotherapy Plus Temozolomide in Glioblastoma Patients, University Hospital Antwerp, ed. (https://ClinicalTrials.gov/show/NCT02649582).

NCT03168139. Olaptesed (NOX-A12) Alone and in Combination With Pembrolizumab in Colorectal and Pancreatic Cancer, TME Pharma AG, Dohme LLC, and Merck Sharp, eds. (https://ClinicalTrials.gov/show/NCT03168139).

NCT03347097. Adoptive Cell Therapy of Autologous TIL and PD1-TIL Cells for Patients With Glioblastoma Multiforme, Huashan Hospital, and Shanghai Cell Therapy Research Institute, eds. (https://ClinicalTrials.gov/show/NCT03347097).

NCT03395587. Efficiency of Vaccination With Lysate-loaded Dendritic Cells in Patients With Newly Diagnosed Glioblastoma, Heinrich-Heine University Duesseldorf, and German Federal Ministry of Education Research, eds. (https://ClinicalTrials.gov/show/NCT03395587).

NCT03743662. Nivolumab With Radiation Therapy and Bevacizumab for Recurrent MGMT Methylated

Glioblastoma, Memorial Sloan Kettering Cancer Center, ed. (https://ClinicalTrials.gov/show/NCT03743662).

NCT03961971. Trial of Anti-Tim-3 in Combination With Anti-PD-1 and SRS in Recurrent GBM, S. Kimmel, and Novartis Pharmaceuticals, eds. (https://ClinicalTrials.gov/show/NCT03961971).

NCT04013672. Study of Pembrolizumab Plus SurVaxM for Glioblastoma at First Recurrence, D. Peereboom, ed. (https://ClinicalTrials.gov/show/NCT04013672).

NCT04047706. Nivolumab, BMS-986205, and Radiation Therapy With or Without Temozolomide in Treating Patients With Newly Diagnosed Glioblastoma, Northwestern University, and National Cancer Institute, eds. (https://ClinicalTrials.gov/show/NCT04047706).

NCT04573192. A Study to Evaluate Safety and Efficacy of L19TNF Plus Lomustine in Patients With Glioblastoma at First Progression, Philogen S.p.A., ed. (https://ClinicalTrials.gov/show/NCT04573192).

NCT04817254. Association of Peripheral Blood Immunologic Response to Therapeutic Response to Adjuvant Treatment With Immune Checkpoint Inhibition (ICI) in Patients With Newly Diagnosed Glioblastoma or Gliosarcoma, National Cancer Institute, and National Institutes of Health Clinical Center, eds. (https://ClinicalTrials.gov/show/NCT04817254).

NCT05131711. Combination of Stereotactic Radiosurgery and Enhanced Immunotherapy for Recurrent Glioblastomas(inSituVac2)(CSREIG), Beijing Tiantan Hospital, ed. (https://ClinicalTrials.gov/show/NCT05131711).

Nduom, E.K., Weller, M., and Heimberger, A.B. (2015). Immunosuppressive mechanisms in glioblastoma. Neuro Oncol *17 Suppl 7*, vii9-vii14. 10.1093/neuonc/nov151

Noffsinger, B., Witter, A., Sheybani, N., Xiao, A., Manigat, L., Zhong, Q., Taori, S., Harris, T., Bullock, T., Price, R.*, et al.* (2021). Technical choices significantly alter the adaptive immune response against immunocompetent murine gliomas in a model-dependent manner. J Neurooncol *154*, 145-157. 10.1007/s11060-021-03822-7

Noman, M.Z., Desantis, G., Janji, B., Hasmim, M., Karray, S., Dessen, P., Bronte, V., and Chouaib, S. (2014). PD-L1 is a novel direct target of HIF-1alpha, and its blockade under hypoxia enhanced MDSC-mediated T cell activation. J Exp Med *211*, 781-790. 10.1084/jem.20131916

Obermajer, N., Muthuswamy, R., Odunsi, K., Edwards, R.P., and Kalinski, P. (2011). PGE(2)-induced CXCL12 production and CXCR4 expression controls the accumulation of human MDSCs in ovarian cancer environment. Cancer Res *71*, 7463-7470. 10.1158/0008-5472.CAN-11-2449

Oberthur, D., Achenbach, J., Gabdulkhakov, A., Buchner, K., Maasch, C., Falke, S., Rehders, D., Klussmann, S., and Betzel, C. (2015). Crystal structure of a mirror-image L-RNA aptamer (Spiegelmer) in complex with the natural L-protein target CCL2. Nat Commun *6*, 6923. 10.1038/ncomms7923

Oh, T., Fakurnejad, S., Sayegh, E.T., Clark, A.J., Ivan, M.E., Sun, M.Z., Safaee, M., Bloch, O., James, C.D., and Parsa, A.T. (2014). Immunocompetent murine models for the study of glioblastoma immunotherapy. J Transl Med *12*, 107. 10.1186/1479-5876-12-107

Ohl, K., and Tenbrock, K. (2018). Reactive Oxygen Species as Regulators of MDSC-Mediated Immune Suppression. Front Immunol *9*, 2499. 10.3389/fimmu.2018.02499

Olson, J.J., Fadul, C.E., Brat, D.J., Mukundan, S., and Ryken, T.C. (2009). Management of newly diagnosed glioblastoma: guidelines development, value and application. J Neurooncol *93*, 1-23. 10.1007/s11060-009-9838-z

Omuro, A., and DeAngelis, L.M. (2013). Glioblastoma and other malignant gliomas: a clinical review. JAMA *310*, 1842-1850. 10.1001/jama.2013.280319

Ondondo, B., Jones, E., Godkin, A., and Gallimore, A. (2013). Home sweet home: the tumor microenvironment as a haven for regulatory T cells. Front Immunol *4*, 197. 10.3389/fimmu.2013.00197

Orrego, E., Castaneda, C.A., Castillo, M., Bernabe, L.A., Casavilca, S., Chakravarti, A., Meng, W., Garcia-Corrochano, P., Villa-Robles, M.R., Zevallos, R.*, et al.* (2018). Distribution of tumor-infiltrating immune cells in glioblastoma. CNS Oncol *7*, CNS21. 10.2217/cns-2017-0037

Orringer, D., Lau, D., Khatri, S., Zamora-Berridi, G.J., Zhang, K., Wu, C., Chaudhary, N., and Sagher, O. (2012). Extent of resection in patients with glioblastoma: limiting factors, perception of resectability, and effect on survival. J Neurosurg *117*, 851-859. 10.3171/2012.8.JNS12234

Ostrand-Rosenberg, S., Horn, L.A., and Haile, S.T. (2014). The programmed death-1 immune-suppressive pathway: barrier to antitumor immunity. J Immunol *193*, 3835-3841. 10.4049/jimmunol.1401572

Pan, P.Y., Ma, G., Weber, K.J., Ozao-Choy, J., Wang, G., Yin, B., Divino, C.M., and Chen, S.H. (2010). Immune stimulatory receptor CD40 is required for T-cell suppression and T regulatory cell activation mediated by myeloid-derived suppressor cells in cancer. Cancer Res *70*, 99-108. 10.1158/0008-5472.CAN-09-1882

Park, H.J., Griffin, R.J., Hui, S., Levitt, S.H., and Song, C.W. (2012). Radiation-induced vascular damage in tumors: implications of vascular damage in ablative hypofractionated radiotherapy (SBRT and SRS). Radiat Res *177*, 311-327. 10.1667/rr2773.1

Park, J.K., Hodges, T., Arko, L., Shen, M., Dello Iacono, D., McNabb, A., Olsen Bailey, N., Kreisl, T.N., Iwamoto, F.M., Sul, J.*, et al.* (2010). Scale to predict survival after surgery for recurrent glioblastoma multiforme. J Clin Oncol *28*, 3838-3843. 10.1200/JCO.2010.30.0582

Patel, M.A., and Pardoll, D.M. (2015). Concepts of immunotherapy for glioma. J Neurooncol *123*, 323-330. 10.1007/s11060-015-1810-5

Perez-Torres, C.J., Engelbach, J.A., Cates, J., Thotala, D., Yuan, L., Schmidt, R.E., Rich, K.M., Drzymala, R.E., Ackerman, J.J., and Garbow, J.R. (2014). Toward distinguishing recurrent tumor from radiation necrosis: DWI and MTC in a Gamma Knife--irradiated mouse glioma model. Int J Radiat Oncol Biol Phys *90*, 446-453. 10.1016/j.ijrobp.2014.06.015

Perng, P., and Lim, M. (2015). Immunosuppressive Mechanisms of Malignant Gliomas: Parallels at Non-CNS Sites. Front Oncol *5*, 153. 10.3389/fonc.2015.00153

Petkovic, V., Moghini, C., Paoletti, S., Uguccioni, M., and Gerber, B. (2004). I-TAC/CXCL11 is a natural antagonist for CCR5. J Leukoc Biol *76*, 701-708. 10.1189/jlb.1103570

Petrecca, K., Guiot, M.C., Panet-Raymond, V., and Souhami, L. (2013). Failure pattern following complete resection plus radiotherapy and temozolomide is at the resection margin in patients with glioblastoma. J Neurooncol *111*, 19-23. 10.1007/s11060-012-0983-4

Petrelli, A., Mijnheer, G., Hoytema van Konijnenburg, D.P., van der Wal, M.M., Giovannone, B., Mocholi, E., Vazirpanah, N., Broen, J.C., Hijnen, D., Oldenburg, B., *et al.* (2018). PD-1+CD8+ T cells are clonally expanding effectors in human chronic inflammation. J Clin Invest *128*, 4669-4681. 10.1172/JCI96107

Phillips, H.S., Kharbanda, S., Chen, R., Forrest, W.F., Soriano, R.H., Wu, T.D., Misra, A., Nigro, J.M., Colman, H., Soroceanu, L., *et al.* (2006). Molecular subclasses of high-grade glioma predict prognosis, delineate a pattern of disease progression, and resemble stages in neurogenesis. Cancer Cell *9*, 157-173. 10.1016/j.ccr.2006.02.019

Platten, M., Kretz, A., Naumann, U., Aulwurm, S., Egashira, K., Isenmann, S., and Weller, M. (2003). Monocyte chemoattractant protein-1 increases microglial infiltration and aggressiveness of gliomas. Ann Neurol *54*, 388-392. 10.1002/ana.10679

Portella, L., and Scala, S. (2019). Ionizing radiation effects on the tumor microenvironment. Semin Oncol *46*, 254-260. 10.1053/j.seminoncol.2019.07.003

Qu, Y., Jin, S., Zhang, A., Zhang, B., Shi, X., Wang, J., and Zhao, Y. (2010). Gamma-ray resistance of regulatory CD4+CD25+Foxp3+ T cells in mice. Radiat Res *173*, 148-157. 10.1667/RR0978.1

Quinn, K.E., Mackie, D.I., and Caron, K.M. (2018). Emerging roles of atypical chemokine receptor 3 (ACKR3) in normal development and physiology. Cytokine *109*, 17-23. 10.1016/j.cyto.2018.02.024

Raber, P.L., Thevenot, P., Sierra, R., Wyczechowska, D., Halle, D., Ramirez, M.E., Ochoa, A.C., Fletcher, M., Velasco, C., Wilk, A., *et al.* (2014). Subpopulations of myeloid-derived suppressor cells impair T cell responses through independent nitric oxide-related pathways. Int J Cancer *134*, 2853-2864. 10.1002/ijc.28622

Rancilio, N.J., Dahl, S., Athanasiadi, I., and Perez-Torres, C.J. (2017). Design, construction, and in vivo feasibility of a positioning device for irradiation of mice brains using a clinical linear accelerator and intensity modulated radiation therapy. Int J Radiat Biol *93*, 1321-1326. 10.1080/09553002.2017.1387305

Raychaudhuri, B., Rayman, P., Huang, P., Grabowski, M., Hambardzumyan, D., Finke, J.H., and Vogelbaum, M.A. (2015). Myeloid derived suppressor cell infiltration of murine and human gliomas is associated with reduction of tumor infiltrating lymphocytes. J Neurooncol *122*, 293-301. 10.1007/s11060-015-1720-6

Reifenberger, G., Hentschel, B., Felsberg, J., Schackert, G., Simon, M., Schnell, O., Westphal, M., Wick, W., Pietsch, T., Loeffler, M., *et al.* (2012). Predictive impact of MGMT promoter methylation in glioblastoma of the elderly. Int J Cancer *131*, 1342-1350. 10.1002/ijc.27385

Rock, K., McArdle, O., Forde, P., Dunne, M., Fitzpatrick, D., O'Neill, B., and Faul, C. (2012). A clinical review of treatment outcomes in glioblastoma multiforme--the validation in a non-trial population of the results of a randomised Phase III clinical trial: has a more radical approach improved survival? Br J Radiol *85*, e729-733. 10.1259/bjr/83796755

Rovere-Querini, P., Capobianco, A., Scaffidi, P., Valentinis, B., Catalanotti, F., Giazzon, M., Dumitriu, I.E., Muller, S., Iannacone, M., Traversari, C., *et al.* (2004). HMGB1 is an endogenous immune adjuvant released by necrotic cells. EMBO Rep *5*, 825-830. 10.1038/sj.embor.7400205

Ryken, T.C., Frankel, B., Julien, T., and Olson, J.J. (2008). Surgical management of newly diagnosed glioblastoma in adults: role of cytoreductive surgery. J Neurooncol *89*, 271-286. 10.1007/s11060-008-9614-5

Sanchez-Martin, L., Sanchez-Mateos, P., and Cabanas, C. (2013). CXCR7 impact on CXCL12 biology and disease. Trends Mol Med *19*, 12-22. 10.1016/j.molmed.2012.10.004

Sanchez-Paulete, A.R., Teijeira, A., Cueto, F.J., Garasa, S., Perez-Gracia, J.L., Sanchez-Arraez, A., Sancho, D., and Melero, I. (2017). Antigen cross-presentation and T-cell cross-priming in cancer immunology and immunotherapy. Ann Oncol *28*, xii44-xii55. 10.1093/annonc/mdx237

Sanchez, V.E., Lynes, J.P., Walbridge, S., Wang, X., Edwards, N.A., Nwankwo, A.K., Sur, H.P., Dominah, G.A., Obungu, A., Adamstein, N., *et al.* (2020). GL261 luciferase-expressing cells elicit an anti-tumor immune response: an evaluation of murine glioma models. Sci Rep *10*, 11003. 10.1038/s41598-020-67411-w

Sato, H., Okonogi, N., and Nakano, T. (2020). Rationale of combination of anti-PD-1/PD-L1 antibody therapy and radiotherapy for cancer treatment. Int J Clin Oncol *25*, 801-809. 10.1007/s10147-020-01666-1

Scaffidi, P., Misteli, T., and Bianchi, M.E. (2002). Release of chromatin protein HMGB1 by necrotic cells triggers inflammation. Nature *418*, 191-195. 10.1038/nature00858

Schaue, D., and McBride, W.H. (2012). T lymphocytes and normal tissue responses to radiation. Front Oncol *2*, 119. 10.3389/fonc.2012.00119

Scheller, J., Chalaris, A., Schmidt-Arras, D., and Rose-John, S. (2011). The pro- and anti-inflammatory properties of the cytokine interleukin-6. Biochim Biophys Acta *1813*, 878-888. 10.1016/j.bbamcr.2011.01.034

Sciume, G., Soriani, A., Piccoli, M., Frati, L., Santoni, A., and Bernardini, G. (2010). CX3CR1/CX3CL1 axis negatively controls glioma cell invasion and is modulated by transforming growth factor-beta1. Neuro Oncol *12*, 701-710. 10.1093/neuonc/nop076

Seo, Y.S., Ko, I.O., Park, H., Jeong, Y.J., Park, J.A., Kim, K.S., Park, M.J., and Lee, H.J. (2019). Radiation-Induced Changes in Tumor Vessels and Microenvironment Contribute to Therapeutic Resistance in Glioblastoma. Front Oncol *9*, 1259. 10.3389/fonc.2019.01259

Simmons, G.W., Pong, W.W., Emnett, R.J., White, C.R., Gianino, S.M., Rodriguez, F.J., and Gutmann, D.H. (2011). Neurofibromatosis-1 heterozygosity increases microglia in a spatially and temporally restricted pattern relevant to mouse optic glioma formation and growth. J Neuropathol Exp Neurol *70*, 51-62. 10.1097/NEN.0b013e3182032d37

Smolders, J., Heutinck, K.M., Fransen, N.L., Remmerswaal, E.B.M., Hombrink, P., Ten Berge, I.J.M., van Lier, R.A.W., Huitinga, I., and Hamann, J. (2018). Tissue-resident memory T cells populate the human brain. Nat Commun *9*, 4593.   10.1038/s41467-018-07053-9

Sousa, J.F., Serafim, R.B., Freitas, L.M., Fontana, C.R., and Valente, V. (2019). DNA repair genes in astrocytoma tumorigenesis, progression and therapy resistance. Genet Mol Biol *43*, e20190066.   10.1590/1678-4685-GMB-2019-0066

Speiser, D.E., Utzschneider, D.T., Oberle, S.G., Munz, C., Romero, P., and Zehn, D. (2014). T cell differentiation in chronic infection and cancer: functional adaptation or exhaustion? Nat Rev Immunol *14*, 768-774.   10.1038/nri3740

Steenken, C., Fleckenstein, J., Kegel, S., Jahnke, L., Simeonova, A., Hartmann, L., Kubler, J., Veldwijk, M.R., Wenz, F., Herskind, C*., et al.* (2015). Impact of flattening-filter-free radiation on the clonogenic survival of astrocytic cell lines. Strahlenther Onkol *191*, 590-596.   10.1007/s00066-015-0823-5

Stessin, A.M., Clausi, M.G., Zhao, Z., Lin, H., Hou, W., Jiang, Z., Duong, T.Q., Tsirka, S.E., and Ryu, S. (2020). Repolarized macrophages, induced by intermediate stereotactic dose radiotherapy and immune checkpoint blockade, contribute to long-term survival in glioma-bearing mice. J Neurooncol *147*, 547-555.   10.1007/s11060-020-03459-y

Stummer, W., Pichlmeier, U., Meinel, T., Wiestler, O.D., Zanella, F., Reulen, H.J., and Group, A.L.-G.S. (2006). Fluorescence-guided surgery with 5-aminolevulinic acid for resection of malignant glioma: a randomised controlled multicentre phase III trial. Lancet Oncol *7*, 392-401.   10.1016/S1470-2045(06)70665-9

Stummer, W., van den Bent, M.J., and Westphal, M. (2011). Cytoreductive surgery of glioblastoma as the key to successful adjuvant therapies: new arguments in an old discussion. Acta Neurochir (Wien) *153*, 1211-1218.   10.1007/s00701-011-1001-x

Stupp, R., Gander, M., Leyvraz, S., and Newlands, E. (2001). Current and future developments in the use of temozolomide for the treatment of brain tumours. Lancet Oncology *2*, 552-560.   Doi 10.1016/S1470-2045(01)00489-2

Stupp, R., Hegi, M.E., Mason, W.P., van den Bent, M.J., Taphoorn, M.J., Janzer, R.C., Ludwin, S.K., Allgeier, A., Fisher, B., Belanger, K*., et al.* (2009). Effects of radiotherapy with concomitant and adjuvant temozolomide versus radiotherapy alone on survival in glioblastoma in a randomised phase III study: 5-year analysis of the EORTC-NCIC trial. Lancet Oncol *10*, 459-466.   10.1016/S1470-2045(09)70025-7

Stupp, R., Mason, W.P., van den Bent, M.J., Weller, M., Fisher, B., Taphoorn, M.J., Belanger, K., Brandes, A.A., Marosi, C., Bogdahn, U*., et al.* (2005). Radiotherapy plus concomitant and adjuvant temozolomide for glioblastoma. N Engl J Med *352*, 987-996.   10.1056/NEJMoa043330

Suarez-Carmona, M., Williams, A., Schreiber, J., Hohmann, N., Pruefer, U., Krauss, J., Jager, D., Fromming, A., Beyer, D., Eulberg, D*., et al.* (2021). Combined inhibition of CXCL12 and PD-1 in MSS colorectal and pancreatic cancer: modulation of the microenvironment and clinical effects. J Immunother Cancer *9*.   10.1136/jitc-2021-002505

Sun, W., Depping, R., and Jelkmann, W. (2014). Interleukin-1beta promotes hypoxia-induced apoptosis of glioblastoma cells by inhibiting hypoxia-inducible factor-1 mediated adrenomedullin production. Cell Death Dis *5*, e1020.   10.1038/cddis.2013.562

Sung, H., Ferlay, J., Siegel, R.L., Laversanne, M., Soerjomataram, I., Jemal, A., and Bray, F. (2021). Global Cancer Statistics 2020: GLOBOCAN Estimates of Incidence and Mortality Worldwide for 36 Cancers in 185 Countries. CA Cancer J Clin *71*, 209-249.   10.3322/caac.21660

Szatmari, T., Lumniczky, K., Desaknai, S., Trajcevski, S., Hidvegi, E.J., Hamada, H., and Safrany, G. (2006). Detailed characterization of the mouse glioma 261 tumor model for experimental glioblastoma therapy. Cancer Sci *97*, 546-553.   10.1111/j.1349-7006.2006.00208.x

Szulzewsky, F., Pelz, A., Feng, X., Synowitz, M., Markovic, D., Langmann, T., Holtman, I.R., Wang, X., Eggen, B.J., Boddeke, H.W*., et al.* (2015). Glioma-associated microglia/macrophages display an expression profile different from M1 and M2 polarization and highly express Gpnmb and Spp1. PLoS One *10*, e0116644.   10.1371/journal.pone.0116644

Tabata, S., Kadowaki, N., Kitawaki, T., Shimaoka, T., Yonehara, S., Yoshie, O., and Uchiyama, T. (2005). Distribution and kinetics of SR-PSOX/CXCL16 and CXCR6 expression on human dendritic cell subsets and CD4+ T cells. J Leukoc Biol *77*, 777-786.   10.1189/jlb.1204733

Tamimi, A.F., and Juweid, M. (2017). Epidemiology and Outcome of Glioblastoma. In Glioblastoma, S. De Vleeschouwer, ed. (Brisbane (AU)).

Tanabe, K., Kozawa, O., and Iida, H. (2011). Midazolam suppresses interleukin-1beta-induced interleukin-6 release from rat glial cells. J Neuroinflammation *8*, 68.   10.1186/1742-2094-8-68

Thakkar, J.P., Dolecek, T.A., Horbinski, C., Ostrom, Q.T., Lightner, D.D., Barnholtz-Sloan, J.S., and Villano, J.L. (2014). Epidemiologic and molecular prognostic review of glioblastoma. Cancer Epidemiol Biomarkers Prev *23*, 1985-1996.   10.1158/1055-9965.EPI-14-0275

Thomas, R.P., Nagpal, S., Iv, M., Soltys, S.G., Bertrand, S., Pelpola, J.S., Ball, R., Yang, J., Sundaram, V., Lavezo, J*., et al.* (2019). Macrophage Exclusion after Radiation Therapy (MERT): A First in Human Phase I/II Trial using a CXCR4 Inhibitor in Glioblastoma. Clin Cancer Res *25*, 6948-6957.   10.1158/1078-0432.CCR-19-1421

Timperi, E., and Barnaba, V. (2021). CD39 Regulation and Functions in T Cells. Int J Mol Sci *22*.   10.3390/ijms22158068

Tomiyama, H., Matsuda, T., and Takiguchi, M. (2002). Differentiation of human CD8(+) T cells from a memory to memory/effector phenotype. J Immunol *168*, 5538-5550.   10.4049/jimmunol.168.11.5538

Torok, J.A., Wegner, R.E., Mintz, A.H., Heron, D.E., and Burton, S.A. (2011). Re-irradiation with radiosurgery for recurrent glioblastoma multiforme. Technol Cancer Res Treat *10*, 253-258.   10.7785/tcrt.2012.500200

Urbanska, K., Sokolowska, J., Szmidt, M., and Sysa, P. (2014). Glioblastoma multiforme - an overview. Contemp Oncol (Pozn) *18*, 307-312. 10.5114/wo.2014.40559

van der Bij, G.J., Oosterling, S.J., Meijer, S., Beelen, R.H., and van Egmond, M. (2005). The role of macrophages in tumor development. Cell Oncol *27*, 203-213. 10.1155/2005/719412

Varricchi, G., Galdiero, M.R., Loffredo, S., Lucarini, V., Marone, G., Mattei, F., Marone, G., and Schiavoni, G. (2018). Eosinophils: The unsung heroes in cancer? Oncoimmunology *7*, e1393134. 10.1080/2162402X.2017.1393134

Vater, A., Sahlmann, J., Kroger, N., Zollner, S., Lioznov, M., Maasch, C., Buchner, K., Vossmeyer, D., Schwoebel, F., Purschke, W.G.*, et al.* (2013). Hematopoietic stem and progenitor cell mobilization in mice and humans by a first-in-class mirror-image oligonucleotide inhibitor of CXCL12. Clin Pharmacol Ther *94*, 150-157. 10.1038/clpt.2013.58

Vatner, R.E., and Formenti, S.C. (2015). Myeloid-derived cells in tumors: effects of radiation. Semin Radiat Oncol *25*, 18-27. 10.1016/j.semradonc.2014.07.008

Veglia, F., Perego, M., and Gabrilovich, D. (2018). Myeloid-derived suppressor cells coming of age. Nat Immunol *19*, 108-119. 10.1038/s41590-017-0022-x

Visser, O., Ardanaz, E., Botta, L., Sant, M., Tavilla, A., Minicozzi, P., and Group, E.-W. (2015). Survival of adults with primary malignant brain tumours in Europe; Results of the EUROCARE-5 study. Eur J Cancer *51*, 2231-2241. 10.1016/j.ejca.2015.07.032

Walters, M.J., Ebsworth, K., Berahovich, R.D., Penfold, M.E., Liu, S.C., Al Omran, R., Kioi, M., Chernikova, S.B., Tseng, D., Mulkearns-Hubert, E.E.*, et al.* (2014). Inhibition of CXCR7 extends survival following irradiation of brain tumours in mice and rats. Br J Cancer *110*, 1179-1188. 10.1038/bjc.2013.830

Wang, C., Chen, W., and Shen, J. (2018). CXCR7 Targeting and Its Major Disease Relevance. Front Pharmacol *9*, 641. 10.3389/fphar.2018.00641

Wang, S.C., Hong, J.H., Hsueh, C., and Chiang, C.S. (2012). Tumor-secreted SDF-1 promotes glioma invasiveness and TAM tropism toward hypoxia in a murine astrocytoma model. Lab Invest *92*, 151-162. 10.1038/labinvest.2011.128

Wang, S.C., Yu, C.F., Hong, J.H., Tsai, C.S., and Chiang, C.S. (2013). Radiation therapy-induced tumor invasiveness is associated with SDF-1-regulated macrophage mobilization and vasculogenesis. PLoS One *8*, e69182. 10.1371/journal.pone.0069182

Wang, X., Schoenhals, J.E., Li, A., Valdecanas, D.R., Ye, H., Zang, F., Tang, C., Tang, M., Liu, C.G., Liu, X.*, et al.* (2017). Suppression of Type I IFN Signaling in Tumors Mediates Resistance to Anti-PD-1 Treatment That Can Be Overcome by Radiotherapy. Cancer Res *77*, 839-850. 10.1158/0008-5472.CAN-15-3142

Wang, Y., and Jiang, T. (2013). Understanding high grade glioma: molecular mechanism, therapy and comprehensive management. Cancer Lett *331*, 139-146. 10.1016/j.canlet.2012.12.024

Wang, Z., Jiang, J., Li, Z., Zhang, J., Wang, H., and Qin, Z. (2010). A myeloid cell population induced by Freund adjuvant suppresses T-cell-mediated antitumor immunity. J Immunother *33*, 167-177. 10.1097/CJI.0b013e3181bed2ba

Ward, S.T., Li, K.K., Hepburn, E., Weston, C.J., Curbishley, S.M., Reynolds, G.M., Hejmadi, R.K., Bicknell, R., Eksteen, B., Ismail, T.*, et al.* (2015). The effects of CCR5 inhibition on regulatory T-cell recruitment to colorectal cancer. Br J Cancer *112*, 319-328. 10.1038/bjc.2014.572

Weenink, B., Draaisma, K., Ooi, H.Z., Kros, J.M., Sillevis Smitt, P.A.E., Debets, R., and French, P.J. (2019). Low-grade glioma harbors few CD8 T cells, which is accompanied by decreased expression of chemo-attractants, not immunogenic antigens. Sci Rep *9*, 14643. 10.1038/s41598-019-51063-6

Weenink, B., French, P.J., Sillevis Smitt, P.A.E., Debets, R., and Geurts, M. (2020). Immunotherapy in Glioblastoma: Current Shortcomings and Future Perspectives. Cancers (Basel) *12*. 10.3390/cancers12030751

Weil, S., Osswald, M., Solecki, G., Grosch, J., Jung, E., Lemke, D., Ratliff, M., Hanggi, D., Wick, W., and Winkler, F. (2017). Tumor microtubes convey resistance to surgical lesions and chemotherapy in gliomas. Neuro Oncol *19*, 1316-1326. 10.1093/neuonc/nox070

Weller, M., Tabatabai, G., Kastner, B., Felsberg, J., Steinbach, J.P., Wick, A., Schnell, O., Hau, P., Herrlinger, U., Sabel, M.C.*, et al.* (2015). MGMT Promoter Methylation Is a Strong Prognostic Biomarker for Benefit from Dose-Intensified Temozolomide Rechallenge in Progressive Glioblastoma: The DIRECTOR Trial. Clin Cancer Res *21*, 2057-2064. 10.1158/1078-0432.CCR-14-2737

West, A.J., Tsui, V., Styllli, S.S., Nguyen, H.P.T., Morokoff, A.P., Kaye, A.H., and Luwor, R.B. (2018). The role of interleukin-6-STAT3 signalling in glioblastoma. Oncol Lett *16*, 4095-4104. 10.3892/ol.2018.9227

Wherry, E.J. (2011). T cell exhaustion. Nat Immunol *12*, 492-499. 10.1038/ni.2035

Wilson, C.M., Gaber, M.W., Sabek, O.M., Zawaski, J.A., and Merchant, T.E. (2009). Radiation-induced astrogliosis and blood-brain barrier damage can be abrogated using anti-TNF treatment. Int J Radiat Oncol Biol Phys *74*, 934-941. 10.1016/j.ijrobp.2009.02.035

Wilson, E.H., Weninger, W., and Hunter, C.A. (2010). Trafficking of immune cells in the central nervous system. J Clin Invest *120*, 1368-1379. 10.1172/JCI41911

Wilson, T.A., Karajannis, M.A., and Harter, D.H. (2014). Glioblastoma multiforme: State of the art and future therapeutics. Surg Neurol Int *5*, 64. 10.4103/2152-7806.132138

Wolburg, H., Noell, S., Fallier-Becker, P., Mack, A.F., and Wolburg-Buchholz, K. (2012). The disturbed blood-brain barrier in human glioblastoma. Mol Aspects Med *33*, 579-589. 10.1016/j.mam.2012.02.003

Won, W.J., Deshane, J.S., Leavenworth, J.W., Oliva, C.R., and Griguer, C.E. (2019). Metabolic and functional reprogramming of myeloid-derived suppressor cells and their therapeutic control in glioblastoma. Cell Stress *3*, 47-65. 10.15698/cst2019.02.176

Wong, E.T., Hess, K.R., Gleason, M.J., Jaeckle, K.A., Kyritsis, A.P., Prados, M.D., Levin, V.A., and Yung, W.K.

(1999). Outcomes and prognostic factors in recurrent glioma patients enrolled onto phase II clinical trials. J Clin Oncol *17*, 2572-2578. 10.1200/JCO.1999.17.8.2572

Woroniecka, K., Chongsathidkiet, P., Rhodin, K., Kemeny, H., Dechant, C., Farber, S.H., Elsamadicy, A.A., Cui, X., Koyama, S., Jackson, C.*, et al.* (2018). T-Cell Exhaustion Signatures Vary with Tumor Type and Are Severe in Glioblastoma. Clin Cancer Res *24*, 4175-4186. 10.1158/1078-0432.CCR-17-1846

Wu, A., Maxwell, R., Xia, Y., Cardarelli, P., Oyasu, M., Belcaid, Z., Kim, E., Hung, A., Luksik, A.S., Garzon-Muvdi, T.*, et al.* (2019). Combination anti-CXCR4 and anti-PD-1 immunotherapy provides survival benefit in glioblastoma through immune cell modulation of tumor microenvironment. J Neurooncol *143*, 241-249. 10.1007/s11060-019-03172-5

Xue, S., Hu, M., Iyer, V., and Yu, J. (2017). Blocking the PD-1/PD-L1 pathway in glioma: a potential new treatment strategy. J Hematol Oncol *10*, 81. 10.1186/s13045-017-0455-6

Yamada, N., Kato, M., Yamashita, H., Nister, M., Miyazono, K., Heldin, C.H., and Funa, K. (1995). Enhanced expression of transforming growth factor-beta and its type-I and type-II receptors in human glioblastoma. Int J Cancer *62*, 386-392. 10.1002/ijc.2910620405

Yang, J., Kumar, A., Vilgelm, A.E., Chen, S.C., Ayers, G.D., Novitskiy, S.V., Joyce, S., and Richmond, A. (2018). Loss of CXCR4 in Myeloid Cells Enhances Antitumor Immunity and Reduces Melanoma Growth through NK Cell and FASL Mechanisms. Cancer Immunol Res *6*, 1186-1198. 10.1158/2326-6066.CIR-18-0045

Yang, L., Yang, J., Li, G., Li, Y., Wu, R., Cheng, J., and Tang, Y. (2017). Pathophysiological Responses in Rat and Mouse Models of Radiation-Induced Brain Injury. Mol Neurobiol *54*, 1022-1032. 10.1007/s12035-015-9628-x

Yao, M., Li, S., Wu, X., Diao, S., Zhang, G., He, H., Bian, L., and Lu, Y. (2018). Cellular origin of glioblastoma and its implication in precision therapy. Cell Mol Immunol *15*, 737-739. 10.1038/cmi.2017.159

Yeung, Y.T., Bryce, N.S., Adams, S., Braidy, N., Konayagi, M., McDonald, K.L., Teo, C., Guillemin, G.J., Grewal, T., and Munoz, L. (2012). p38 MAPK inhibitors attenuate pro-inflammatory cytokine production and the invasiveness of human U251 glioblastoma cells. J Neurooncol *109*, 35-44. 10.1007/s11060-012-0875-7

Yoshida, K., Okamoto, M., Sasaki, J., Kuroda, C., Ishida, H., Ueda, K., Ideta, H., Kamanaka, T., Sobajima, A., Takizawa, T.*, et al.* (2020). Anti-PD-1 antibody decreases tumour-infiltrating regulatory T cells. BMC Cancer *20*, 25. 10.1186/s12885-019-6499-y

Yoshimoto, Y., Suzuki, Y., Mimura, K., Ando, K., Oike, T., Sato, H., Okonogi, N., Maruyama, T., Izawa, S., Noda, S.E.*, et al.* (2014). Radiotherapy-induced anti-tumor immunity contributes to the therapeutic efficacy of irradiation and can be augmented by CTLA-4 blockade in a mouse model. PLoS One *9*, e92572. 10.1371/journal.pone.0092572

Youn, J.I., Nagaraj, S., Collazo, M., and Gabrilovich, D.I. (2008). Subsets of myeloid-derived suppressor cells in tumor-bearing mice. J Immunol *181*, 5791-5802. 10.4049/jimmunol.181.8.5791

Zagzag, D., Salnikow, K., Chiriboga, L., Yee, H., Lan, L., Ali, M.A., Garcia, R., Demaria, S., and Newcomb, E.W. (2005). Downregulation of major histocompatibility complex antigens in invading glioma cells: stealth invasion of the brain. Lab Invest *85*, 328-341. 10.1038/labinvest.3700233

Zanoni, M., Sarti, A.C., Zamagni, A., Cortesi, M., Pignatta, S., Arienti, C., Tebaldi, M., Sarnelli, A., Romeo, A., Bartolini, D.*, et al.* (2022). Irradiation causes senescence, ATP release, and P2X7 receptor isoform switch in glioblastoma. Cell Death Dis *13*, 80. 10.1038/s41419-022-04526-0

Zboralski, D., Hoehlig, K., Eulberg, D., Fromming, A., and Vater, A. (2017). Increasing Tumor-Infiltrating T Cells through Inhibition of CXCL12 with NOX-A12 Synergizes with PD-1 Blockade. Cancer Immunol Res *5*, 950-956. 10.1158/2326-6066.CIR-16-0303

Zeng, J., See, A.P., Phallen, J., Jackson, C.M., Belcaid, Z., Ruzevick, J., Durham, N., Meyer, C., Harris, T.J., Albesiano, E.*, et al.* (2013). Anti-PD-1 blockade and stereotactic radiation produce long-term survival in mice with intracranial gliomas. Int J Radiat Oncol Biol Phys *86*, 343-349. 10.1016/j.ijrobp.2012.12.025

Zhan, Y., Wang, N., Vasanthakumar, A., Zhang, Y., Chopin, M., Nutt, S.L., Kallies, A., and Lew, A.M. (2020). CCR2 enhances CD25 expression by FoxP3(+) regulatory T cells and regulates their abundance independently of chemotaxis and CCR2(+) myeloid cells. Cell Mol Immunol *17*, 123-132. 10.1038/s41423-018-0187-8

Zhang, Y., Hu, K., Beumer, J.H., Bakkenist, C.J., and D'Argenio, D.Z. (2017). RAD-ADAPT: Software for modelling clonogenic assay data in radiation biology. DNA Repair (Amst) *52*, 24-30. 10.1016/j.dnarep.2017.02.004

Zhao, H., Bo, C., Kang, Y., and Li, H. (2017). What Else Can CD39 Tell Us? Front Immunol *8*, 727. 10.3389/fimmu.2017.00727

Zhou, M., Bracci, P.M., McCoy, L.S., Hsuang, G., Wiemels, J.L., Rice, T., Zheng, S., Kelsey, K.T., Wrensch, M.R., and Wiencke, J.K. (2015a). Serum macrophage-derived chemokine/CCL22 levels are associated with glioma risk, CD4 T cell lymphopenia and survival time. Int J Cancer *137*, 826-836. 10.1002/ijc.29441

Zhou, W., Jiang, Z., Li, X., Xu, Y., and Shao, Z. (2015b). Cytokines: shifting the balance between glioma cells and tumor microenvironment after irradiation. J Cancer Res Clin Oncol *141*, 575-589. 10.1007/s00432-014-1772-6

Zhou, W., Xu, Y., Li, X., Gao, G., Jiang, Z., and Shao, Z. (2014). Irradiation enhances expression of cxcr4 in murine glioma cells via HIF-1alpha-independent pathway. J Int Med Res *42*, 926-931. 10.1177/0300060514533522

Zlotnik, A., and Yoshie, O. (2012). The chemokine superfamily revisited. Immunity *36*, 705-716. 10.1016/j.immuni.2012.05.008

8   DISCLOSURES

9 APPENDIX

Table A-1: Staining panels for the flow cytometric analysis

maker	fluorochrome	clone	manufacturer
CD4 Panel			
Live Dead	7AAD		Miltenyi Biotec, Bergisch Gladbach, Germany
CD45	V500	30-F11	BD Biosciences, San Jose, USA
CD3	PerCP-Cy5.5	SK7	BD Biosciences, San Jose, USA
CD4	PE	RPA-T4	BD Biosciences, San Jose, USA
FoxP3	FITC	L78	eBioscience /Thermo Fisher, San Diego, USA
CD39	PE-Cy7	Duha59	Biolegend, San Diego, USA
CD73	BV421	TY/11.8	Biolegend, San Diego, USA
CD69	APC	H1.2F3	BD Biosciences, San Jose, USA
PD-L1	BV421	MIH5	BD Biosciences, San Jose, USA
CD8 Panel			
Live Dead	7AAD		Miltenyi Biotec, Bergisch Gladbach, Germany
CD45	V500	30-F11	BD Biosciences, San Jose, USA
CD3	PerCP-Cy5.5	SK7	BD Biosciences, San Jose, USA
CD8	PE-Cy7	RPA-T8	BD Biosciences, San Jose, USA
CD31	PE	MEC 13.3	Biolegend, San Diego, USA
CD69	APC	H1.2F3	BD Biosciences, San Jose, USA
PD-1	BV421	29F.1A12	BD Biosciences, San Jose, USA
MDSC Panel 1			
Live Dead	7AAD		Miltenyi Biotec, Bergisch Gladbach, Germany
CD45	V500	30-F11	BD Biosciences, San Jose, USA
CD11b	APC-Cy7	M1/70	BD Biosciences, San Jose, USA
Ly6G	APC	1A8	BD Biosciences, San Jose, USA
Ly6C	PE	AL-21	BD Biosciences, San Jose, USA
ROS	APF		CellTechnology, Hayward, USA
NO	DAF-FM DA		Cayman Chemicals, Ann Arbor, USA
MDSC Panel 2			
Live Dead	7AAD		Miltenyi Biotec, Bergisch Gladbach, Germany
CD45	V500	30-F11	BD Biosciences, San Jose, USA
CD11b	APC-Cy7	M1/70	BD Biosciences, San Jose, USA
Ly6G	APC	1A8	BD Biosciences, San Jose, USA
Ly6C	PE	AL-21	BD Biosciences, San Jose, USA
CCR4	PE-Cy7	2G12	Biolegend, San Diego, USA
CCR2	BV605	475301	BD Biosciences, San Jose, USA
CXCR4	BV421	2B11	BD Biosciences, San Jose, USA
CXCR2	FITC	SA044G4	Biolegend, San Diego, USA
MDSC Panel 3			
Live Dead	7AAD		Miltenyi Biotec, Bergisch Gladbach, Germany
CD45	V500	30-F11	BD Biosciences, San Jose, USA
CD11b	APC-Cy7	M1/70	BD Biosciences, San Jose, USA
Ly6G	APC	1A8	BD Biosciences, San Jose, USA
Ly6C	PE	AL-21	BD Biosciences, San Jose, USA
CXCR7	PE-Cy7	8F11-M16	Biolegend, San Diego, USA

		MDSC Panel 4	
maker	**fluorochrome**	**clone**	**manufacturer**
Live Dead	7AAD		Miltenyi Biotec, Bergisch Gladbach, Germany
CD45	V500	30-F11	BD Biosciences, San Jose, USA
CD11b	APC-Cy7	M1/70	BD Biosciences, San Jose, USA
Ly6G	APC	1A8	BD Biosciences, San Jose, USA
Ly6C	PE	AL-21	BD Biosciences, San Jose, USA
CD39	PE-Cy7	Duha59	Biolegend, San Diego, USA
CD73	BV605	TY/11.8	Biolegend, San Diego, USA
PD-L1	BV421	MIH5	BD Biosciences, San Jose, USA
CCR5	AF488	HM-CCR5	Biolegend, San Diego, USA
FcBlock		2.4G2	BD Biosciences, San Jose, USA

Table A-2: Staining panels for the flow cytometric analysis of the receptors

		Treg Panel	
maker	**fluorochrome**	**clone**	**manufacturer**
Live Dead	7AAD		Miltenyi Biotec, Bergisch Gladbach, Germany
CD45	V500	30-F11	BD Biosciences, San Jose, USA
CD3	PerCP-Cy5.5	SK7	BD Biosciences, San Jose, USA
CD4	APC-Cy7	GK1.5	BD Biosciences, San Jose, USA
FoxP3	APC	FJK-16s	ThermoFisher, Waltham, USA
CCR2	BV605	475301	BD Biosciences, San Jose, USA
CCR4	PE	2G12	Biolegend, San Diego, USA
CCR5	AF488	HM-CCR5	Biolegend, San Diego, USA
CXCR4	BV421	2B11	BD Biosciences, San Jose, USA
CXCR7	PE-Cy7	8F11-M16	Biolegend, San Diego, USA

		CD8 Panel	
maker	**fluorochrome**	**clone**	**manufacturer**
Live Dead	7AAD		Miltenyi Biotec, Bergisch Gladbach, Germany
CD45	V500	30-F11	BD Biosciences, San Jose, USA
CD3	PerCP-Cy5.5	SK7	BD Biosciences, San Jose, USA
CD8	APC-Cy7	53-6.7	BD Biosciences, San Jose, USA
CCR2	BV605	475301	BD Biosciences, San Jose, USA
CCR4	PE	2G12	Biolegend, San Diego, USA
CCR5	AF488	HM-CCR5	Biolegend, San Diego, USA
CXCR4	BV421	2B11	BD Biosciences, San Jose, USA
CXCR7	PE-Cy7	8F11-M16	Biolegend, San Diego, USA

		MDSC Panel	
maker	**fluorochrome**	**clone**	**manufacturer**
Live Dead	7AAD		Miltenyi Biotec, Bergisch Gladbach, Germany
CD45	V500	30-F11	BD Biosciences, San Jose, USA
CD11b	APC-Cy7	M1/70	BD Biosciences, San Jose, USA
PD-L1	PerCP-Cy5.5	10F.9G2	Biolegend, San Diego, USA
Gr1	APC	RB6-8C5	BD Biosciences, San Jose, USA
CCR2	BV605	475301	BD Biosciences, San Jose, USA
CCR4	PE	2G12	Biolegend, San Diego, USA
CCR5	AF488	HM-CCR5	Biolegend, San Diego, USA
CXCR4	BV421	2B11	BD Biosciences, San Jose, USA
CXCR7	PE-Cy7	8F11-M16	Biolegend, San Diego, USA
FcBlock		2.4G2	BD Biosciences, San Jose, USA

Table A-3: Mouse data – survival experiments

Undef = undefined, tumor mass verifiable but not measurable

mouse	treatment	implanted cell amount	treatment start (days after tumor inoculation)	trail length (days)	treatment length (days)	tumor volume day 7 (mm³)	last tumor volume (mm³)	day last MRI (days after tumor inoculation)	max tumor volume (mm³)	day max tumor volume (days after tumor inoculation)
C57-1	untreated	1.5×10^6	-	21	-	-	6.8	21		
C57-2	untreated	1.5×10^6	-	21	-	-	15.3	21		
C57-3	untreated	1.5×10^6	-	21	-	-	11.1	21		
C57-4	untreated	2.5×10^6	-	21	-	-	16.8	21		
C57-5	untreated	2.5×10^6	-	21	-	-	18.8	21		
C57-6	untreated	2.5×10^6	-	21	-	-	4.3	21		
C57-7	untreated	1.5×10^5	-	25	-	3.7	4.6	20		
C57-8	untreated	1.5×10^5	-	20	-	9.6	26.4	20		
C57-9	untreated	1.5×10^5	-	20	-	1.1	0.67	20		
C57-10	untreated	1.5×10^5	-	25	-	2.4	2.4	20		
C57-11	control	1.5×10^5	-	26	-	undef	31	26		
C57-16	control	1.5×10^5	-	32	-	undef	16.1	32		
C57-19	control	1.5×10^5	-	21	-	6.8	14.3	21		
C57-21	control	1.5×10^5	-	25	-	11.6	28.6	25		
C57-33	control	1.5×10^5	-	22	-	6.6	26	22		
C57-34	control	1.5×10^5	-	22	-	undef	68.6	22		
C57-35	control	1.5×10^5	-	30	-	undef	45.1	30		
C57-36	control	1.5×10^5	-	34	-	undef	56.7	34		
C57-39	control	1.5×10^5	-	24	-	undef	22.1	24		
C57-44	control	1.5×10^5	-	28	-	undef	56.7	28		
C57-45	control	1.5×10^5	-	28	-	undef	31.4	28		
C57-47	Anti-PD1	1.5×10^5	7	42	35	0.51	33.5	41		
C57-48	Anti-PD1	1.5×10^5	7	25	18	1.66	23.7	24		
C57-49	control	1.5×10^5	-	25	-	9.19	37.5	34		
C57-50	control	1.5×10^5	-	32	-	0.78	30.9	32		
C57-51	Anti-PD1	1.5×10^5	7	28	21	1.47	25.5	28		
C57-52	Anti-PD1	1.5×10^5	7	100	93	undef	0	98	2.98	11
C57-53	Anti-PD1	1.5×10^5	7	22	15	0.76	19.9	22		
C57-54	Anti-PD1	1.5×10^5	7	32	25	5.2	43.4	32		

mouse	treatment	implanted cell amount	treatment start (days after tumor inoculation)	trail length (days)	treatment length (days)	tumor volume day 7 (mm³)	last tumor volume (mm³)	day last MRI (days after tumor inoculation)	max tumor volume (mm³)	day max tumor volume (days after tumor inoculation)
C57-55	Anti-PD1	1.5x10^5	7	100	93	undef	0	97	3.75	13
C57-56	Anti-PD1	1.5x10^5	7	29	22	0.64	23.8	28		
C57-57	control	1.5x10^5	-	20	-	0.62	21.6	19		
C57-58	Anti-PD1	1.5x10^5	7	32	25	0.75	25.4	32		
C57-59	RT	1.5x10^5	10	100	-	0.31	0	100	2.12	44
C57-60	RT	1.5x10^5	10	100	-	1.15	0	100	2.7	17
C57-62	control	1.5x10^5	-	28	-	undef	80	28		
C57-63	RT	1.5x10^5	10	49	-	1.37	55.7	49		
C57-65	RT 1x20 Gy	1.5x10^5	10	100	-	1.95	0	100	4.19	17
C57-66	RT 1x20 Gy	1.5x10^5	10	100	-	0.35	0	100	1.3	17
C57-67	RT 1x20 Gy	1.5x10^5	10	100	-	1.36	1.24	100	5.4	52
C57-68	RT 1x20 Gy	1.5x10^5	10	52	-	undef	76.3 (M)	52		
C57-69	RT 1x20 Gy	1.5x10^5	10	87	-	0.95	27.5 (M)	87		
C57-70	RT	1.5x10^5	11	55	-	3.41	29.9	54		
C57-71	RT 2x10 Gy	1.5x10^5	11	55	-	6.45	22.8	55		
C57-72	RT 1x20 Gy	1.5x10^5	11	70	-	3.52	20.6	70		
C57-73	RT 2x10 Gy	1.5x10^5	11	100	-	2.71	0	98	3.69	20
C57-74	RT 2x10 Gy	1.5x10^5	11	70	-	2.66	22	70		
C57-75	RT 2x10 Gy	1.5x10^5	11	100	-	undef	0	98	2.16	20
C57-76	RT 2x10 Gy	1.5x10^5	11	55	-	undef	77.8 (M)	55		
C57-77	RT	1.5x10^5	11	55	-	6.23	37.8	54		
C57-78	RT 2x10 Gy	1.5x10^5	11	100	-	0.67	0	98	0.67	10
C57-96	RT + Anti-PD1	1.5x10^5	7	100	93	1.15	0	98	5.74	16
C57-97	RT + Anti-PD1	1.5x10^5	7	100	93	1.51	0	98	4.51	23
C57-99	RT + Anti-PD1	1.5x10^5	7	100	93	undef	0	98	4.1	16
C57-102	RT + NOX-A12	1.5x10^5	7	100	94	undef	0	100	2.44	22
C57-103	RT + NOX-A12	1.5x10^5	7	100	94	0.39	0	100	3.11	29
C57-104	RT + NOX-A12	1.5x10^5	7	74	67	undef	58.1	74		
C57-105	RT + NOX-A12	1.5x10^5	7	100	94	undef	0	100	1.02	22
C57-107	RT + Anti-PD1	1.5x10^5	7	100	94	undef	0	100	0.93	15

mouse	treatment	implanted cell amount	treatment start (days after tumor inoculation)	trail length (days)	treatment length (days)	tumor volume day 7 (mm³)	last tumor volume (mm³)	day last MRI (days after tumor inoculation)	max tumor volume (mm³)	day max tumor volume (days after tumor inoculation)
C57-108	RT + Anti-PD1	1.5x10⁵	7	82	75	undef	55.2	81		
C57-111	RT + NOXE36	1.5x10⁵	7	52	45	1.94	25.6	50		
C57-112	RT + NOXE36	1.5x10⁵	7	52	45	1.01	48	50		
C57-113	RT + NOXE36	1.5x10⁵	7	46	39	1.26	67.9	46		
C57-114	RT + NOXE36	1.5x10⁵	7	60	53	1.39	27.7	60		
C57-115	RT + NOXE36	1.5x10⁵	7	66	59	2.83	91	65		
C57-116	RT + NOXE36	1.5x10⁵	7	100	93	0.37	0	100	4.12	14
C57-117	RT+ NOX-A12 + Anti-PD1	1.5x10⁵	7	100	93	1.06	0	100	3.19	14
C57-118	RT+ NOX-A12 + Anti-PD1	1.5x10⁵	7	99	92	undef	37.7	99		
C57-119	RT+ NOX-A12 + Anti-PD1	1.5x10⁵	7	100	93	1.63	0	99	11.2	21
C57-120	RT+ NOX-A12 + Anti-PD1	1.5x10⁵	7	100	93	1.03	0	99	9.72	21
C57-121	RT+ NOX-A12 + Anti-PD1	1.5x10⁵	7	68	61	1.08	16.3	66		
C57-122	RT+ NOX-A12 + Anti-PD1	1.5x10⁵	7	60	53	0.5	56.5	60		
C57-123	RT + NOXE36 + Anti-PD1	1.5x10⁵	7	100	93	1.1	0	95	4.79	28
C57-124	RT + NOXE36 + Anti-PD1	1.5x10⁵	7	100	93	0.77	0	95	2.75	21
C57-125	RT + NOXE36 + Anti-PD1	1.5x10⁵	7	100	93	0.52	0.76	95	5.17	21
C57-126	RT + NOXE36 + Anti-PD1	1.5x10⁵	7	100	93	3.21	0	95	5.25	
C57-127	RT + NOXE36 + Anti-PD1	1.5x10⁵	7	100	93	1	1.64	95	7	
C57-128	RT + NOXE36 + Anti-PD1	1.5x10⁵	7	100	93	0.5	0	95	1.94	
C57-129	RT + NOXE36 + NOX-A12 + Anti-PD1	1.5x10⁵	7	69	62	1.33	24.3	68		
C57-130	RT + NOXE36 + NOX-A12 + Anti-PD1	1.5x10⁵	7	100	93	0.61	0	100	4.34	14
C57-131	RT + NOXE36 + NOX-A12 + Anti-PD1	1.5x10⁵	7	100	93	0.7	0	100	3.04	21

mouse	treatment	implanted cell amount	treatment start (days after tumor inoculation)	trail length (days)	treatment length (days)	tumor volume day 7 (mm³)	last tumor volume (mm³)	day last MRI (days after tumor inoculation)	max tumor volume (mm³)	day max tumor volume (days after tumor inoculation)
C57-133	RT + NOXE36 + NOX-A12 + Anti-PD1	1.5×10^5	7	69	62	1.13	65.6	68		
C57-135	NOX-A12	1.5×10^5	7	24	17	0.82	41.7	24		
C57-136	NOX-A12	1.5×10^5	7	28	21	1.89	31	28		
C57-137	NOX-A12	1.5×10^5	7	24	17	1.63	62.8	24		
C57-138	NOX-A12	1.5×10^5	7	42	35	0.39	61.1	41		
C57-139	NOX-A12	1.5×10^5	7	28	21	0.54	83.5	28		
C57-140	NOX-A12	1.5×10^5	7	28	21	0.78	34.8	28		
C57-141	NOXE36	1.5×10^5	7	23	16	0.56	97.6	23		
C57-142	NOXE36	1.5×10^5	7	23	16	1.56	53.3	23		
C57-143	NOXE36	1.5×10^5	7	23	16	1.26	85.2	23		
C57-144	NOXE36	1.5×10^5	7	23	16	1.31	127.7	23		
C57-145	NOXE36	1.5×10^5	7	23	16	1.07	95.3	23		
C57-146	NOXE36	1.5×10^5	7	23	16	undef	210.1	23		
C57-163	NOX-A12 + Anti-PD1	1.5×10^5	7	42	35	11.1	47.8	41		
C57-164	NOX-A12 + Anti-PD1	1.5×10^5	7	100	93	3.24	0	99	3.24	7
C57-165	NOX-A12 + Anti-PD1	1.5×10^5	7	28	21	2.12	71.2	28		
C57-166	NOX-A12 + Anti-PD1	1.5×10^5	7	25	18	12.4	44.7	23		
C57-167	NOX-A12 + Anti-PD1	1.5×10^5	7	46	39	2.64	64.3	46		
C57-168	NOX-A12 + Anti-PD1	1.5×10^5	7	30	23	4.66	36.9	30		
C57-169	NOXE36 + Anti-PD1	1.5×10^5	7	42	35	1.43	46.3			
C57-170	NOXE36 + Anti-PD1	1.5×10^5	7	25	18	3.48	58.2	42		
C57-171	NOXE36 + Anti-PD1	1.5×10^5	7	25	18	1.31	21.5	23		
C57-172	NOXE36 + Anti-PD1	1.5×10^5	7	25	18	1.01	42.2	23		
C57-173	NOXE36 + Anti-PD1	1.5×10^5	7	46	39	2.48	106.2	46		
C57-174	NOXE36 + Anti-PD1	1.5×10^5	7	100	93	0.91	0	99	6.73	30
C57-175	RT + Anti-PD1	1.5×10^5	7	100	93	undef	0	99	1.66	14
C57-176	RT + Anti-PD1	1.5×10^5	7	100	93	0.87	0	99	1.91	14
C57-177	RT + Anti-PD1	1.5×10^5	7	100	93	2.32	0	99	3.04	14

mouse	treatment	implanted cell amount	treatment start (days after tumor inoculation)	trail length (days)	treatment length (days)	tumor volume day 7 (mm³)	last tumor volume (mm³)	day last MRI (days after tumor inoculation)	max tumor volume (mm³)	day max tumor volume (days after tumor inoculation)
C57-178	RT + Anti-PD1	1.5×10^5	7	100	93	2.22	0	99	3.58	14
C57-179	RT + Anti-PD1	1.5×10^5	7	67	60	0.71	54.9	67		
C57-181	NOX-A12	1.5×10^5	7	23	16	0.88	54.6	21		
C57-182	RT + NOX-A12	1.5×10^5	7	53	46	1.11	185.3	53		
C57-183	RT + NOX-A12	1.5×10^5	7	55	48	0.6	65.5	54		
C57-184	NOX-A12	1.5×10^5	7	28	21	0.64	75.8	28		
C57-185	RT + NOX-A12	1.5×10^5	7	100	93	undef	0	99	9.55	21
C57-186	NOX-A12	1.5×10^5	7	25	18	0.89	70.5	25		
C57-203	NOX-A12 + Anti-PD1	1.5×10^5	7	100	93	0.45	0	99	6.16	15
C57-207	NOX-A12 + Anti-PD1	1.5×10^5	7	29	22	0.7	49.8	29		
C57-208	NOX-A12 + Anti-PD1	1.5×10^5	7	47	40	1.01	124	46		
C57-209	NOXE36	1.5×10^5	7	24	17	0.94	63.9	24		
C57-210	NOXE36 + Anti-PD1	1.5×10^5	7	47	40	0.595	60.6	46		
C57-211	NOXE36	1.5×10^5	7	24	17	0.53	45.8	24		
C57-212	NOXE36 + Anti-PD1	1.5×10^5	7	29	22	0.49	64	28		
C57-213	NOXE36 + Anti-PD1	1.5×10^5	7	35	28	undef	95.8	35		
C57-214	NOXE36	1.5×10^5	7	38	31	0.475	42.2	35		
C57-215	RT + NOXE36	1.5×10^5	7	88	81	1.7	15.6	87		
C57-216	RT	1.5×10^5	10	59	-	2	73.2	58		
C57-217	RT + NOXE36	1.5×10^5	7	67	60	1.59	72.9	66		
C57-218	RT + NOXE36	1.5×10^5	7	88	81	0.84	23.7	87		
C57-219	RT	1.5×10^5	10	88	-	1.98	16.3	87		
C57-220	RT	1.5×10^5	10	56	-	1.28	75.4	56		
C57-221	RT+ NOX-A12 + Anti-PD1	1.5×10^5	7	100	93	0.34	0	100	3.1	15
C57-222	RT + NOXE36 + Anti-PD1	1.5×10^5	7	67	60	1.52	24.5	66		
C57-223	RT + NOXE36 + Anti-PD1	1.5×10^5	7	100	93	5.78	0	100	6.87	15
C57-224	RT + NOXE36 + Anti-PD1	1.5×10^5	7	100	93	undef	0	100	8.56	15
C57-225	RT+ NOX-A12 + Anti-PD1	1.5×10^5	7	44	37	0.71	34.9	42		

mouse	treatment	implanted cell amount	treatment start (days after tumor inoculation)	trail length (days)	treatment length (days)	tumor volume day 7 (mm³)	last tumor volume (mm³)	day last MRI (days after tumor inoculation)	max tumor volume (mm³)	day max tumor volume (days after tumor inoculation)
C57-226	RT+ NOX-A12 + Anti-PD1	1.5x10⁵	7	100	93	4.71	0	100	18.1	15
C57-228	RT + NOXE36 + NOX-A12 + Anti-PD1	1.5x10⁵	7	100	93	1.22	0	100	1.52	12
C57-230	RT + NOXE36 + NOX-A12 + Anti-PD1	1.5x10⁵	7	100	93	0.5305	0	100	7.75	12
C57-231	RT + NOXE36 + NOX-A12 + Anti-PD1	1.5x10⁵	7	55	48	1.01	40.1	54		
C57-233	RT + NOX-A12	1.5x10⁵	7	100	93	0.825	0	98	6.09	
C57-234	RT + NOXE36	1.5x10⁵	7	48	41	0.58	65.6	47		
C57-235	RT + NOXE36	1.5x10⁵	7	100	93	0.61	0	98	2.91	
C57-236	RT + NOX-A12	1.5x10⁵	7	98	91	undef	58.1	98		
C57-237	RT + NOXE36	1.5x10⁵	7	63	56	0.54	53.5	61		
C57-238	RT + NOX-A12	1.5x10⁵	7	74	67	0.36	33.9	73		
C57-257	RT + NOXE36 + NOX-A12 + Anti-PD1	1.5x10⁵	7	63	56	0.74	48.4	63		
C57-258	RT + NOXE36 + NOX-A12 + Anti-PD1	1.5x10⁵	7	100	93	0.72	0	100	2.2	14
C57-259	RT + Anti-PD1	1.5x10⁵	7	100	93	1.1	0	100	5.1	14
C57-260	RT + Anti-PD1	1.5x10⁵	7	100	93	0.49	0	100	4.03	14
C57-261	RT + NOXE36 + Anti-PD1	1.5x10⁵	7	100	93	undef	0	100	11	14
C57-262	RT+ NOX-A12 + Anti-PD1	1.5x10⁵	7	100	93	1.54	0	100	7.63	14
C57-263	RT+ NOX-A12 + Anti-PD1	1.5x10⁵	7	95	88	1.06	92	95		
C57-264	RT + NOXE36 + Anti-PD1	1.5x10⁵	7	100	93	1.26	0	100	4.18	14
C57-265	RT + NOXE36 + Anti-PD1	1.5x10⁵	7	80	73	1.34	79.8	80		
C57-266	RT+ NOX-A12 + Anti-PD1	1.5x10⁵	7	100	93	2	0	100	2	14

Table A-4: Mouse data – FACS analysis

mouse	treatment	implanted cell amount	treatment start (days after tumor inoculation)	trail length (days)	treatment length (days)	tumor volume day 7 (mm³)	tumor volume day 20 (mm³)
C57-147	control	1.5×10^5	-	19	-	1.69	16.7
C57-148	control	1.5×10^5	-	20	-	1.57	6.76
C57-149	control	1.5×10^5	-	20	-	0.75	3.97
C57-150	control	1.5×10^5	-	19	-	1.01	12.1
C57-151	NOX-A12	1.5×10^5	7	20	13	1.05	11.9
C57-152	NOX-A12	1.5×10^5	7	20	13	0.87	9.21
C57-153	NOX-A12	1.5×10^5	7	19	12	1.66	12.1
C57-154	NOX-A12	1.5×10^5	7	19	12	2.36	40.1
C57-155	RT	1.5×10^5	10	19	-	0.63	4.42
C57-156	RT	1.5×10^5	10	20	-	1.01	6.55
C57-157	RT	1.5×10^5	10	19	-	1.56	0.85
C57-158	RT	1.5×10^5	10	20	-	1.74	5.87
C57-159	RT + NOX-A12	1.5×10^5	7	19	12	1.33	10.3
C57-160	RT + NOX-A12	1.5×10^5	7	20	13	1.034	5.89
C57-161	RT + NOX-A12	1.5×10^5	7	20	13	0.79	4.35
C57-162	RT + NOX-A12	1.5×10^5	7	19	12	1.28	2.71
C57-187	RT	1.5×10^5	10	20	-	undef	1.47
C57-188	RT	1.5×10^5	10	19	-	0.57	4.21
C57-189	RT	1.5×10^5	10	20	-	undef	2.68
C57-190	RT	1.5×10^5	10	19	-	1.31	3.62
C57-191	NOX-A12	1.5×10^5	7	20	13	undef	14.3
C57-192	NOX-A12	1.5×10^5	7	19	12	undef	14.5
C57-193	NOX-A12	1.5×10^5	7	20	13	undef	9.65
C57-194	NOX-A12	1.5×10^5	7	19	12	0.56	4.89
C57-195	control	1.5×10^5	-	19	-	0.37	7.62
C57-196	control	1.5×10^5	-	20	-	undef	3.86
C57-197	control	1.5×10^5	-	19	-	0.62	7.85
C57-198	control	1.5×10^5	-	20	-	0.6	13.5
C57-199	RT + NOX-A12	1.5×10^5	7	19	12	1.3	6.5
C57-200	RT + NOX-A12	1.5×10^5	7	19	12	0.29	4.58

mouse	treatment	implanted cell amount	treatment start (days after tumor inoculation)	trail length (days)	treatment length (days)	tumor volume day 7 (mm³)	tumor volume day 20 (mm³)
C57-201	RT + NOX-A12	1.5×10^5	7	20	13	undef	7.12
C57-202	RT + NOX-A12	1.5×10^5	7	20	13	0.63	3.36
C57-239	NOX-A12	1.5×10^5	7	19	12	undef	15.1
C57-240	NOX-A12	1.5×10^5	7	20	13	undef	28.3
C57-241	NOX-A12	1.5×10^5	7	19	12	undef	13.9
C57-242	NOX-A12	1.5×10^5	7	20	13	0.785	35.4
C57-243	RT + NOX-A12	1.5×10^5	7	20	13	3.46	3.26
C57-244	RT + NOX-A12	1.5×10^5	7	19	12	1.37	6.77
C57-245	RT + NOX-A12	1.5×10^5	7	20	13	1.36	3.61
C57-246	RT + NOX-A12	1.5×10^5	7	19	12	1.56	10.3
C57-247	RT	1.5×10^5	10	19	-	0.35	6.07
C57-248	RT	1.5×10^5	10	19	-	0.51	6.1
C57-250	RT	1.5×10^5	10	20	-	0.475	5.66
C57-251	control	1.5×10^5	-	19	-	0.62	11.9
C57-252	control	1.5×10^5	-	20	-	1.59	37.5
C57-253	control	1.5×10^5	-	20	-	1.9	15.8
C57-254	control	1.5×10^5	-	19	-	0.82	26.2

Table A-5: Mouse data – Immune assay

mouse	treatment	implanted cell amount	treatment start (days after tumor inoculation)	trail length (days)	treatment length (days)	tumor volume day 7 (mm³)	tumor volume day 20 (mm³)
C57-267	RT + NOX-A12	1.5×10^5	7	20	13	0.55	4.7
C57-268	RT + NOX-A12	1.5×10^5	7	20	13	undef	3.15
C57-269	RT	1.5×10^5	10	21	-	undef	2.49
C57-270	RT	1.5×10^5	10	20	-	undef	3.69
C57-271	RT + NOX-A12	1.5×10^5	7	20	13	0.63	1.36
C57-272	RT	1.5×10^5	10	20	-	1.54	3
C57-273	RT + NOX-A12	1.5×10^5	7	20	13	undef	3.05
C57-274	RT	1.5×10^5	10	21	-	0.78	3.56
C57-275	control	1.5×10^5	-	20	-	0.88	27.2
C57-276	control	1.5×10^5	-	20	-	0.68	13.6

mouse	treatment	implanted cell amount	treatment start (days after tumor inoculation)	trail length (days)	treatment length (days)	tumor volume day 7 (mm³)	tumor volume day 20 (mm³)
C57-277	NOX-A12	1.5×10^5	7	21	14	undef	9.48
C57-278	control	1.5×10^5	-	20	-	undef	24.1
C57-279	NOX-A12	1.5×10^5	7	21	14	0.65	21
C57-280	NOX-A12	1.5×10^5	7	21	14	undef	7
C57-281	control	1.5×10^5	-	20	-	2.05	16.2
C57-282	NOX-A12	1.5×10^5	7	21	14	2.58	1.03
C57-283	control	1.5×10^5	-	20	-	undef	6.83
C57-284	control	1.5×10^5	-	20	-	undef	27.3
C57-285	NOX-A12	1.5×10^5	7	20	13	undef	10.2
C57-286	control	1.5×10^5	-	20	-	0.72	15.3
C57-287	NOX-A12	1.5×10^5	7	20	13	undef	9.29
C57-288	control	1.5×10^5	-	20	-	0.51	30.3
C57-289	NOX-A12	1.5×10^5	7	20	13	undef	9.05
C57-290	NOX-A12	1.5×10^5	7	20	13	0.6	8.1
C57-291	RT + NOX-A12	1.5×10^5	7	20	13	1.13	4.21
C57-292	RT	1.5×10^5	10	20	-	undef	5.5
C57-293	RT + NOX-A12	1.5×10^5	7	20	13	undef	3.68
C57-294	RT	1.5×10^5	10	20	-	undef	7.93
C57-295	RT + NOX-A12	1.5×10^5	7	20	13	1.74	5.94
C57-296	RT + NOX-A12	1.5×10^5	7	20	13	undef	2.96
C57-297	RT	1.5×10^5	10	20	-	1.28	4.49
C57-298	RT	1.5×10^5	10	20	-	undef	5.55

Table A-6: Treatment groups–survival data

* p ≤ 0.05; ** p ≤ 0.01; *** p ≤ 0.001

treatment	N animals	median survival (days)	N survival animals	comparison of survival curves	comparison treatment	p-value Log-rank (Mantel-Cox) test	Are the survival curves sig different?
control	15	26	0				
RT (1x 12 Gy)	8	57.5	2	vs.	control	≤ 0.0001	***
1x 20 Gy	6	93.5	3	vs.	control	≤ 0.0001	***
				vs.	RT (1x 12 Gy)	0.3156	
2x 10 Gy	6	85	3	vs.	control	≤ 0.0001	***
				vs.	RT (1x 12 Gy)	0.3593	
				vs.	1x 20 Gy	0.9377	
NOX-A12	9	28	0	vs.	control	0.6486	
mNOX-E36	9	23	0	vs.	control	0.5253	
				vs.	NOX-A12	0.0402	*
Anti-PD1	9	32	2	vs.	control	0.0251	*
				vs.	RT (1x 12 Gy)	0.0282 Gehan-Breslow-Wilcoxon test	*
				vs.	NOX-A12	0.0673	
				vs.	mNOX-E36	0.0133	*
NOX-A12 + Anti-PD1	9	42	2	vs.	control	0.0029	**
				vs.	NOX-A12	0.0063	**
				vs.	Anti-PD1	0.6687	
mNOX-E36 + Anti-PD1	9	35	1	vs.	control	0.0067	**
				vs.	mNOX-E36	0.0010	***
				vs.	Anti-PD1	0.9769	
RT + Anti-PD1	12	undefined	10	vs.	control	< 0.0001	***
				vs.	RT (1x 12 Gy)	0.0035	**
				vs.	Anti-PD1	0.0009	***
RT + NOX-A12	10	99	5	vs.	control	< 0.0001	***
				vs.	RT (1x 12 Gy)	0.1959	
				vs.	NOX-A12	< 0. 0001	***
RT + NOX-A12 + Anti-PD1	12	undefined	7	vs.	RT (1x 12 Gy)	0.0632	
				vs.	RT + Anti-PD1	0.1916	
				vs.	RT + NOX-A12	0.7003	
				vs.	NOX-A12 + Anti-PD1	0.0131	*

teatment	N animals	median survival (days)	N survival animals	comparison of survival curves	comparison treatment	p-value Log-rank (Mantel-Cox) test	Are the survival curves sig different?
RT + mNOX-E36	12	64.5	2	vs.	control	< 0.0001	***
				vs.	RT (1x 12 Gy)	0.8689	
				vs.	mNOX-E36	< 0. 0001	***
RT + mNOX-E36 + Anti-PD1	12	undefined	10	vs.	RT (1x 12 Gy)	0.4164	
				vs.	RT + Anti-PD1	0.9808	
				vs.	mNOX-E36 + Anti-PD1	0.2708	
RT + NOX-A12 + NOX-E36 + Anti-PD1	9	undefined	5	vs.	RT (1x 12 Gy)	0.1250	
				vs.	RT + Anti-PD1	0.1448	
				vs.	RT + NOX-A12	0.9283	
				vs.	RT + mNOX-E36	0.0578	
				vs.	RT + NOX-A12 + Anti-PD1	0.8768	
				vs.	RT + mNOX-E36 + Anti-PD1	0.1448	

10 CURRICULUM VITAE

PARTICULARS

last and first name:	Link, Barbara
date of birth:	13.05.1985
place of birth:	Hardheim

SCHOOL CAREER

1995 – 2001	Realschule Hardheim - Middle School
2001 - 2004	Frankenlandschule Walldürn – Commercial high school
June 29, 2004	University-entrance qualification Grade: 1.7

UNIVERSITY CAREER

2004 - 2008	Pädagogische Hochschule Heidelberg - University of Education Heidelberg Teacher for middle schools - mathematics, biology, chemistry
November 14, 2008	1. State examination teacher for middle schools Grade: 1,9
2011 – 2014	Hochschule Mannheim - Mannheim University of Applied Sciences Biotechnology, Bachelor of Science
March – September 2013	Internship German Cancer Research Center/National Center for Tumor Diseases Heidelberg, Department of Translational Oncology, Section Molecular and Gene Therapy *Sensitivity investigation of various integration sites analysis methods in preclinical gene therapy studies*
April – September 2014	Bachelor thesis German Cancer Research Center/National Center for Tumor Diseases Heidelberg, Department of Translational Oncology, Section Molecular and Gene Therapy Title: *Integration site analysis of wtHIV using LAM-PCR and Next Generation Sequencing*
December 10, 2014	Biotechnology, Bachelor of Science Grade: 1,7
2015 – 2017	Hochschule Mannheim - Mannheim University of Applied Sciences Biotechnology- Biomedical Science and Technology, Master of Science
September – February 2017	Master thesis University Medical Centre Mannheim, Clinic for Radiotherapy and Radiooncology, Translational Radiation Oncology sponsored by Carl Zeiss Meditec, Oberkochen

Title: *Antitumor immune responses of glioblastoma patients after intraoperative radiotherapy with INTRABEAM*

21. Februar 2017	Biotechnology- Biomedical Science and Technology, Master of Science Grade: 1,5

PROFESSIONAL ACTIVITY

2009 - 2010	Realschule am Karlsberg, Crailsheim – trainee teacher
2010	Realschule Krautheim - trainee teacher
2020 - 2023	University Hospital Bonn (UKB), Rheinische Friedrich-Wilhelms Universität Bonn, Clinic for Radiotherapy and Radiooncology, Experimental Radiobiology – research associate
2023 - today	University Medical Centre Mannheim, Clinic for Radiotherapy and Radiooncology, Laboratory for Radiobiology – research associate

PUBLICATIONS

1. Giordano, Frank A.; Appelt, Jens-Uwe; *Link, Barbara*; Gerdes, Sebastian; Lehrer, Christina; Scholz, Simone et al. (2015): High-throughput monitoring of integration site clonality in preclinical and clinical gene therapy studies. In: Molecular Therapy-Methods & Clinical Development 2. DOI: 10.1038/mtm.2014.61.
2. Giordano, Frank A.; *Link, Barbara*; Glas, Martin; Herrlinger, Ulrich; Wenz, Frederik; Umansky, Viktor et al. (2019): Targeting the Post-Irradiation Tumor Microenvironment in Glioblastoma via Inhibition of CXCL12. In: Cancers 11 (3). DOI: 10.3390/cancers11030272.
3. Torres Crigna, Adriana; *Link, Barbara*; Samec, Marek; Giordano, Frank A.; Kubatka, Peter; Golubnitschaja, Olga (2021): Endothelin-1 axes in the framework of predictive, preventive and personalised (3P) medicine. In: EPMA JOURNAL 12 (3), S. 265–305. DOI: 10.1007/s13167-021-00248-z.
4. *Link, Barbara*; Torres Crigna, Adriana; Hölzel, Michael; Giordano, Frank A.; Golubnitschaja, Olga (2021): Abscopal Effects in Metastatic Cancer: Is a Predictive Approach Possible to Improve Individual Outcomes? In: Journal of clinical medicine 10 (21). DOI: 10.3390/jcm10215124
5. Kubatka, Peter; Mazurakova, Alena; Koklesova, Lenka; Samec, Marek; Sokol, Juraj; Samuel, Samson Mathews; Kudela, Erik; Biringer, Kamil; Bugos, Ondrej; Pec, Martin; *Link, Barbara* et al. (2022). Antithrombotic and antiplatelet effects of plant-derived compounds: a great utility potential for primary, secondary, and tertiary care in the framework of 3P medicine. EPMA J 13, 407-431. 10.1007/s13167-022-00293-2

11 ACKNOWLEDGEMENTS